PB-241 390

SELECT RESEARCH GROUP IN AIR POLLUTION METEOROLOGY, SECOND ANNUAL PROGRESS REPORT

VOLUME I

The Pennsylvania State University

Prepared for
National Environmental Research Center

September 1974

DISTRIBUTED BY:

NTIS
National Technical Information Service
U. S. DEPARTMENT OF COMMERCE

TECHNICAL REPORT DATA

(Please read Instructions on the reverse before comp

PB 241 390

1. REPORT NO.
EPA-650/4-74-045-a

2.

4. TITLE AND SUBTITLE
Select Research Group in Air Pollution Meteorology,
Second Annual Progress Report: Volume I

5. REPORT DATE
September 1974

6. PERFORMING ORGANIZATION CODE

7. AUTHOR(S)
Select Research Group

8. PERFORMING ORGANIZATION REPORT NO.

9. PERFORMING ORGANIZATION NAME AND ADDRESS
Department of Meteorology and Center for Air
Environment Studies, The Pennsylvania State
University, University Park, PA 16802

10. PROGRAM ELEMENT NO.
1AA009

11. CONTRACT/GRANT NO.
R-800397

12. SPONSORING AGENCY NAME AND ADDRESS
Environmental Protection Agency
National Environmental Research Center
Meteorology Laboratory
Research Triangle Park, North Carolina 27711

13. TYPE OF REPORT AND PERIOD COVERED
Annual Progress 6/1/73-9/30/74

14. SPONSORING AGENCY CODE

15. SUPPLEMENTARY NOTES
Issued as Volume I of 2 Volumes
The First Annual Report is not available to the public.

16. ABSTRACT

Progress reports are included by the SRG task groups involved in: the development of mesoscale air pollution related prediction models, modeling of planetary boundary layer (PBL) turbulence and structure, the analysis of acdar signals for wind and temperature measurements in the PBL, studies of atmospheric aerosol properties and aerosol-atmosphere interactions, and airborne measurements on the urban to mesoscale of atmospheric aerosol, turbulence and radiation.

Reproduced by
NATIONAL TECHNICAL
INFORMATION SERVICE
US Department of Commerce
Springfield, VA. 22151

17. KEY WORDS AND DOCUMENT ANALYSIS

a. DESCRIPTORS	b. IDENTIFIERS/OPEN ENDED TERMS	c. COSATI Field/Group
Mesoscale Prediction Models Boundary Layer Modeling Pollutant Removal Processes Acdar, Acoustic Sounding Airborne Measurements		

PRICES SUBJECT TO CHANGE

18. DISTRIBUTION STATEMENT
Unlimited

19. SECURITY CLASS *(This Report)*
Unclassified

20. SECURITY CLASS *(This page)*
Unclassified

21. NO. OF PAGES
289

22. PRICE
$10.25-2.25

EPA Form 2220-1 (9-73)

EPA-650/4-74-045-a

SELECT RESEARCH GROUP IN AIR POLLUTION METEOROLOGY, SECOND ANNUAL PROGRESS REPORT: VOLUME I

by

Select Research Group

Department of Meteorology and
Center for Air Environment Studies
The Pennsylvania State University
University Park, Pennsylvania 16802

Grant No. R-800397
Program Element No. 1AA009
ROAP No. 21ADO
Task No. 14

Project Officer: Kenneth L. Calder

Meteorology Laboratory
National Environmental Research Center
Research Triangle Park, North Carolina 27711

Prepared for

OFFICE OF RESEARCH AND DEVELOPMENT
ENVIRONMENTAL PROTECTION AGENCY
WASHINGTON, D.C. 20460

September 1974

This report has been reviewed by the Environmental Protection Agency and approved for publication. Approval does not signify that the contents necessarily reflect the views and policies of the Agency, nor does mention of trade names or commercial products constitute endorsement or recommendation for use.

ACKNOWLEDGEMENT

The Select Research Group gratefully acknowledges the financial support provided by research grant No. R800397 from the office of Research and Development, Environmental Protection Agency. The group also appreciates the financial support and use of facilities from the Department of Meteorology and the Center for Air Environment Studies of The Pennsylvania State University.

An interdisciplinary research program such as the SRG effort cannot possibly succeed without the contributions of the many individuals who assisted on this project. The group wishes to particularly thank the many faculty and staff members and graduate students for their assistance.

Preceding page blank

TABLE OF CONTENTS

VOLUME I (of 2 Volumes)

Page

ACKNOWLEDGEMENTS v
CONTENTS OF VOLUME II ix
LIST OF FIGURES xii

I INTRODUCTION AND SCIENTIFIC OBJECTIVES 1

II THE DEVELOPMENT OF MESOSCALE MODELS SUITABLE FOR AIR POLLUTION STUDIES 6

ACKNOWLEDGEMENTS 7

1.0 INTRODUCTION 8

- 1.1 Potential use for regional and urban dynamical prediction models 8
- 1.2 Some general considerations of the mesoscale predictability problem 10
- 1.3 Overview of mesoscale modeling effort 14

2.0 THE REGIONAL MODEL 16

- 2.1 The basic equations in sigma coordinates for a Lambert Conformal map projection 16
- 2.2 The horizontal and vertical grid structures 20
- 2.3 Finite difference equations 21
- 2.4 The two-dimensional analog 24
- 2.5 Kinetic energy budget equations for 2-D and 3-D models 25
- 2.6 Lateral boundary conditions 28
  - 2.6.1 Equations for mean motion over domain 29
  - 2.6.2 Lateral boundary conditions for the 2-D model 34
  - 2.6.3 Lateral boundary conditions for the 3-D model 36
- 2.7 Initial conditions 37
- 2.8 Two-dimensional flow across the Appalachian terrain 38
  - 2.8.1 Specifications of the 2-D experiments 39
  - 2.8.2 Results with geostrophic initial conditions 43
  - 2.8.3 Initialization of the boundary layer winds considering the effects of surface friction 49

APPENDIX - CHAPTER 2.0 57

TABLE OF CONTENTS

VOLUME I (of 2 Volumes)

Page
ACKNOWLEDGEMENTS v
CONTENTS OF VOLUME II.. ix
LIST OF FIGURES xii

I INTRODUCTION AND SCIENTIFIC OBJECTIVES.................... 1

II THE DEVELOPMENT OF MESOSCALE MODELS SUITABLE FOR AIR POLLUTION STUDIES.................................... 6

ACKNOWLEDGEMENTS 7

1.0 INTRODUCTION 8

1.1 Potential use for regional and urban dynamical prediction models 8
1.2 Some general considerations of the mesoscale predictability problem 10
1.3 Overview of mesoscale modeling effort............ 14

2.0 THE REGIONAL MODEL 16

2.1 The basic equations in sigma coordinates for a Lambert Conformal map projection................ 16
2.2 The horizontal and vertical grid structures....... 20
2.3 Finite difference equations...................... 21
2.4 The two-dimensional analog 24
2.5 Kinetic energy budget equations for 2-D and 3-D models 25
2.6 Lateral boundary conditions...................... 28
  2.6.1 Equations for mean motion over domain...... 29
  2.6.2 Lateral boundary conditions for the 2-D model.................................... 34
  2.6.3 Lateral boundary conditions for the 3-D model.................................... 36
2.7 Initial conditions.............................. 37
2.8 Two-dimensional flow across the Appalachian terrain 38
  2.8.1 Specifications of the 2-D experiments...... 39
  2.8.2 Results with geostrophic initial conditions................................ 43
  2.8.3 Initialization of the boundary layer winds considering the effects of surface friction 49

APPENDIX - CHAPTER 2.0.............................. 57

Page

3.0 PRELIMINARY THREE-DIMENSIONAL EXPERIMENT USING REAL DATA WITH AND WITHOUT TERRAIN 62

3.1 Synoptic Discussion on 12Z Oct. 16 - 00Z Oct. 17, 1973.................................... 63
3.2 Initialization and verification analyses and specification of time-dependent boundary conditions. 67
3.3 Specification of parameters.......................... 75
3.4 Qualitative discussion of results.................. 77
3.4.1 Low-level results.......................... 77
3.4.2 Middle level results........................ 82
3.4.3 Upper level results......................... 84
3.5 Budget equations for the model domain and the implications of the lateral boundary conditions..... 84
3.5.1 Mean kinetic energy budget for the 12-hour forecast period............................ 87
3.5.2 Time variation of the mean motion............ 89

4.0 NUMERICAL EXPERIMENTS WITH A TWO-DIMENSIONAL NESTED GRID. 97

4.1 The basic equations................................ 98
4.2 The meshed grid system 99
4.3 Experimental results............................... 103
4.3.1 Background experiment with uniform mesh...... 103
4.3.2 The treatment of the interface momentum points in the meshed grid experiments........ 104
4.3.3 Meshed grid experiments with a mean wind of 10 ms^{-1} 110
4.3.4 Experiment with mutually interacting grids with the fine mesh moving through the coarse mesh................................ 112
4.4 Mesh grid experiments initialized with Haurwitz waves...................................... 116
4.4.1 Initial conditions and the linear solutions.................................. 117
4.4.2 Quantitative analysis of errors.............. 123
4.4.3 Long-wave results: Exp. 1-5................. 125
4.4.4 Short wave results: Exp. 6-8................ 140
4.4.5 Mixed long and short wave results........... 149

5.0 INVESTIGATION OF SEMI-IMPLICIT MODELS................... 158

5.1 Advantages of semi-implicit models over explicit models 158
5.2 Comparison of one-dimensional explicit and semi-implicit shallow fluid model.................. 160
5.2.1 Development of explicit model................ 160
5.2.2 Development of semi-implicit model........... 161
5.2.3 Initialization of models..................... 165
5.2.4 Results...................................... 165

Page

5.3 Comparison of two-dimensional explicit and semi-implicit models.......................... 171
5.3.1 Development of the two-dimensional S.I. model............................ 171
5.3.2 Initialization 175
5.3.3 Results................................ 176
5.4 Conclusions of preliminary tests of semi-implicit models 186

APPENDIX - CHAPTER 5.............................. 187

6.0 DETERMINATION OF INITIAL DATA REQUIREMENTS.......... 190

6.1 Development of Stochastic-Dynamic Equations··· 192
6.2 Initialization Procedure ···················· 203
6.3 Energetics of the model······················ 208
6.4 Interpretation of Predicted Variances········· 210
6.5 Pure gravity wave experiments················· 211
6.6 A Monte Carlo comparison····················· 219
6.7 Synoptic Scale Error Compatability············ 224
6.8 Summary and Plans for Future Research ········ 229

REFERENCES... 232

7.0 EXPERIMENTS WITH SIMPLIFIED SECOND-MOMENT APPROXIMATIONS FOR USE IN REGIONAL SCALE MODELS...... 234

7.1 Introduction................................. 234
7.2 The "Poor Man's Method"........................ 236
7.3 Semicomprehensive Methods...................... 244

ACKNOWLEDGEMENTS................................... 270

REFERENCES... 271

TABLE OF CONTENTS

VOLUME II (of 2 Volumes)

Page

ACKNOWLEDGEMENTS v

CONTENTS OF VOLUME I.. ix

LIST OF FIGURES xii

III TASK 1-C BOUNDARY LAYER MODELING 272

1.0 SUMMARY OF PROGRESS 273

2.0 SHORT-TERM FORECASTS OF TEMPERATURE AND MIXING HEIGHT ON SUNNY DAYS 275

3.0 ATMOSPHERIC TURBULENCE MODELING 281

4.0 ATMOSPHERIC BOUNDARY LAYERS AND THE PRESSURE GRADIENT-VELOCITY CORRELATION MODEL 284

5.0 NUMERICAL MODELING OF TURBULENCE FLOWS 289

6.0 MODELING TURBULENT FLUX OF PASSIVE SCALAR QUANTITIES IN INHOMOGENEOUS FLOWS 293

7.0 EULERIAN AND LAGRANGIAN TIME MICROSCALES IN ISOTROPIC TURBULENCE 304

8.0 NOTES ON TURBULENT FLOW IN TWO AND THREE DIMENSIONS 313

IV SRG ON AIR-POLLUTION METEOROLOGY 326

Part 1

1.0 ATMOSPHERIC EFFECTS ON PARTICULATE POLLUTANTS 327
  1.1 The sampling program 329
  1.2 Chemical analysis of particulate matter 331
  1.3 The numerical modeling program 334
  1.4 Progress in field sampling of agglomeration 337

REFERENCES 341

Part 2

1.0 ATMOSPHERIC REMOVAL PROCESSES FOR AIR POLLUTANTS 349
  1.1 Synopsis 350
  1.2 Personnel 351
  1.3 Accomplishments 352
    1.3.1 Global Emissions and Natural Processes For Removal of Gaseous Pollutants 352
    1.3.2 Rock 416
    1.3.3 SO_2 Solubility 419
    1.3.4 Rate of SO_2 absorption by sea water 426

REFERENCES 431

Page

V OBSERVING SYSTEMS FOR URBAN AND REGIONAL ENVIRONMENTS........ 433

Part 1

Preface.. 434

1.0 TASK 1-D INTERPRETATION OF ACDAR SOUNDING OBSERVATIONS.. 437
  1.1 Introduction...................................... 437

2.0 ANALYSIS OF DOPPER-SHIFTED MONOSTATIC ACDAR SIGNALS 441
  2.1 System geometry 441
  2.2 Surfaces of constant Doppler Shift 444
  2.3 Horizontal wind................................... 450
  2.4 Antenna weighting................................. 465
  2.5 Total spectrum.................................... 468
  2.6 With antenna weighting............................ 475
  2.7 Wind shear included 483

3.0 MONTE CARLO METHOD FOR EVALUATING ACDAR SCATTERING VOLUMES AND SYSTEM FUNCTIONS................. 503

4.0 MEASUREMENTS OF SOUND REFRACTIVELY TRANSMITTED IN THE PLANETARY BOUNDARY LAYER 510
  4.1 Introduction...................................... 510
  4.2 System description................................ 510
  4.3 Measurement of inversion layer temperature gradients... 517
  4.4 Fluctuations of signal levels and possible association with atmospheric gravity wave motions... 520

REFERENCES... 526

5.0 TEMPERATURE PROFILE MEASUREMENTS IN INVERSIONS FROM REFRACTIVE TRANSMISSION OF SOUND.................. 527

6.0 ANALYSIS AND SIMULATION OF PHASE-COHERENT ACDAR SOUNDING MEASUREMENTS............................. 547

Part 2

1.0 AIRBORNE MEASUREMENT SYSTEMS............................ 592
  1.1 Introductory Remarks.............................. 593

2.0 PSU ISOKINETIC INTAKE FOR AIRBORNE AIR SAMPLING......... 594
  2.1 Design of the PSU Model II Probe.................. 595
  2.2 Sampler Performance............................... 600
  2.3 Conclusions....................................... 602

Page

3.0 INSTRUMENTATION FOR MULTIWAVELENGTH AIRBORNE PRECISION SPECTRAL RADIOMETER MEASUREMENTS 604
    3.1 The radiometers 604
    3.2 Radiometer mounting 610
    3.3 Radiometer signal conditioning 612
    3.4 Correction of radiometer outputs 619
    3.5 Data analysis 621

REFERENCES 622

4.0 AIRBORNE MEASUREMENTS OF TURBULENCE IN THE PLANETARY BOUNDARY LAYER 623

5.0 AIRBORNE MEASUREMENTS OF AEROSOL IN THE ST. LOUIS URBAN AREA 633

6.0 SURFACE MEASUREMENTS OF AEROSOL IN A RURAL AREA USING DIFFERENT METHODS 641
    6.1 Introduction 641
    6.2 Instrumentation 641
    6.3 Summary of a selected data 643

7.0 TECHNIQUES FOR THE "MESOSCALE" INTERPRETATION OF AIRCRAFT MEASUREMENTS 651

VI OTHER CONTRIBUTIONS 659

Part 1

1.0 A GENERAL APPROACH TO DIFFUSION FROM CONTINUOUS SOURCES 660
    1.1 Theory 660
    1.2 Analysis 662

Part 2

2.0 THE NIGHT-TIME MIXING DEPTH AT PHILADELPHIA 666
    2.1 Introduction 667
    2.2 Analysis of observations 668
    2.3 Results 668

Part 3

3.0 SO_2 CONCENTRATIONS AT KEYSTONE, PA 671
    3.1 The purpose of the project 672
    3.2 Analysis 672

LIST OF FIGURES

VOLUME I

No. Title Page

Chapter I

I SRG Task Group Organization and Interactions 2

Chapter II - Part 2

2.1 30 x 50 grid on Lambert Conformal map projection.... 18

2.2 Error in geostrophic wind as a function of horizontal distance for a 1°C temperature error integrated over 200 mb depths centered at 300, 500, 700 and 900 mb.......................... 32

2.3 Magnitude of acceleration due to boundary flux of momentum as function of wind speed and domain size (L) The isotachs are labeled in ms^{-1}...................... 35

2.4 Temperature sounding for Washington, D. C., 12Z Oct. 16, 1973.................................. 40

2.5 Time-averaged vertical cross section of u for Exp. 2D-1 44

2.6 Time-averaged vertical cross section temperature departure from Exp. 2D-1 45

2.7 Time-averaged vertical cross section of vertical velocity (cm s^{-1}) for Exp. 2D-1........... 46

2.8 Kinetic energy budget for Exp. 2D-1................ 48

2.9 East-west profiles of u-component in boundary layer at various times in Exp. 2D-1................ 50

2.10 Hodograph of non-linear solution to simplified boundary layer equations with geostrophic initial conditions.. 53

2.11 Hodograph of non-linear solution of simplified boundary layer equations with initial conditions given by linear solution.......................... 55

2.12 East-west profiles of u-component in boundary layer at various times in Exp. 2D-2................ 56

No. Title Page

CHAPTER II - Part 3

3.1 The 850 mb analysis for 12Z Oct. 16, 1973 65
3.2 The 850 mb analysis for 00Z Oct. 17, 1973 66
3.3 The 500 mb analysis for 12Z Oct. 16, 1973 68
3.4 The 500 mb analysis for 00Z Oct. 17, 1973 69
3.5 The 300 mb analysis for 12Z Oct. 16, 1973 70
3.6 The 300 mb analysis for 00Z Oct. 17, 1973 71
3.7 Observed u-component and geostrophic u-component at level 2 ($\sigma = 0.325$) at $t = 0$ 73
3.8 Forecast 12-hour surface pressure change (mb) for Exp. 1 ending 00Z Oct. 17, 1973 78
3.9 Observed 12-hour surface pressure change (mb) ending 00Z Oct. 17, 1973 79
3.10 Twelve-hour forecast velocities at level 6 ($\sigma = 0.925$, $\bar{p} = 939$ mb) from Exp. 1. Contours of terrain are labeled in m 80
3.11 Twelve-hour forecast velocities at level 6 ($\sigma = 0.925$, $\bar{p} = 929$ mb) from Exp. 1A, no terrain 80
3.12 Verficiation velocities at level 6 ($\sigma = 0.925$, $\bar{p} = 929$ mb) from interpolation of synoptic analysis to mesoscale grid 81
3.13 Twelve-hour forecast velocities at level 4 ($\sigma = 0.625$, $\bar{p} = 709$ mb) from Exp. 1 83
3.14 Twelve-hour forecast velocities at level 4 ($\sigma = 0.625$, $\bar{p} = 709$ mb) from Exp. 1, no terrain 83
3.15 Twelve-hour forecast velocities at level 2 ($\sigma = 0.325$, $\bar{p} - 489$ mb) from Exp. 1 85
3.16 Twelve hour forecast velocities at level 2 ($\sigma = 0.325$, $\bar{p} = 489$ mb) 85

No. Title Page

3.17 Twelve-hour forecast temperature change at level 2 ($\bar{p}$ - 489 mb) from Exp. 1A, no terrain.............. 86

3.18 Twelve-hour forecast temperature change at level 2 ($\bar{p}$ - 489 mb) from Exp. 1, with terrain............. 86

3.19 Components of kinetic energet budget from Exp. 1 and 1A.................................... 88

3.20 Solution of mean vector motion over domain for constant $\underset{\sim}{B}$ and $\underset{\sim}{V}_g$ 91

3.21 Components B_u/f and B_v/f (mean non-linear accelerations scaled by f) for Exp. 1A..................... 93

3.22 Hodograph of mean wind (V), mean geostrophic wind (V_g), and $-i\underset{\sim}{B}/f$ for various times in Exp. 1a at level 1 ($\bar{p}$ = 342 mb)............................ 94

3.23 $\underset{\sim}{V}_g$ at t = 0 and t = 12 hours and hodograph of mean velocity, $\underset{\sim}{V}$ for 12-hour forecast, Exp. 1A.......... 95

CHAPTER II - Part 4

4.1 Boxes representing incremental volumes of mass in the 4:1 meshed grid system......................... 100

4.2 Boxes representing incremental volumes of momentum in the 4:1 meshed grid system..................... 100

4.3 Time variation of total energy in uniform CMG experiment (Exp. 1).............................. 105

4.4 Time variation of total energy in Exp. 2-7......... 107

4.5 Time variation of total energy and maximum v-component in Exp. 8, 9, 10...................... 111

4.6 Illustration of movement of FMG within CMG......... 114

4.7 Time variation of total energy and maximum north-south velocity component in Exp. 11................ 115

4.8 Initial height and vorticity field on CMG for Exp. 1-5.. 127

4.9 Initial u- and v-component fields on CMG for Exp. 1-5.. 128

No.	Title	Page
4.10	Initial height and vorticity field on CMG for Exp. 1-5..................................	129
4.11	Initial u- and v-component fields on CMG for Exp. 1-5..................................	130
4.12	Forecast height and vorticity fields on CMG for Exp. 1..................................	131
4.13	Forecast u- and v-component fields on CMG for Exp. 1..................................	132
4.14	Forecast relative vorticity and height field in Exp. 2 (1-way no diffusion).......................	134
4.15	Forecast relative vorticity and height field in Exp. 3 (2-way no diffusion).......................	135
4.16	Forecast relative vorticity and height field in Exp. 4 (1-way with diffusion).....................	136
4.17	Forecast relative vorticity and height field in Exp. 5 (2-way with diffusion).....................	137
4.18	Initial height and v-component field on CMG for for Exp. 6-8..................................	141
4.19	Initial height and v-component field on FMG for Exp. 6-8..................................	142
4.20	Forecast v-component and height field on FMG at 6 hours for Exp. 7 (1-way with diffusion)..........	144
4.21	Forecast v-component and height field on FMG at 6 hours for Exp. 8 (2-way with diffusion)..........	145
4.22	Forecast v-component and height field on FMG at 12 hours for Exp. 7 (1-way with diffusion).........	146
4.23	Forecast v-component and height field on FMG at 12 hours for Exp. 8 (2-way with diffusion).........	147
4.24	Ratio of variance to MSE for Exp. 6-8.............	148
4.25	Initial ϕ for Experiments 9-11 (mixed long and short wave)..	150
4.26	Initial v-component for Exp. 9-11 (mixed long and short waves)..................................	152

No.	Title	Page
4.27	Forecast v-component at 13.3 h from Exp. 9 (uniform FMG)......................................	153
4.28	Forecast v-component at 13.3 h from Exp. 10 (1-way meshed system).............................	154
4.29	Forecast v-component at 13.3 h from Exp. 11 (2-way meshed system).............................	155

CHAPTER II - Part 5

No.	Title	Page
5.1	Comparison of one dimensional explicit and S.I. forecasts at 24 hours.............................	167
5.2	Number of iterations required per time step as a function of α for four different first guesses.....	170
5.3	Two dimensional staggered grid....................	174
5.4	Twenty-five hour forecast of h by explicit model...	178
5.5	"Error" height fields for the explicit model at 25 hours...	181
5.6	"Error" height fields for the S.I. model at 25 hours...	182
5.7	Root-mean square differences between explicit and S.I. model height forecasts and the linear solution...	183
5.8	Number of iterations required per time step as a function of α for 2 different first guesses........	185

CHAPTER II - Part 6

No.	Title	Page
6.1	Spatial and temporal variation of σ_u, σ_h, and h for the pure gravity wave integration. Graph (a) pertains to 0 minutes; (b) 10 minutes; (c) 20 minutes; and (d) 30 minutes.......................	213
6.2	Spatial and temporal variation of the standard deviations of u and h during the first five minutes of the pure gravity wave integration. Curves are labeled in minutes....................	214

No.	Title	Page
6.3	Time variation of the certain energy modes. TCE is the total certain energy, CPE is the certain potential energy and CKE is the certain kinetic energy....................................	216
6.4	Time variation of the uncertain energy modes. TUE is the total uncertain energy, UPE is the uncertain potential energy and UKE is the uncertain kinetic energy. TCE, the total certain energy, is included for comparison with the total uncertain energy.....................	217
6.5	Time variation of the total energy modes. TPE is the total potential energy, TKE is the total kinetic energy and TE is the total energy...........	218
6.6	Monte Carlo solution with 500 trials (dashed line) and the stochastic-dynamic solution after 20 minutes of integration for conditions of pure gravity wave motion...	221
6.7	Monte Carlo solution with 500 trials (dashed line) and the stochastic-dynamic solution after 30 minutes of integration for conditions of pure gravity wave motion...	222
6.8	Transition of the uncertain kinetic energy of the v velocity component for various initial, standard errors of the v component. The curves are labeled in terms of the magnitude of the standard deviation of the initial v error, in m s^{-1}. The initial standard deviation of the equivalent temperature error was 1°C......................................	228
6.9	Transition of the standard deviation of v in terms of its spatial average for various initial, standard errors of the v component. The curves are labeled in terms of the magnitude of the standard deviation of the initial v error, in m s^{-1}. The initial standard deviation of the equivalent temperature error was 1°C......................................	230

No. Title Page

CHAPTER II - Part 7

1. Buoyancy Compensation 248

2. Comparison of predicted relation between σ_w/u_* and z/L with observations from the AFCRL Kansas 1968 Field Program 263

3. Comparison of predicted relation between $1/\phi_m$ (unstable side) or ϕ_m (stable side) and z/L with observations from the AFRCL Kansas 1968 Field Program 264

4. Comparison of predicted relation between $1/\phi_h$ (unstable side) or ϕ_h (stable side) and z/L with observations from the AFCRL Kansas 1968 Field Program 265

5. Comparison of predicted relation between $|\sigma_\theta/T_*|$ and z/L with observations from the AFCRL Kansas 1968 Field Program 266

6. Comparison of predicted relation between $R_i/(z/L)$ and z/L with observations from the AFCRL Kansas 1968 Field Program 267

7. Comparison of predicted relation between $-\overline{u\theta'}/\overline{w\theta'}$ and z/L with observations from the AFCRL Kansas 1968 Field Program 268

I INTRODUCTION AND SCIENTIFIC OBJECTIVES

The "Select Research Group in Air Pollution Meteorology" (SRG) sponsored by the U. S. Environmental Protection Agency (EPA) under the auspices of the Meteorology Laboratory was established to identify and research long range, interdisciplinary problems in air pollution meteorology. Following national competition, the proposal by The Pennsylvania State University for a five year program was selected and first funded in May, 1972.

This report is a progress report from the SRG which summarizes, in particular, research activities it conducted and work it completed during the IInd year of the grant program.

The primary objective of the SRG program is to develop a comprehensive air pollution model which can be used to examine fundamental problems which require solutions in order for operational air pollution prediction models to be constructed and used. Clearly, a control agency such as the EPA must have the capability of quantitatively relating air pollution sources to their subsequent distribution in an urban or regional environment.

The development, testing, and evaluation of a regional model by the SRG (Task Group 1A) is, of necessity, an intra and interdisciplinary enterprise (see Fig. I). The design and coding of the basic numerical model requires, firstly, expertise in numerical weather prediction and dynamic and synoptic meteorology.

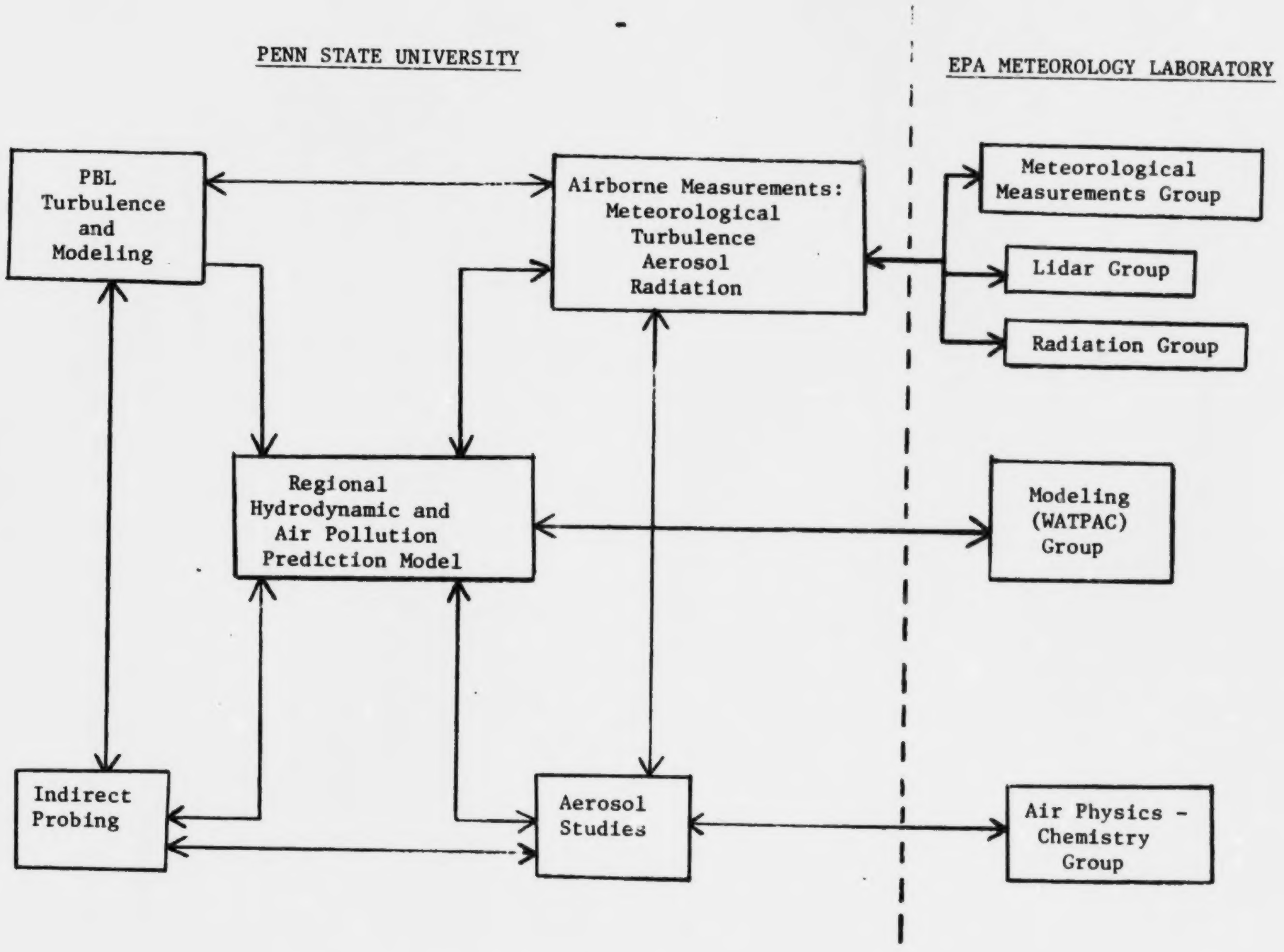
PENN STATE UNIVERSITY
EPA METEOROLOGY LABORATORY
PBL Turbulence and Modeling
Airborne Measurements: Meteorological Turbulence Aerosol Radiation
Meteorological Measurements Group
Lidar Group
Radiation Group
Regional Hydrodynamic and Air Pollution Prediction Model
Modeling (WATPAC) Group
Indirect Probing
Aerosol Studies
Air Physics - Chemistry Group

FIGURE I: SRG Task Group Organization and Interactions

Since many of the important physical processes which determine meteorological conditions on the mesoscale occur within the atmosphere's planetary boundary layer, it is essential to have scientists specializing in atmospheric turbulence and boundary layer processes (Task Groups 1B and 1C) actively contributing to the modeling effort.

Some of our most powerful continuous measurement techniques for space-time variations of the meteorological structure in the lower atmosphere are based on indirect atmospheric probing systems such as acdar and lidar. Thus, it is also essential to include an indirect probing effort (Task 1D) in order to provide specialized observations and advice concerning data assimilation techniques to the modeling groups.

If air pollutants were simply inert particles or gases carried about by the wind, it would be possible to develop a straight-forward dynamical model to predict concentrations of pollutants as a function of time and location. However, most pollutants are in a state of constant modification by the atmosphere -- through processes such as photochemical reactions and washout. It is, thus, necessary for the dynamic modeling group to also interact on a continuing basis with atmospheric chemists (Tasks 2 and 3). Cross fertilization between these groups better enables the modelers to develop optimal procedures for treating those variables which determine, for example, atmospheric aerosol properties and, also, provides the chemists with a better, and necessary, appreciation for the characteristics of the atmospheric "laboratory" environment.

Finally, an instrumented aircraft is, presently, the most practical and economical sensor platform available capable of providing a large variety of meteorological and air pollution-related observations on the mesoscale. Direct "synoptic-type" observations on a regional scale are both prohibitively expensive and difficult to effectively utilize. An aircraft can transport sensors over mesoscale distances so that both horizontal and vertical profiles of meteorological variables, and/or air pollution parameters, may be obtained. The airborne measurements group (Task IV), thus, has the responsibility of providing measurements support to each of the others. For these purposes, specialized meteorological, turbulence, aerosol and radiation airborne measurement capabilities have been developed for use both at PSU and by scientists in the EPA Meteorology Laboratory.

The principal goal of the Select Research Group is one that guides nearly every large research group in Air Pollution Meteorology. It is widely recognized that the ultimate achievement of this goal will not be reached in any limited period. The objective that will be attained within the SRG project period is significant progress toward the development of a regional-scale air hydrodynamic model suitable for studying mesoscale perturbations to large-scale flows that are important in the transport of air pollutants. The model will be applicable to at least a limited number of practical situations and may be used in conjunction with Lagrangian Puff models to simulate the modification of pollutant concentrations. Also, the forecast wind and temperature distributions and the height of the mixed layer may be used in other more simplified air pollution models. Of course, the ultimate perfection of air pollution modelling will require efforts and time far beyond the lead-off research presently being performed by the SRG scientists.

II THE DEVELOPMENT OF MESOSCALE MODELS SUITABLE FOR AIR POLLUTION STUDIES

Richard A. Anthes

Nelson Seaman

Joseph Sobel

Thomas T. Warner

ACKNOWLEDGEMENTS

Mr. James Hoke contributed to the solutions of the linear and non-linear boundary layer equations in Section 2.8.2. Mr. Ed O'Lenic did the synoptic analyses of Part 3. The three-dimensional model experiments were run on the NCAR computer. NCAR is supported by the National Science Foundation.

THE DEVELOPMENT OF MESOSCALE MODELS SUITABLE FOR AIR POLLUTION STUDIES

Richard A. Anthes, Nelson Seaman,
Joseph Sobel, Thomas T. Warner

1.0 INTRODUCTION

The Pennsylvania State University (PSU) and EPA are in the early stages of developing time-dependent dynamic models for use in air pollution studies. PSU is developing a general, hydrostatic model suitable for forecasting flows with characteristic horizontal wavelengths of 100-600 km under a variety of synoptic conditions. EPA is working on a general, non-hydrostatic model for forecasting smaller scale circulations (horizontal wavelengths 5 to 30 km). The EPA model is designed for prediction of flow over and in cities (in particular, St. Louis in support of the RAPS program) while PSU is modeling perturbations to the synoptic flow induced by terrain variations, land-sea and land-lake contrasts, etc. The PSU model is termed a regional model.

1.1 Potential use for regional and urban dynamical prediction models.

The primary goal of EPA in developing the above model lies in utilizing the models as research tools capable of providing meteorological information that is necessary for rational decision making over questions concerning air standards. Specifically, information such as expected flow patterns and concentrations of pollutants under a variety of weather conditions at diverse locations is required in the preparation of environmental impact statements that are now required before proposed actions such as nuclear power plant construction are approved.

Both the urban and regional models will predict flows for time periods of 1 to 24 hours, and hence, will be directly suitable for estimating maximum and average pollutant concentrations over a few hours. The models will not be directly capable of predicting annual averages, but stratification of short-range model forecasts according to synoptic conditions, together with frequency distributions of synoptic regimes, may make annual estimates possible.

Both the regional and urban models are basically hydrodynamic models rather than direct pollutant prediction models. Presumably, if the dynamics are modeled correctly, so that the three-dimensional wind, temperature, and moisture structure are known, Lagrangian dispersion models may be utilized with the help of the output from the dynamic models to predict concentrations associated with individual plumes. Of course, if the plume size becomes larger than roughly six times the grid size of the model, explicit prediction of the plume's subsequent behavior is possible. This latter event is likely to occur often in the urban model, and may occur occasionally in the regional model under regional air pollution episodes caused by emission of pollutants from multiple sources over a long period of unfavorable weather conditions.

Although neither the urban nor the regional model is contemplated for operational use on a daily basis, it is possible that data from realistic 3-D models could be used in lieu of expensive observational networks to provide dense, accurate data for use in statistical air pollution models. It may also be noted that the interest in and potential benefits of general three-dimensional models are not restricted to air pollution studies, but include resolution of regional and urban variability in cloud cover, rain and snowfall, temperatures, etc. that are important for effective land use. Finally, the 3-D models are powerful tools for increasing our understanding of the smaller scales of atmospheric motion.

Eventually, it may be desirable to allow the urban and regional models to interact. The most obvious mode of interaction is to use the output from the regional model to provide time-dependent boundary conditions for the urban model. Assuming that the important transfers of energy are downscale, the regional model could be run for 12 hours independently of the urban model. The mean values of wind, temperature and moisture in the vicinity of the city could be saved, and used on the boundaries of the fine mesh urban model.

1.2 Some general considerations of the mesoscale predictability problem

A basic problem in the development of both the urban and regional models is the lack of knowledge concerning the predictability of flows on these scales. Unlike large-scale, quasi-geostrophic flow, no scaling of the basic hydrodynamic and thermodynamic equations will produce a simplified set of equations that will apply under most meteorological conditions. For example, the release of latent heat by condensation, a secondary effect for planetary flows over short (1-2 day) time periods, varies from being totally negligible under many conditions to dominant under others. Similarly, non-hydrostatic effects may not be ignored under all situations.

The general prediction problem may be discussed by consideration the equation

$$\frac{\partial \alpha-\bar{\alpha}}{\partial t} = -\vec{V}\cdot\nabla(\alpha-\bar{\alpha}) + F(\alpha,\underset{\sim}{x},t) \tag{1.1}$$

where α is the variable to be forecast (e.g., wind component, temperature, humidity, pollutant concentration), $\bar{\alpha}$ is a climatological or large-scale mean, $\vec{V}$ is the three-dimensional vector velocity, $\underset{\sim}{x}$ is the three-dimensional position vector, and F is some (complicated) function of time and space. The first term represents the *redistribution* of initial perturbations by the wind field, while the second term represents modifications of the initial perturbation by *local forcing*. Integrating in time, we find

$$\begin{aligned}(\alpha-\bar{\alpha})\ (\underset{\sim}{x},t) = (\alpha-\bar{\alpha})\ (\underset{\sim}{x},t_o) - \int_{t_o}^{t} \vec{V}\cdot\nabla\ (\alpha-\bar{\alpha})\ dt \\ + \int_{t_o}^{t} F(\alpha,\underset{\sim}{x},t)\ dt \quad ,\end{aligned} \tag{1.2}$$

that is, the perturbation to be forecast is determined by the *initial distribution* of the perturbation, the redistribution of the perturbation by the wind, and the production of additional perturbations by the local forcing.

The predictability of various scales of flow under different synoptic conditions can now be discussed in terms of (1.2). In general, a prognostic model must include:

1. knowledge of the initial conditions,
2. specification of boundary conditions on the horizontal and vertical boundaries, and
3. representation of the local forcing function by either explicit or parameterized methods.

Accurate treatment of all three aspects of the problem for the urban and regional models presents a formidable challenge. It is doubtful whether simultaneous initial observations will ever be possible on a 30 x 30 x 6 computational mesh. Neither is it likely that a dense network of time-dependent boundary conditions will ever be realizable, because larger-scale models are only able to provide mean values along the lateral boundaries. Finally, the local forcing function will, under various circumstances, include:

1. complex terrain effects,
2. condensation heating and evaporative cooling,
3. infrared and short wave radiation,
4. conduction of heat at the earth-air interface and turbulent transfer of heat upward in the boundary layer.

While a general dynamic model demands accurate treatment of the initial conditions, boundary conditions, and forcing function, under particular situations the problem may be simplified so that one or more of the above effects dominates and the other(s) may be treated fairly simply. For example, the evolution of large-scale flows (wavelengths 2,000-10,000 km) over 1-2 days is determined mainly by the conservation of potential vorticity. Local forcing is weak, as evidenced by the success of barotropic models. Lateral boundary conditions are eliminated by considering the entire global domain. Here the specification of the initial conditions is of supreme importance in the prediction of synoptic-scale flows. We might then ask whether a comparable set of initial data is necessary for the regional and urban models. Fortunately, we suspect that they are not. As the horizontal wavelength of atmospheric disturbances decreases, the solutions are determined more by local forcing than by initial conditions, i.e., the atmosphere "forgets" its initial state more quickly and adjusts to the regional and urban scale forcing. Preliminary numerical experiments with the regional model indicate that large perturbations to the mean flow develop within about 6 hours as a consequence of mesoscale terrain variations. Certainly, the adjustment time of flows over cities is much less, so we hypothesize that in many synoptic situations, if local forcing is modeled correctly, the details of the initial perturbations are not particularly important.[1]

The relative importance of the lateral boundary conditions varies tremendously under differing synoptic flows. For stagnant air situations, the treatment at the boundaries is relatively straightforward. However, when even slight flow occurs across the boundaries, it becomes important to specify at least the mean values of α correctly. Larger scale models may be used to provide lateral boundary conditions for the regional model, which in turn could provide boundary conditions to the urban model.

---

[1] Exceptions to this hypothesis occur when temperature or moisture discontinuities such as those associated with fronts or "dry lines" exist. In these situations the initial location of the discontinuity will be important.

The one aspect of the mesoscale prediction problem that will nearly always be important is the numerical treatment of the local forcing function (if the local forcing were unimportant, a mesoscale model would be unnecessary). Included in the representation of the local forcing is the parameterization of important physical processes. Parameterization is the inclusion of the effect of some physical process in the model in terms of one or more simplified parameters. For example, the representation of the effects of surface friction by the quadratic stress law and a drag coefficient is a parameterization. At first, we are planning to parameterize:

1. the long- and short-wave radiation effects,
2. conduction of heat at the ground, and
3. the transfer of heat and momentum by subgrid-scale motions (the eddy fluxes).

Eventually, we may want to parameterize condensation and evaporation; however, since many dynamic and air pollution problems are not affected by phase changes of water, we will neglect these processes for the time being.

1.3 Overview of mesoscale modeling effort

The next sections summarize the research supported by EPA under Tasks 1A and 1B since the First Annual Project Report (June 1973). First, the numerical aspects of the three-dimensional regional model and its two-dimensional analog are presented. Results from several preliminary experiments with the 3-D and 2-D models are presented. These include a first attempt at forecasting with real data, obtained from the field experiment in the Middle Atlantic States in October 1973.

An important part of the mesoscale modeling problem is the meshing of the regional model with large-scale models, and perhaps eventually with small-scale models. Section 4 presents results from one-, two-, and three-dimensional meshed grid experiments.

Because mesoscale models, meshed or otherwise, are voracious consumers of computer time, we are investigating the feasibility of semi-implicit rather than explicit modeling techniques. In Section 5, results from one- and two-dimensional semi-implicit models are compared with their explicit counterparts. Indications are that an increase in computational efficiency by a factor of four may be possible with the semi-implicit technique.

Finally, a major effort is being directed toward the theoretical investigation of the initialization requirements and the predictability of the mesoscale flows. Through the use of stochastic-dynamic models, insight into the initial data requirements in terms of spatial density and error requirements may be made. The growth of uncertain energy provides estimates for the time scale of the predictability of the mesoscale.

2.0 THE REGIONAL MODEL

The numerical details of the three-dimensional (3-D) model are described in this section. First the basic equations are presented in generalized σ-coordinates written for Lambert Conformal map coordinates. Then the structure of the grid, the finite difference equations, and the lateral boundary conditions are described. Finally, some results from the 3-D model and its two-dimensional analog are presented.

2.1 The basic equations in sigma coordinates for a Lambert Conformal map projection

For middle latitude regions, Lambert Conformal map coordinates produce less distortion of the earth's geometry than either polar stereographic or Mercator map coordinates (Saucier, 1955). Because the authors were not able to locate in the literature the derivation of the equations of motion, thermodynamic equation, and continuity equation for the Lambert Conformal projection, an abbreviated derivation is presented in Appendix 2.1. The vertical coordinate is σ, defined by

$$\sigma = \frac{p - p_t}{p_s - p_t} \quad , \qquad (2.1)$$

where p is pressure, p_t is the pressure at the top of the model (assumed constant) and p_s is the surface pressure. This coordinate system follows the terrain, and allows the top of the model to be placed at any pressure surface.

The complete equations of motion in σ-coordinates, written for Lambert Conformal map coordinates in flux form are

$$\frac{\partial p^*u}{\partial t} = -m^2 \left(\frac{\partial p^*u\ u/m}{\partial x} + \frac{\partial p^*u\ v/m}{\partial y}\right) - \frac{\partial p^*\ u\dot{\sigma}}{\partial \sigma}$$

$$-mp^*\left[\frac{RT}{(p^*+p_t/\sigma)}\frac{\partial p^*}{\partial x} + \frac{\partial \phi}{\partial x}\right] + p^*\ v\ (f+\underline{\gamma}) \qquad (2.2)$$

$$+ \underline{p^*\ w\ \left(\frac{2\Omega \cos \phi\ y}{r} - \frac{u}{a}\right)} + FU$$

$$\frac{\partial p^*v}{\partial t} = -m^2 \left(\frac{\partial p^*u\ v/m}{\partial x} + \frac{\partial p^*v\ v/m}{\partial y}\right) - \frac{\partial p^*v\dot{\sigma}}{\partial \sigma}$$

$$-mp^*\left[\frac{RT}{(p^*+p_t/\sigma)}\frac{\partial p^*}{\partial y} + \frac{\partial \phi}{\partial y}\right] - p^*(f+\gamma)u \qquad (2.3)$$

$$- \underline{p^*w\ \left(\frac{2\Omega \cos \phi\ x}{r} + \frac{v}{a}\right)} + FV$$

where x and y are the Lambert Conformal map coordinates (Fig. 2.1), u and v are the speeds relative to the earth in the x and y directions, w is the vertical velocity, $p^* = p_s(x,y)-p_t$, p_s is surface pressure, R is the gas constant for dry air, T is temperature, f is the Coriolis parameter, a is the radius of the earth and FU and FV are the frictional forces (to be discussed later). The quantities m, r, and γ are defined by

$$m = \frac{\sin \psi_1}{\sin \psi}\left[\frac{\tan \psi/2}{\tan \psi_1/2}\right] \qquad (2.4)$$

$$\gamma = \frac{(\sin \phi - n)}{a \cos \phi}\left(\frac{-uy}{r} + \frac{vx}{r}\right) \qquad (2.5)$$

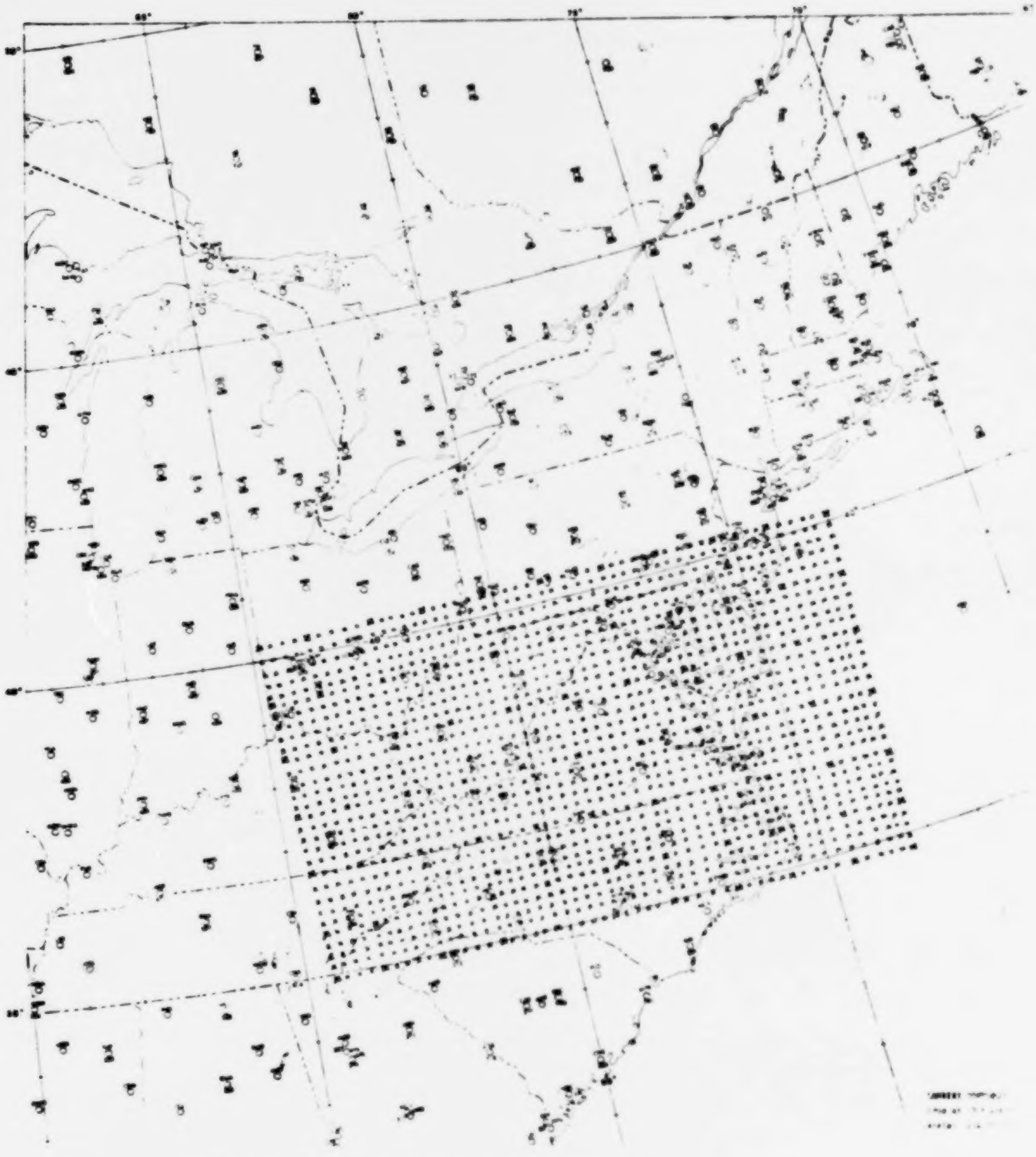

Figure 2.1 30 x 50 grid on Lambert Conformal map projection

$$r = \frac{a}{n} \sin \psi_1 \left[\frac{\tan \psi/2}{\tan \psi_1/2}\right]^n \qquad (2.6)$$

where $n = 0.716$, and $\psi_1 = 30°$, ϕ is latitude and ψ is colatitude. For these choices of n and ψ_1, the projection is true at 30°N and 60°N. Note that a Mercator projection, true at the equator and $\phi_1 = 90-\psi_1$, is obtained by setting $n = 0$, and the polar stereographic, projection is obtained by setting n to equal 1.

For consistency in the kinetic energy equation when the hydrostatic equation is used instead of the vertical component of the equation of motion, the terms multiplied by w are neglected in (2.2) and (2.3). Furthermore, γ is at least two orders of magnitude smaller than f in middle latitudes, and may be neglected. The equations of motion utilized in the model are therefore given by (2.2) and (2.3) without the underlined terms.

The complete continuity equation in Lambert Conformal, σ-coordinates is

$$\frac{\partial p^*}{\partial t} = -m^2 \left[\frac{\partial u/m}{\partial x} + \frac{\partial v/m}{\partial y}\right] - \frac{\partial p^* \dot{\sigma}}{\partial \sigma} \underline{\frac{-2wp^*}{a}} \quad . \qquad (2.7)$$

The last term in (2.7) is small and is neglected in order to conserve mass. The thermodynamic equation is

$$\frac{\partial p^* T}{\partial t} = -m^2 \left[\frac{-\partial u p^* T/m}{\partial x} + \frac{\partial v p^* T/m}{\partial y}\right] - \frac{\partial p^* T \dot{\sigma}}{\partial \sigma}$$

$$+ \frac{RT}{c_p \sigma} \omega + \frac{p^* Q}{c_p} + FT \qquad (2.8)$$

where Q is the diabatic heating per unit mass, c_p is the specific heat at constant pressure, and $\omega = dp/dt$ is related to $\dot{\sigma}$ by

$$\omega = p^*\dot{\sigma} + \sigma \frac{dp^*}{dt} , \tag{2.9}$$

where

$$\frac{dp^*}{dt} = \frac{\partial p^*}{\partial t} + m \left(u \frac{\partial p^*}{\partial x} + v \frac{\partial p^*}{\partial y}\right) . \tag{2.10}$$

The term FT represents the lateral diffusion of heat by subgrid-scale eddies. In the σ-system, the hydrostatic equation may be written

$$\frac{\partial \phi}{\partial \sigma} = - \frac{p^*RT}{p^*\sigma + p_t} . \tag{2.11}$$

2.2 The horizontal and vertical grid structures

The staggered horizontal grid is identical to the S1 grid described by Anthes (1972) and Anthes and Warner (1974), and is not illustrated here. The vertical grid is also staggered, with the velocity components and temperature defined at one set of levels while geopotential height and vertical velocity ($\dot{\sigma}$) are defined at adjacent levels. The horizontal and vertical grid spacings and the domain size are variable. The model has been tested with 30 x 30 and 30 x 50 grids of 20 km resolution and a 30 x 30 grid with 5 km resolution.

2.3 Finite difference equations

The finite difference equations for the S1 grid conserve mass, momentum, and total energy.

We first define the following finite-difference operators:

$$\alpha_x \equiv \frac{\alpha_{i,\ j+1/2} - \alpha_{i,\ j-1/2}}{\Delta x}$$

$$\alpha_y \equiv \frac{\alpha_{i+1/2,\ j} - \alpha_{i-1/2,\ j}}{\Delta y} \tag{2.12}$$

$$\overline{\alpha}^x \equiv (\alpha_{i,\ j+1/2} + \alpha_{i,\ j-1/2})/2$$

and

$$\overline{\alpha}^y \equiv (\alpha_{i+1/2,\ j} + \alpha_{i-1/2,\ j})/2$$

where j is the east-west index and i is the north-south index.

We also introduce the following four-point operators:

$$\widetilde{\alpha}^y \equiv \frac{\alpha_{i+1,\ j} + 2\alpha_{i,\ j} + \alpha_{i-1,\ j}}{4}$$

and

$$\widetilde{\alpha}^x \equiv \frac{\alpha_{i,\ j+1} + 2\alpha_{i,\ j} + \alpha_{i,\ j-1}}{4} \tag{2.13}$$

For vertical differences and averages, we define

$$\overline{\alpha}^{\sigma} \quad \frac{(\alpha_{k+1/2} + \alpha_{k-1/2})}{2}$$

and (2.14)

$$\delta\alpha \equiv (\alpha_{k+1/2} - \alpha_{k-1/2})$$

The finite-difference equations associated with the staggered grid for the u- and v-component equations of motion are

$$\frac{\partial p^*u}{\partial t} \approx - m^2[(\overline{u}^{x}\,\overline{\overbrace{\frac{p^*u}{m}}^{y}}^{x})_x + (\overline{u}^{y}\,\overline{\overbrace{\frac{p^*v}{m}}^{x}}^{y})_y] - \frac{\overline{\delta\dot{\sigma}}^{xy}\,\overline{p^*u}^{\sigma}}{\delta\sigma} - m\overline{p^*}^{xy}\,\overline{\overline{\phi}^{\sigma}}^{y}_{x}$$

$$- \overline{\frac{m\,RT}{(1+P_t/p^*\sigma)}}^{xy}\,\overline{p^*}^{y}_{x} + fp^*v + p^*[(K_H u)_x]_x \qquad (2.15)$$

$$+ p^*[(K_H u)_y]_y + FU_v$$

and

$$\frac{\partial p^*v}{\partial t} \approx - m^2[(\overline{v}^{x}\,\overline{\overbrace{\frac{p^*u}{m}}^{y}}^{x})_x + (\overline{v}^{y}\,\overline{\overbrace{\frac{p^*v}{m}}^{x}}^{y})_y] - \frac{\overline{\delta\dot{\sigma}}^{xy}\,\overline{p^*v}^{\sigma}}{\delta\sigma}$$

$$- m\overline{p^*}^{xy}\,\overline{\overline{\phi}^{\sigma}}^{x}_{y} - \overline{\frac{m\,RT}{(1+P_t/p^*\sigma)}}^{xy}\,\overline{p^*}^{x}_{y} - fp^*u \qquad (2.16)$$

$$+ p^*[K_H v_x]_x + p^*[K_H v_y]_y + FV_v \quad ,$$

where the finite-difference analogs for the vertical friction terms, FU_v and FV_v are discussed later. In this section the terms (p^*u) and (p^*v) represent $(u\overline{p^*}^{xy})$ and $(v\overline{p^*}^{xy})$, respectively.

The analogs for the continuity and thermodynamic equations are

$$\frac{\partial p^*}{\partial t} - (\overline{m}^{xy})^2\left[\left(\frac{\overline{p^*u}^{y}}{m}\right)_x + \left(\frac{\overline{p^*v}^{x}}{m}\right)_y\right] - p^*\frac{\delta\dot{\sigma}}{\delta\sigma} \qquad (2.17)$$

and

$$\frac{\partial p^*T}{\partial t} \approx - (\overline{m}^{xy})^2 \left[\left(\frac{\overline{p^*u}^{y}}{m}\,\overline{T}^{x}\right)_x + \left(\frac{\overline{p^*v}^{x}}{m}\,\overline{T}^{y}\right)_y\right] - p^*\frac{\delta\dot{\sigma}\hat{T}^{\sigma}}{\delta\sigma}$$

$$+ \frac{RT\omega}{c_p\sigma} + \frac{p^*}{c_p}Q + p^*\,[K_H\,T_x]_x + p^*\,[K_H\,T_y]_y \qquad (2.18)$$

The notation $\hat{T}^{\sigma}$ in equation (2.18) signifies that potential temperature, rather than temperature itself, is linearly interpolated between σ-levels. This provides for a substantial improvement in the calculation of static stability since potential temperature is much more nearly linear in σ than is temperature. Mintz and Arakawa (see Langlois and Kwok 1969), have adopted a similar procedure for their general circulation models. The finite difference expression for ω is

$$\omega = \frac{dp}{dt} = p^*\dot{\sigma} + \sigma\left(\frac{\partial p^*}{\partial t} + \overline{u}^{xy}\,\overline{p^*_x}^{x} + \overline{v}^{xy}\,\overline{p^*_y}^{y}\right) \qquad (2.19)$$

In equations (2.15) and (2.16) the use of the four-point averaging operator is necessary if the finite-difference equations are to conserve kinetic energy (Anthes, 1972). For the approximation of the time derivatives, the centered-time or leapfrog scheme, which has second order accuracy, is adopted.

2.4 The two-dimensional analog

Because of the complexity and relatively high cost of the three-dimensional model, it is frequently useful to test numerical aspects of the model (such as vertical resolution) or the parameterization of physical processes (such as turbulent transfers of heat and momentum in the planetary boundary layer) with a two-dimensional analog to the 3-D model. The 2-D model is designed to be as much like the 3-D in structure as possible, so that the many properties of the model that are not inherently three-dimensional may be investigated with this more economical model. The 2-D analog is a vertical, east-west cross section through the atmosphere in which the y-variation of the forecast quantities are neglected. For simplicity, the map scale factors are considered to be unity. With these assumptions, the equations of motion, continuity equation, and thermodynamic equation for this model corresponding to (2.2), (2.3), (2.7), and (2.8) are

$$\frac{\partial p^*u}{\partial t} = -\frac{\partial p^*uu}{\partial x} - \frac{\partial p^*u}{\partial \sigma} - \frac{RT}{(1 + p_t/p^*\sigma)}\frac{\partial p^*}{\partial x} - p^*\frac{\partial \phi}{\partial x} \qquad (2.20)$$

$$+ fp^*v + FU$$

$$\frac{\partial p^* v}{\partial t} = -\frac{\partial p^* uv}{\partial x} - \frac{\partial p^* v\dot{\sigma}}{\partial \sigma} - f(u - u_g) + FV \qquad (2.21)$$

$$\frac{\partial p^*}{\partial t} = -\frac{\partial p^* u}{\partial x} - \frac{\partial p^* \dot{\sigma}}{\partial \sigma} \qquad (2.22)$$

and

$$\frac{\partial p^* T}{\partial t} = -\frac{\partial u p^* T}{\partial x} - \frac{\partial p^* T\dot{\sigma}}{\partial \sigma} + \frac{RT}{c_p \sigma}\,\omega + \frac{p^* Q}{c_p} + FT \quad , \qquad (2.23)$$

where u_g is the specified geostrophic wind.

The equation for ω is given by (2.9) and (2.10) after neglecting $(v \frac{\partial p^*}{\partial y})$, and the hydrostatic equation is given by (2.11).

The vertical grid structure is identical to that of the 3-D model. The horizontal grid is staggered with u and v defined at points $x_j = (j-1)\Delta x$ and all other variables defined at points $x_j = (j - 1/2)\Delta x$, $j = 1, 2, \ldots J_{MAX}$.

2.5 Kinetic energy budget equations for 2-D and 3-D models

The kinetic energy equation, formed by the multiplication of (2.2) by u and (2.3) by v and the use of the continuity equation, is

$$\frac{\partial p^*k}{\partial t} + \nabla \cdot \underset{\sim}{V}\, p^*\, k + \frac{\partial \dot{\sigma} p^* k}{\partial \sigma} = - p^* \underset{\sim}{V} \cdot \nabla \phi$$

$$- RT\, \underset{\sim}{V} \cdot \nabla p^* + u \cdot FU + v \cdot FV \quad , \tag{2.24}$$

where $k = (u^2 + v^2)/2$.

For diagnostic purposes, it is convenient to integrate the kinetic energy equations over the mesoscale domain in order to obtain the equation for the time rate of change of the mean kinetic energy,

$$\frac{1}{g} \int_{\sigma} \int_{x} \int_{y} \frac{\partial p^*k}{\partial t} = \frac{1}{g} \int_{\sigma} [\int_{y_S}^{y_N} - (up^*k)_E + (up^*k)_W \, dy$$

$$+ \int_{x_W}^{x_E} - (vp^*k)_N + (vp^*k)_s \, dx - \overline{\frac{\partial \dot{\sigma} p^* k}{\partial \sigma}}^D - \overline{p^* \underset{\sim}{v} \cdot \nabla \phi}^D \tag{2.25}$$

$$- \overline{RT\, \underset{\sim}{V} \cdot \nabla p^*}^D + \overline{(u \cdot FU + v \cdot FV)]}^D d\sigma \quad ,$$

where the subscripts N, E, S, and W denote the northern, eastern, southern, and western boundaries, respectively, and the $\overline{(\ \ )}^D$ operator denotes an average over the horizontal domain.

For the first two terms on the right side of (2.25) represent the change in mean kinetic energy in the volume by the net flux of kinetic energy across the east-west and north-south lateral boundaries respectively. Unlike their relatively insignificant role in large-scale models, these terms may be very important in mesoscale models, contributing as much or more as the linear terms. This fact emphasizes the need for accurate specification of the velocities on the lateral boundaries. The third term on the right side of (2.25) is the vertical flux divergence of kinetic energy, and vanishes if the entire depth of the model is considered, since $\dot{\sigma} = 0$ at the upper and lower boundaries. The next two terms represent the conversion of potential to kinetic energy by cross-isobar flow. Over variable terrain the terms are individually very large, but are of opposite sign and tend to cancel with each other. The last term in (2.25) represents the loss of kinetic energy by frictional dissipation.

While the interpretation of the total kinetic energy over the 3-D mesoscale model domain is straightforward, a total kinetic energy cannot be assigned to the 2-D domain, which represents a slice through the atmosphere. Instead, the kinetic energy per unit area, K, is defined

$$K = \frac{1}{Lg} \int_{\sigma} \int_{x_W}^{x_E} kp^* \, dx \, d\sigma = g^{-1} \int_{\sigma} \overline{kp^*}^{x} \, d\sigma \quad , \qquad (2.26)$$

where L is the length of the 2-D domain and equal to $(x_E - x_W)$. Similarly, the time rate of change of kinetic energy per unit area in the 2-D model is

$$\frac{\partial K}{\partial t} = -\frac{1}{g}\int_{\sigma} \frac{(up^*k)_E - (up^*k)_W}{L}$$

$$- \overline{u\left(p^* \frac{\partial \phi}{\partial x} + \frac{RT}{(1 + p_t/p^*\sigma)} \frac{\partial p^*}{\partial x}\right)}^{L} + \overline{fv\, u_g\, p^*}^{L} \qquad (2.27)$$

$$+ \overline{(u \cdot FU + v \cdot FV)}^{x}$$

where the operator $\overline{(\quad)}^{L}$ indicates an average along the entire length of the domain.

2.6 Lateral boundary conditions

The numerical treatment of the lateral boundaries is a difficult but very important aspect of a limited area forecast model. The problem on the interior of the domain is well posed only when the proper set of boundary conditions is prescribed. The solution on the interior may be completely different for apparently minor variations in the boundary conditions. Much discussion has appeared in the literature concerning the proper specification of variables on the open boundaries (Moretti, 1969; Shapiro, 1970). As discussed by Moretti, the only straightforward case occurs when the flow is supersonic, in which case the value on an inflow boundary may be arbitrarily specified, and the values on an outflow boundary obtained by a linear extrapolation outward from the interior of the domain.

In the subsonic case, however, waves may propagate upstream, so that values at inflow boundaries are partially dependent upon the flow on the interior of the domain. Thus the arbitrary specification of either constant or time-dependent boundary values may make the problem ill-posed. However, in the absence of proven computational methods to compute boundary variables correctly under general conditions, we are forced to take the pragmatic view that if the lateral boundaries are located far enough away from the region of interest, the errors introduced at the boundaries will remain within some acceptable tolerance in the interior of the domain during the forecast period. We must therefore search for a set of conditions which minimize the errors generated by the boundaries and their feedback into the interior.

Although it is normally recognized that a set of boundary conditions that minimizes the generation of high temporal and spatial frequency components to the numerical solution is desirable, if not absolutely necessary, it is less generally recognized that smoothly varying solutions near the boundary are not sufficient to guarantee accurate solutions on the interior of the grid. It is apparent that as the size of the horizontal domain decreases, the specification of the velocity components and temperature along the boundaries affects the mean (wave number zero) values of these quantities over the entire domain to an ever increasing degree. Thus on a mesoscale domain of 600 x 600 km, a set of boundary conditions may be computationally "stable" and produce "smooth" results, but even small errors in the treatment of temperature or velocity may profoundly affect the mean kinetic and internal energy budgets over the domain.

2.6.1 Equations for mean motion over domain. The importance of specifying accurate values of temperature, surface pressure, and velocity components on the lateral boundaries may be shown by deriving the equations for the mean motion over the domain. For convenience, we will neglect vertical velocities, friction, and the covariance of p^* with the velocity components, and integrate (2.2) and (2.3) over area, obtaining

$$\frac{\partial \overline{v}^{D}}{\partial t} = - \frac{\overline{(uv)_E - (uv)_W}^{Ly}}{L_x} - \frac{\overline{(v_N^{\,2} - v_S^{\,2})}^{Lx}}{L_y}$$

$$-f\overline{u}^{D} + f\overline{u_g}^{D} \tag{2.28}$$

and

$$\frac{\partial \overline{u}^{D}}{\partial t} = - \frac{\overline{u_E^{\,2} - u_W^{\,2}}^{Ly}}{L_x} - \frac{\overline{(uv_N) - (uv_S)}^{Lx}}{L_y}$$

$$+ f\overline{v}^{D} - f\overline{v_g}^{D} \tag{2.29}$$

where

$$fu_g = - \frac{RT}{(p^* + p_t/\sigma)} \frac{\partial p^*}{\partial y} - \frac{\partial \phi}{\partial y}$$

$$fv_g = \frac{RT}{(p^* + p_t/\sigma)} \frac{\partial p^*}{\partial x} + \frac{\partial \phi}{\partial x} \tag{2.30}$$

and L_x and L_y are the lengths of the domains in the east-west and norht-south directions, respectively.

For simplicity, let us consider only the u-component equation. The importance of the specification of mass (given by the surface pressure and temperature) on the lateral boundaries rests in the term $f\overline{v_g}^{D}$, which (neglecting the covariance of $\frac{RT}{(p^* + p_t/\sigma)}$ with $\frac{\partial p^*}{\partial x}$ across the domain) simply represents the difference in surface pressure and geopotential (which is determined by the temperature) across the domain. Thus the mass variables on the lateral boundaries determine (together with the mean Coriolis acceleration) the net linear acceleration of the air in the domain. Of course this is true for any non-periodic domain, but the larger the domain, the greater error that may be tolerated. This point is illustrated in Figure 2.2 which shows the errors in the calculated geostrophic wind as a function of horizontal distance when RMS temperature errors of 1°C are hydrostatically integrated over a 200 mb depth centered at the given pressure level. For synoptic scale domains (L $\gtrsim$ 3000 km), the error is about one ms^{-1} at all levels. The error increases rapidly as the domain size decreases below 1000 km. For a regional scale model, with a domain size of 1000 x 600 km, a 1°C temperature error on the lateral boundaries will produce large ($\sim$5 ms^{-1}) errors in the mean geostrophic wind across the grid, especially in the upper levels. These errors, if they persist in time, may produce large erroneous accelerations of the mean motion over the domain. For example, with $f = 10^{-4}$ s^{-1}, a 5 ms^{-1} error in geostrophic wind which persists for six hours would produce an erroneous change of 11 ms^{-1} in the mean velocity over the domain.

The preceding analysis indicates that although it might be tempting for computational stability purposes to calculate the temperature on the lateral boundaries by some type of outward extrapolation from the interior of the domain, or one-sided differencing scheme, the extreme sensitivity of the mean acceleration to small temperature errors leads to us reject these possibilities. Instead, we conclude that for mesoscale domains, it is preferable to specify the mass variables at all boundary points in a realistic and accurate way, in order to insure that the mean geostrophic

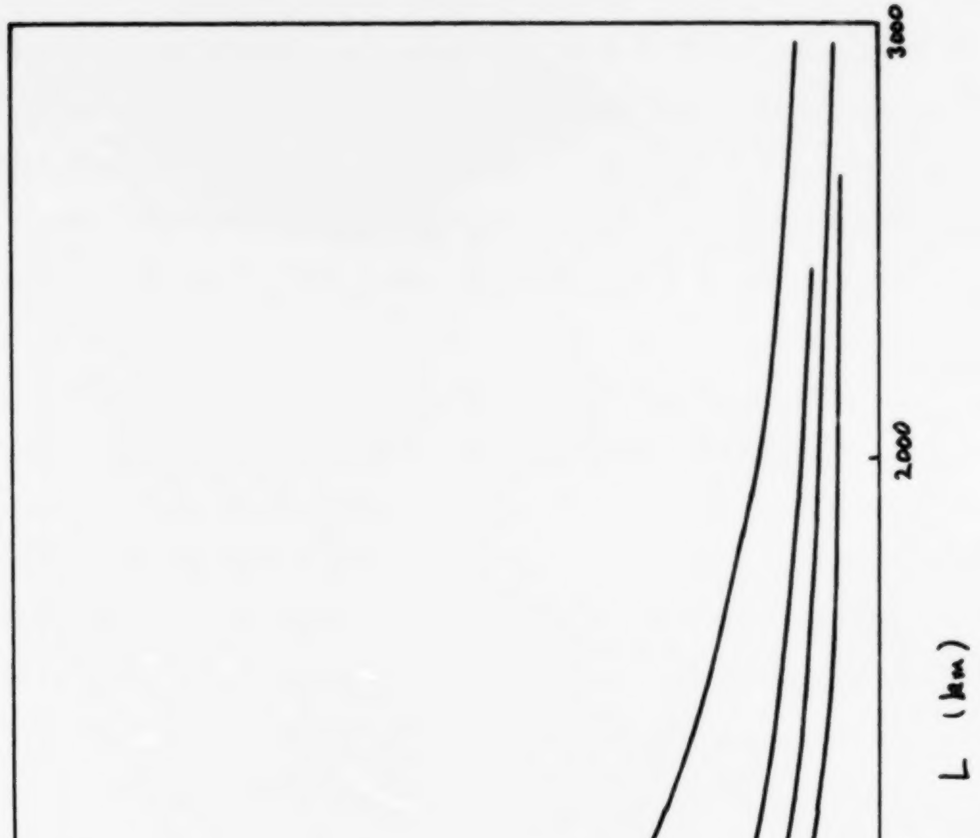

Figure 2.2 Error in geostrophic wind as a function of horizontal distance for a 1°C temperature error integrated over 200 mb depths centered at 300, 500, 700 and 900 mb

wind and the associated linear acceleration term remain accurate during the integration. This specification may come from a large-scale model (one-way interaction), or in the research mode, from consistent analyses of observations.

While the specification of surface pressure and temperature on the lateral boundaries affects the pressure gradient force terms, the importance of accurately specifying the velocity components on the boundary is exemplified by the term

$$-\frac{\overline{u_E^2 - u_W^2}^{Ly}}{L_x} \equiv B_k \text{ in (2.29).}$$

To illustrate the magnitude of this term, let $u_E = u_W + \Delta u$, where Δu may consist of either a physical variation across the domain or an error. Then, neglecting the variation of u with y, the boundary flux term is

$$B_k = -\frac{[u_W \Delta u + \Delta u^2]}{L_x} \quad .$$

With moderate to strong winds when the non-linear terms are important, Δu is smaller than u_W so that the boundary term is of order $\frac{u_W \Delta u}{L_x}$.

Figure 2.3 shows the magnitude of B_k (divided by f equal to 10^{-4} s^{-1} for comparison with $\overline{v_g}^D$ discussed earlier) as a function of wind speed and domain size, L, for a value of Δu equal to 10% of the mean wind speed.

Non-linear accelerations greater than 10^{-4} ms^{-2} (corresponding to a value of B_k/f equal to 1 ms^{-1} in Fig. 2.3) become comparable in magnitude to the linear acceleration term, $f(v-v_g)$, especially if they persist over the entire 12-hour forecast. From Fig. 2.3, we see that this value is exceeded by a considerable margin for wind speeds in excess of 30 ms^{-1} and mesoscale domain sizes of the order 1000 km or less. On the other hand, for domain sizes in excess of 5000 km, the mean non-linear accelerations are very small, except when the mean wind approaches 100 ms^{-1}. In the discussion of the preliminary 3-D experiment (see Section 3), we will see that in the upper layer where the wind speeds are greatest, the values of B_k/f are of order 5 ms^{-1} and therefore of comparable magnitude to the linear acceleration over the domain.

2.6.2. Lateral boundary conditions for the 2-D model. A technique which has found widespread use in theoretical numerical calculations is the specification of cyclic or periodic boundary conditions in the direction of the mean flow. This treatment has the desirable numerical property that all calculations utilize the same finite difference equations and therefore have similar truncation errors. Physically, however, these conditions imply an infinite repetition of solutions downstream. If the domain is not large enough, disturbances generated in the interior of the domain may propagate downstream, pass through the cyclic boundary, and eventually return to the interior of the domain. For this reason, we have chosen to experimentally determine a set of non-periodic, open conditions that allow gravity waves to pass out of the domain.

A set of open lateral boundary conditions which appear to give computationally stable results was found through experimentation. A suggestion that these conditions do not adversely affect the solutions on the

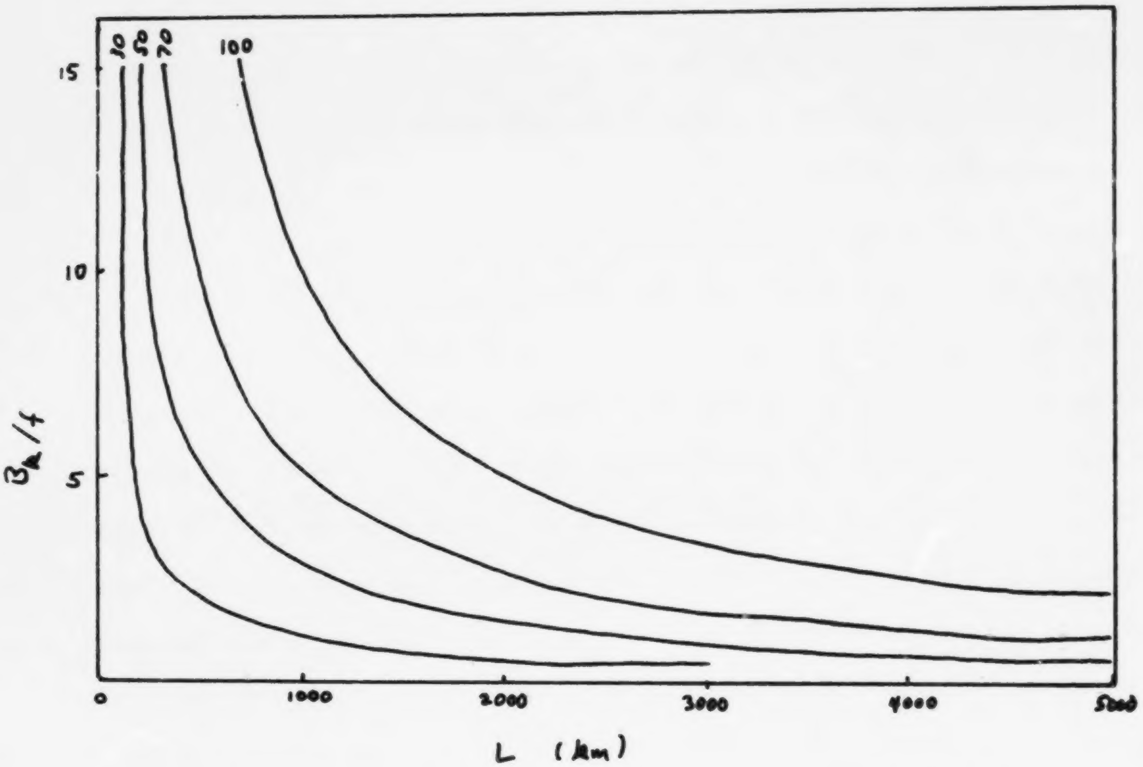

Figure 2.3. Magnitude of acceleration due to boundary flux of momentum as function of wind speed and domain size (L). The isotachs are labeled in ms^{-1}.

interior to a large degree is supported by the experiments in which the lateral boundaries are moved farther away from the interior of the domain. (See Anthes and Warner, 1974, p. 52-56).

In adiabatic experiments (Q = 0 in (2.8)), the surface pressure and temperature on both the inflow and outflow boundaries are specified as a smoothly varying function of time. This specification prevents any spurious pressure difference across the domain, which would lead to an unrealistic net acceleration of the flow.

For the velocity components, the values at the inflow points are specified in a manner similar to the specification of temperature and pressure. The values on the outflow boundary are obtained by a Lagrangian extrapolation outward from the interior. These boundary values are required only in the computation of the non-linear horizontal momentum flux divergence terms; they are not required in the computation of the horizontal divergence. In fact, this is an advantage of the horizontally staggered grid. The first computation point for pressure utilizes only velocity points interior to the grid. Since the divergence calculation is very sensitive, this property appears to be quite important in obtaining smooth solutions near the boundaries. Also, these boundary conditions allow gravity waves to propagate out of the domain in both directions, with no reflection at the boundaries.

2.6.3 Lateral boundary conditions for the 3-D model. The lateral boundary conditions for the 3-D model are more complex than those for the 2-D model, because of the staggering of the grid in two dimensions. Again, the surface pressure and temperature on all the boundaries are specified as smoothly varying functions of time. Boundary values for the velocity components are needed only in calculating the non-linear horizontal flux divergence terms, such as $\partial(up^*)\alpha/\partial x$ where α may be u or v. For evaluation of these terms in the preliminary experiment to be described in Section 3, the quantity α is specified on the inflow boundaries, and extrapolated outward on outflow points. The pressure-weighted flux velocity component normal to the boundary ((up*) on the east-west boundaries and (vp*) on the north-south boundaries) is extrapolated outward regardless of the direction of flow.

The above lateral boundary conditions on the velocity components, while yielding computationally smooth solutions, produced a large source or sink term in the kinetic energy budget for each layer, as discussed in Section 3. In order to obtain realistic values for the net boundary flux of kinetic energy, it is probable that the velocity components should be specified on all boundaries, even if this amounts to an overspecification. In any case, we find that because of the large contribution to the kinetic energy budget by the boundary flux term, great care must be taken in the actual values of the velocity components used in the specification.

2.7 Initial conditions

The initialization of numerical models with real data is usually considered to be a problem of obtaining an initial quasi-balance between the mass and momentum fields so that the amplitude of gravitational oscillations is minimized. Although it is certainly desirable to minimize the small scale imbalances, we have found that for mesoscale models with open domains, the presence of small scale imbalances is less injurious than with large-scale models in closed or cyclic domains. In short, the mesoscale model adjusts to initial imbalances very rapidly through the propagation out of the domain of internal and external gravity waves. More important than the small-scale imbalances appears to be the large-scale imbalances induced by the incompatibility of the lateral boundary conditions on mass and the mean wind over the domain.

These large-scale imbalances produce low-frequency inertial gravity waves which affect the mean motion over the domain to a large extent. These somewhat surprising results are discussed in Section 3.5, which presents preliminary results from a real data experiment.

Prior to the experimentation with real data, fictitious initial conditions are specified in order to study the effects of topography, diffusion parameterization, and the numerical aspects of the model. Both the artificial initial conditions and the real data initial conditions consist of specifying the sea-level pressure and the three-dimensional temperature and wind fields. The surface pressure on terrain above sea level is calculated iteratively from the sea-level pressure and the vertical temperature profile, using the hydrostatic equation and alternatively improving the surface pressure and mean temperature estimates until convergence occurs.

2.8 Two-dimensional flow across the Appalachian terrain

To illustrate the nature of the perturbation flow induced by the smoothed Appalachian terrain, the importance of the fluxes of kinetic energy across the boundaries, and some of the aspects of mesoscale model initialization, the results from two experiments with the 2-D analog are presented.

2.8.1 Specifications of the 2-D experiments. In both 12-hour experiments, the model was run with six layers (velocity components defined at $\sigma = 0.95, 0.85, 0.7, 0.5, 0.3$, and 0.1), $p_t = 0$, and the temperature sounding for Washington, D. C., Oct. 16, 1973 (shown in Fig. 2.4). The horizontal grid is constant (20 km) over most of the interior of the domain and stretched at both ends to increase the distance of the lateral boundaries from the central region of interest. The x-coordinates of the grid points at which the velocity is defined are given by

0, 120, 220, 300, 360, 400, 420...1360, 1400,....1460, 1540, 1640, 1760 km.

In these experiments the effects of vertical diffusion of momentum are modeled according to

$$FU_v = -g \frac{\delta \tau_{zx}}{\delta \sigma} \qquad k = 1,2\ldots6 \text{ (velocity levels)}$$

where (2.31)

$$\tau_{zx} = \bar{\rho}(z)\, K_z \frac{\delta u}{\delta z} \qquad k = 1,2\ldots6 \text{ (ϕ levels)}$$

and

$$\tau_{zx} = \rho_s C_D \left|\underset{\sim}{V}_6\right| u_6 \qquad k = 7 \text{ (surface stress)} \quad . \tag{2.32}$$

Similar expressions are written for the v-component.

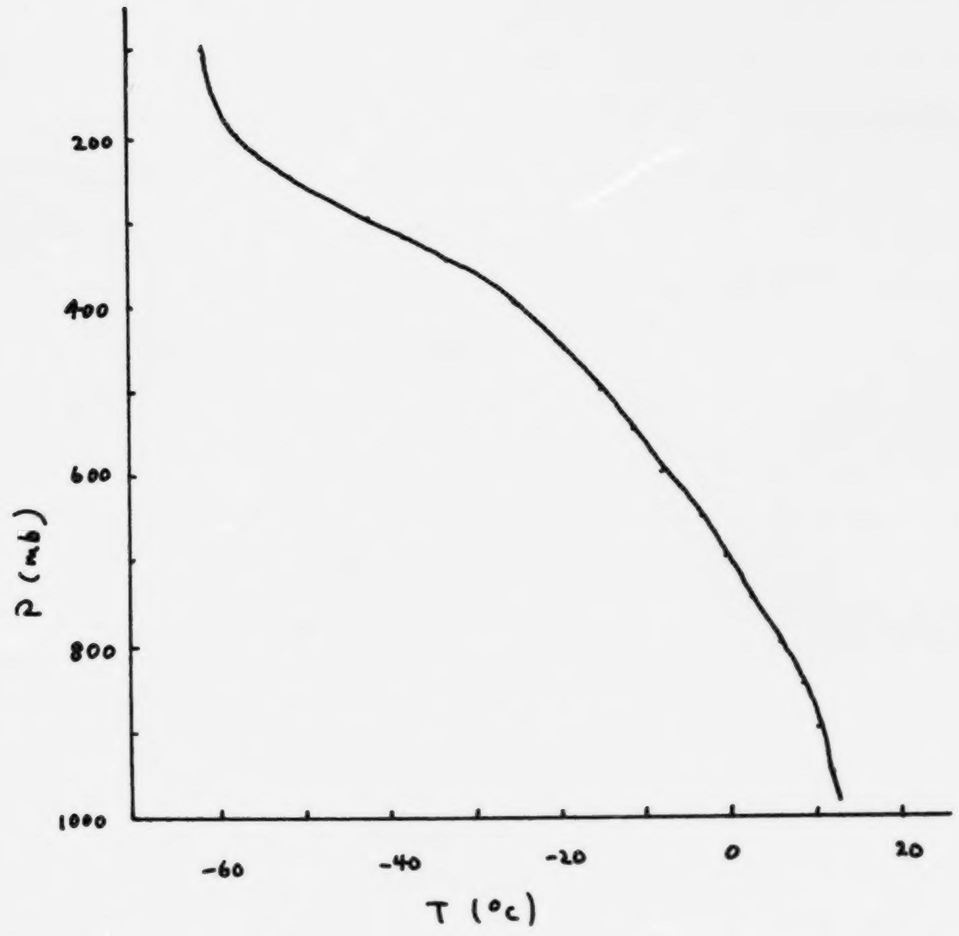

Figure 2.4 Temperature sounding for Washington, D. C., 12Z Oct. 16, 1973

In (2.31) and (2.32), τ_{zx} is the stress in the x-direction due to vertical mixing, $\bar{\rho}(z)$ and ρ_s are constant densities, C_D is the drag coefficient (equal to 3×10^{-3} over land and 1.5×10^{-3} over water), and K_z is the eddy diffusivity coefficient and is equal to $25 m^2 s^{-1}$.

The above crude formulation of the PBL is to be utilized while a more realistic parameterization is developed.

In the 2-D model the horizontal diffusion terms take the form

$$FU_H = \overline{p^*} K_H \frac{\partial^2 u}{\partial x^2}$$

$$FV_H = \overline{p^*} K_H \frac{\partial^2 v}{\partial x^2} \quad , \qquad (2.33)$$

and are added to the momentum tendencies mainly to prevent the accumulation of energy in the short wavelengths. In these experiments, K_H varies with grid size according to the formulation

$$K_H = [5 \times 10^4 + k_o^2 \left| \frac{\partial \underset{\sim}{V}}{\partial x} \right|] \left(\frac{\Delta x}{\Delta x_{min}} \right)^2 \; m^2 \, s^{-1} \quad , \qquad (2.34)$$

where $k_o = 0.4$ and Δx_{min} equals the constant grid spacing of 20 km over the interior of the domain.

The lateral boundary conditions consist of steady state pressures and temperatures on both the eastern and western boundaries On the outflow (eastern) boundary, the velocity components are extrapolated from the interior using a Lagrangian extrapolation. On the inflow (western) boundary, the velocity components are set equal to the next inner value provided the speed at the inner point is less than the geostrophic wind speed. This procedure prevents an unrealistically large horizontal shear from developing in the boundary layer where surface friction reduces the wind speed to roughly 60% of the geostrophic value.

The only difference between the two experiments is the initialization of the winds in the boundary layer. In Exp. 2D-1, the u-component is set equal to a geostrophic value of 30 ms^{-1} at all points. As surface friction destroys the geostrophic balance, the boundary layer winds undergo a large oscillation before reaching quasi-steady values, which is undesirable for a short-range forecast. Exp. 2D-2 illustrates that by taking surface friction into account initially, the amplitude of the oscillation during the adjustment period may be reduced.

As revealed by previous experiments on this scale with the early version of the regional model, an undisturbed initial flow adjusts to a quasi-steady state after roughly six hours. Actually, the solution never reaches a steady-state, because high frequency inertia gravity waves are continuously propagating through the model domain. Furthermore, for long integrations, the absence of any effective mechanism (horizontal and vertical diffusion are too small) for removing the upward propagating energy near the top of the model, produces a gradual modification of the solutions by the reflection of energy at the top of the model. Aliasing of the vertically propagating waves produced by the inadequate vertical resolution near the top also contributes to the problem for long integrations. However, in most of these experiments with steady forcing, the most rapid adjustment occurs during the first six hours, the changes in the low-level solution between six and twelve hours are considerably smaller than between zero and six hours.

In order to minimize the effect of the transient part of the solution due to traveling gravity waves, and to emphasize the stationary portion of the perturbed large-scale flow, it is convenient to present time-averaged cross sections from the last six hours of the forecast. These are obtained by averaging the solution at one hour intervals from 7 to 12 hours. Because the high frequency gravity waves affect the vertical velocity field more strongly than the horizontal velocity or temperature fields, the averaged cross sections of vertical velocity show a greater departure from the hourly solutions than do these latter sections.

2.8.2 Results with geostrophic initial conditions: Exp. 2D-1. Figures 2.5, 2.6, and 2.7 show the time averaged cross sections of u, temperature departure (from the horizontally isothermal initial state), and vertical velocity. Even with only six layers, the classic characteristics of perturbed flow over a wide ridge are evident. (Queney, 1960; Hovermale, 1965). A maximum in the wind velocity over the crest of the mountain is crudely resolved. In the boundary layer, surface friction reduces the u-component to about 60% of the geostrophic value.

The maximum cold temperature anomally of 3°C occurs at the top of the mountain, while warm air tilts upward from the Piedmont region over the top of the mountain.

The time-averaged vertical velocity cross section indicates a mean maximum updraft of over 10cm s^{-1} over the upwind slopes, extending to an upper pressure level of about 700 mb. This mean upward motion in the lower troposphere appears to be sufficient to account for the low deck of

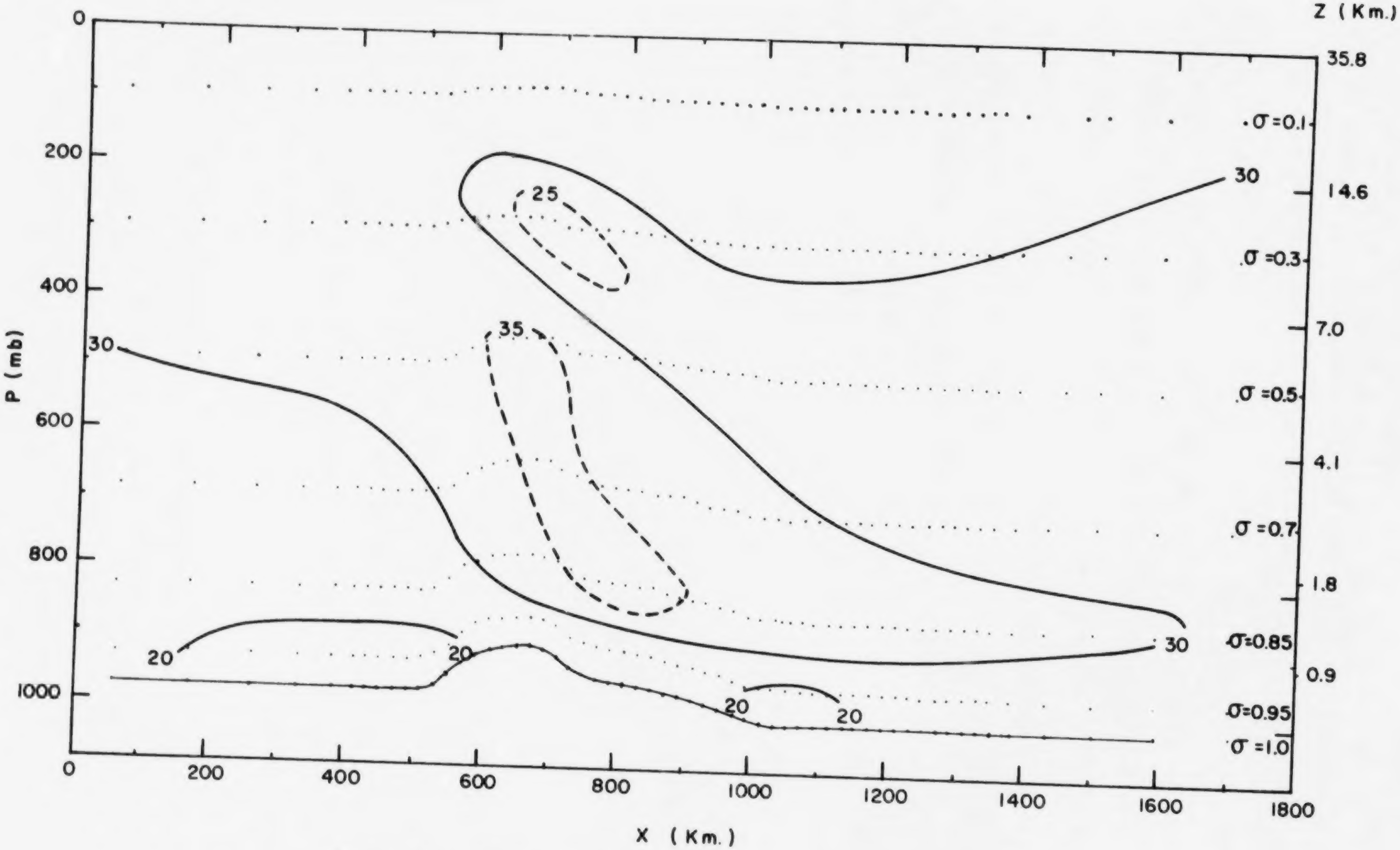

Figure 2.5 Time-averaged vertical cross section of u for Exp. 2D-1

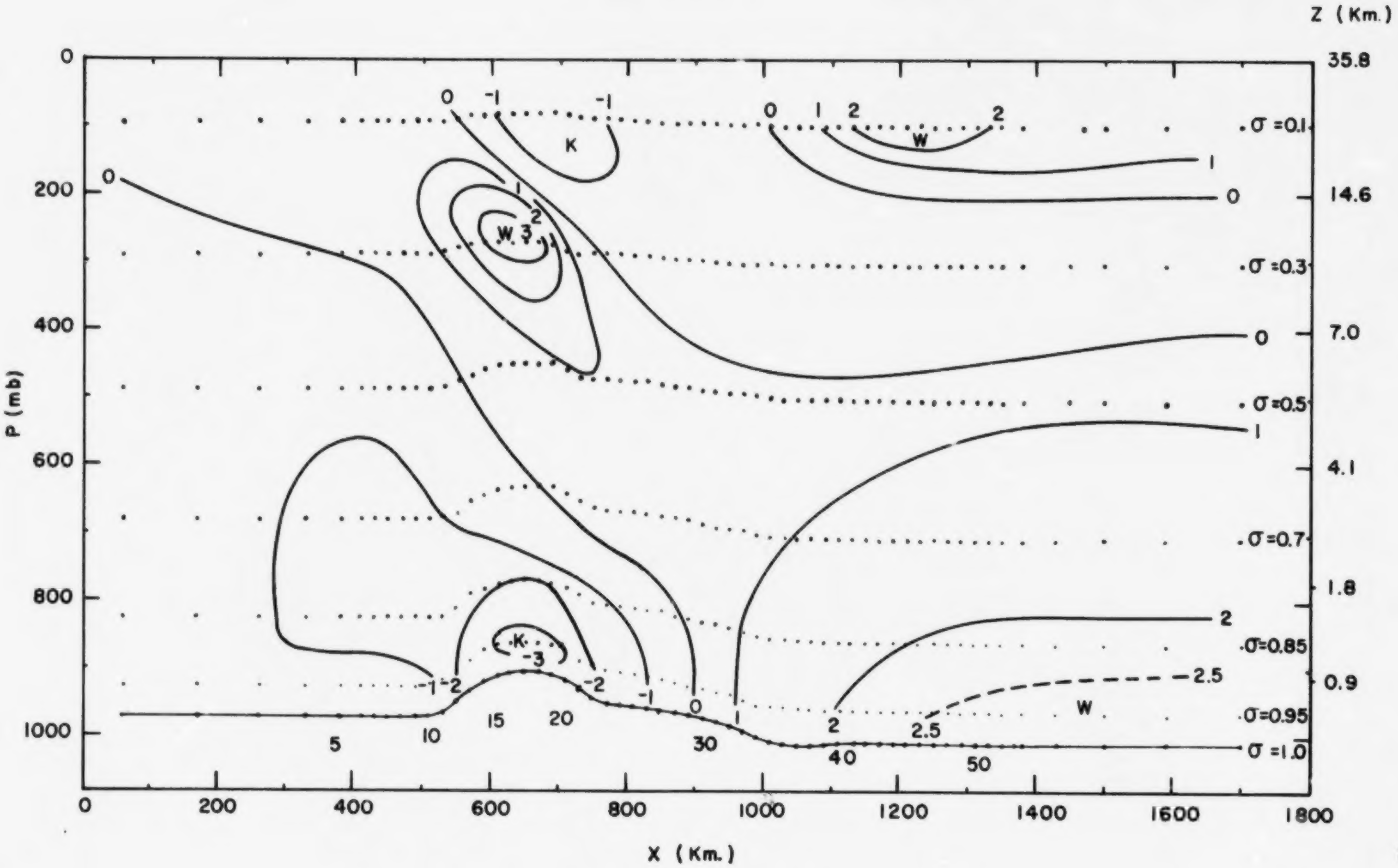

Figure 2.6 Time-averaged vertical cross section temperature departure from Exp. 2D-1

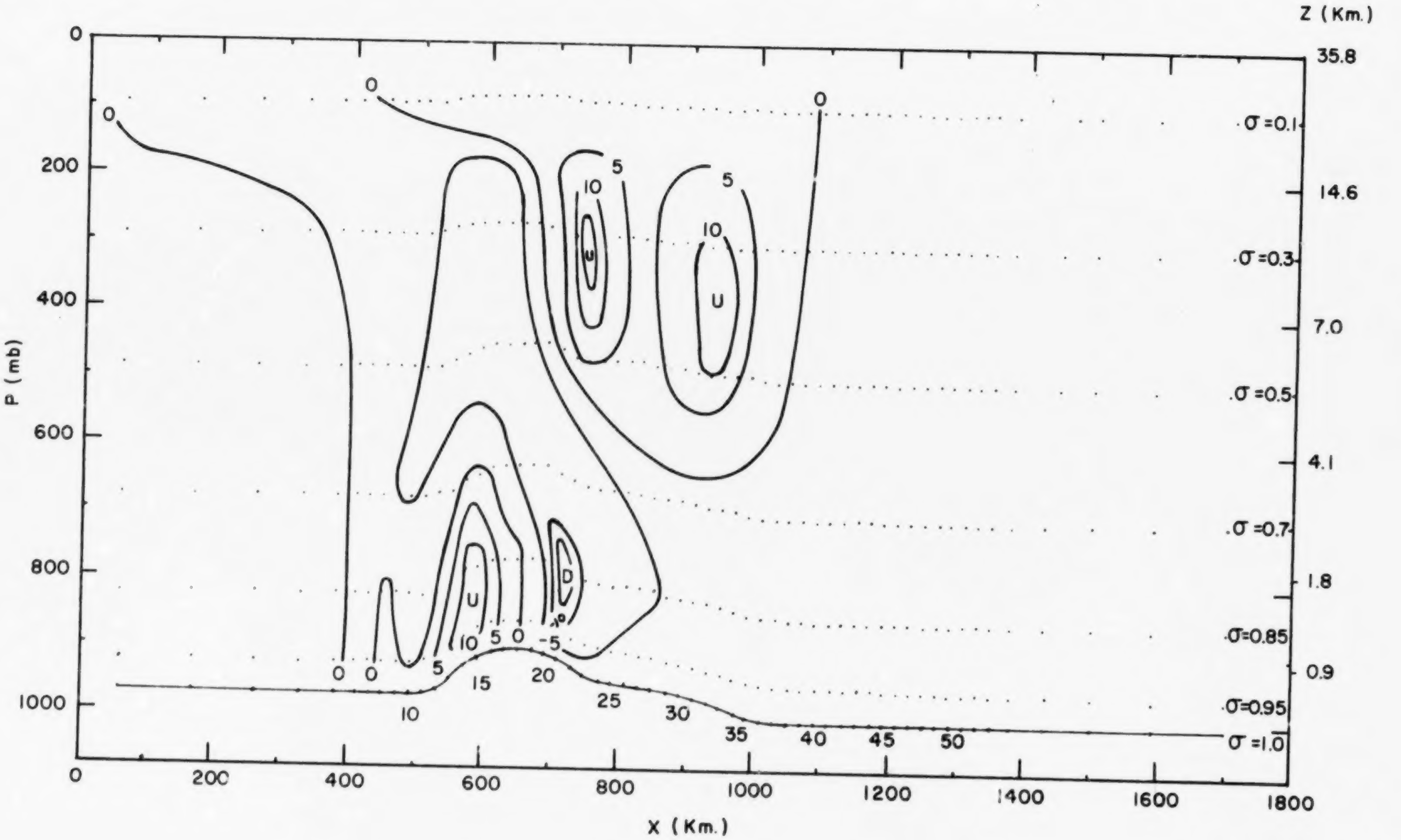

Figure 2.7 Time-averaged vertical cross section of vertical velocity (cm s^{-1}) for Exp. 2D-1

stratocumulus clouds that is frequently observed over the Appalachians in strong northwesterly flow. Mean subsidence of 10cm s^{-1} occurs over the lee slopes.

We now consider the components of the kinetic energy budget in Exp. 2D-1, shown for each hour of the 12-hour forecast in Fig. 2.8. Because the western boundary of the domain is at a higher elevation than the eastern boundary, the conversion of potential to kinetic energy by the u-component (labeled A) is positive over the domain (about 20 watts/m^2). This generation is more than offset by the frictional dissipation (E), which represents mainly the effect of surface friction. The conversion of potential to kinetic energy by the term ($fvu_g p^*$) in (2.27) oscillates slowly around zero as the v-component adjusts to the ageostrophic u-component produced by surface friction and the mountain-induced wave.

The net flux of kinetic energy across the lateral boundaries is represented by B in Fig. 2.8. This term is positive, indicating that kinetic energy is being advected into the region. The magnitude of the net boundary flux exceeds the sum of the generation term and the frictional dissipation term, and in fact, the total kinetic energy tendency (D) closely follows the variation of the boundary flux of kinetic energy. This large flux of kinetic energy across the boundaries, even in this simple experiment in which there is no variation of the geostrophic wind across the domain, is one indication of the importance of the boundary term. (In an identical experiment, in which the velocity at the inflow boundary was held constant rather than allowed to decrease as friction reduced the velocities on the interior, the boundary flux was much larger and the wind speed significantly higher far into the domain.)

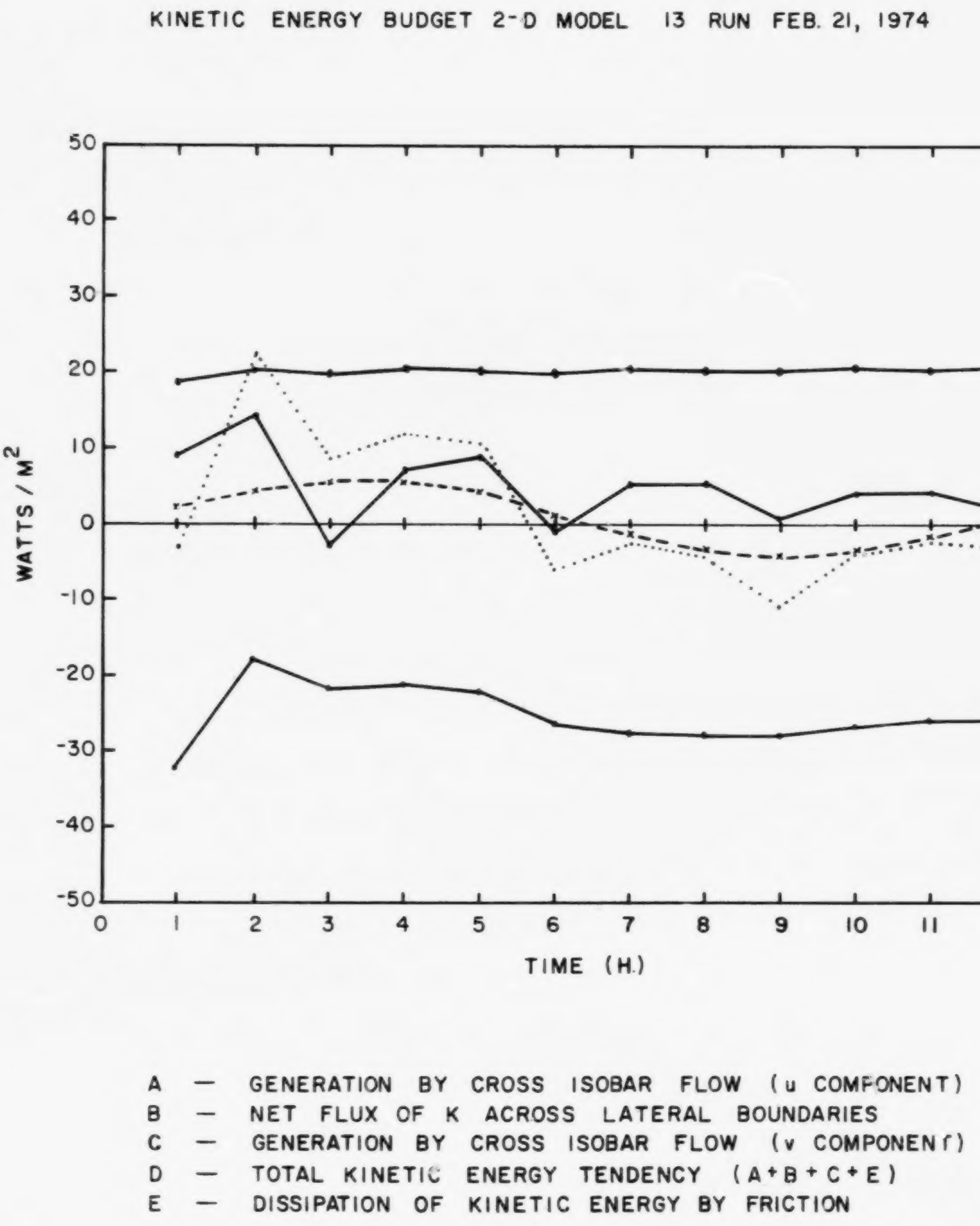

Figure 2.8 Kinetic energy budget for Exp. 2D-1

2.8.3 Initialization of the boundary layer winds considering the effects of surface friction. One of the difficulties with mesoscale forecasts is that the short time scale of the forecast means that greater care will have to be taken with the initialization procedure; a 6-hour "adjustment" period is undesirable in a 12-hour forecast. If only gravity wave modes, which traverse the entire domain in an hour or so, were present, the adjustment period would be tolerably short. However, inertial modes with periods of roughly 15-20 hours in middle latitudes are also present, and for short-range forecasts, it is desirable to minimize the amplitude of these waves that are generated by initial imbalances.

One source of initial imbalance is the sudden introduction of surface friction in a geostrophic current. Fig. 2.9 shows the x-profiles of the u-component in the boundary layer at 0.67h, 3.33h, and the 7-12h average in Exp. 2D-1. The u-components decrease rapidly at first from the geostrophic value of 30 m s^{-1}, but instead of converging monotonically toward the 7-12 hour average, they "overshoot" their equilibrium values. This large imbalance and subsequent overshooting produces a large amplitude inertial wave which persists throughout the 12-hour forecast.

To illustrate the nature of this frictionally induced oscillation, we consider the following simplified boundary layer equations in which the non-linear terms are neglected, and the geostrophic north-south wind component is zero,

$$\frac{\partial u}{\partial t} = fv - Ku \tag{2.35}$$

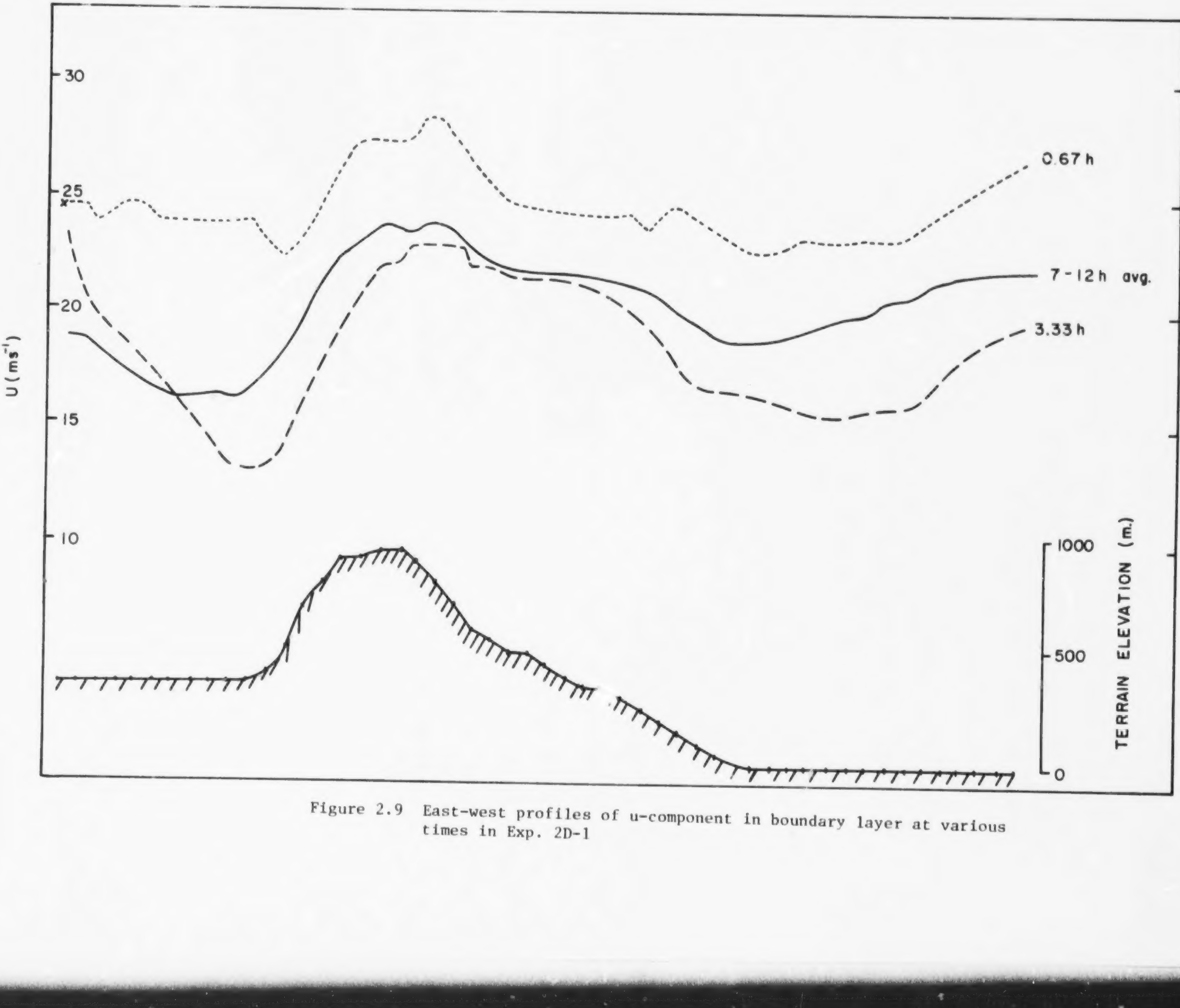

Figure 2.9 East-west profiles of u-component in boundary layer at various times in Exp. 2D-1

$$\frac{\partial v}{\partial t} = -f(u - u_g) - Kv \tag{2.36}$$

where K represents a frictional coefficient. A multiplication of (2.36) by $i = \sqrt{-1}$ and addition to (2.35) yields

$$\frac{\partial \underset{\sim}{V}}{\partial t} + [K + if]\, \underset{\sim}{V} = if\underset{\sim}{V}_g, \tag{2.37}$$

where $\underset{\sim}{V} = u + iv$ and $\underset{\sim}{V}_g = u_g + iV_g$. The general solution is

$$\underset{\sim}{V} = c_1 e^{-(K + if)t} + \frac{if\underset{\sim}{V}_g}{K+if} \tag{2.38}$$

and with the initial conditions that $\underset{\sim}{V} = \underset{\sim}{V}_g$ at $t = 0$, the solution is

$$\underset{\sim}{V} = \frac{K\underset{\sim}{V}_g}{(K + if)}\, e^{-(K + if)t} + \frac{if\underset{\sim}{V}_g}{K+if} \quad . \tag{2.39}$$

A separation into the real and imaginary parts yields

$$u = \frac{U_g}{[1 + (\frac{K}{f})^2]} \{1 + e^{-Kt} [(\frac{K}{f})^2 \cos ft - \frac{K}{f} \sin ft]\} \tag{2.40}$$

$$v = \frac{U_g}{[1 + (\frac{K}{f})^2]} (\frac{K}{f}) \{1 + e^{-Kt} [-(\frac{K}{f}) \sin ft - \cos ft]\} \tag{2.41}$$

The time dependent solutions (2.40) and (2.41) contain a transient part (an inertial oscillation which damps with time) and a stationary part, given by

$$u(t \to \infty) = \frac{U_g}{[1 + (\frac{K}{f})^2]} \qquad (2.42)$$

$$v(t \to \infty) = \frac{U_g}{[1 + (\frac{K}{f})^2]} (\frac{K}{f}) \quad . \qquad (2.43)$$

If the friction is abruptly introduced in a geostrophic current, the transient part is meaningless as far as the mesoscale forecast is concerned. The time constant for the damped oscillation is 1/K. In the simple PBL parameterization in which the surface stress is given by the quadratic stress law (eq. 2.32) and the stress is assumed to vanish at the top (H) of the PBL, K takes the form in (2.35) and (2.36)

$$K(t) = \frac{C_D |\underset{\sim}{V}(t)|}{H} \qquad (2.44)$$

so that K is not strictly a constant. As an approximation, let $|\underset{\sim}{V}(t)| = |\underset{\sim}{V}_g| = 20 \text{ ms}^{-1}$, $C_D = 1.5 \times 10^{-3}$, and H = 1 km, which yields a time constant of 9.3 hours. Fig. 2.10 shows the hodograph of the non-linear solution (obtained by a numerical integration of eqs. (2.35) and (2.36)) for these parameters. The three hourly positions are indicated by the symbol x. As shown by Fig. 2.10, the u-component decreases rapidly during the first three hours and overshoots its equilibrium value by about 4 ms^{-1}. This behavior is similar to the variation of the boundary layer u-component in the 2-D model.

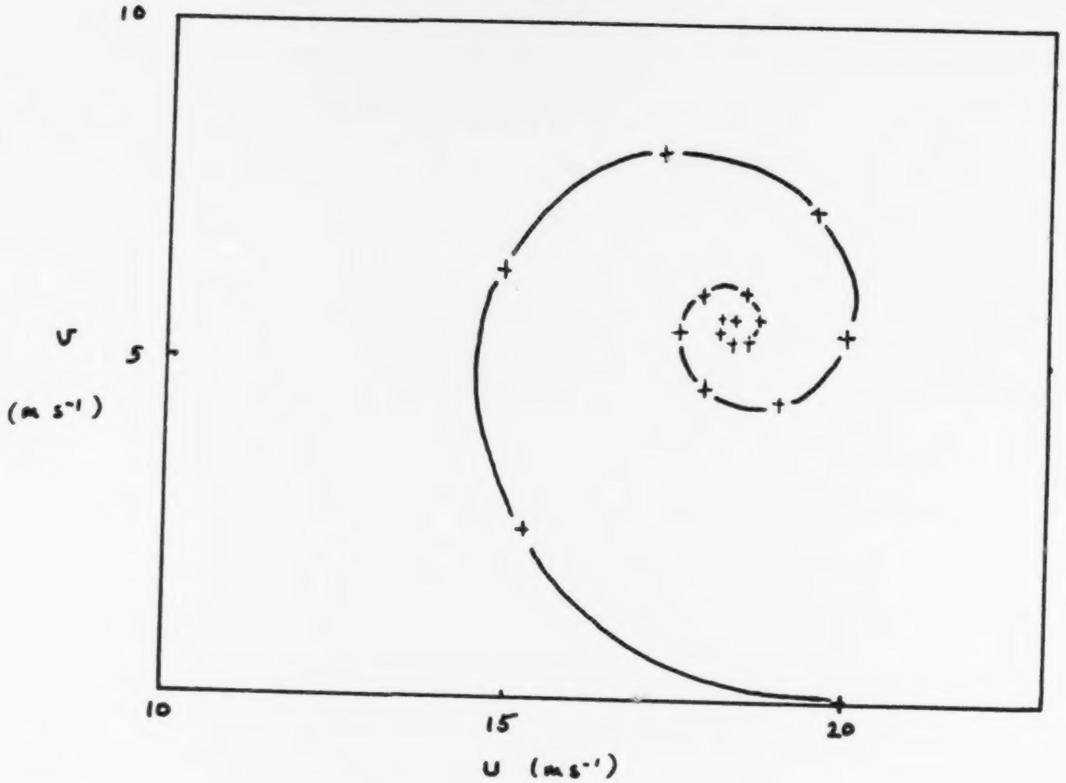

Figure 2.10 Hodograph of non-linear solution to simplified boundary layer equations with geostrophic initial conditions

If it is desirable to eliminate or at least minimize the amplitude of the transient part of the boundary layer solution, the model must be initialized to include the effects of surface friction. In the simple model, this may be done by initializing the u- and v-components with their linear, steady state values. Fig. 2.11 shows the time variation of the hodograph for the non-linear model with the initial conditions given by the solutions to the linear model ($K = \frac{C_D |\underset{\sim}{V}_g|}{H}$). The amplitude of the oscillation is reduced by an order of magnitude.

Of course in the mesoscale model, the non-linear advective terms and the terrain induced gravity winds interact with the boundary layer winds in a complicated way, nevertheless the amplitude of the frictionally induced inertial oscillation may be reduced by initializing the u and v components according to (2.42) and (2.43). Exp. 2D-2 is identical to Exp. 2D-1 except that the boundary layer winds are initialized in this way, with $u = 20.1 \text{ ms}^{-1}$ and $v = 9.8 \text{ ms}^{-1}$. Fig. 2.12 shows the time evolution of the x-profiles of u in Exp. 2D-2. Compared to Exp. 2D-1, the amplitude of the initial oscillation is significantly reduced. Although the solutions in Exp. 2D-1 and 2D-2 differ considerably during the first six hours, the 7-12 hour averages are very similar in both experiments since the time constant for $C_D = .003$, $|V_g| = 20$, and $H = 1$ km is about 4.6h.

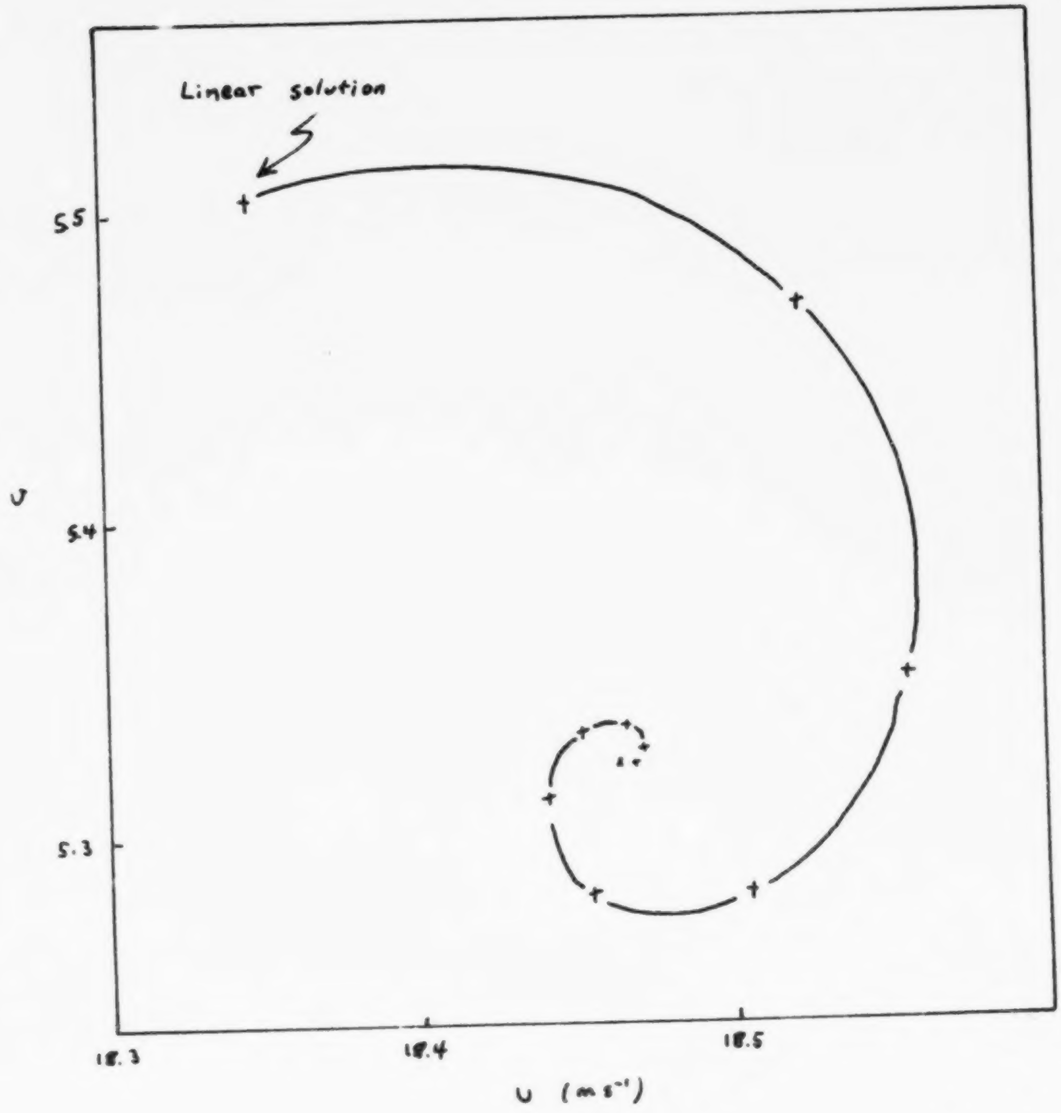

Figure 2.11 Hodograph of non-linear solution to simplified boundary layer equations with initial conditions given by linear solution

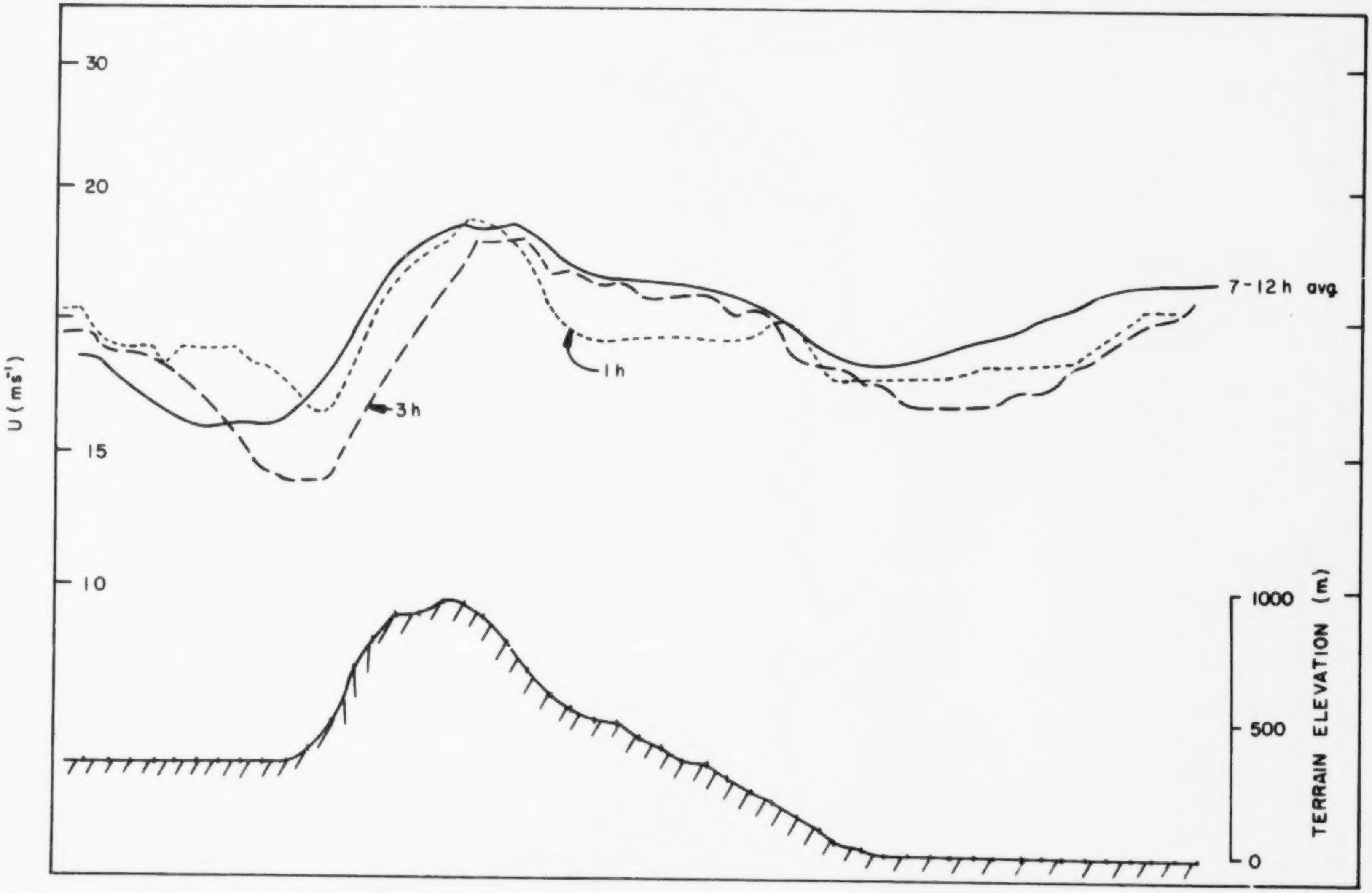

Figure 2.12 East-west profiles of u-component in boundary layer at various times in Exp. 2D-2

APPENDIX - CHAPTER 2.0

EQUATIONS OF MOTION FOR THE LAMBERT CONFORMAL PROJECTION

The Lambert Conformal projection is obtained by projecting the image of the earth's surface on a right circular cone which intersects the earth's surface at two latitudes, ϕ_1 and ϕ_2. The axis of the cone coincides with the north pole. The cone is then cut along one side and flattened. A cartesian (x - y) grid is oriented on the flattened image, and the latitude and longitude coordinate of any point related to its cartesian coordinate (x,y).

Normally, the x-axis (y = 0) coincides with 0° longitude, and the relationships between x and y and latitude (ϕ) and longitude (λ) are given by

$$x = r \cos \lambda' \qquad (1)$$

$$y = r \sin \lambda' \qquad (2)$$

$$\lambda' = n \lambda \qquad (3)$$

$$r = \left(\frac{a}{n}\right) \sin \psi_1 \left[\frac{\tan \psi/2}{\tan \psi_1/2}\right]^n \qquad (4)$$

where λ is the longitude (positive east, negative west), n is the constant of the cone, ψ_1 is the colatitude of ϕ_1, ψ is colatitude (90° - ϕ), and a is the radius of the earth.

The above projection produces an x - y grid for which the y-axis is oriented north-south at longitude 125.7°W. Since the regional model is centered near 80°W, the x and y directions on this grid are significantly different from the east-west and north-south directions on the earth. Therefore, in our model, the projection is rotated 45.70° so that the y-axis coincides with 80°W longitude. To accomplish this rotation, we define

$$\lambda'' = \lambda - 45.70 \tag{5}$$

$$\lambda' = n\lambda'' \quad . \tag{6}$$

The relations (1), (2), and (4) remain the same. With this rotation, the point at 35°N 80°W is located on the grid at x = 0, y = -7157 km (See Fig. 2.1).

To derive the equations of motion for Lambert Conformal coordinate, we make the following definitions:

x,y,z	map coordinates (projected system).
x_s,y_s,z_s	curvilinear earth coordinates, x positive eastward, y positive northward, z positive upward.
U,V,W	velocity components relative to earth along the x_s,y_s,z_s directions.
u,v,w	velocity components relative to earth along the x,y,z directions.

The equations of motion are

$$\frac{dU}{dt} - \frac{UV\tan\phi}{r_e} + \frac{UW}{r_e} = -\alpha\frac{\partial p}{\partial x_s} + fV - 2\,\Omega W\cos\phi + Fx_s \tag{7}$$

$$\frac{dV}{dt} + \frac{U^2\tan\phi}{r_e} + \frac{VW}{r_e} = -\alpha\frac{\partial p}{\partial y_s} - fU + Fy_s \tag{8}$$

$$\frac{dW}{dt} - \frac{U^2 + V^2}{r_e} = -\alpha\frac{\partial p}{\partial z_s} - g + 2\,U\Omega\cos\phi + Fz_s\ , \tag{9}$$

where
$$U = r \cos\phi \frac{d\lambda}{dt}$$

$$V = r_e \frac{d\phi}{dt}$$

$$W = \frac{dr_e}{dt}$$

$$dx_s = r_e \cos\phi \, d\lambda$$

$$dy_s = r_e \, d\phi$$

$$dz_s = dr_e \qquad (10)$$

and r_e is the radius measured from the center of the earth, Ω is the angular velocity of the earth, α is specific volume, and Fx_s and Fy_s are the frictional forces in the curvilinear earth coordinates.

Now, from the definitions of x and y in (1) - (2), it may be shown that

$$\begin{pmatrix} dx \\ dy \end{pmatrix} = m \, r_e \begin{pmatrix} -\cos\lambda' & -\sin\lambda' \cos\phi \\ -\sin\lambda' & \cos\lambda' \cos\phi \end{pmatrix} \begin{pmatrix} d\phi \\ d\lambda \end{pmatrix} \qquad (11)$$

$$= m \begin{pmatrix} -\cos\lambda' & -\sin\lambda' \cos\phi \\ -\sin\lambda' & \cos\lambda' \cos\phi \end{pmatrix} \begin{pmatrix} dy_s \\ dx_s \end{pmatrix} \qquad (12)$$

where
$$m = \frac{\sin\psi_1}{\sin\psi} \left[\frac{\tan\psi/2}{\tan\psi_1/2}\right]^n \qquad (13)$$

Furthermore, the relationship between the velocity components in the map coordinates (u,v) and in the curvilinear earth coordinates (U,V) is

$$\begin{pmatrix} u \\ v \end{pmatrix} = \begin{pmatrix} -\sin\lambda' & -\cos\lambda' \\ \cos\lambda' & -\sin\lambda' \end{pmatrix} \begin{pmatrix} U \\ V \end{pmatrix} \qquad (14)$$

which may be inverted to yield

$$\begin{pmatrix} U \\ V \end{pmatrix} = \begin{pmatrix} -\sin\lambda' & \cos\lambda' \\ -\cos\lambda' & -\sin\lambda' \end{pmatrix} \begin{pmatrix} u \\ v \end{pmatrix} \quad . \tag{15}$$

Next, the relationship between the acceleration in the (x,y) and (x_s, y_s) coordinates must be found. A differentiation of (14) yields

$$\begin{pmatrix} \frac{du}{dt} \\ \frac{dv}{dt} \end{pmatrix} = \begin{pmatrix} -\sin\lambda' & -\cos\lambda' \\ \cos\lambda' & -\sin\lambda' \end{pmatrix} \begin{pmatrix} \frac{dU}{dt} \\ \frac{dV}{dt} \end{pmatrix} + \frac{d\lambda'}{dt} \begin{pmatrix} 0 & -1 \\ 1 & 0 \end{pmatrix} \begin{pmatrix} u \\ v \end{pmatrix} \tag{16}$$

Finally, the relationship between the derivatives in the two coordinates is

$$\begin{pmatrix} \frac{\partial}{\partial x_s} \\ \frac{\partial}{\partial y_s} \end{pmatrix} = m \begin{pmatrix} -\sin\lambda' & \cos\lambda' \\ -\cos\lambda' & -\sin\lambda' \end{pmatrix} \begin{pmatrix} \frac{\partial}{\partial x} \\ \frac{\partial}{\partial y} \end{pmatrix} \quad . \tag{17}$$

Now, with the use of (17), (16) and (14), the horizontal component equations of motion may be written

$$\frac{\partial u}{\partial t} = - m \left(u \frac{\partial u}{\partial x} + v \frac{\partial u}{\partial y}\right) + v\ (\gamma + f) - m\alpha \frac{\partial p}{\partial x} + w\ 2\Omega\ \cos\phi\ \sin\lambda' - \frac{u}{r_e}\ )$$

$$- Fx_s \sin\lambda' - Fy_s \cos\lambda' \tag{18}$$

$$\frac{\partial v}{\partial t} = -m\left(u\frac{\partial v}{\partial x} + v\frac{\partial v}{\partial y}\right) + (Fx_s \cos\lambda' - Fy_s \sin\lambda')$$

$$- (\gamma + f)\,u - m\alpha\frac{\partial p}{\partial y} - \quad w\left(2\Omega\cos\phi\cos\lambda' + \frac{v}{r_e}\right) \tag{19}$$

The derivation of the equation for $\frac{dw}{dt}$ is much simpler, since $\frac{\partial}{\partial z} = \frac{\partial}{\partial z_s}$ and $w = W$, so that after substitution for u,v,and w in terms of U,V, and W, we obtain

$$\frac{dw}{dt} = \frac{u^2 + v^2}{r_e} + 2\Omega\cos\phi\left(-\frac{uy}{r} + \frac{vx}{r}\right) - \alpha\frac{\partial p}{\partial z} - g + Fz_s \tag{20}$$

where r is given by (4). For hydrostatic systems, in which (20) is approximated by

$$\alpha\frac{\partial p}{\partial z} + g = 0 \tag{21}$$

the kinetic energy equation will contain $\frac{1}{2}(u^2 + v^2)$ rather than $\frac{1}{2}(u^2 + v^2 + w^2)$. Hence, for consistency, the small terms involving w in the horizontal component equation (18) and (19) are usually neglected.

To obtain the equations given in (2.2) and (2.3), the vertical coordinate z is transformed to σ (for example, see Haltiner, 1971) and the equations are written in flux form with the aid of the continuity equation.

3.0 PRELIMINARY THREE-DIMENSIONAL EXPERIMENT USING REAL DATA WITH AND WITHOUT TERRAIN

In this section we describe our first attempt at initializing the 3-D regional model with real data. Since the primary purpose was to test the numerical stability of the model under strong winds and time-dependent boundary conditions for a 12-hour forecast, a very crude initialization scheme was tested. This scheme consisted of simply interpolating data from large-scale, hand analyses to the 20-km grid. The reaction of the model to this set of unbalanced data has revealed several important aspects of this model in particular and mesoscale modeling in general. For example, it has shown (1) that the model is quite stable numerically, (2) that high frequency, short-wavelength noise does not cause much difficulty even with unbalanced data, and (3) the use of unbalanced data apparently produces large linear and non-linear acclerations of the mean flow over the domain. Because of the crude initialization scheme, the forecasts do not appear to be very accurate, although lack of verification data on the scale of the model hampers their evaluation. Nevertheless, a comparison of 12-hour forecasts with and without the complex terrain of the Appalachians, but identical in every other respect, indicates the importance of terrain on this scale of motion.

3.1 Synoptic Discussion on 12Z Oct. 16 - 00Z Oct. 17, 1973

As part of the SRG research program, The Pennsylvania State University conducted a pilot field experiment during the period Oct 16-17, 1973. One of the purposes of this program was to obtain data to supplement the conventional surface and upper air data network and to be used in the verification of the regional model. Part of the program included the flying of the Penn State aircraft over the central portion of the regional model's domain. Although it was realized that one aircraft could not provide an adequate data base for mesoscale model verification, we hoped to obtain enough low-level data to partially verify the model and to aid in the identification of the scales of the perturbations caused by moderate to strong flow over rough terrain.

From the beginning of the regional model development, we have concentrated on the modification of synoptic-scale flow by gravity waves produced when statically stable air flows over rough terrain. Because the terrain in the regional model's domain contains appreciable energy in the wavelengths resolvable by the model (100 - 600 km), variations in terrain should be a major cause of mesoscale variation in weather (temperature, wind, cloudiness, rainfall, turbidity) in this area.

The synoptic situation chosen for the first test of the model was one in which terrain-induced gravity waves were expected to produce measurable (and hopefully predictable) mesoscale perturbations to the large scale flow. Upward propagating gravity waves are favored over mountainous terrain when the basic current is strong, statically stable, perpendicular to the ridge, and nearly constant in direction with height. A strong northwesterly flow of cool air over the eastern third of the U. S. satisfies these requirements, since the mean terrain contours are oriented from the southwest to northeast. Furthermore, a strong cross-domain flow was desired to test the computational stability of the model under strong advection conditions, which are known to be difficult to handle numerically.

The weather situation chosen for the field program and subsequent modeling tests included the two day period from Oct. 16 to Oct. 17, 1973, and satisfies the preceding conditions quite well. During this period, northwesterly flow behind a cold front intensified slowly. At 12Z Oct. 16 the mean wind speed increased with increasing elevation from about 15 ms^{-1} at 850 mb to 50 ms^{-1} at 300 mb. During the next 12 hours, a strongly baroclinic zone and an associated jet maximum of 65 ms^{-1} drifted southward through the model domain, providing a good test for the time-dependent boundary conditions.

The lower tropospheric flow during this period is shown in the 850 mb maps for 12Z Oct. 16 and 00Z Oct. 17 (Figures 3.1 and 3.2). Although the temperature gradient is rather weak at this level, cold advection increases throughout the period. Furthermore, the geostrophic winds become more northerly during the 12 hours as a broad trough moves eastward. As discussed later, this tendency for increasing northerly winds is correctly predicted by the model.

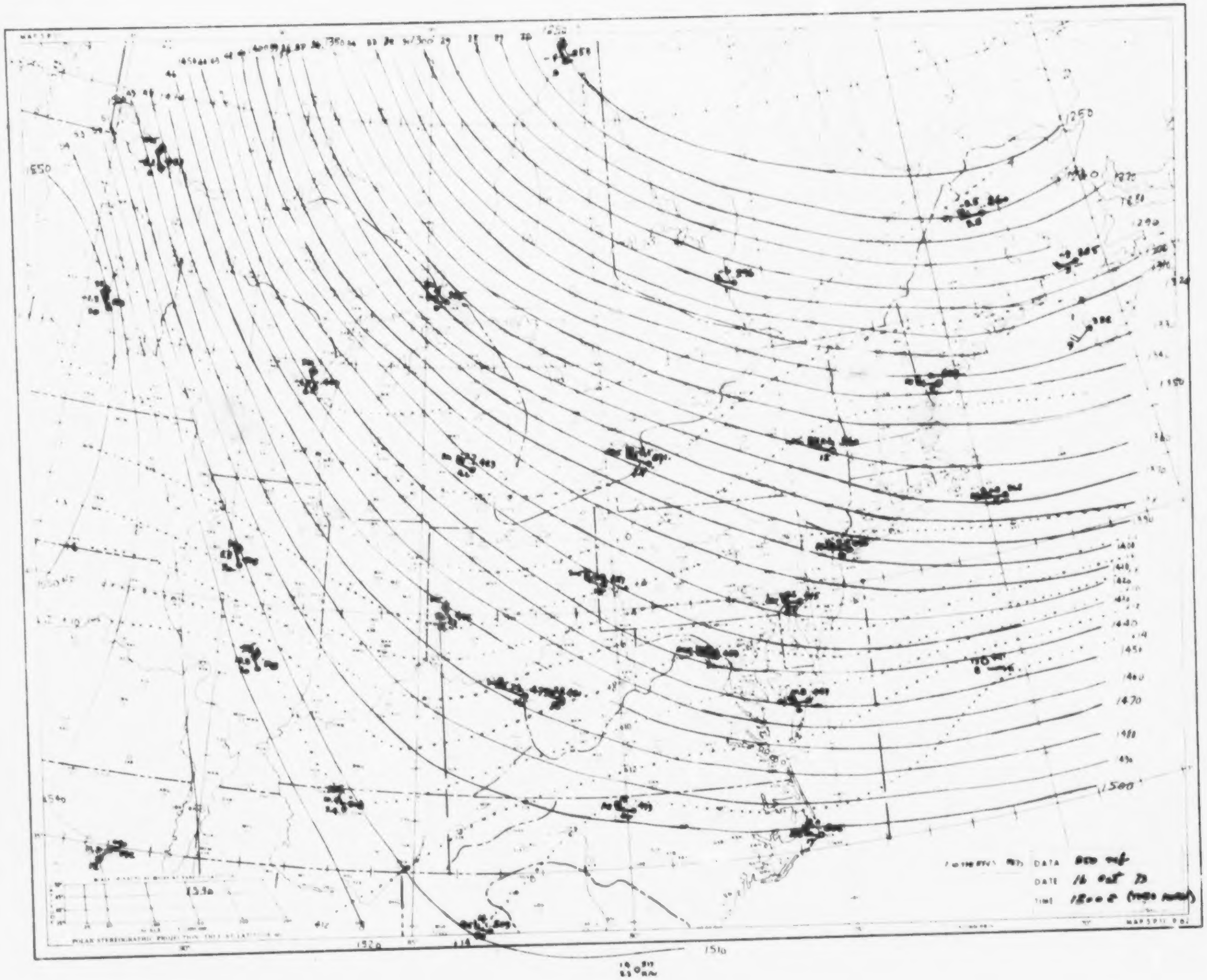
1250
1500
DATA
DATE
TIME

Figure 3.1 The 850 mb analysis for 12Z Oct. 16, 1973

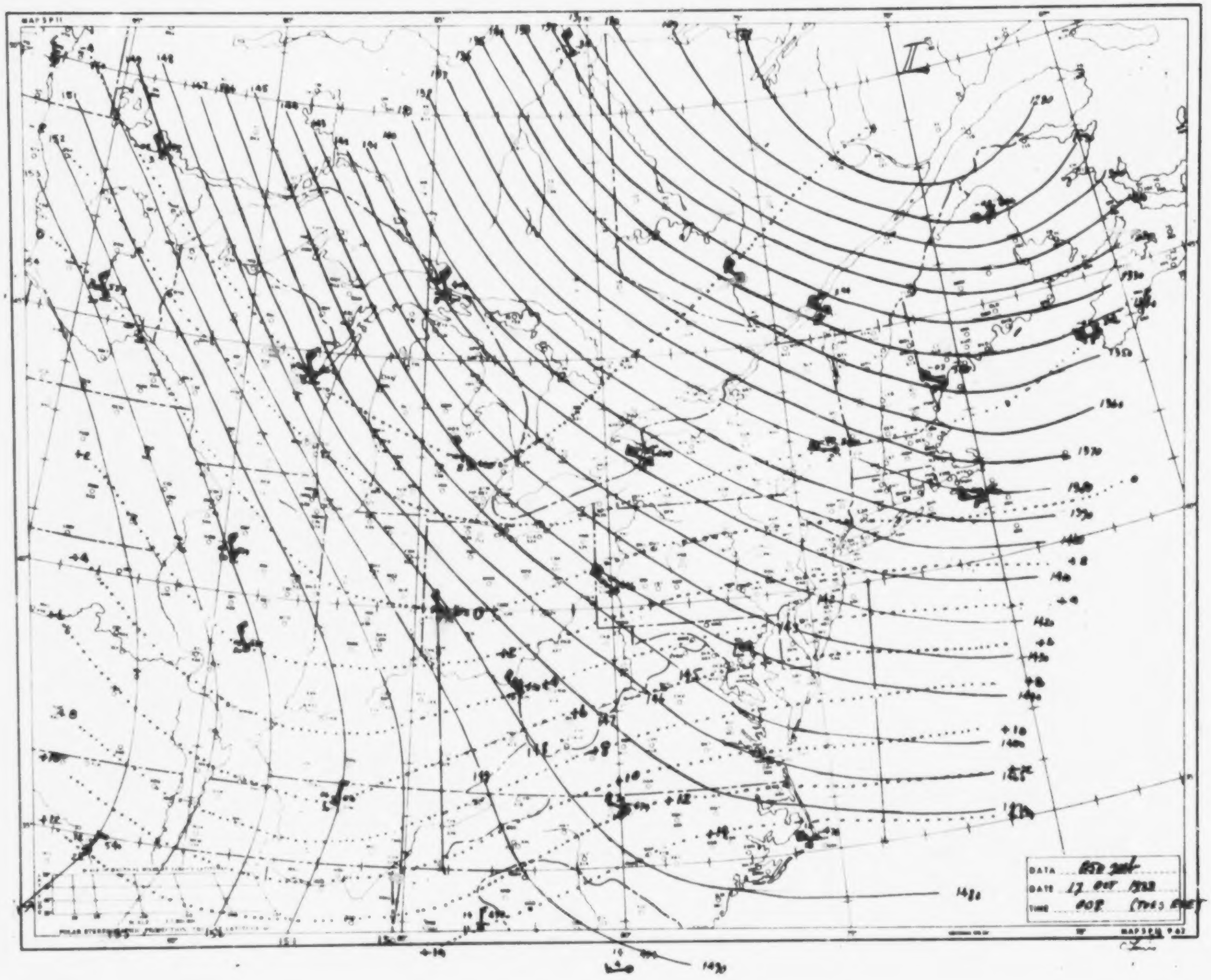
DATA 850 mb
DATE 17 OCT 1973
TIME 00Z (TUES) EDT
L
MAPSPN 9-62

Figure 3.2 The 850 mb analysis for 00Z Oct. 17, 1973

The middle tropospheric flow at 12Z Oct 16 and 00Z Oct 17 is illustrated in the 500 mb maps shown in Figures 3.3 and 3.4. The upper level front is much sharper at this level, as the packing of the isotherms over Pennsylvania and New York in Fig. 3.3 indicates. During the 12-hour forecast period, this intense baroclinic zone drops southward into the mesoscale model domain -- the temperature at 500 mb along the northern boundary falls by about 10°C. At 500 mb, as well as at 850 mb, the winds veer with time, becoming more northerly.

The upper level flow is shown in the 300 mb maps at 12Z Oct 16 and 00Z Oct 17 (Figures 3.5 and 3.6). The upper level front reaches the northern part of the mesoscale domain by 00Z Oct 17. The wind speeds over the model domain increase with time as the baroclinic zone in the middle and lower levels intensifies.

Thus the synoptic pattern of Oct. 16 and 17 should be quite favorable for the production of mesoscale perturbations to the mean flow. Northwesterly flow of stable air increased in speed with height but changed direction only slightly. Strong cold advection in the middle troposphere was present to check the model's reaction to time-dependent boundary conditions.

3.2 Initialization and verification analyses and specification of time-dependent boundary conditions

As mentioned earlier, the initial data for the 30 x 50 grid pictured in Figure 2.1 were obtained by reading temperature and

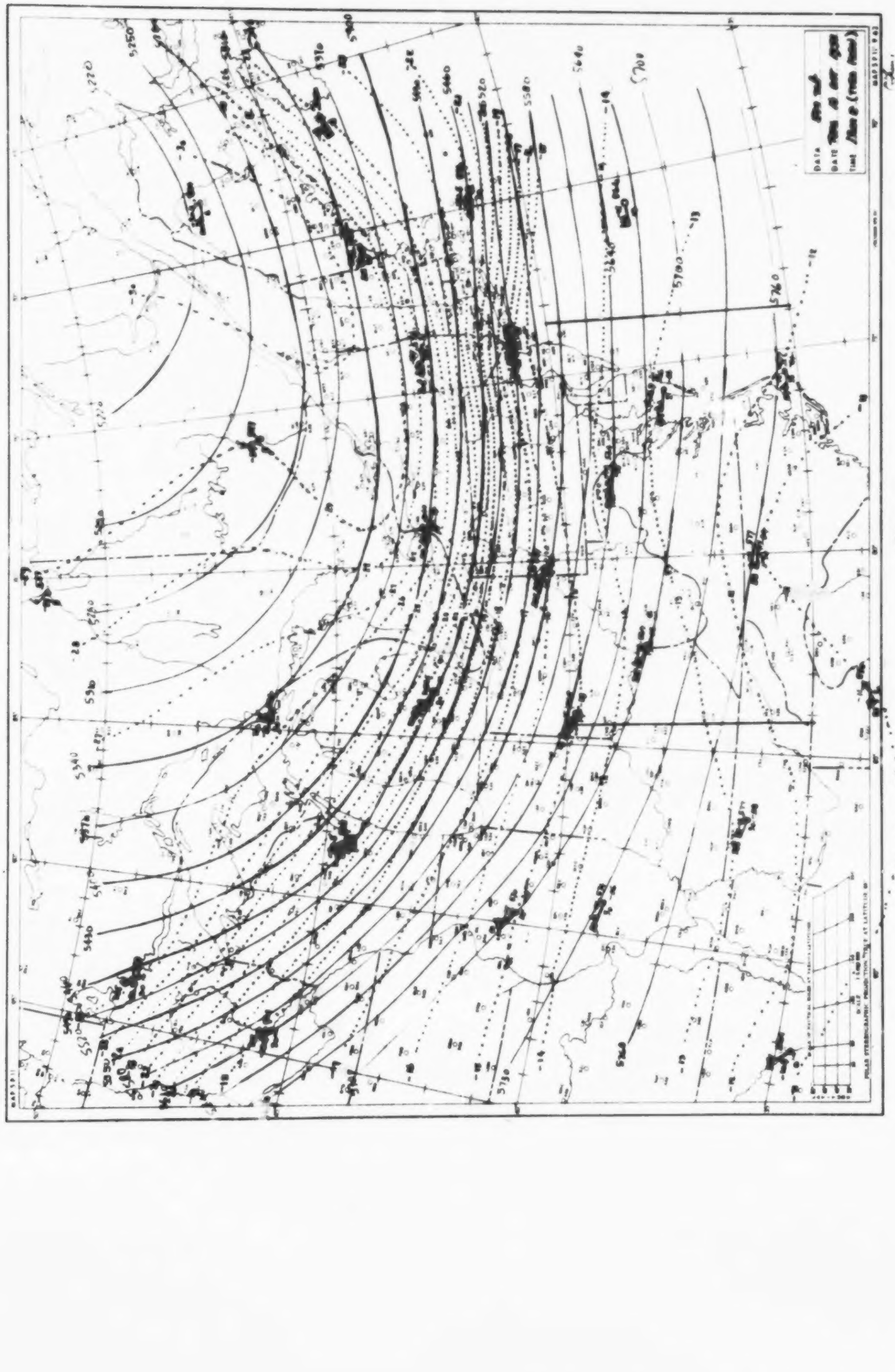

Figure 3.3 The 500 mb analysis for 12Z Oct. 16, 1973

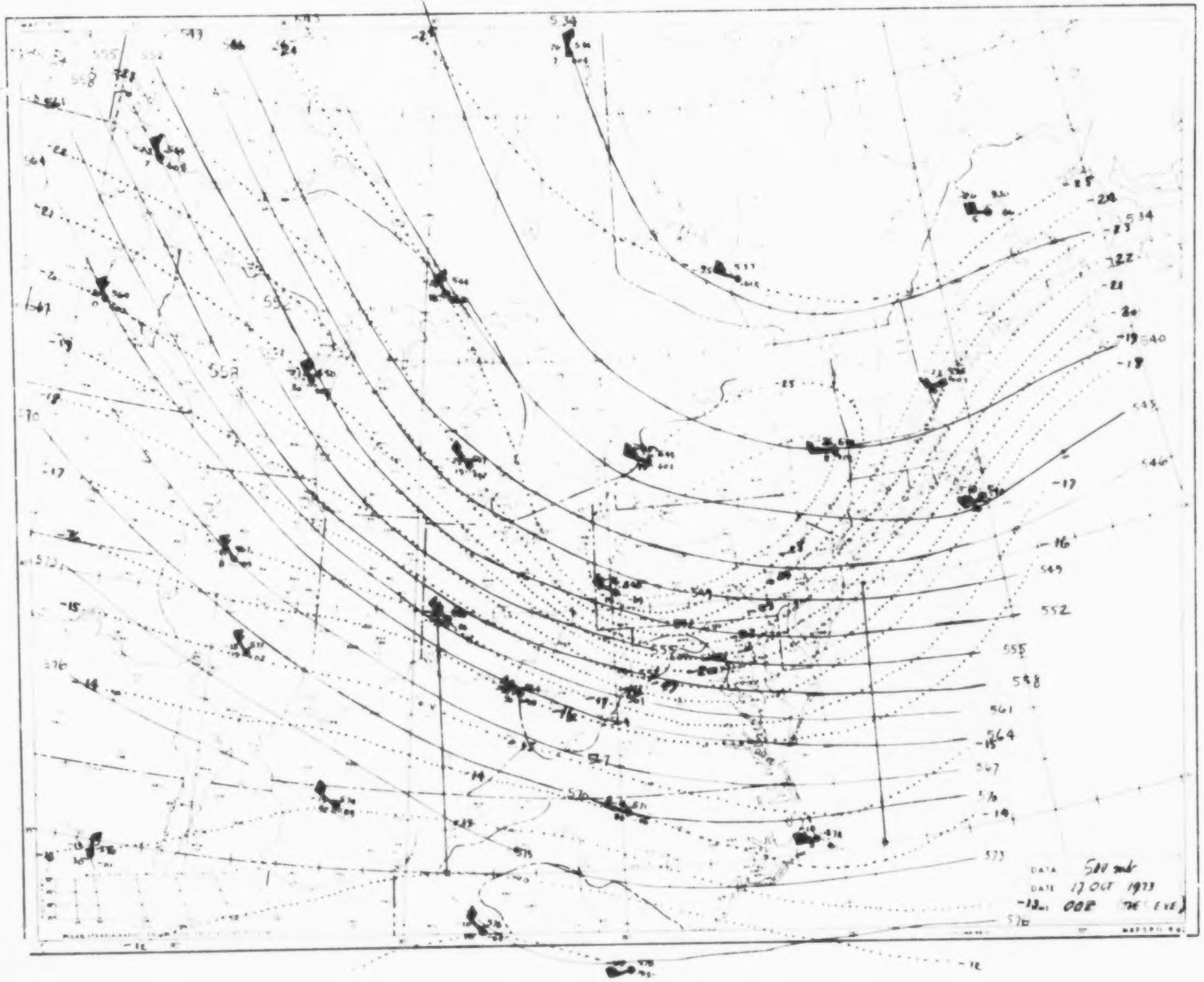
DATA 500 mb
DATE 17 OCT 1973
00Z
534
540
546
549
552
555
558
561
564
567
570
573
576

Figure 3.4 The 500 mb analysis for 00Z Oct. 17, 1973

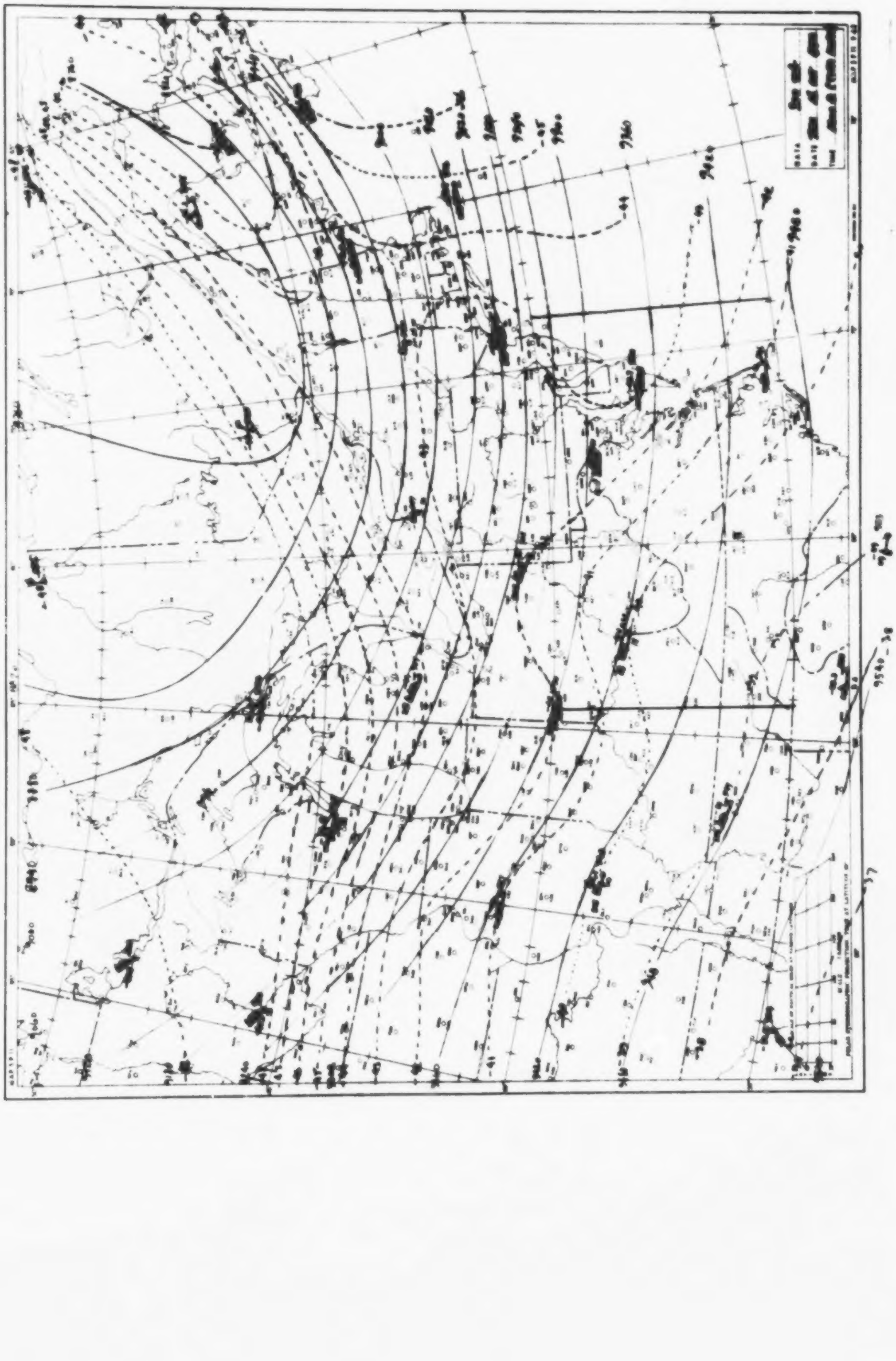

Figure 3.5 The 300 mb analysis for 12Z Oct. 16, 1973

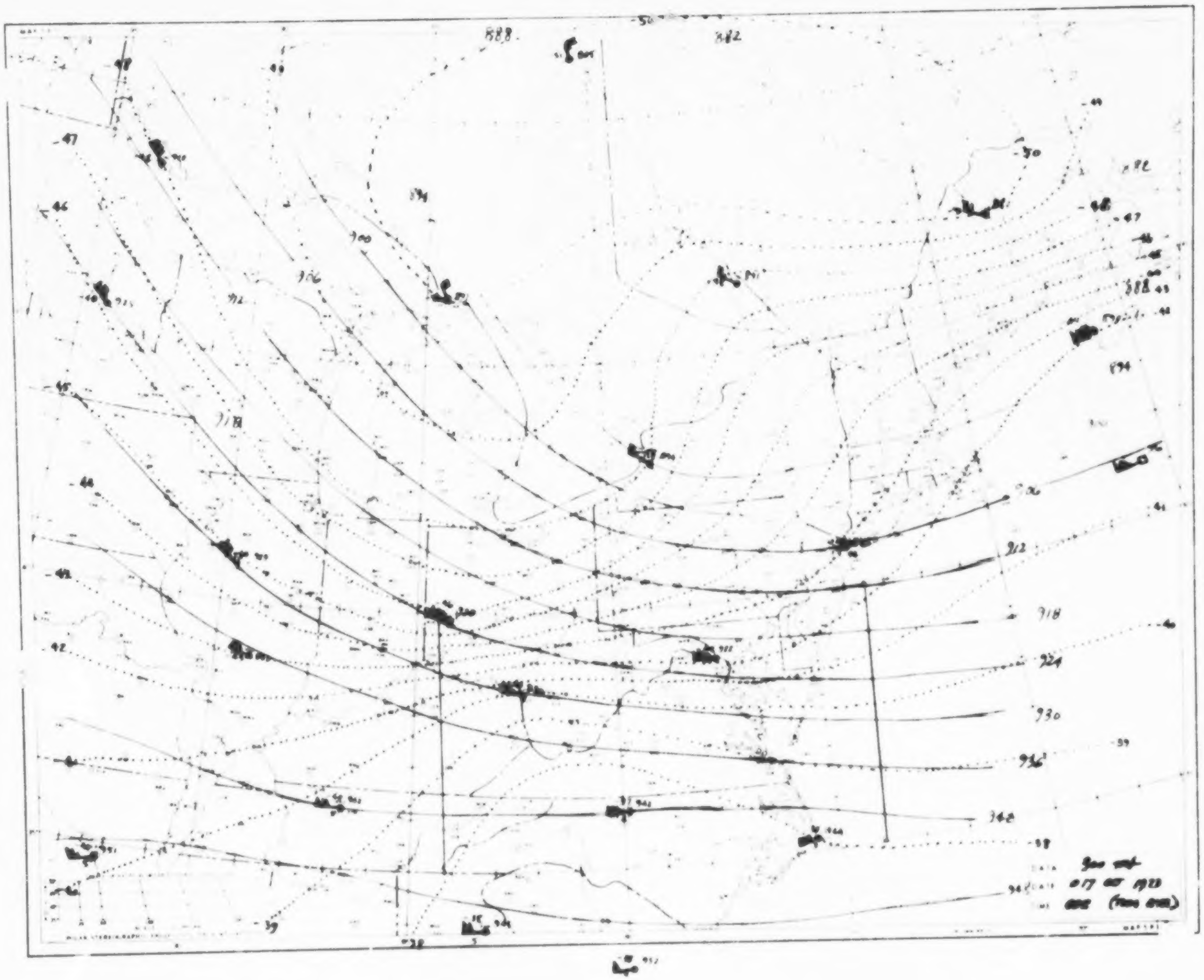
888
882
894
900
906
912
918
924
930
936
942

Figure 3.6   The 300 mb analysis for 00Z Oct. 17, 1973

wind data for every tenth grid point from the hand analyses at the surface, 850, 700, 500, 300 and 200 mb pressure levels. These data were linearly interpolated to the remaining grid points on the surface and constant pressure charts. The data were then linearly interpolated to the σ-surfaces defined in Table 3.1.

Table 3.1 Sigma surfaces for velocity and temperature in 3-D model experiment (p_t = 250 mb)

Level Index	$\sigma = \frac{p - p_t}{p_s - p_t}$	Mean pressure of σ - surface (mb) at t = 0, Exp 1
1	0.125	342
2	0.325	489
3	0.475	599
4	0.625	709
5	0.775	819
6	0.925	929

Figure 3.7 shows an example of the unsmoothed analyses of u and the geostrophic u calculated from the analysis of the mass field on the sigma = 0.325 surface. The observed u-field is fairly smooth, but errors in the temperature analysis and the errors introduced by the bi-linear interpolation scheme produce a very noisy geostrophic wind field. It is noteworthy that even though imbalances of over 10 ms^{-1} between the mass and momentum fields

GEOSTROPHIC U (M/S) LEVEL 2 (σ = 0.325) 12Z OCTOBER 16, 1973

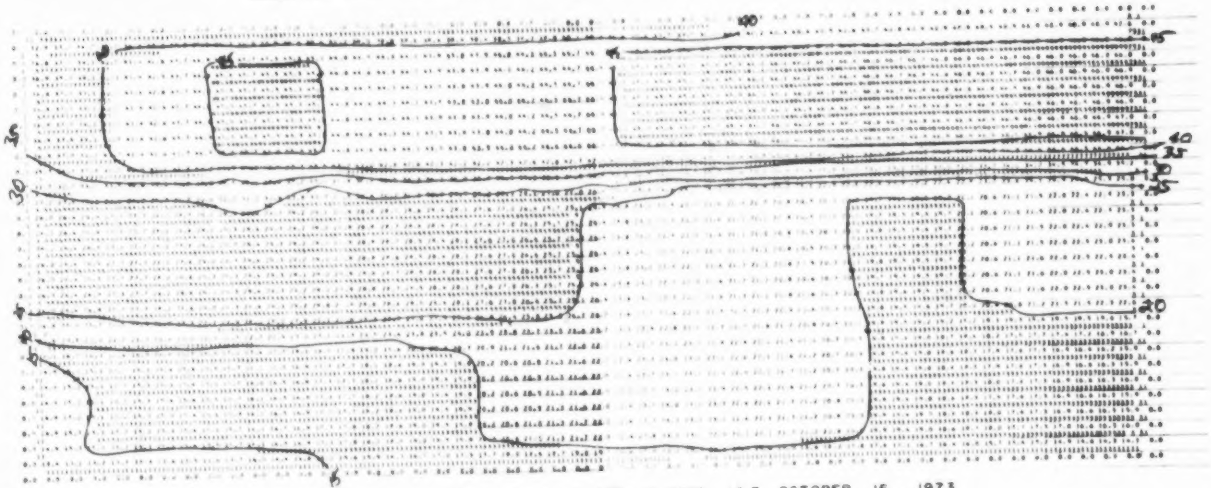

OBSERVED U (M/S) LEVEL 2 (σ = 0.325) 12Z OCTOBER 16, 1973

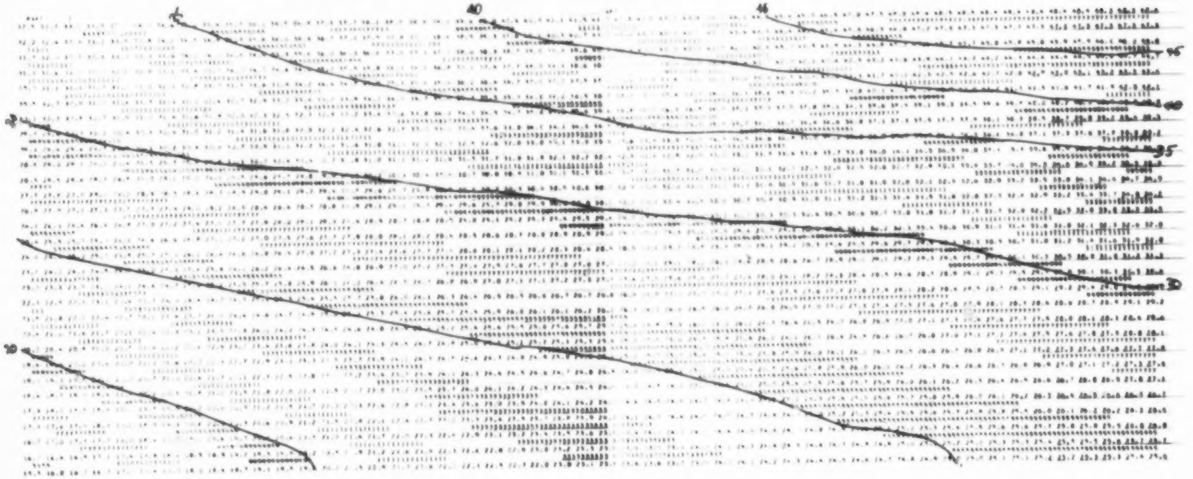

Figure 3.7 Observed u-component and geostrophic u-component at level 2 (σ = 0.325) at t = 0

exist initially, the horizontal scale of the imbalances is so small that the irregular mass field quickly adjusts to the smooth wind analysis. This rapid adjustment of the mass (temperature) field to the wind field on the small scale means that fine scale temperature perturbations, whether real or introduced as a result of analysis errors, will quickly disappear unless the small-scale features appear in the wind field as well. Thus it is important to realize that *a very accurate observation and analysis of the temperature field will have little value in mesoscale models unless the winds are initialized with comparable detail and accuracy*.

The unsmoothed and unbalanced data were used as initial conditions for a 12-hour forecast. The same procedure was used to obtain analyses at 00Z Oct 17. The temperatures, surface pressures, and wind components from the analyses at these two times were used to specify the time dependent lateral boundary conditions.

For temperature and pressure, the boundary values at every time step in the forecast were specified by a linear interpolation in time between the 12Z and 00Z analyses. The specification of the wind components was somewhat more complicated. Based on experiments with fictitious data, the most stable set of boundary conditions for the velocity components consisted of an outward extrapolation of the pressure-weighted velocity components regardless of direction of flow, but treating the velocity components themselves differently depending on whether the velocity component normal to the boundary was inward or outward. These conditions, needed only for the evaluation of the non-linear momentum flux terms, are given in Table 3.2.

Although these boundary conditions produce smooth solutions, the previous discussion on the importance of the boundary values of the velocity components and the results to be presented later suggest that a complete specification of the velocity components on all lateral boundaries may be desirable, even if this amounts to an overspecification. The resultant generation of short wavelength noise near the boundary can be controlled by the eddy viscosity term, without significantly affecting the mean motion over the domain.

3.3 Specification of parameters

In both experiments (with and without terrain) the upper pressure surface, p_t, is 250 mb. The grid size is 20 km and the time step is 30 s. The vertical diffusion of momentum is neglected except in the lowest layer of the model where the quadratic stress law, discussed in Section 2.8, is utilized. However, the drag coefficient, C_D, was inadvertantly set to rather low value (for this rough terrain) of 1×10^{-3}, so that surface friction is probably underestimated in these experiments.

The horizontal diffusion of heat and momentum, included mainly for the purpose of preventing the accumulation of energy in the short wavelengths, is modeled according to (2.15), (2.16) and (2.18), where K_H is given by

$$K_H = 5.0 \times 10^4 + \frac{k_o^2}{2} (\Delta s)^2 \; |D| \qquad (3.1)$$

Table 3.2 Lateral boundary conditions for momentum components u and v. (p*u and p*v on all boundaries are set equal to the values on the next interior row or column.)

BOUNDARY:	NORTH	EAST	SOUTH	WEST
TERM $(\overline{\overline{u}^x\,\overbrace{\frac{p^*u}{m}}^{y}}^{x})_x$	Not Needed	$u_{JMAX} = u_{JMAX-1}$ if $(p^*u)_{JMAX-1} \geq 0$ = specified if $(p^*u)_{JMAX-1} < 0$	Not Needed	$u_1 = u_2$ if $(p^*u)_2 \leq 0$ u_1 = specified if $(p^*u)_2 > 0$
$(\overline{\overline{u}^y\,\overbrace{\frac{p^*v}{m}}^{x}}^{y})_y$	$u_{IMAX} = u_{IMAX-1}$ if $(p^*v)_{IMAX-1} \geq 0$ u_{IMAX} specified if $(p^*v)_{IMAX-1} < 0$	Not Needed	$u_1 = u_2$ if $(p^*v)_2 \leq 0$ u_1 = specified if $(p^*v)_2 > 0$	Not Needed
$(\overline{\overline{v}^x\,\overbrace{\frac{p^*u}{m}}^{y}}^{x})_x$	Not Needed	$v_{JMAX} = v_{JMAX-1}$ if $(p^*u)\ JMAX-1 \geq 0$ v_{JMAX} = specified if $(p^*u)_{JMAX-1} < 0$	Not Needed	$v_1 = v_2$ if $(p^*u)_2 \leq 0$ v_1 = specified if $(p^*u)_2 > 0$
$(\overline{\overline{v}^y\,\overbrace{\frac{p^*v}{m}}^{x}}^{y})_y$	$v_{IMAX} = v_{IMAX-1}$ if $(p^*v)_{IMAX-1} \geq 0$ v_{IMAX} = specified if $(p^*v)_{IMAX-1} < 0$	Not Needed	$v_1 = v_2$ if $(p^*v)_2 \leq 0$ v_1 = specified if $(p^*v)_2 > 0$	Not Needed

where $k_o = 0.4, \Delta s = 20$ km, and $D = [(\frac{\partial u}{\partial x} - \frac{\partial v}{\partial y})^2 + (\frac{\partial v}{\partial x} + \frac{\partial u}{\partial y})^2]^{1/2}$. After an initial forward time step, the centered-in-time differencing scheme is utilized without time smoothing. The model was run on the NCAR CDC 7600 system, and requires about 30 min. of computer time for a 12-hour forecast.

3.4 Qualitative discussion of results

3.4.1. Low-level results. Figure 3.8 shows the forecast surface pressure change in the experiment with the smoothed Appalachian terrain, which is contoured in Figure 3.10. (Hereafter, this experiment, which includes terrain, will be denoted as Exp. 1; the identical experiment except for the setting of the terrain elevations to zero will be designated Exp. 1A.) The observed 12-hour pressure change is shown in Figure 3.9.

Both the forecast and observed pressures over the mesoscale domain have risen during the 12-hour forecast; however, the forecast pressures in the center of the domain have risen 2 mb more than the observed pressures. This erroneous rise cannot be attributed to inaccurate treatment of the terrain effects, since nearly the same rise is observed in Exp. 1A when the terrain is absent. Instead this error is probably a manifestation of the "pillow effect" (Benwell and Bretherton, 1968), and is related to the inaccurate initialization procedure, and in particular the treatment of the velocity components. This possibility will be investigated further after a more sophisticated analysis of the initial data that produces the time-dependent boundary conditions is tested.

The low-level velocity fields at 12 hours (00Z Oct. 17) for Exp. 1 and 1A are shown in Figures 3.10 and 3.11, and the verification map is shown in Figure 3.12. In both experiments the winds have become

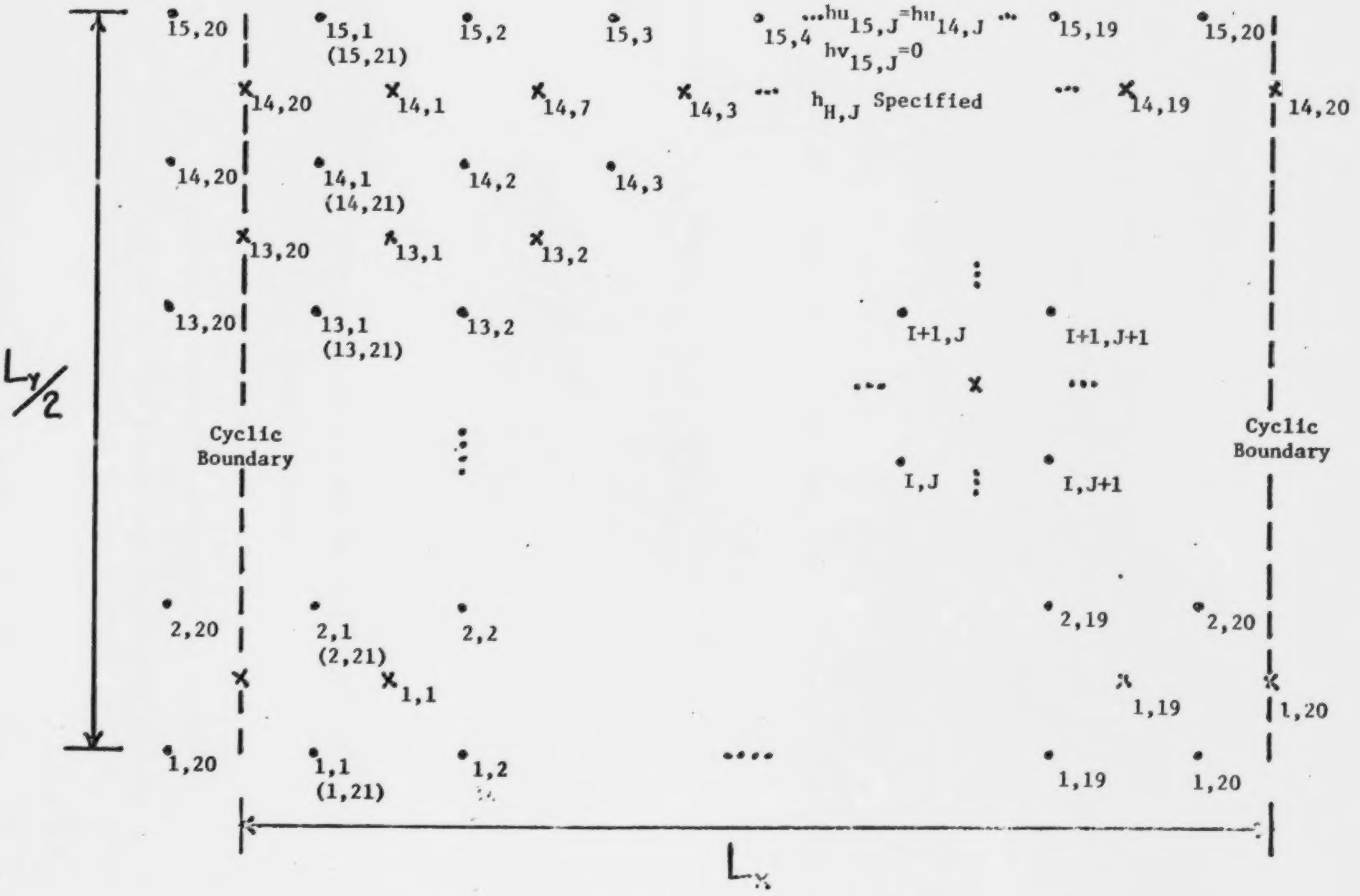

15,20
15,1
(15,21)
15,2
15,3
15,4
...$hu_{15,J}=hu_{14,J}$ ...
$hv_{15,J}=0$
15,19
15,20
14,20
14,1
14,7
14,3
...
$h_{H,J}$ Specified
...
14,19
14,20
14,20
14,1
(14,21)
14,2
14,3
13,20
13,1
13,2
13,20
13,1
(13,21)
13,2
I+1,J
I+1,J+1
Cyclic
Boundary
I,J
I,J+1
Cyclic
Boundary
2,20
2,1
(2,21)
2,2
2,19
2,20
1,1
1,19
1,20
1,20
1,1
(1,21)
1,2
1,19
1,20
$L_y/2$
L_x

Figure 5.3 Two dimensional staggered grid

example, if one wishes that the maximum height difference between successive relaxations be less than X, then by definition of T we require

$$\left| T_{ij}^{m+1} - T_{ij}^{m} \right| = \left| \frac{\alpha R_{ij}^{m}}{4 + \lambda^2} \right| < X/2 \tag{5.35}$$

for all i and j, and ε must satisfy $|\varepsilon| < \frac{X\,(4 + \lambda^2)}{2\alpha}$.

Once a value of T is found for each grid points, $\overline{hu}^{2t}$ and $\overline{hv}^{2t}$ are easily obtained from equations (5.26) and (5.27). Forecast values of h, hu, and hv at $\tau + 1$ are then recovered by use of equation (5.11).

5.3.2 Initialization. Both of the 2-D models were initialized in the same manner. The grid consists of 20 x 15 "dot" points and 20 x 14 cross points (Fig. 5.3) with a spacing of 120 km. Cyclic conditions are assumed to eliminate the east and west boundaries. Free-slip walls are assumed along the north and south boundaries so that

$$\begin{aligned}
(hu)_{1,j} &= (hu)_{2,j} \\
(hu)_{15,j} &= (hu)_{14,j} \\
(hv)_{1,j} &= (hv)_{15,j} = 0 \quad .
\end{aligned} \tag{5.36}$$

The heights on the boundary row of x points are specified from the analytic linear wave solution for the Haurwitz wave. The initial perturbation of the height surface consists of a Haurwitz wave superimposed on a north-south height gradient corresponding to a mean geostrophic wind of 20 ms^{-1},

$$h' = [A \frac{f}{kg} \cos \ell y - A \frac{\beta \ell}{kg} (\frac{1}{k^2 - \ell^2}) \sin \ell y] \cos kx \qquad (5.37)$$

$$u' = A \frac{\ell}{k} \sin \ell y \cos kx \qquad (5.38)$$

$$v' = A \cos \ell y \sin kx \quad , \qquad (5.39)$$

where h', u', v' are the perturbations superimposed on the mean fields. A is an amplitude, k and ℓ are wave numbers in x and y directions respectively (see Fig. 5.3), and β is the north-south variation of Coriolis parameter, f. With the initialization given by (5.37) - (5.39), the analytic linear phase speed of the Haurwitz wave is

$$C = U - \frac{\beta}{\ell^2 + k^2} \qquad (5.40)$$

The same three equations imply a balance between the height and velocity fields. However because h is specified rather than calculated from the finite difference equation along the north and south boundaries, there is some flux of momentum and mass across the lateral boundaries, and total mass is not conserved exactly. The errors associated with the lateral boundary conditions also excite high frequency gravity waves, which will be discussed later. As with the 1-D model, both 2-D explicit and S.I. models are started with an initial forward-in-time, explicit, time step.

5.3.3 Results. The 2-D explicit model used a 300 second time step. The linear gravity wave speed for this model with H = 4816 m and g = 9.8 m is 217 ms^{-1}. Therefore, $\frac{c\Delta t}{\Delta x}$ equals 0.542 s which satisfies the stability requirement for the 2-D staggered grid ($\frac{C\Delta t}{\Delta x} < \frac{\sqrt{2}}{2}$).

The 25 hour forecast of h by the explicit model is shown in Fig. 5.4. In this experiment, the computational phase speed was 16.48 m/sec, or about 95.4% of the analytic linear phase speed of 17.28 ms^{-1}. The mass flux across the lateral boundaries was large enough to cause some distortion in the height and velocity fields. The distortion does not become severe enough to destroy the wave pattern, but is evident in the velocity field (not shown) along the southern boundary. The total mass loss is 0.095%, which represents an average decrease of height of almost 5 meters. This mass (height) loss is not uniformly distributed, but tends to be concentrated in the central channel of the grid where the wave amplitude is greatest.

Inspection of the deviation of the explicit model results from the linear solution showed that the period of the mass oscillations was between 1/2 and 2 hours, and apparently caused height errors greater than those associated with phase speed errors. The dependency of these errors upon the boundary conditions was demonstrated by varying the lateral boundary conditions. Use of steady state conditions on h on the northern and southern boundaries caused total mass fluctuations of about the same range as those described above, but their distribution in time and space was such that the distortions of the velocity field were about five times as great as those associated with the analytic boundary conditions on h. On the other hand, an explicit calculation of h of the heights along the boundaries, eliminated the mass fluctuations and the distortion in the velocity fields.

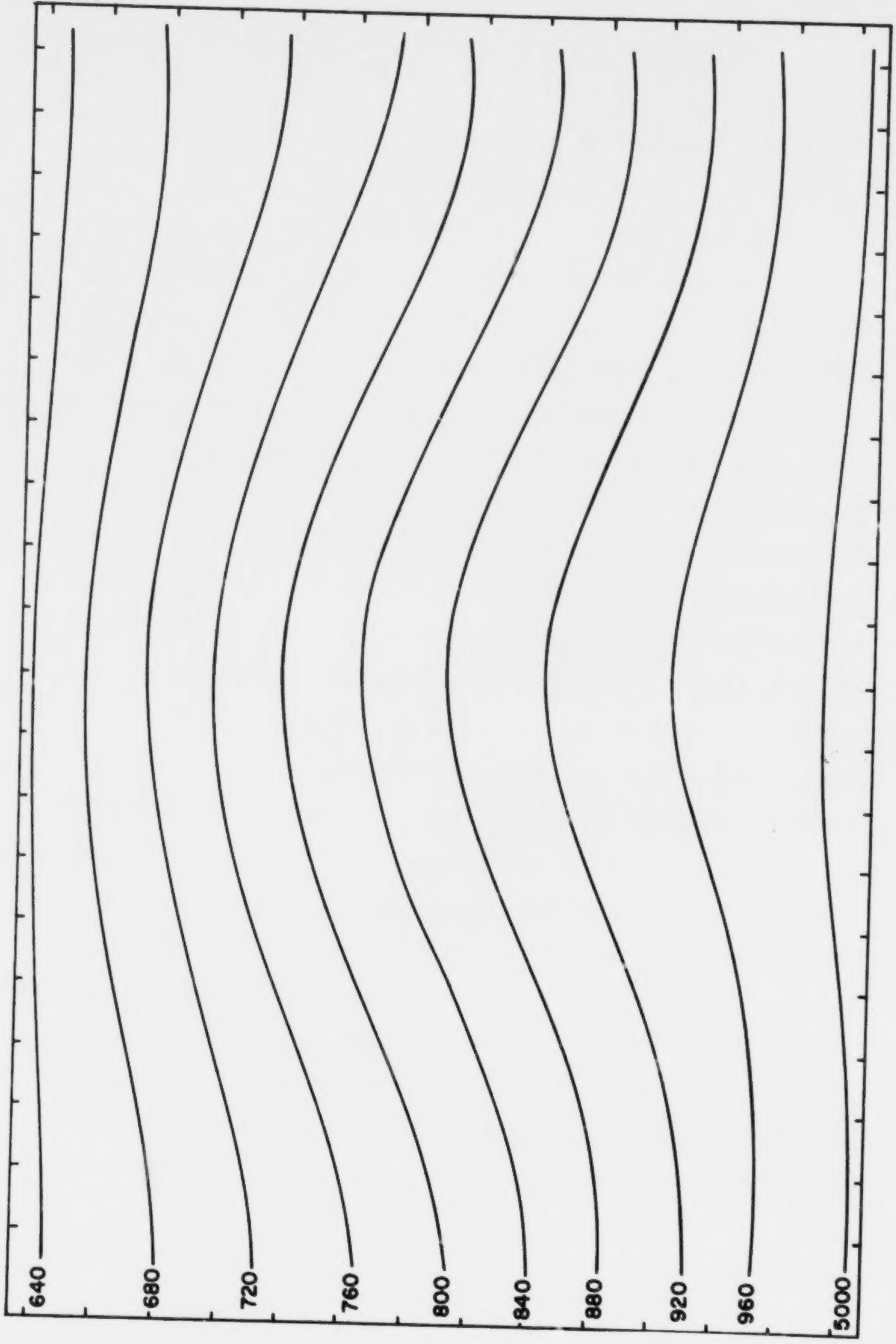

Figure 5.4 Twenty-five hour forecast of h by explicit model

However, the amplitude of the height wave increased noticeably. The direct calculation of h on the lateral boundaries might have been the best choice if it were possible to do the same for the semi-implicit case. However, since lateral boundary values for height could not be calculated directly in the S.I. model, but instead had to be specified, the analytic boundary conditions on h were used for both models.

Based on the 1-D experiments, an optimum over-relaxation coefficient was quickly found to be 1.4 for an ε of 0.149 and a Δt of 1800 s ($\lambda^2 = .094$). This value of ε corresponds to a tolerance of 0.1 m between successive relaxations for the height field (see eq. (5.35)). A number of experiments with the S.I. model were carried out and the results compared to those from the explicit model.

The oscillations in mass associated with the S.I. model were of the same order of magnitude as those from the explicit model, reaching as much as 0.103%. Because of the non-uniformity of the mass (height) losses across the grid, it was desirable to compare implicit and explicit model results by normalizing the height fields. This normalization consisted of adding or subtracting the mean mass loss or gain from the heights for output purposes only. The oscillations of the total mass in the two models were not in phase because of the unequal time steps.

The 25-hour forecast of height contours from the S.I. model with a time step of 1800 s, an α of 1.4, and an ε of 0.149 was very similar to the 25-hour explicit model forecast shown in Fig. 5.4. The contours from the S.I. model would appear identical to those in Fig. 5.4 and are therefore not shown. The computed phase speed of the wave in the S.I.

model was identical to the speed in the explicit model (16.48 ms^{-1}). Also, the forecast velocity fields (not shown) were very similar in both models. Even the distortions in the velocities near the lateral boundary were similar in both models. Fig. 5.5 and 5.6 show the "error" fields (linear solution minus the non-linear, numerical solution[1]) from the explicit and S.I. models. The error patterns are similar both in magnitude and in distribution. The greatest mass loss in both models occurred in advance of the ridge, while the greatest loss occurred in advance of the trough. The S.I. model showed no greater tendency to develop high spatial frequency (2Δx) noise.

The root-mean-square (RMS) difference between the numerical forecasts and the analytic linear solution is another measure of the quality of a numerical forecast. The linear solution should be a good approximation to the non-linear solution because only one "long" wave was present initially, and therefore non-linear effects should be small. Root-mean square differences were computed for both models at each time step for 50 hours of forecast time. The results, shown in Fig. 5.7, indicate that the RMS differences oscillate with periods of about 2-5 hours. These oscillations reflect the gravity waves generated near the boundaries. According to Kurihara (1965) and McPherson (1973), semi-implicit models damp short waves (the 4 Δx wave is damped the most), without significantly altering the longer waves. In Fig. 4.7, the oscillations of RMS differences are well correlated during the first 24 hours, indicating that the two models

---

[1] This field is not strictly an error since the analytic non-linear solutio is unknown. However, if the non-linear effects are small, the linear solution will approximate the non-linear solution. In any case, the line solution serves as a useful basis for comparison.

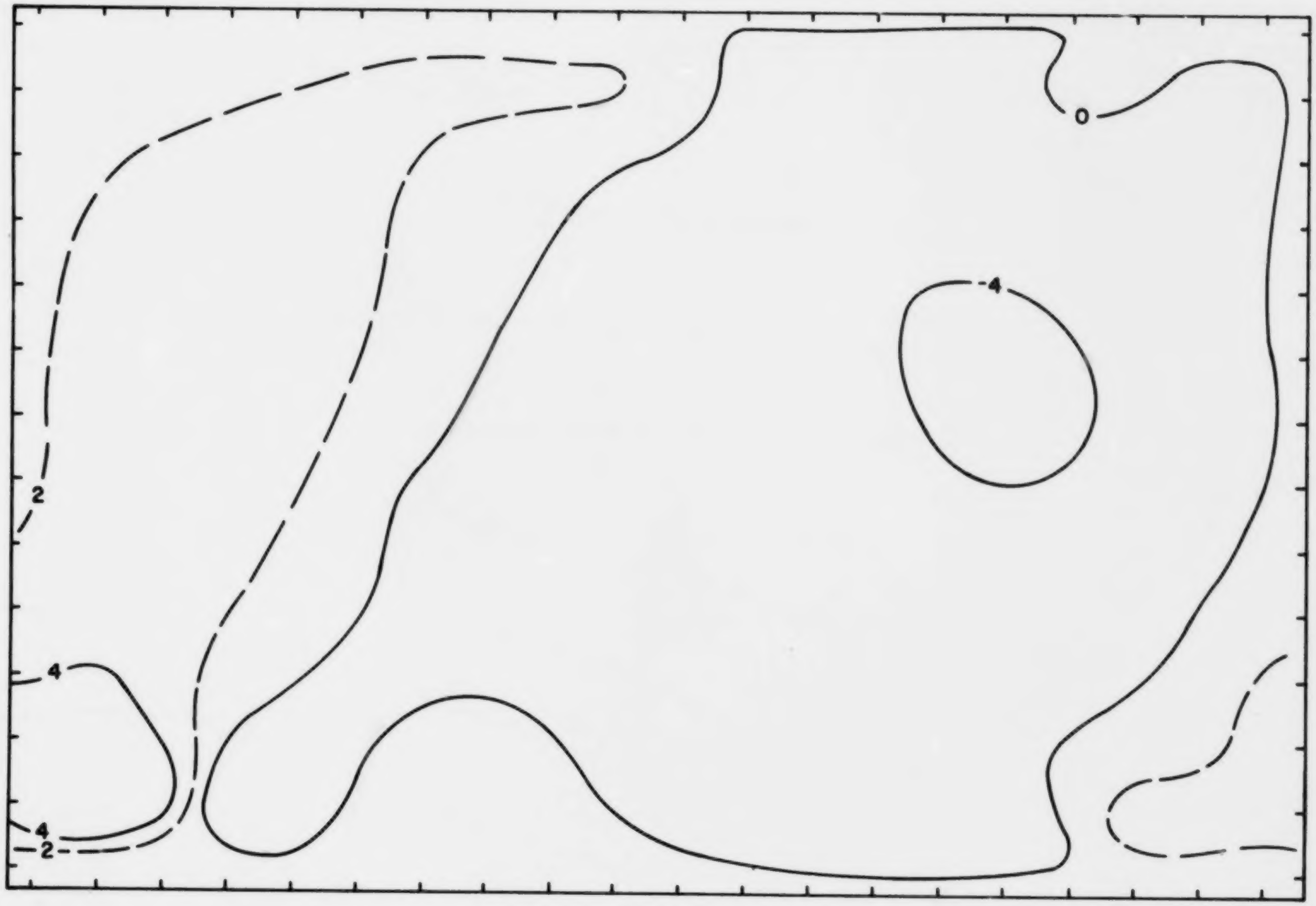

Figure 5.5 "Error" height fields for the explicit model at 25 hours

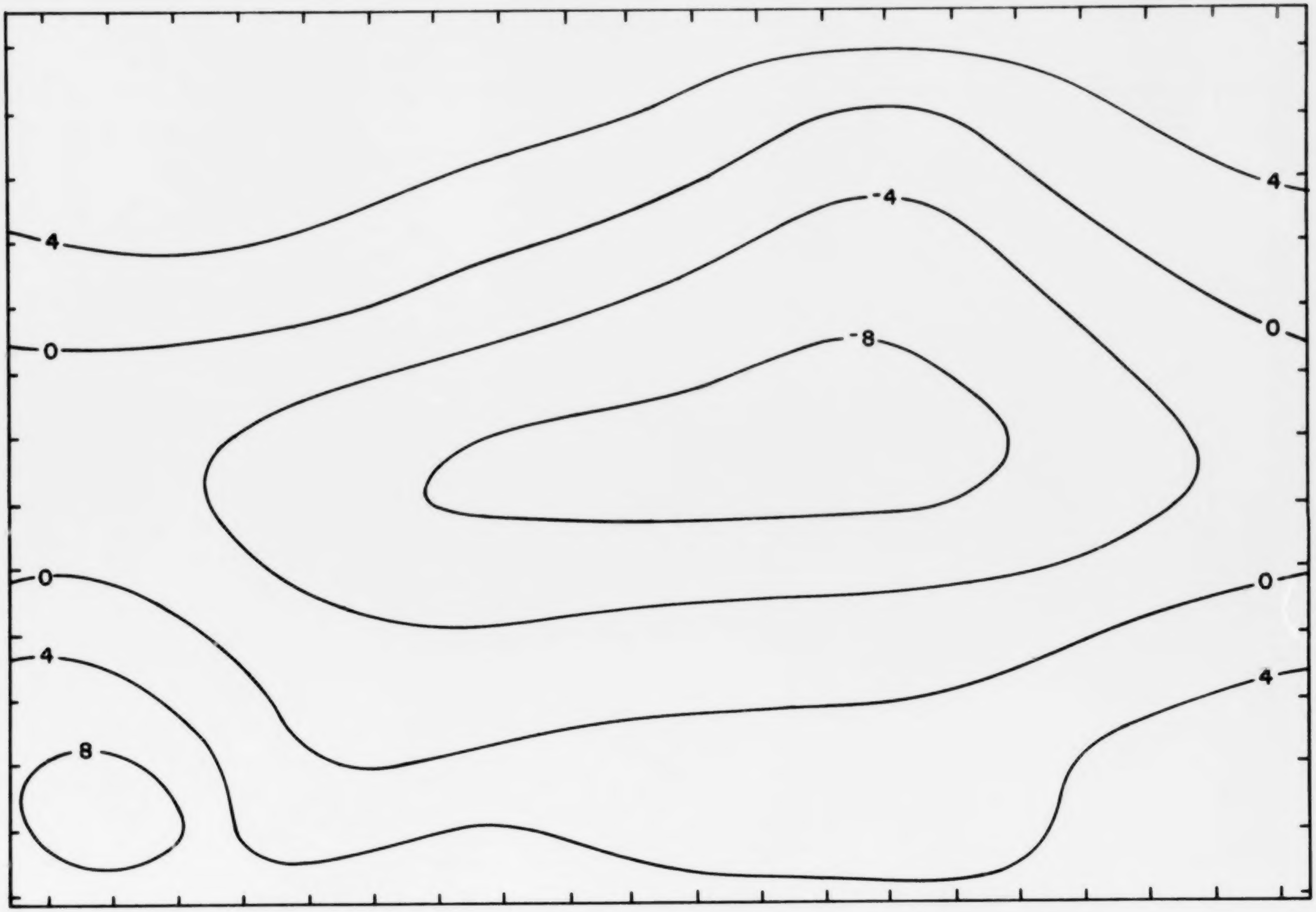

Figure 5.6 "Error" height fields for the S.I. model at 25 hours

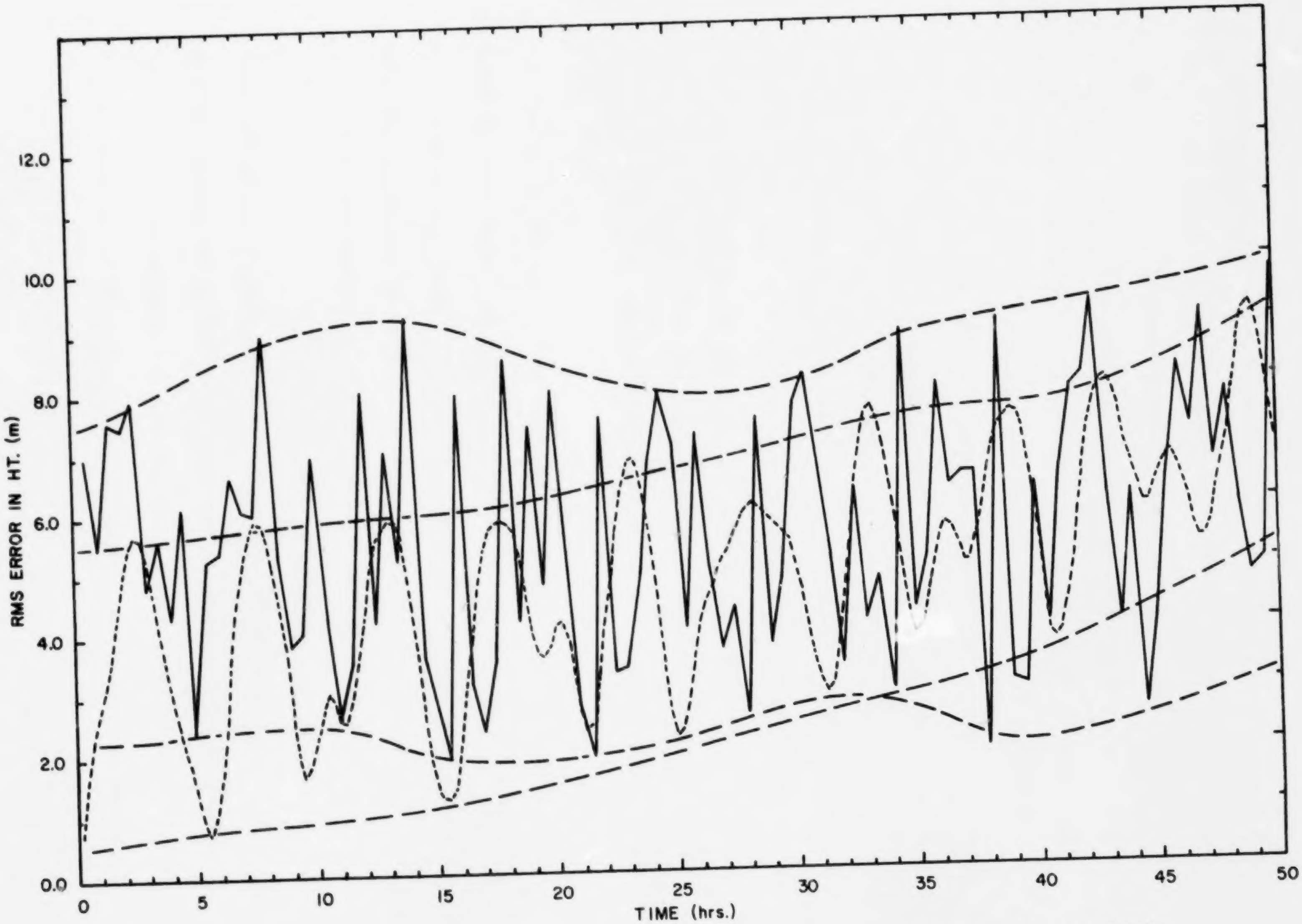

Figure 5.7 Root-mean square differences between explicit and S.I. model height forecasts and the linear solution

are generating gravity waves in the same manner. While no obvious damping with time of the RMS differences in the S.I. model is evident, it is easily seen that the explicit RMS differences are steadily growing. Thus, it is possible that the damping of short wavelengths in the S.I. model might be suppressing growth of RMS differences with time. In summary, the solutions from the S.I. model are considered to be of nearly equal accuracy compared to the explicit model results; the major errors in both models are associated with the lateral boundary conditions.

Finally, it is necessary to consider the efficiency of the 2-D S.I. model. A number of experiments with different over-relaxation coefficients were conducted. The results are summarized in Fig. 5.8, which shows the number of iterations per 25 hour forecast for two methods of specifying the first guess. Values of α between 1.4 and 1.6 proved optimal. It can also be seen in Fig. 5.8 that changing the initial guess has only a minor effect.

An interesting result from the efficiency study was the effect of the size of the time step on the number of iterations. With Δt = 300 seconds, each time step required an average of 3.55 relaxation iterations. With Δt = 1800 seconds, the average number of relaxation iterations per time step increased to 13.6, but the total number of iterations per 25 hour forecast decreased from 1065 to 688.

The large increase in the number of relaxations required for each time step as Δt increases, is apparently related to the greater distance travelled by the fast moving, short-wavelength gravity waves,and, to a lesser extent, the slower moving Haurwitz wave. The first guess of T is

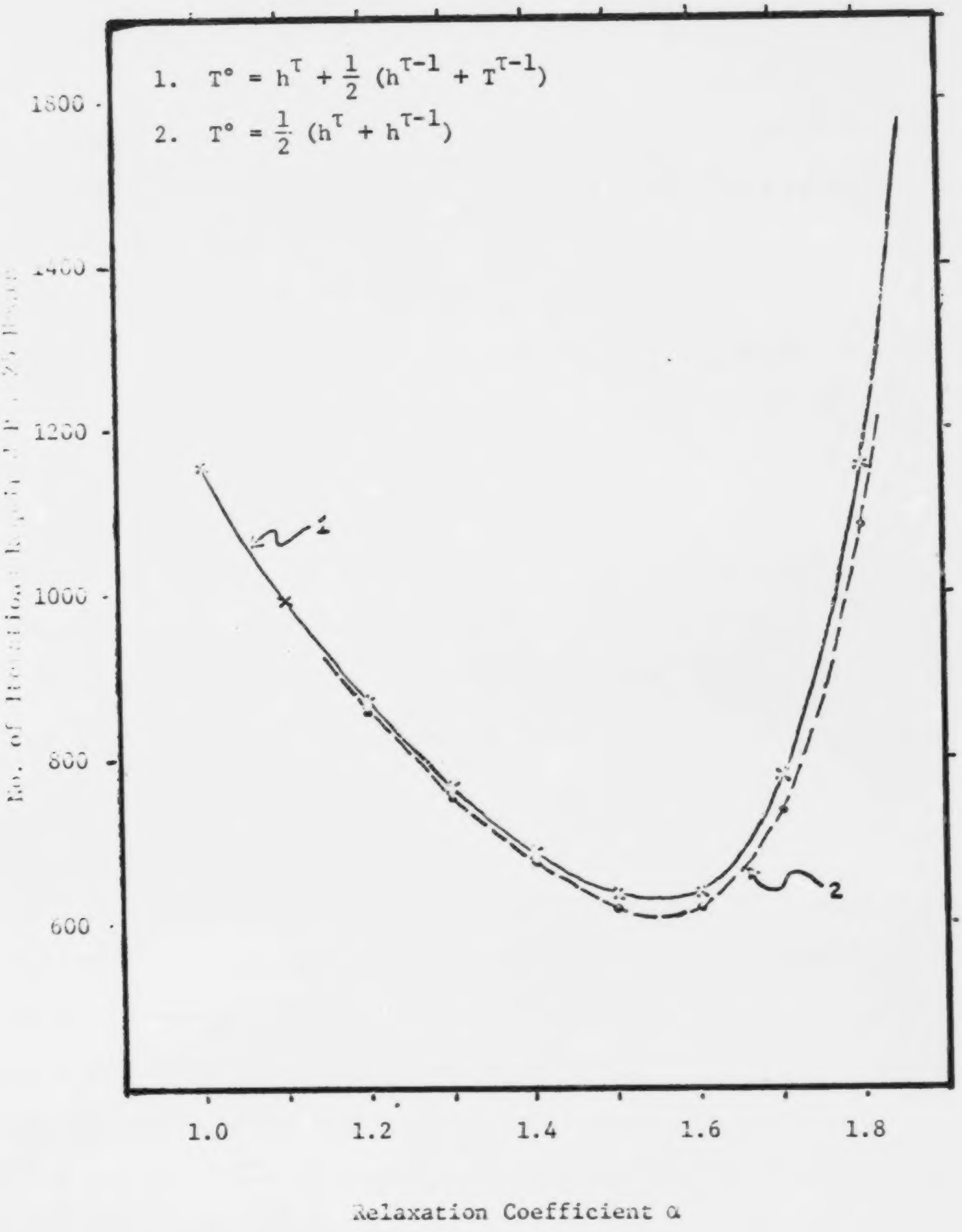

Figure 5.8 Number of iterations required per time step as a function of α for 2 different first guesses

based on an approximately linear advection of the wave, expressed as a continuity of the previous time steps height tendency at each grid point. This first guess was quite good when Δt equalled 300 seconds, but when Δt was increased to 1800s, the high frequency gravity waves travel a significant distance between time steps. This large distance travelled produces large changes in the heights, so that the first guess becomes a rather bad guess. It then requires many more iterations to recover and reduce the maximum residual to less than ε. The implications are that the speed of the convergence in the relaxation part of the S.I. forecast would be increased if the amplitude of the high frequency gravity waves were reduced.

A comparison of the computational speed of the explicit and most efficient S.I. model ($\alpha = 1.5$, $\Delta t = 1800$), described by the efficiency ratio E (in (5.25), shows a significant increase of speed in the S.I. model. The efficiency, E, is 3.725, which approaches the efficiency ratio of 4.0 described for two-dimensional models in the literature.

5.4 Conclusions of preliminary tests of semi-implicit models

It is apparent that the development of the one and two dimensional semi-implicit models was reasonably successful. The forecast accuracies of the S.I. models were comparable to the accuracies of the explicit models, and the S.I.models were roughly two to four times faster. With this encouraging result and with the experience gained in the 1-D and 2-D S.I. models, it is reasonable to begin the development of a three-dimensional semi-implicit numerical mesoscale model.

APPENDIX - CHAPTER 5

TRIANGULARIZATION OF THE COEFFICIENT MATRIX PRODUCED BY 3-DIMENSIONAL IMPLICIT MODELS

Sela and Scolnik (1972) describe the transformation of a square coefficient matrix into an equivalent lower triangular matrix. This procedure is required for efficient solution of the family of Helmholtz type equations which is produced by a three-dimensional implicit model. In the two dimensional case there is one Helmholtz equation for the one layer considered and the "coefficient matrix" is one by one. As the layers increase, unknown parameters multiply and are contained in a system of Helmholtz equations as a square matrix. From Gerrity, McPherson, and Scolnik (1973), these are represented in the matrix equation

$$\nabla^2 C\vec{T} + E\vec{T} = \vec{F} \quad , \qquad (1)$$

where $\vec{T}$ is the vector of unknown parameters to be forecast and $\vec{F}$ is the vector of known atmospheric parameters at $t = \tau$, and $t = \tau - 1$. C and E are square coefficient matrices. The length of the vectors is determined by the number of layers, so that there is one individual Helmholtz equation in the system (1) for each layer.

The solution of (1) can be accomplished by simultaneously relaxing in three dimensions, but this is very inefficient and would destroy any possibility for an increase in efficiency using S.I. models. The use of the following matrix algorithm effectively decouples the layers of the model by triangularization of the coefficient matrices. Then, relaxation can be performed on each layer individually, roughly doubling the efficiency of the model.

If the original matrix to undergo triangularization is C_1, the process, after Sela and Scolnik (1972) is given by

$$\begin{aligned} C_1 &= L_1U_1 \\ &\quad U_1L_1 = C_2 \\ C_2 &= L_2U_2 \qquad\qquad (2) \\ &\quad U_2L_2 = C_3 \\ C_3 &= L_3U_3 \\ &\quad\vdots \\ &\quad U_{k-1}L_{k-1} = C_k \end{aligned}$$

where C_k is now lower traingular. The U matrices are upper triangular and L matrices are lower triangular. The step ...

$$C_n = L_nU_n$$

is the key. The code for performing this operation numerically was supplied by NMC and the example given by Sela and Scolnik on a 10 x 10 matrix has been duplicated.

As a check, the original matrix can be recovered. If

$$B = U_{k-1}U_{k-2} \cdots U_2U_1 \tag{3}$$

then

$$C_1 = B^{-1} L_kU_kB = B^{-1} C_kB \tag{4}$$

and likewise

$$C_k = B\,C_1\,B^{-1} \tag{5}$$

6.0 DETERMINATION OF INITIAL DATA REQUIREMENTS

In consonance with the historical emphasis placed on the numerical modeling of *large* scale motion fields, there has been much research dealing with the predictability of atmospheric motions of this scale. That is, given certain limitations on (1) the initial data density and accuracy, (2) knowledge of the local forcing and (3) the ability to utilize realistic and mathematically correct lateral boundary values, over how long a period of time will the forecast errors remain within some definable limit? Our objective in this section will be to investigate the effect of the first type of error, which results from inaccuracies in the initial data, on numerical prediction models of the regional scale atmosphere.

That it is possible to experimentally seperate the error sources according to the three ways listed above is not completely obvious and deserves some discussion. Consider a method of categorizing fluid flows in terms of whether initial conditions, boundary conditions or local forcing dominate. Initial conditions almost completely dominate the solution early in the integration. Local forcing becomes progressively more important with time. Boundary effects, whether real or fictitious, permeate the solution in the interior of the domain at a rate that is directly proportional to the group velocity of the waves that are generated at the boundary and inversely proportional to the size of the domain. These same considerations that explain the dominance of one factor over the others in determining the general solution, also may be used to explain in what sense the forecast is most susceptible to error. For example, the impact of erroneously specified initial data will be most severe under circumstances where the boundary conditions and local forcing are dominated by the effect of the initial conditions. Therefore, if the predictability experiments are structured such that the state of the flow at any point in time is determined almost entirely by the initial conditions, all unwanted error sources are esentially precluded.

Conventional predictability studies involve performing a control integration of a numerical model and using the solution to represent the true atmosphere. The solution at some arbitrary time is then perturbed by a specified amount to simulate measurement or analysis errors and a new forecast is made. The growth rate of root-mean-square errors between the "true" atmosphere and the forecast reflects some average measure of predictability of the atmosphere _as represented by the model_. This technique has also been used to evaluate the "compatability" among the errors in the dependent variables. That is, it is possible for an excessive amount of error in one of the variables used for asynoptic updating or the initialization of a model to nullify the informational content of the others. Since there will always be errors in the initial data used as input to numerical models of the atmosphere applied at any scale, it is pertinent to consider the implications of error "compatability". This concept of error compatability will be useful in addressing the problem of determining initial data requirements for regional scale numerical models. The modeling technique used, however, will differ completely from the one discussed above, in that it will embody the concept of stochastic-dynamic prediction (Epstein, 1969; Fleming, 1970).

6.1 Development of Stochastic-Dynamic Equations

The equations for this particular stochastic-dynamic model describe the barotropic flow of an inviscid, incompressible, hydrostatic fluid in a rotating coordinate system. Invariance of all forecast variables in the y (north-south) direction has been assumed. The equations of motion and continuity equation are

$$\frac{\partial u}{\partial t} + u\frac{\partial u}{\partial x} - fv + g\frac{\partial}{\partial x}(s + h) = 0 \quad , \qquad (6.1)$$

$$\frac{\partial v}{\partial t} + u\frac{\partial v}{\partial x} + fu + g\frac{\partial \bar{H}}{\partial y} = 0 \quad , \qquad (6.2)$$

and

$$\frac{\partial h}{\partial t} + u\frac{\partial h}{\partial x} + v\frac{\partial \bar{H}}{\partial y} + h\frac{\partial u}{\partial x} = 0 \quad , \qquad (6.3)$$

where s is the elevation of the lower boundary and h is the depth of the fluid above the lower surface. Note that the mean north-south height gradient, $\frac{\partial \bar{H}}{\partial y}$, is constant and is geostrophically balanced by a mean east-west velocity, $\bar{U}$, where

$$\frac{\partial \bar{H}}{\partial y} = - \frac{f}{g} \bar{U} \quad . \qquad (6.4)$$

The model consists of two layers, the top layer being inert and serving only to simulate a stratosphere by exerting a buoyant effect on the lower layer. Prior to considering the influence of the upper layer, the total depth of the model must be scaled so that the dynamic behavior of the model will be comparable to the behavior of the atmosphere. This depth can be considered as the sum of a mean depth and a variable quantity h' which is a function of time and space. To develop a realistic magnitude for this mean depth, we consider the atmospheric scale height, $\bar{H}$, where

$$\bar{H} = \frac{RT_o}{g} \quad , \qquad (6.5)$$

which equals 8 km for a surface temperature, T_o, of 280°C.

The effect of an upper layer of less density on the motion of the lower layer may be accounted for in two ways. One method is to adjust the gravitational forcing in the lower layer so that it is effectively reduced by a factor proportional to the potential temperature difference between the upper stratospheric layer and the lower tropospheric layer. If we define the effective gravity by g*, it can be shown that

$$g^* = \frac{\theta_s - \theta_T}{\theta_T} \, g \quad , \qquad (6.6)$$

where θ_s and θ_T refer to stratospheric and tropospheric means respectively. Cressman (1958) found that barotropic forecast errors were minimized when the gravitational forcing was reduced by a factor of 4 or greater. This factor of 4 is consistent with (6.6) if appropriate values of θ are substantiated. An alternative to using g^* in the equations of motion is to reduce the depth of the lower layer by a factor proportional to the reduction in gravitational forcing. This is justified by the fact that in the linear solution for the phase speed of external gravity waves, acceleration of gravity appears multiplied by the mean depth of the fluid. Application of either method would then have the same desired effect of decreasing the phase speed of the external gravity waves to one that is more characteristic of the more prevalent internal waves. Since direct use of g^* would drastically affect the geostrophic relationship, the condition for inertial instability, etc., the mean depth will be reduced by the factor of 4. The time dependent depth can be represented as

$$h = a\bar{H} + h' = \frac{a\,RT_o}{g} + h' \quad , \qquad (6.7)$$

where a is equal to 1/4.

Equations (6.1) - (6.3) will be converted to spectral form by representing the dependent variables in terms of truncated Fourier series. Specifically

$$u(x,t) = \sum_{|m| \leq K} U_m(t)e^{imkx} \quad , \qquad (6.8)$$

$$v(x,t) = \sum_{|m| \leq K} V_m(t) e^{imkx} \quad , \qquad (6.9)$$

and

$$h(x,t) = \sum_{|m| \leq K} H_m(t) e^{imkx} \qquad (6.10)$$

where m is an integer wavenumber, k = 2π/L, L is the domain length, $i = \sqrt{-1}$ and $U_m(t)$ equals $[U_{-m}(t)]^*$. The spectral forms of equations (6.1) - (6.3) are

$$\dot{U}_m = - ik \sum_{\substack{|p| \leq K \\ |m-p| \leq K}} (m-p)\, U_{m-p}\, U_p + f\, V_m - ikgm(S_m + H_m) \quad , \qquad (6.11)$$

$$\dot{V}_m = - ik \sum_{\substack{|p| \leq K \\ |m-p| \leq K}} (m-p)\, U_p\, V_{m-p} - f\, U_m - g \frac{\partial \bar{H}}{\partial y} \delta_m \quad , \qquad (6.12)$$

and

$$\dot{H}_m = - ik \sum_{\substack{|p| \leq K \\ |m-p| \leq K}} (m-p)\, H_{m-p}\, U_p - V_m \frac{\partial \bar{H}}{\partial y} - ik \sum_{\substack{|p| \leq K \\ |m-p| \leq K}} (m-p)\, H_p\, U_{m-p} \qquad (6.13)$$

where

$$s(x) = \sum_{|m| \leq K} S_m e^{imkx} \qquad (6.14)$$

and

$$\delta_m = 1 \quad , \quad m = 0$$

$$\delta_m = 0 \quad , \quad m \neq 0 \quad .$$

In the first annual report of the Select Research Group (hereafter referred to as SRG-1) we reported on some preliminary experiments using a slightly simpler version of this set of spectral equations. The purpose of the experiments was to gain a familiarity with the spectral shallow fluid equations, since they will be used as a basis for the stochastic-dynamic model. The derivation of the stochastic-dynamic equation was outlined in SRG-1 and will be reproduced here for reference. For notational convenience let

$$A_m = - ikm \quad ,$$

$$B_{m,p} = - ik(m-p) \quad ,$$

$$C_m = - ikgm \quad ,$$

$$D_1 = - g \frac{\partial \bar{H}}{\partial y} \quad ,$$

and

$$D_2 = - \frac{\partial \bar{H}}{\partial y} \quad .$$

The spectral equations (6.11) - (6.13) become

$$\dot{U}_m = \sum_p B_{m,p} U_p U_{m-p} + fV_m + C_m(S_m + H_m) \quad , \qquad (6.15)$$

$$\dot{V}_m = \sum_p B_{m,p} U_p V_{m-p} - fU_m + D_1 \delta_m \qquad (6.16)$$

and

$$\dot{H}_m = \sum_p B_{m,p} U_p H_{m-p} + V_m D_2 + \sum_p B_{m,p} H_p U_{m-p} \quad . \qquad (6.17)$$

Summation subscript limits will be unstated for convenience, but it will be assumed that only those expansion coefficients pertaining to wavenumbers inside the permitted region will be included in the summation; for example,

$$\Sigma_p \text{ implies } \sum_{\substack{|p| \leq K \\ |m-p| \leq K}} \quad .$$

An application of the expected value operator (E) to (6.15) - (6.17) yields

$$E(\dot{U}_m) = \sum_p B_{m,p} E(U_p U_{m-p}) + f E(V_m) + C_m[E(S_m) + E(H_m)] \quad , \qquad (6.18)$$

$$E(\dot{V}_m) = \sum_p B_{m,p} E(U_p V_{m-p}) - f E(U_m) + D_1 \delta_m \quad , \qquad (6.19)$$

and

$$\dot{E}(H_m) = \sum_p B_{m,p} \, [E(U_p H_{m-p}) + E(H_p U_{m-p})] \tag{6.20}$$
$$+ D_2 \, E(V_m) \quad .$$

Using the definition of covariance,

$$COV(x_1,x_2) = E(x_1 x_2) - E(x_1) \, E(x_2) \tag{6.21}$$

and the commutability of E( ) and d( )/dt (Epstein, 1969) we obtain

$$\dot{E}(U_m) = \sum_p B_{m,p} \, [COV(U_p,U_{m-p}) + E(U_p) \, E(U_{m-p})] \tag{6.22}$$
$$+ fE(V_m) + C_m (E(S_m) + E(H_m)] \quad ,$$

$$\dot{E}(V_m) = \sum_p B_{m,p} \, [COV(U_p,V_{m-p}) + E(U_p) \, E(V_{m-p})] \tag{6.23}$$
$$- fE(U_m) + D_1 \delta_m \quad ,$$

and

$$\dot{E}(H_m) = \sum_p B_{m,p} \, [COV(U_p,H_{m-p}) + E(U_p) \, E(H_{m-p})$$
$$+ COV(H_p,U_{m-p}) + E(H_p) \, E(U_{m-p})] \tag{6.24}$$
$$+ D_2 E(V_m) \quad .$$

We now have the prognostic equations for the first moments of the Fourier coefficients of u, v and h. To obtain prognostic equations for the second moments, we first obtain, from the definition of the covariance, the relationship

$$\dot{\mathrm{COV}}(x_1,x_2) = E(\dot{x}_1 x_2 + x_1 \dot{x}_2) - \dot{E}(x_1)\, E(x_2) - E(x_1)\, \dot{E}(x_2) \quad . \tag{6.25}$$

The expression for the expected value of a triple product will also be required and is obtained from the definition of a third moment (τ). Specifically

$$E(x_1 x_2 x_3) = E(x_1)\,\mathrm{COV}(x_2,x_3) + E(x_2)\,\mathrm{COV}(x_1,x_3) + E(x_3)\,\mathrm{COV}(x_1,x_2) + E(x_1)\,E(x_2)\,E(x_3) + \tau\,(x_1,x_2,x_3) \quad . \tag{6.26}$$

Through application of equations (6.15) - (6.17), (6.22) - (6.24) and the definition (6.26) to the relationship (6.25), the forecast equations for the 6 covariance matrices may be derived. They are

$$
\begin{aligned}
\mathrm{CO\dot{V}}(U_i,V_j) = {} & \sum_p B_{i,p}\,[E(U_p)\ \mathrm{COV}(U_{i-p},V_j) \\
& + E(U_{i-p})\ \mathrm{COV}(U_p,V_j) + \tau(U_p,U_{i-p},V_j)] \\
& + \sum_p B_{j,p}\,[E(U_p)\ \mathrm{COV}(V_{j-p},U_i) \\
& + E(V_{j-p})\ \mathrm{COV}(U_p,U_i) + \tau(U_p,V_{j-p}),U_i)] \\
& + f\ \mathrm{COV}(V_i,V_j) + C_i\ [\mathrm{COV}(S_i,V_j) \\
& + \mathrm{COV}(H_i,V_j)] - f\ \mathrm{COV}(U_i,U_j) \quad ,
\end{aligned}
\tag{6.27}
$$

$$
\begin{aligned}
\mathrm{CO\dot{V}}(U_i,H_j) = {} & \sum_p B_{i,p}\,[E(U_p)\ \mathrm{COV}(H_j,U_{i-p}) \\
& + E(U_{i-p})\ \mathrm{COV}(H_j,U_p)] \\
& + \sum_p B_{j,p}\,[E(U_p)\ \mathrm{COV}(U_i,H_{j-p}) \\
& + E(H_{j-p})\ \mathrm{COV}(U_i,U_p)] \\
& + \sum_p B_{j,p}\,[E(H_p)\ \mathrm{COV}(U_i,U_{j-p})
\end{aligned}
\tag{6.28}
$$

(continued on following page)

$$+ E(U_{j-p})\ \mathrm{COV}(U_i,H_p)] + f\ \mathrm{COV}(H_j,V_i)$$

$$+ C_i\ [\mathrm{COV}(H_j,{}_i) + \mathrm{COV}(H_j,H_i)]$$

$$+ D_2\ \mathrm{COV}(U_i,V_j) \qquad (6.28\ \text{cont'd})$$

$$+ \sum_p \{\tau(H_j,U_p,U_{i-p}) + B_{i,p} + \tau(U_i,U_p,H_{j-p})\ B_{j,p}$$

$$+ \tau(U_i,H_p,U_{j-p})\ B_{j,p}\} \quad ,$$

$$\mathrm{CO}\dot{\mathrm{V}}(U_i,U_j) = \sum_p B_{i,p}\ [E(U_p)\ \mathrm{COV}(U_j,U_{i-p})$$

$$+ E(U_{i-p})\ \mathrm{COV}(U_j,U_p) + \tau(U_j,U_p,U_{i-p})]$$

$$+ \sum_p B_{j,p}\ [E(U_p)\ \mathrm{COV}\ (U_i,U_{j-p})$$

$$(6.29)$$

$$+ E(U_{j-p})\ \mathrm{COV}(U_i,U_p) + \tau(U_i,U_p,U_{j-p})]$$

$$+ f\ \mathrm{COV}(U_j,V_i) + C_i\ [\mathrm{COV}(U_j,S_i)$$

$$+ \mathrm{COV}(U_j,H_i)] + f\ \mathrm{COV}(U_i,V_j)$$

$$+ C_j\ [\mathrm{COV}(U_i,S_j) + \mathrm{COV}(U_i,H_j)]$$

$$
\begin{aligned}
\mathrm{CO\dot{V}}(V_i,H_j) = {} & \sum_p B_{i,p}\,[E(U_p)\ \mathrm{COV}(H_j,V_{i-p}) \\
& + E(V_{i-p})\ \mathrm{COV}(H_j,U_p) + \tau(H_j,U_p,V_{i-p})] \\
& + \sum_p B_{j,p}\,[E(U_p)\ \mathrm{COV}(V_i,H_{j-p}) \\
& + E(H_{j-p})\ \mathrm{COV}(V_i,U_p) + \tau(V_i,U_p,H_{j-p})] \\
& + \sum_p B_{j,p}\,[E(H_p)\ \mathrm{COV}(V_i,U_{j-p}) \\
& + E(U_{j-p})\ \mathrm{COV}(V_i,H_p) + \tau(V_i,H_p,U_{j-p})] \\
& - f\ \mathrm{COV}(H_j,U_i) + D_2\ \mathrm{COV}(V_i,V_j) \quad ,
\end{aligned}
\tag{6.30}
$$

$$
\begin{aligned}
\mathrm{CO\dot{V}}(V_i,V_j) = {} & \sum_p B_{i,p}\,[E(U_p)\ \mathrm{COV}(V_j,V_{i-p}) \\
& + E(V_{i-p})\ \mathrm{COV}(V_j,U_p) + \tau(V_j,U_p,V_{i-p})] \\
& + \sum_p B_{j,p}\,[E(U_p)\ \mathrm{COV}(V_i,V_{j-p}) \\
& + E(V_{j-p})\ \mathrm{COV}(V_i,U_p) + \tau(V_i,U_p,V_{j-p})] \\
& - f\ \mathrm{COV}(V_j,U_i) - f\ \mathrm{COV}(V_i,U_j) \quad ,
\end{aligned}
\tag{6.31}
$$

and

$$\begin{aligned}
\mathrm{CO}\dot{\mathrm{V}}(H_i,H_j) = \sum_p B_{i,p}\, & [E(U_p)\ \mathrm{COV}(H_j,H_{i-p}) \\
& + E(H_{i-p})\ \mathrm{COV}(H_j,U_p) + \tau(H_j,U_p,H_{i-p}) \\
& + E(H_p)\ \mathrm{COV}(H_j,U_{i-p}) \\
& + E(U_{i-p})\ \mathrm{COV}(H_j,H_p) + \tau(H_j,H_p,U_{i-p})] \\
& + \sum_p B_{j,p}\, [E(U_p)\ \mathrm{COV}(H_i,H_{j-p}) \\
& + E(H_{j-p})\ \mathrm{COV}(H_i,U_p) + \tau(H_i,U_p,H_{j-p}) \\
& + E(H_p)\ \mathrm{COV}(H_i,U_{j-p}) \\
& + E(U_{j-p})\ \mathrm{COV}(H_i,H_p) + \tau(H_i,H_p,U_{j-p})] \\
& + D_2\ \mathrm{COV}(H_j,V_i) + D_2\ \mathrm{COV}(H_i,V_j) \quad .
\end{aligned} \tag{6.32}$$

6.2 Initialization Procedure

The covariance matrices for the complex expansion coefficients U, V and H contain the uncertainty information about u, v and h. To define these matrices from the knowledge of the initial data errors, a multiple, linear regression approach will be utilized (Mood and Graybill, 1963). Let B be a column vector representing the p coefficients of a set of p expansion functions that are orthogonal in physical space, and X be a matrix whose elements $X_{i,j}$ represent the values of the jth function at the ith of n gridpoints. Let Φ be some measure of the state of the atmosphere such that

$$\Phi = BX \tag{6.33}$$

where

$$\Phi = \begin{pmatrix} \phi_1 \\ \vdots \\ \phi_n \end{pmatrix} , \quad X = \begin{pmatrix} X_{11} & X_{12} & \cdots & X_{1p} \\ X_{21} & X_{22} & \cdots & X_{2p} \\ \vdots & \vdots & & \vdots \\ X_{n1} & X_{n2} & \cdots & X_{np} \end{pmatrix}$$

$$B = \begin{pmatrix} \beta_1 \\ \vdots \\ \beta_p \end{pmatrix} ,$$

and

$$\phi_i = \sum_{j=1}^{p} \beta_j X_{ij} \quad . \tag{6.34}$$

If the β_j must be obtained, we first must observe Φ at some set of regularly or irregularly spaced points. The following assumptions will be made about the observations of Φ at each i point: the observations, say Y_i, of ϕ_i, consist of a true value plus random errors; the true values of ϕ_i are the expected values of the observations. The observation errors, ε_i, have a mean of zero and a known variance σ^2, i.e.,

$$E(Y_i) = \phi_i \tag{6.35}$$

and
$$Y_i = \phi_i + \varepsilon_i \tag{6.36}$$

or
$$Y = \Phi + \varepsilon \tag{6.37}$$

where

$$\varepsilon = \begin{pmatrix} \varepsilon_1 \\ \varepsilon_2 \\ \vdots \\ \varepsilon_n \end{pmatrix} .$$

It will also be assumed that the ε_i are independent. We now have

$$Y_i = \sum_{j=1}^{p} \beta_j X_{ij} + \varepsilon_i \tag{6.38}$$

or

$$Y = BX + \varepsilon \quad . \tag{6.39}$$

Equation (6.39) corresponds to a functional relationship type of multiple linear regression problem. The Y and E are random variables, X is a known physical variable (non-random) and B represents a set of unknown parameters. Estimates of β_j, which will be referred to as $\hat{\beta}_j$, will be obtained. In matrix notation

$$\hat{B} = \begin{pmatrix} \hat{\beta}_1 \\ \hat{\beta}_2 \\ \vdots \\ \hat{\beta}_p \end{pmatrix} \tag{6.40}$$

which is the value of B such that the sum of the squares

$$\sum_{i=1}^{n} \varepsilon_i^2$$

is a minimum. We need not know the density function of Y. It can be shown (Mood and Graybill, 1963) that

$$\hat{B} = S^{-1} X^T Y \tag{6.41}$$

where

$$S = X^T X \quad . \tag{6.42}$$

The Gauss-Markoff Theorem verifies that $\hat{B}$ is the best linear unbiased estimate of B. Further calculations show that

$$\mathrm{COV}(\hat{B}) = \sigma^2 S^{-1} \quad . \tag{6.43}$$

The covariance matrix is a function of the data error (σ being independent of x in this case) as well as the form of S, which is determined by the nature of the expansion function used and the position of the observations.

As an example of an application of this approach, consider evenly spaced observations of the u component of the wind velocity

The observed values of u, representing the true value with the superimposed error, as well as the variance of the observation error of u, are the initial conditions represented in physical space. Using previous notation, this corresponds to a knowledge of Y and σ. This information must be used to obtain a probability statement about the initial conditions in Fourier space, i.e., the first and second moments of the Fourier expansion coefficients of u. The elements of the matrix X consist of the values of the exponential expansion function as it is evaluated for all x corresponding to the location of the observations and for all allowed wavenumbers. Column vector B represents the expansion coefficients for the unknown true values of u, and $\hat{B}$ is the best estimate of B based on error contaminated data. The expected values (first moments) of the coefficients, U_i, are obtained from equation (6.41) since $\hat{B} = E(B)$, and the second moments, in terms of the covariance matrix $COV(U_i,U_j)$, are calculated using equation (6.43).

Thus, given the location of the observations of u, v, and h along with the respective error variance for each variable, we can calculate $COV(H_i,H_j)$, $COV(U_i,U_j)$ and $COV(V_i,V_j)$ from equation (6.43). Having no information about covariances among expansion coefficients for different variables, these are initially set equal to zero. The specification of statistical moments of higher order than the second will not be required since, thus far, the assumption that they remain small and can be neglected has proved to be an acceptable stochastic closure scheme, especially for the limited duration of time over which we require integrations.

6.3 Energetics of the Model

The energetics of a stochastic-dynamic model are considerably more complicated than for a deterministic system of equations, since the conventional modes of energy must now be partitioned because of the uncertainty in the variables that define the energies. That is, there is energy associated with the expected values of the variables as well as uncertain modes of energy that are related to the errors in the initial data.

The total energy of the analogous deterministic system of equations is equal to the sum of the kinetic and potential energies defined by

$$KE = \frac{1}{2}\int_0^L hu^2 dx \tag{6.44}$$

and

$$PE = \frac{g}{2}\int_0^L h^2 dx \quad , \tag{6.45}$$

where L is the length of the domain of integration. In wavenumber space these become

$$KE = \frac{L}{2}\sum_m \sum_n H_m U_n U_{-m-n} \tag{6.46}$$

and

$$PE = \frac{Lg}{2}\sum_m H_m H_{-m} \quad . \tag{6.47}$$

The stochastic-dynamic energy modes for this model are the certain and uncertain potential energy and certain and uncertain kinetic energy, denoted by CPE, UPE, CKE and UKE respectively. They are defined as

$$\mathrm{CPE} = \frac{gL}{2} \sum_m E(H_m)\ E(H-m) \quad , \tag{6.48}$$

$$\mathrm{UPE} = \frac{gL}{2} \left[2 \sum_m \mathrm{COV}(H-m, Hm) + \mathrm{COV}(H_o, H_o)\right] \quad , \tag{6.49}$$

$$\begin{aligned} \mathrm{CKE} = \frac{L}{2} \sum_m \sum_n [&E(H_m)\ E(U_n)\ E(U_{-m-n}) \\ &+ E(H_m)\ E(V_n)\ E(V_{-m-n})] \end{aligned} \tag{6.50}$$

and

$$\begin{aligned} \mathrm{UKE} = \frac{L}{2} \sum_m \sum_n [&E(H_m)\ \mathrm{COV}(U_n, U_{-m-n}) + E(H_m)\ \mathrm{COV}(V_n, V_{-m-n}) \\ &E(U_n)\ \mathrm{COV}(H_m, U_{-m-n}) + E(U_{-m-n})\ \mathrm{COV}(H_m, U_n) \\ &+ E(V_n)\ \mathrm{COV}(H_m, V_{-m-n}) + E(V_{-m-n})\ \mathrm{COV}(H_m, V_n)] \ . \end{aligned} \tag{6.51}$$

Also, the total energy (TE) of the system is given by the sum of the certain and uncertain energies,

$$\mathrm{TE} = \mathrm{CPE} + \mathrm{UPE} + \mathrm{CKE} + \mathrm{UKE} \tag{6.52}$$

and should be conserved. In utilizing the information in the energy budgets, it is convenient to subtract the large amount of potential energy, associated with the mean fluid depth, that is unavailable for conversion to other modes of energy. Therefore, certain potential energy will hereafter be defined as

$$CPE = \frac{gL}{2} \left[\sum_m E(Hm)\, E(H-m) - E^2(H_o)\right] \quad , \tag{6.53}$$

so that now the total energy is given by

$$TE = CPE + UPE + CKE + UKE + \frac{gL}{2} E^2(H_o) \quad . \tag{6.54}$$

The information obtained from a study of the time variation of these energy components will be both necessary in studying the effect of initial data errors on mesoscale predictability as well as helpful in verifying the proper formulation and coding of the forecast equations.

6.4 Interpretation of Predicted Variances

The stochastic-dynamic model produces time-dependent covariance matrices that contain the uncertainty information about the expansion coefficients. For a physical interpretation of these results, the point variances in physical space must be obtained. Substitution of

$$h = \sum_m H_m F_m \tag{6.55}$$

into the definition for the variance,

$$VAR(h) = E(h^2) - E(h)\, E(h) \quad , \tag{6.56}$$

provides

$$\begin{aligned} VAR(h) = {} & \sum_m \sum_n E(H_m H_n)\, F_m F_n \\ & - \sum_m \sum_n E(H_m)\, E(H_n)\, F_m F_n \quad . \end{aligned} \tag{6.57}$$

The quantity F_m is the basis function for the expansion, in this case e^{imkx}. Using the definition of covariance provided by equation (6.21), the above expression becomes simply

$$\mathrm{var}(h) = \sum_m \sum_n \mathrm{COV}(H_m, H_n)\, F_m\, F_n \quad . \tag{6.58}$$

Given the covariance matrix for H or any other dependent variable, the more physically meaningful spatial variations of the standard deviations may be obtained from equations of the form of (6.58).

6.5 Pure Gravity Wave Experiments

An experiment was performed with the stochastic-dynamic model for conditions of pure gravity wave motion (no mean advection). Initial conditions that produce strong nonlinear interactions were chosen, to provide a non-trivial test of the model. Highly nonlinear conditions also allow for a relatively rapid transfer of energy from certain to uncertain modes. Under these conditions we expect a relatively smooth increase in the amount of uncertain energy, meaning the forecast is becoming less credible with time.

The initial standard error of each of the depth observations was 200 meters. The initialization routine used 17 evenly spaced information or observation points and allowed 16 Fourier components (8 complex expansion coefficients). There was no uncertainty in the wind field. The Coriolis parameter and the v wind component were set equal to zero, the domain size was 600 km, the depth of the unperturbed fluid was one kilometer and the centered time differencing method was used after a single forward time step. The initial first moments consisted of a mass perturbation, situated in the center of the domain, with an amplitude of one kilometer above the unperturbed level. The initial velocity first moments were zero.

Figure 6.1 shows the initial conditions as well as the evolution of the second moments and the depth with time. The uncertainty in both the u and h fields grew most rapidly on the leading edge of the propagating gravity wave. This is reasonable in the sense that uncertainties in the wave position produce the greatest "point uncertainties" where the gradients of the wave are greatest. Although there is some tendency for large uncertainties at the trailing edge of the separate waves, this large gradient in h did not exist until the waves completely separated, so the total uncertainty growth should probably not be comparable to that on the forward edge of the wave. The regions of large σ_u are more highly correlated with the values of high σ_h rather than with gradients of u. Figure 6.2 shows the changes in σ_u and σ_h during the first five minutes of the forecast and reveals a smooth transfer of uncertainty from the mass field to the wind field. Except in the center of the domain where transfers of uncertain energy are being affected by nonlinear interactions among the first moments, the second moments approach an equilibrium value. Although a detailed

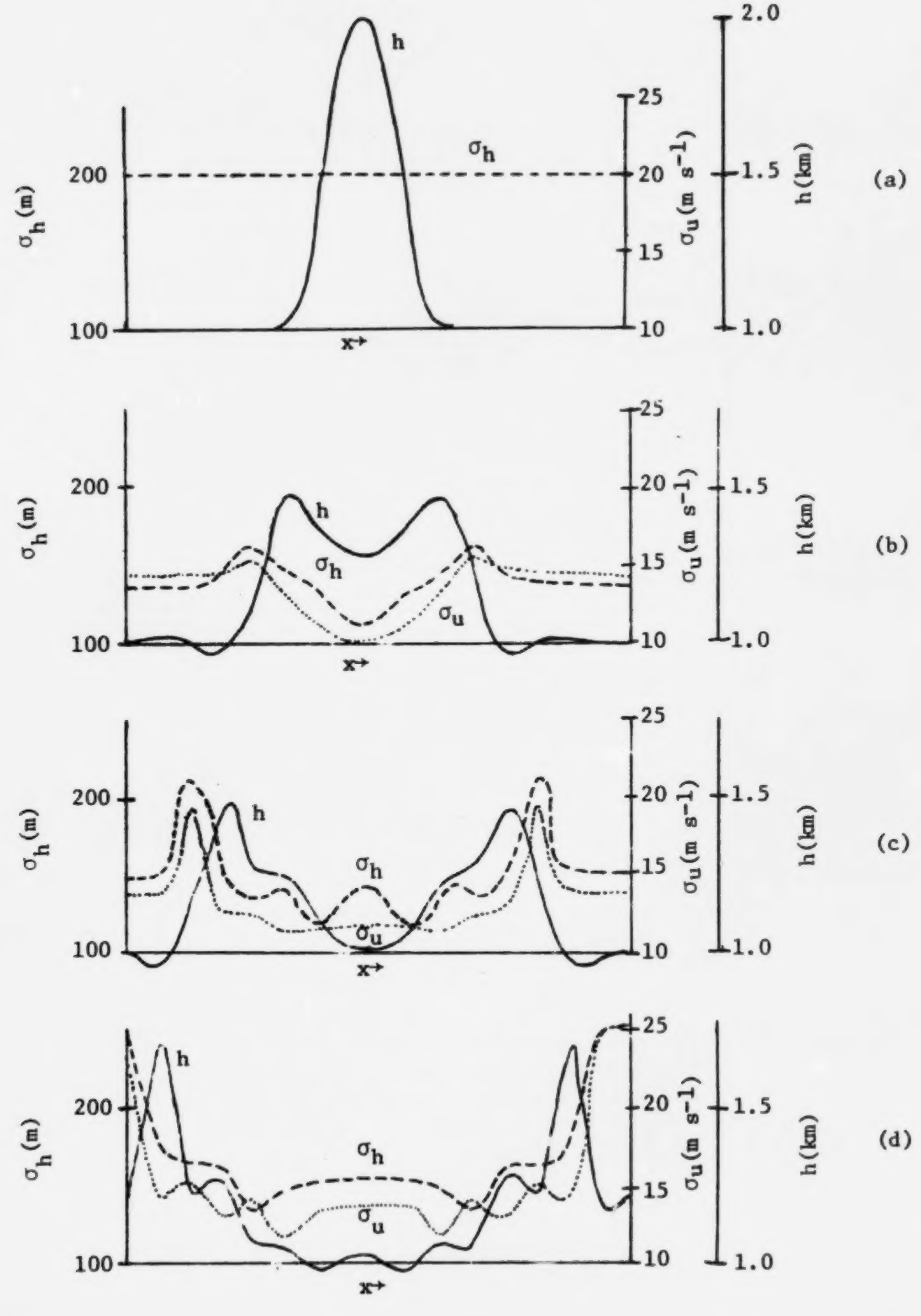

Figure 6.1. Spatial and temporal variation of σ_u, σ_h and h for the pure gravity wave integration. Graph (a) pertains to 0 minutes; (b) 10 minutes; (c) 20 minutes; and (d) 30 minutes.

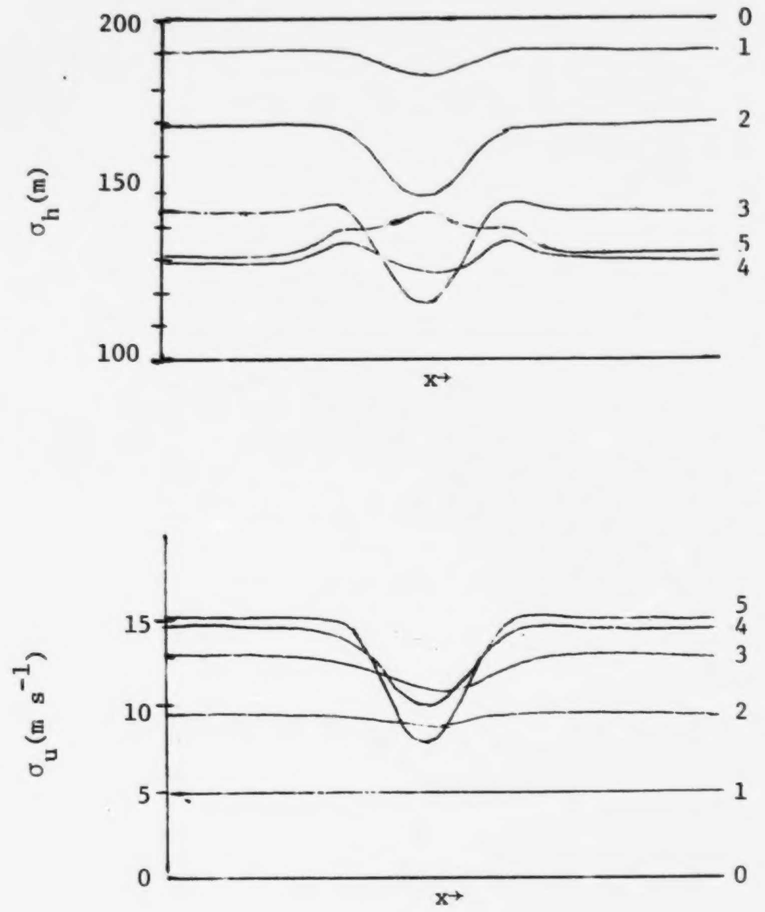

Figure 6.2. Spatial and temporal variation of the standard deviations of u and h during the first five minutes of the pure gravity wave integration. Curves are labeled in minutes.

discussion of the initial adjustment of σ_u and σ_h will be provided in a section to follow, we point out the following in regard to this experiment. Errors in h ($\sigma_h \neq 0$) cause random gravity wave components which are reflected in the initially zero u field as error components ($\sigma_u \neq 0$). Uncertainty about the fluid depth breeds uncertainty in the velocities, the mechanism for this transfer of uncertain energy being the normal modes of energy exchange characteristic of gravity wave generation and propagation. These uncertain energy exchanges take place irrespective of the prevailing first moment fields.

Figures 6.3, 6.4, and 6.5 show the energy transitions for the certain modes, the uncertain modes and the total energies respectively. Initially, the accelerations produced along the leading edge of the height perturbation are reflected in the growth of the certain kinetic energy. The uncertain component of the height observation is responsible for the simultaneous growth of the uncertain kinetic energy. The certain and uncertain potential energies show corresponding decreases. The total energy is conserved to an acceptable degree and the changes in the certain energy modes correspond to what one might expect from two gravity waves propagating in opposite directions on a domain with cyclic boundaries. For example, at about 30 minutes, the two waves begin to come into phase again. The total uncertain energy shows little change during the early period of the integration, but soon begins to grow rapidly eventually exceeding in magnitude the total certain energy at 43 minutes.

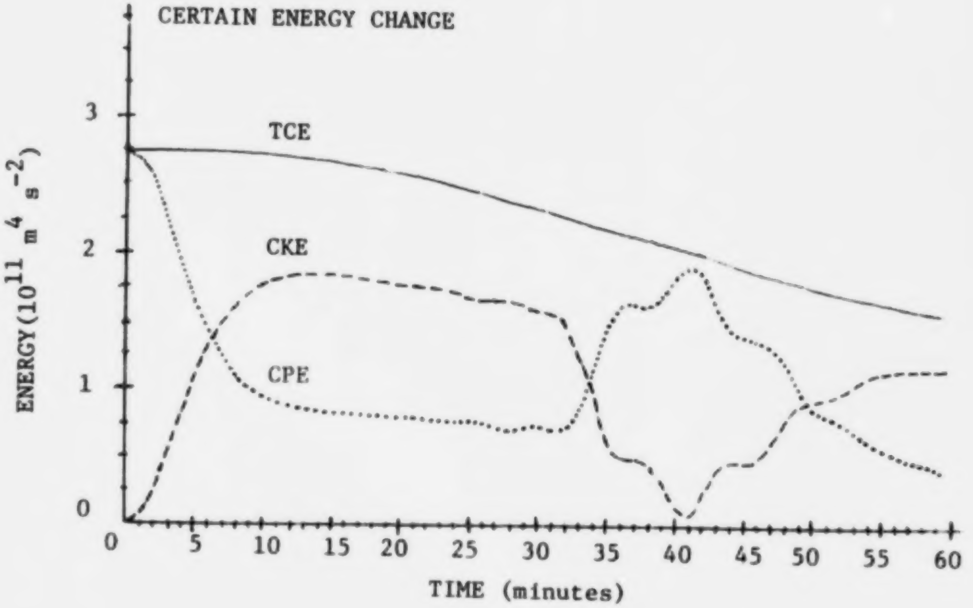

Figure 6.3. Time variation of the certain energy modes. TCE is the total certain energy, CPE is the certain potential energy and CKE is the certain kinetic energy.

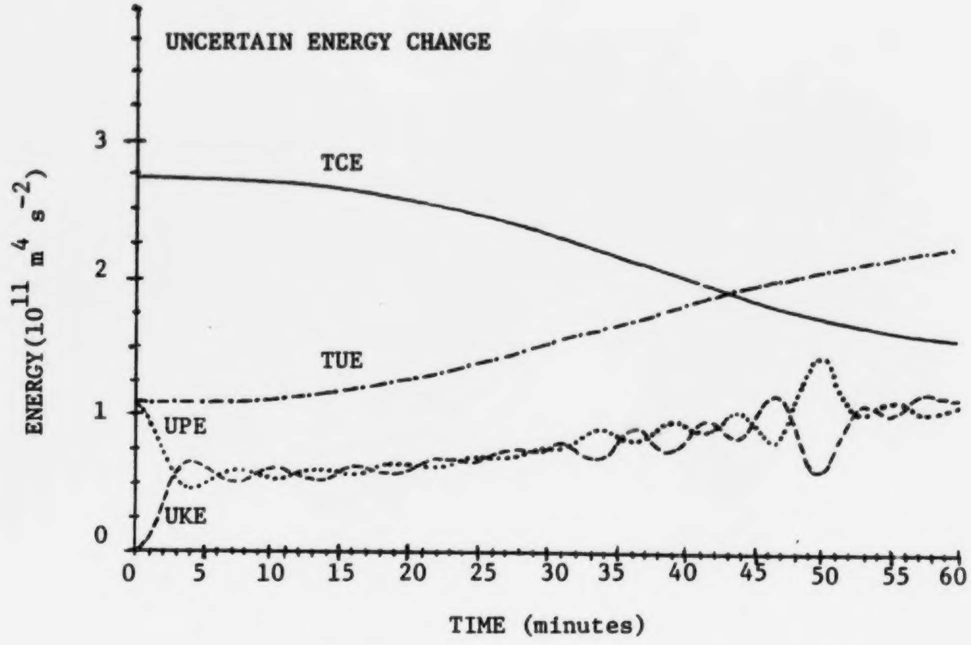

Figure 6.4. Time variation of the uncertain energy modes. TUE is the total uncertain energy, UPE is the uncertain potential energy and UKE is the uncertain kinetic energy. TCE, the total certain energy, is included for comparison with the total uncertain energy.

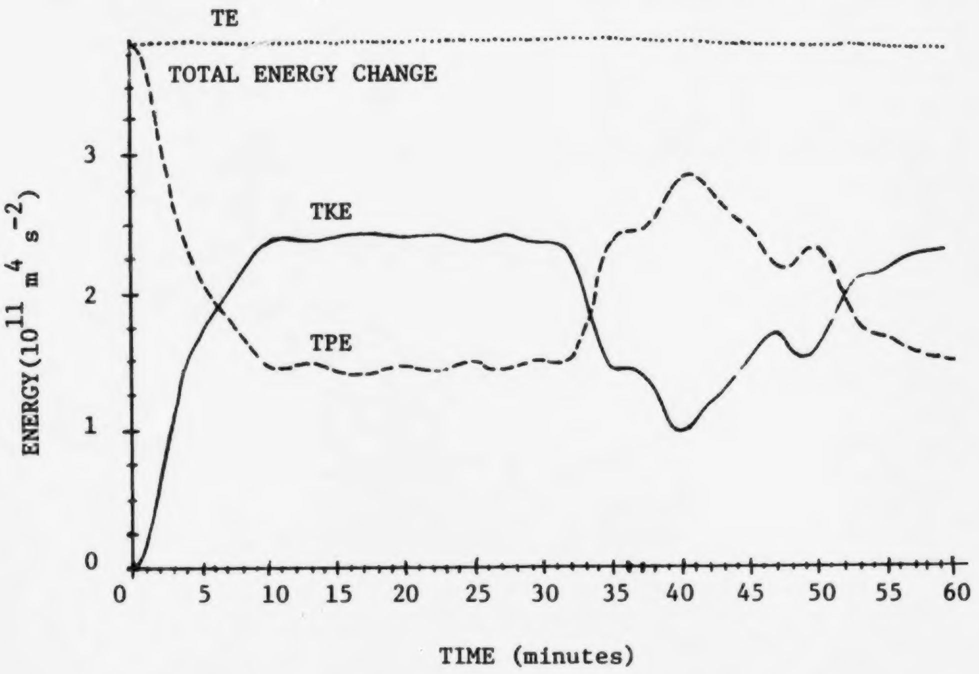

Figure 6.5. Time variation of the total energy modes. TPE is the total potential energy, TKE is the total kinetic energy and TE is the total energy.

6.6 A Monte Carlo Comparison

The results from the stochastic-dynamic model may be compared with the results from a Monte Carlo procedure that also provides error growth information about a numerical forecast. In the Monte Carlo scheme, the deterministic, spectral, model equations (to which the stochastic-dynamic equations degenerate if second and higher order moments are assumed to be zero) are applied successively to members of an ensemble of initial conditions. Each member is obtained by using a "quasi-random" number generator that simulates the observation errors by producing deviations to some "known" state of the fluid. The errors are normally distributed, with a given variance, and are applied at each point. If there are p distinct grid points and n Monte Carlo trials, there are n x p random, independent errors generated. This method does not suffer from the requirement of an artificial stochastic closure scheme and has an unlimited potential accuracy as the number of trials is increased. It is thus a desirable method of verifying solutions obtained from the integration of a set of stochastic-dynamic equations. The large amount of machine time required by this method, however, prevents its routine use.

A Monte Carlo solution to the gravity wave problem, discussed in the last section, was carried out to check the overall performance of the stochastic-dynamic model, both in terms of the correctness of the machine coding as well as the appropriateness of the stochastic closure scheme. The deterministic, spectral model used in the Monte Carlo runs did, out of necessity, have machine coding that was not structured identically to that used in the stochastic-dynamic model. The possibility exists therefore that differential roundoff and conversion errors may have produced some unknown degree of difference between the solutions from the two methods. All other conditions were held identical between the two models and any significant differences in the solutions are probably due to the closure scheme utilized.

It is possible to compare the two solutions in terms of the energetics as well as in terms of the actual spatial variation of the uncertainties. The latter method was chosen because it seemed more demanding in the sense that compensating errors could be hidden in the spatially integrated energy modes. Figure 6.6 shows the Monte Carlo solution for σ_h and σ_u after 20 minutes of integration time. The number of trials was 500. Figure 6.7 provides the same information but corresponds to 30 minutes of integration time. The true solution, at any point in the time scale, should be symmetric about the location of the original perturbation in h, however, the 30 minute Monte Carlo solution for σ_h does show some asymetry in the center of the domain. In other experiments with 50 and 200 trials, this central region seemed to have less asymetry and did not exhibit errors of any greater magnitude. In most other respects, the solutions agree well,

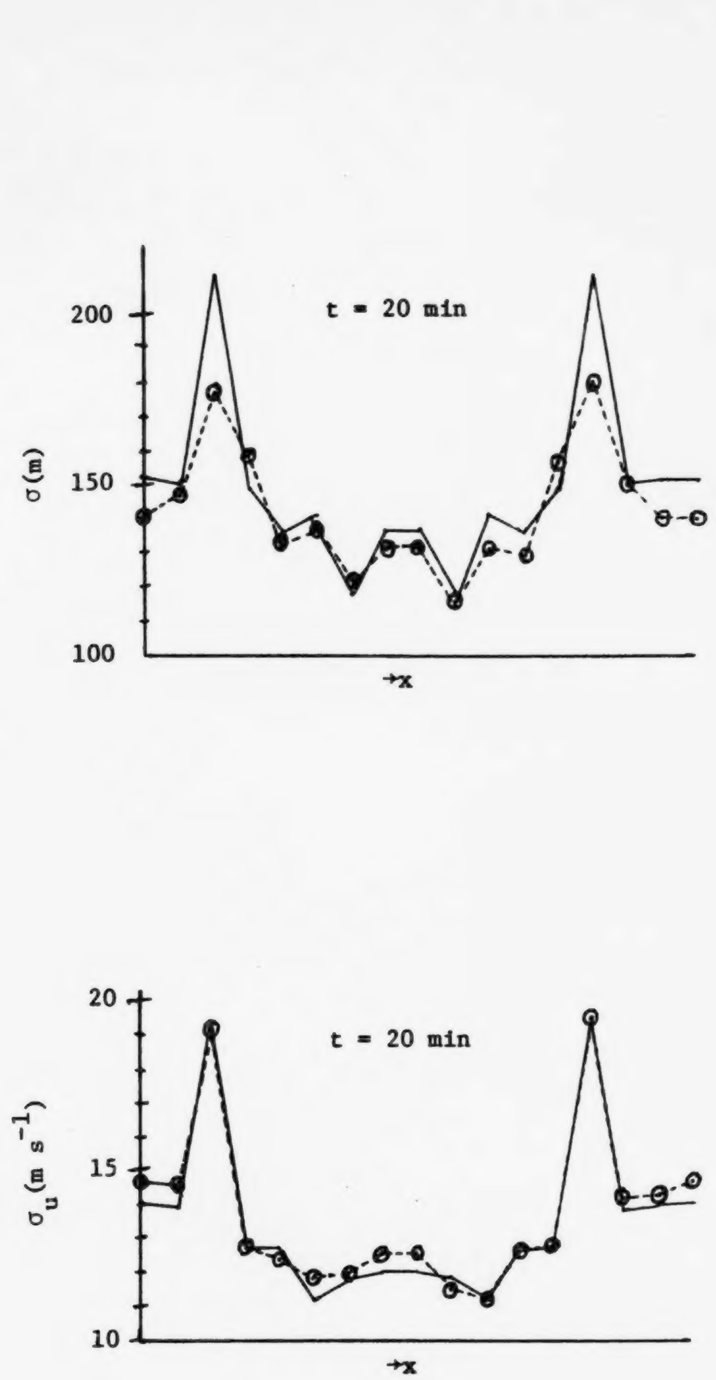

Figure 6.6. Monte Carlo solution with 500 trials (dashed line) and the stochastic-dynamic solution after 20 minutes of integration for conditions of pure gravity wave motion.

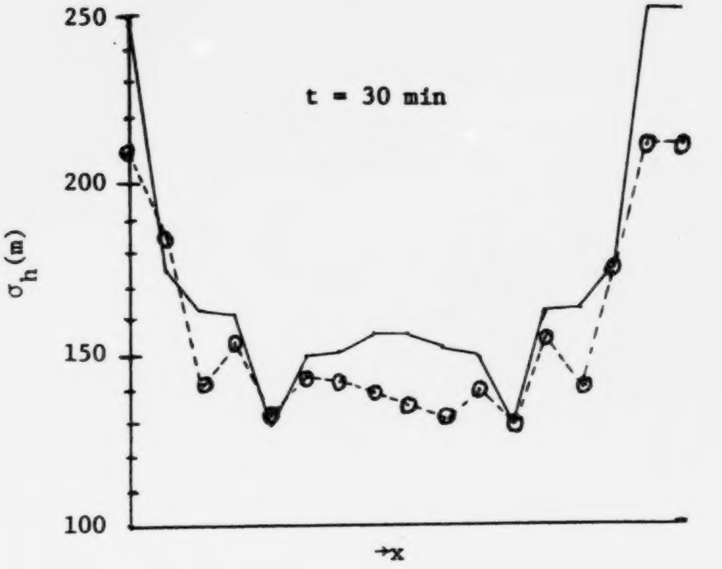

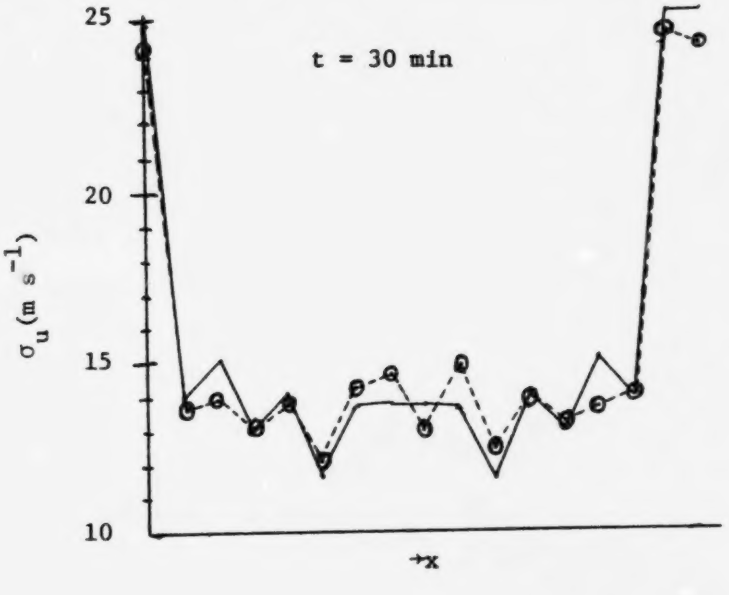

Figure 6.7. Monte Carlo solution with 500 trials (dashed line) and the stochastic-dynamic solution after 30 minutes of integration for conditions of pure gravity wave motion.

especially at 20 minutes, even though there does appear to be some difficulty in preserving the amplitude of the peak in σ_h.

Fleming (1970) points out that the third moments do not affect the energy conservation nor are they directly involved in the conversion from the certain to uncertain energy modes. They are, however, directly involved in the transfer between uncertain energy components. Since the conclusions concerning the compatability or errors in the mass and momentum variables will be strongly dependent upon the modeled exchange between uncertain kinetic and uncertain potential energy, the Monte Carlo control experiment should be examined carefully to determine if the stochastic-dynamic solution is strongly affected by this closure assumption. In this example, the results appear to be encouraging. The initial σ_h was 200 meters and σ_u was zero in this particular experiment. The results in Figure 6.6 show the maximum discrepency between the Monte Carlo and stochastic-dynamic solution for σ_u to be only 3 or 4% of the total change in σ_u up to that point in the forecast. The spatially averaged discrepency is on the order of 1 or 2% of the total change. These percentages are approximately the same for the σ_u solution at 30 minutes, shown in Figure 6.7. The average difference of σ_u at 20 minutes, again in terms of percentage of the total change, is about 12 percent. By 30 minutes, this percentage has increased somewhat but it is still less than 20%.

Considering the highly nonlinear character of the flow, it is probable that these relatively small observed discrepencies were due to the neglect of the third and higher moments. For flow conditions more representative of the atmosphere (i.e., much smaller amplitude waves) this source of error should be significantly reduced. Further Monte Carlo control experiments will be performed, however, as the model is applied to differing atmospheric flow conditions, to insure that the closure method remains satisfactory.

6.7 Synoptic Scale Error Compatability Experiments

To visualize the process of error or uncertainty exchange between variables, consider one member of the ensemble of forecasts that the stochastic-dynamic method represents. Let the model, defined by equations (6.15-6.17) be initialized with values that represent the exact state of the fluid plus observation errors superimposed as perturbations. After the integration begins, the variables attempt to adjust to a state of dynamic compatability. This adjustment will occur because of true imbalances in the actual fluid as well as because of imbalances inherent in the random observation errors. The scale of the true imbalance is physically determined, while the scale of the error-related imbalances is artifically imposed by the grid point or observation point spacing. The mode of adjustment of the mass and velocity fields to a dynamically consistent state is scale dependent. Linear geostrophic adjustment theory provides guidance in understanding the adjustment mechanisms (Washington, 1965). Briefly, small-scale imbalances are eliminated rapidly through the adjustment of the mass field by gravity waves. Large-scale imbalances respond slowly to inertially dominated gravity-inertia waves that attempt to alter the velocity field. Thus, the velocity field dominates the adjustment process on the small scale and the mass field dominates on the large scale. At intermediate scales, the adjustment is more mutual. In all cases, the process is manifested by damped inertial oscillations around the equilibrium state, the damping rate being rapid for small-scale and slow for large-scale disturbances.

A knowledge about the relative dominance of these adjustment mechanisms in a particular situation can provide information about the flow of uncertain energy during the adjustment process. For purposes of illustration, assume no errors exist in the initial wind field, but that the mass field data have a random component with prescribed variance. Also, assume no imbalances exist in the true state of the system. If the adjustment to equilibrium is mutual, an error in the observation of the mass field will be rapidly reflected in the velocity field, producing an increase in the uncertain kinetic energy from its initial value of zero. As the velocities increase, they approach a condition of geostrophic equilibrium. These geostrophic velocities represent uncertain kinetic energy since they resulted solely from errors in the mass field. Since the adjustment is mutual, the mass field perturbation has a tendency to disperse and become smooth so as to be in balance with the initially smooth momentum field. The net effect of the mutual adjustment is that some of the initial uncertain potential energy is partitioned to uncertain kinetic energy related to the geostrophic velocities and some is partitioned to the ageostrophic velocities related to gravity waves. Transfer of uncertain energy during the adjustment has contaminated one variable with the uncertainty from another. If random errors are present in both mass and velocity fields, which is generally the case, the adjustment process becomes somewhat more complicated, with uncertain energies traveling both ways between the mass and velocity fields. The condition in which neither velocity nor mass related variables have a net effect of increasing the errors of the other variables is defined as one of error consistency or compatability.

Thus far, the discussion of uncertain error transfer in terms of the adjustment process has been confined to a single deterministic forecast in order to simplify the consideration of the dynamics involved. Since the stochastic-dynamic method represents an infinite ensemble of such forecasts, each initialized with different errors drawn from the same distribution, the modeled transfers between uncertain energy modes pertain to an infinite number of adjustments toward equilibrium. The statistics of such an ensemble of forecasts are produced by the stochastic-dynamic model discussed in Section 6.1, which has been used to investigate this question of error consistency for the synoptic scale. The domain size for the initial experiments was 10,000 km which means that the shortest allowed harmonic was 1250 km.

The first moments of the forecast variables defined a pair of "highs" and "lows" on the grid. A geostrophic u component of 25 m s^{-1} was specified and the v component was defined by the spectral form of the geostrophic wind equation

$$V_m = i \frac{g}{f} mkH_m \quad . \tag{6.59}$$

The hydrostatic approximation and gas law for an incompressible fluid can be used to yield a correspondence between depth errors in the barotropic model and temperature errors in the atmosphere. The relationship is

$$\delta h = \frac{R}{g} \left(1 - \frac{P_t}{P_o}\right) \delta T_o \tag{6.60}$$

where the t subscript refers to the top of the fluid layer and a zero subscript refers to the bottom. As discussed in Section 6.1, the top of the active layer has been modeled to be at the tropopause level, so P_t has been taken to be 200 mb. For P_o of 1000 mb, a temperature increment of 1°C corresponds to 23.4 m. This relationship will be used to interpret depth or mass field errors in terms of temperature errors.

Figure 6.8 shows the transition of the uncertain kinetic energy of the v component of the wind velocity for various values of the initial standard error of the v component. The curves are labled in terms of the standard deviation of the error, in m s^{-1}. In all cases, the magnitude of the standard deviations of the initial

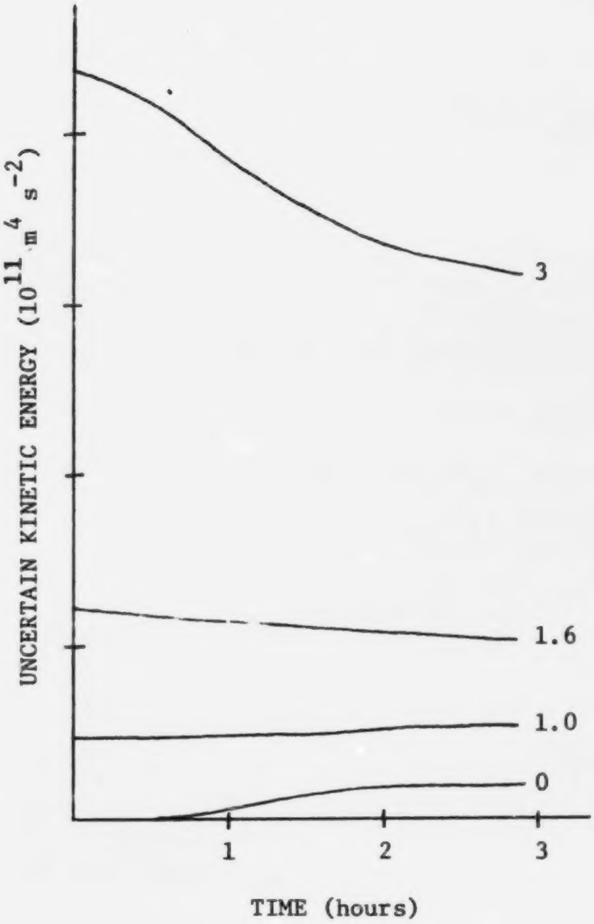

Figure 6.8. Transition [illegible] the uncertain kinetic energy of the v velocity component for various initial, standard errors of the v component. The curves are labeled in terms of the magnitude of the standard deviation of the initial v error, in m s^{-1}. The initial standard deviation of the equivalent temperature error was 1°C.

equivalent temperature error was 1C°. When no uncertainty existed in the wind field, the uncertain kinetic energy of the v component increased as the uncertain potential energy decreased (not shown). For a three m s^{-1} standard error in v, a large amount of uncertain energy was transferred to the potential mode. The standard error in the wind field that corresponds to 1C° standard error in the temperature field is shown to be about 1.0 m s^{-1}. As the standard error is changed above or below this value of 1.0 m s^{-1}, the direction of the flux of uncertain energy between the two modes is changed. Another way of looking at the same results is in terms of the space average of the point values of the standard deviations. Figure 6.9 displays the change in $\bar{\sigma}^x_v$ during the same time period that Figure 6.8 results apply. If the error in the initial wind field was excessive, in terms of its consistency with the mass field error (e.g., an initial $\bar{\sigma}^x_v$ of 3 m s^{-1}), the $\bar{\sigma}^x_v$ decreased from its initial value to the consistent value during the first 2 hours of the integration. Similarlty, if the wind field observations had an accuracy that was higher than the level of consistency, their accuracy was degraded by the errors in the observations of the mass field.

In the error consistency experiments thus far performed, the results have proved to be independent of the synoptic situation reflected by the first moments.

6.8 Summary and Plans for Future Research

When the stochastic-dynamic model was tested for conditions of pure gravity wave motion, reasonable solutions were produced in terms

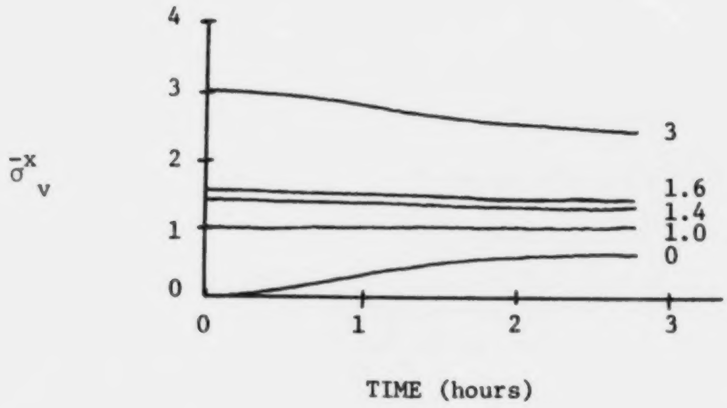

Figure 6.9. Transition of the standard deviation of v in terms of its spatial average for various initial, standard errors of the v component. The curves are labeled in terms of the magnitude of the standard deivation of the initial v error, in m s^{-1}. The initial standard deviation of the equivalent temperature error was 1°C.

of total uncertain energy increase, the spatial variability of the uncertainty and the flux of uncertain energy between the potential and kinetic modes. The Monte-Carlo analog of this experiment, which was used as a "control", indicated that the stochastic closure scheme of dropping third and higher moments was acceptable for these particular flow conditions and for integrations of up to 30 minutes in this case. The question of error compatability or consistency was investigated for the synoptic scale. It was determined that, for a standard error of 1°C in the temperature observations, the wind field had to be determined to an accuracy corresponding to a standard error of about 1.0 m s^{-1}, in order that neither field contaminate the other with its error. Similar experiments will be performed for regional scale domains and flow conditions. The Monte Carlo technique will be used periodically to verify the adequacy of the stochastic closure technique under new experimental conditions.

REFERENCES

Anthes, R. A., "Development of Asymmetries in a Three-Dimensional Numerical Model of the Tropical Cyclone", Monthly Weather Review, 100(6), 1972, 461-476.

Anthes, R. A., and T. T. Warner, "Prediction of Mesoscale Flows over Complex Terrain", Research and Development Tech. Report ECOM-5532, Atmospheric Science Laboratory, White Sands Missle Range, New Mexico 88002, March 1974, 101 pp.

Benwell, G. R. and F. Bretherton, "A pressure oscillation in a 10-level atmospheric model", Quarterly Journal of the Royal Meteorological Society, 94, (400), April 1968, 123-131.

Epstein, E. S., "Stochastic Dynamic Prediction", Tellus, 21,, 1969, 739-759.

Fleming, R. J., "Concepts and Implications of Stochastic Dynamic Prediction", NCAR Cooperative Thesis No. 22, The University of Michigan and Laboratory of Atmospheric Science, NCAR, 1970, 171 pp.

Gerrity, J. P., McPherson, R. D., and S. Scolnik, "A Semi-Implicit Version of the Shuman-Hovermale Model", NOAA Technical Memorandom NWS NMC-53, National Meteorological Center, Suitland, Maryland, July 1973, 44 pp.

Haltiner, G. J., Numerical Weather Prediction, Wiley, New York, 1971, 317 pp.

Harrison, E., and R. Elsberry, A method for incorporating nested finite grids in the solution of systems of geophysical equations. J. Atmos. Sci., 29, 1972, 1235-1245.

Hovermale, John B., 1974, Personal communication.

Koss, W. J., Numerical integration experiments with variable resolution two-dimensional Cartesian grids using the box method. Monthly Weather Review, 99, 10, 1971, p. 725-738.

Kurihara, Y., On the use of implicit and Interactive methods for the time integration of the wave equation, Monthly Weather Review, Vol. 93, No. 1, 1965, pp. 33-46.

Kwizak, M., and A. J. Robert, A semi-implicit scheme for grid point atmospheric models of the primitive equations, Monthly Weather Review, Vol. 99, No. 1, 1971, pp. 32-36.

REFERENCES (Cont'd)

Langlois, W. R. and H. C. W. Kwok, Description of the Mintz-Arakawa numerical general circulation model, Numerical Simulation of Weather and Climate, Tech. Report, No. 3, Dept. of Meteorology, U.C.L.A., Feb. 1969, 95 pp.

McPherson, R. D., Damping properties of the implicit-backward integration method, NOAA Office Note 81, National Meteorological Center, Suitland, Maryland, April, 1973, 23 pp.

Mood, A. M., and F. A. Graybill, Introduction of the Theory of Statistics, Second Edition, McGraw-Hill, New York, 1963, 443 pp.

Moretti, G., Importance of boundary conditions in the numerical treatment of hyperbolic equations, The Physics of Fluids, Supplement 11, 1969, 13-20.

Phillips, N. A. and A. Shukla, On the Strategy of Combining Coarse and Fine Grid Meshes in Numerical Weather Prediction, J. Appl. Meteor., 12, 1973, 763-770.

Saucer, W. J., Principles of Meteorological Analysis, University of Chicago Press, Chicago, Illinois, 1955, 438 pp.

Seaman, N. L., "A Numerical Investigation into Effects Contributing to Nocturnal Low Level Jet Oscillations, Master of Science Thesis, Department of Meteorology, Pennsylvania State University, August 1973, 86 pp.

Sela, J. and S. Scolnik, "Method for Solving Simultaneous Helmholtz Equations", Monthly Weather Review, Vol. 100, No. 8, 1972, pp. 644-645.

Shapiro, R., "Smoothing, Filtering, and Boundary Effects", Reviews of Geophysics and Space Physics, 8(2), 1970, 359-387.

Thompson, P. D., Numerical Weather Analysis and Prediction, The Macmillan Co., 1961, 170 pp.

Washington, W. W., "Initialization of Primitive-Equation Models for Numerical Weather Prediction", Ph.D. Dissertation, The Pennsylvania State University, 1964, 84 pp.

7.0 EXPERIMENTS WITH SIMPLIFIED SECOND-MOMENT APPROXIMATIONS FOR USE IN REGIONAL SCALE MODELS

Alfred K. Blackadar

7.1 Introduction

In connection with the development of the regional air-pollution model, it has been recognized that there is a need for a very simple method for taking approximate account of the rates of exchange of momentum, heat, water-vapor, and other properties that result from the action of sub-grid scale motions. The method that has been tried up to this time has been equivalent to a K-type closure with the turbulent energy constituting the most important parameter for the determination of the value of K. The method was based on a Prandtl type of argument, and since such an argument has only a very limited physical basis, it was not possible to be very confident of its applicability to situations that are likely to depart rather widely from the familar situations in the surface layers.

During the past year emphasis has been placed on the use of the 2nd-order closure schemes to derive and experiment with various sets of simplified equations that might be incorporated into a regional scale model for the purpose of calculating the most important fluxes of heat and momentum. As in earlier studies, it is recognized that any abridgement of the complete set of equations for the second moments carries with it the likelihood of inferior results. However, as a practical matter, the demands placed upon the most advanced modern computers by the regional scale model are such that operational applications will require the use of simple methods wherever these suffice, and that if the more sophisticated methods are needed, it may be for only a limited portion of the total space-time domain of the forecast. In this regard, it appears quite feasible to operate the regional model in several modes so that various schemes of varying complexity can be called in response to particular situations.

The second moment equations on which the last year's experiments have been based are the following (see Lumley and Khajeh-Nouri, 1973)

$$\frac{\partial \overline{u_i u_k}}{\partial t} + U_j \frac{\partial}{\partial x_j} \overline{u_i u_k} = - \overline{u_j u_k} \frac{\partial U_i}{\partial x_j} - \overline{u_j u_i} \frac{\partial U_k}{\partial x_j} - \frac{\partial}{\partial x_j} (\overline{u_i u_j u_k})$$

$$- \frac{1}{\rho_o} (\overline{u_k \frac{\partial p}{\partial x_i} + u_i \frac{\partial p}{\partial x_k}}) + \frac{g}{\bar{\theta}} (\delta_{3i} \overline{u_k \theta'} + \delta_{3k} \overline{u_i \theta'}) \qquad (1)$$

$$- \frac{2}{3} \bar{\varepsilon} \, \delta_{ik}$$

$$\frac{\partial}{\partial t} \overline{u_i \theta'} + U_j \frac{\partial}{\partial x_j} \overline{u_i \theta'} = - \overline{u_j \theta'} \frac{\partial U_i}{\partial x_j} - \overline{u_i u_j} \frac{\partial \bar{\theta}}{\partial x_j} - \frac{\partial}{\partial x_j} \overline{u_i u_j \theta'}$$

$$(2)$$

$$- \frac{1}{\rho_o} \overline{\theta' \frac{\partial p}{\partial x_i}} + \delta_{3i} \frac{g}{\bar{\theta}} \overline{\theta'^2}$$

$$\frac{\partial}{\partial t} \overline{\theta'^2} + U_j \frac{\partial}{\partial x_j} \overline{\theta'^2} = - 2 \overline{u_j \theta'} \frac{\partial \bar{\theta}}{\partial x_j} - \frac{\partial \overline{u_j \theta'^2}}{\partial x_j} = - 2 \bar{\varepsilon}_\theta \qquad (3)$$

In these equations, U_i and u_i are the components of the mean and fluctuation velocities, respectively; $\bar{\theta}$ and θ' the same for potential temperature; δ_{ik} the Kroenecker tensor; p the pressure fluctuation; and $\bar{\varepsilon}$ and $\bar{\varepsilon}_\theta$ are the rates of dissipation of turbulent energy and $\overline{\theta'^2}$ respectiv

The limitations of the computers likely to be available for operational use require that all reasonable simplifying assumptions be incorporated into to the use of these equations. It is a property of these models that the horizontal grid spacing is one to two orders of magnitude larger than the vertical spacing. It is also fairly well established that there exists a deficiency of energy in the wavelength spectrum in the neighborhood of the dimension of the horizontal spacing (20-30 km). For these reasons the horizontal sub-grid scale fluxes have been neglected and the vertical fluxes have been treated as if the turbulence is horizontally homogeneous in mean properties. It is also assumed that the time rate of change of the second moment is small compared to other terms in the second-moment equations. This assumption is less easily justified when diurnal variations are involved, and should be abandoned if computational limitations permit. In some cases, it may be simpler to retain time-change terms so as to permit the equations to be solved prognostically rather than diagnostically.

In writing equation (1) for the stresses we have omitted the Coriolis term $-2(\varepsilon_{ij\ell}\,\Omega_j\,\overline{u_\ell u_k} + \varepsilon_{k\ell m}\,\Omega_\ell\,\overline{u_m u_i})$ from the right side. Wyngaard et al (1974) have discussed the possible importance of these terms. Further study must be made to determine whether these terms need to be retained in the regional-scale model.

7.2 The "Poor Man's Method"

In accordance with the simplifications proposed in the previous section, we may obtain the following equations for the cases $k = 3$, $i = 1,2$:

$$\frac{1}{\rho_o}\left(\overline{w\frac{\partial p}{\partial x}} + \overline{u\frac{\partial p}{\partial z}}\right) = -\sigma_w^{2}\frac{\partial U}{\partial z} - \frac{\partial}{\partial z}\overline{uw^{2}} + \frac{g}{\bar{\theta}}\overline{u\theta'}$$
$$\frac{1}{\rho_o}\left(\overline{w\frac{\partial p}{\partial y}} + \overline{v\frac{\partial p}{\partial z}}\right) = -\sigma_w^{2}\frac{\partial V}{\partial z} - \frac{\partial}{\partial z}\overline{vw^{2}} + \frac{g}{\bar{\theta}}\overline{v\theta'} \qquad (4)$$

where $\sigma_w^{2} = \overline{w'^{2}}$.

In accordance with the views of Rotta (1951 a,b) the pressure-correlation terms on the left side constitute the mechanism for the restoration of isotropy. It is easily shown that if the turbulent motions are non-divergent, these terms contribute at most only to the flux divergen but do not constitute a source of turbulent energy. Accordingly, we put

$$\frac{1}{\rho_o}\left(\overline{u\frac{\partial p}{\partial z}} + \overline{w\frac{\partial p}{\partial x}}\right) = + c_m \ell^{-1} q\,\overline{uw}$$
$$\frac{1}{\rho_o}\left(\overline{v\frac{\partial p}{\partial z}} + \overline{w\frac{\partial p}{\partial y}}\right) = + c_m \ell^{-1} q\,\overline{vw} \qquad (5)$$

where c_m is some universal constant. This parameterization is equivalent to the first order term in Lumley's expansion if the relaxation time T is set equal to ℓ/q where ℓ is the length scale of the largest sub-grid scale motions and

$$q^{2} = 2E = \overline{u'^{2}} + \overline{v'^{2}} + \overline{w'^{2}}$$

It has more recently been shown by Lilly (1967) and Crow (1968) that t pressure-correlation term also contains a portion that is proportional to the shear. Accordingly, equation (4) takes the form

$$c_m \ell^{-1} q \overline{uw} = - \alpha_m \sigma_w^2 \frac{\partial U}{\partial z} + \frac{g}{\bar{\theta}} \overline{u\theta'} - \frac{\partial}{\partial z} \overline{uw^2}$$

$$c_m \ell^{-1} q \overline{vw} = - \alpha_m \sigma_w^2 \frac{\partial V}{\partial z} + \frac{g}{\bar{\theta}} \overline{v\theta'} - \frac{\partial}{\partial z} \overline{vw'^2} \qquad (6)$$

The value of α_m for isotropic turbulence is 2/5. Lumley (1973) has suggested a functional expansion to terms of third order of anisotropic invariants by which the value of α_m can be estimated. Difficulties with the use of this expression have not yet been resolved, and it appears necessary at the present time to treat this factor as one of the quantities to be derived empirically.

Following a procedure suggested by Mahrt (1973) we neglect the flux-divergence in our following discussion and introduce the so-called stress-Richardson number Rs defined by

$$\frac{g}{\bar{\theta}} \overline{u_i\theta'} = \sigma_w^2 \, Rs \, \frac{\partial U_i}{\partial z} \qquad i = 1,2 \qquad (7)$$

which, of course, implies that the vector $\overline{u_i\theta'}$ is parallel to the shear vector. As we shall see, this assumption is entirely reasonable.

These assumptions result in the following equations for the stresses:

$$\overline{uw} = [c_m^{-1} (\alpha_m - Rs) \frac{\sigma_w}{q}] \, \ell\sigma_w \frac{\partial U}{\partial z}$$

$$\overline{vw} = [c_m^{-1} (\alpha_m - Rs) \frac{\sigma_w}{q}] \, \ell\sigma_w \frac{\partial V}{\partial z} \qquad (8)$$

These equations are K-type fluxes and are quite similar to Prandtl's mixing-length result.

Although the exact meaning of ℓ in (5) and (8) is not clear, it must ultimeately be identifiable with either the grid spacing (which defines the turbulence to be parameterized) or some length scale of the turbulence spectrum. It is therefore relevant to investigate the order of magnitude of the bracketed expression. At the present time, this can only be done for isotropic turbulence, and we are mostly interested in the case of free-convection, as this state presumably characterizes the free-atmosphere whenever convection is occurring. Under these conditions, w and θ' may be expected to be well correlated and we can find a reasonable estimate of θ' by using the regression formula

$$\theta' = \frac{\overline{w\theta'}}{\sigma_w^2}\, w$$

Therefore,

$$\begin{aligned} \overline{u\theta'} &= \frac{\overline{w\theta'}}{\sigma_w^2}\ \overline{uw} \\ \overline{v\theta'} &= \frac{\overline{w\theta'}}{\sigma_w^2}\ \overline{vw} \end{aligned} \tag{9}$$

Since $\overline{uw}$ and $\overline{vw}$ are proportional to the corresponding shear components, the assumption underlying (7) is justified. We may now look to the surface boundary layer for further indication as to the limit approached in free convection. Introducing

$$\overline{uw} = - u_*^{\,2}$$

$$\phi_m = \frac{kz}{u_*}\frac{\partial U}{\partial z}$$

$$L = - \frac{\overline{\theta}}{g}\frac{u_*^{\,3}}{\overline{w\theta'}}$$

we obtain for free-convection

$$Rs \to - \left(\frac{u_*}{\sigma_w}\right)^4 \gamma^{1/3} \left(\frac{z}{-L}\right)^{4/3}$$

where γ is the constant in the KEYPS equation, which is most likely close to 9.0 (Businger, 1971). For free convection, several authors find

$$\frac{\sigma_w}{u_*} = 1.8 \left(\frac{z}{-L}\right)^{1/3}$$

Accordingly, we estimate that Rs approaches a limit of about -.16 and, for isotropic turbulence,

$$\frac{\sigma_w^{\,2}}{q^2} (\alpha_m - Rs) = 0.19$$

Subsequent work indicates that c_m as defined here is of very similar order of magnitude. We thus have reasonably good justification (subject to the assumptions made previously, for putting

$$K_m = c_1 \ell q \tag{10}$$

where c_1 is a constant of order unity.

A detailed analysis of the heat flux will be given later. It can be shown that, subject to the same simplifications, a k-type transfer takes place, with K_h of the form,

$$K_h = c_2 \ell q \tag{11}$$

It appears that under free convection c_2 does approach a limit which is a little more than twice c_1.

It may be expected that c_1 and c_2 will be functions of stability, and the treatment of these quantities as constants is an undesirable, but necessary, feature of the Poor Man's Method. Removal of these restrictions can be accomplished by going to more complicated schemes as will be shown later.

To obtain a closure it is necessary to define ℓ and to obtain an expression for q. The latter follows from (1) by putting i = k and summing over k. Under conditions of horizontal homogeneity, this equation becomes

$$\begin{aligned} \frac{\partial q^2}{\partial t} + U \frac{\partial q^2}{\partial x} + V \frac{\partial q^2}{\partial y} &= - 2[\overline{uw} \frac{\partial U}{\partial z} + \overline{wv} \frac{\partial V}{\partial z}] + 2 \frac{g}{\bar{\theta}} \overline{w\theta'} \\ &- \frac{\partial}{\partial z} \overline{w' (q'^2 + 2 \frac{p}{\rho_o})} - 2\bar{\varepsilon} \end{aligned} \tag{12}$$

We finally introduce the flux-gradient expression

$$w\overline{(q'^2 + 2\frac{p}{\rho_o})} = -c_3\ \ell q \frac{\partial}{\partial z} q^2$$

together with (10) and (11). We also assume

$$\bar{\varepsilon} = \frac{c_E\ q^3}{\ell} \tag{13}$$

The result is

$$\frac{1}{2}\frac{\partial q^2}{\partial t} + \frac{1}{2}[U \frac{\partial q^2}{\partial x} + V \frac{\partial q^2}{\partial y}] = c_1\ \ell q\ [(\frac{\partial U}{\partial z})^2 + (\frac{\partial V}{\partial z})]^2 - \frac{g}{\bar{\theta}} c_2\ \ell q \frac{\partial \bar{\theta}}{\partial z} + \frac{\partial}{\partial z} c_3\ \ell q \frac{\partial q^2}{\partial z} - c_E \ell^{-1}\ q^3 \tag{14}$$

If we assume stationarity and neglect the turbulent flux of q^2, we can solve this expression for q^2

$$q^2 = (\frac{c_i}{c_E})\ \ell^2\ [(\frac{\partial U}{\partial z})^2 + (\frac{\partial V}{\partial z})^2] - (\frac{c_2}{c_E}) \frac{g}{\bar{\theta}} \ell^2 \frac{\partial \bar{\theta}}{\partial z} \tag{15}$$

This expression was the basis of the experiments reported during the first year of the SRG grant.

It has been found by E. Müller (1973), in connection with a much finer grid-mesh model employing a similar parameterization scheme, that the omission of the flux-divergence of the energy caused the gradients of K_m and K_h to become unrealistically large. Whether this problem develops in the regional scale model is not yet known. If it appears that retention of the flux divergence is required in (14), then, as pointed out by Hinkelmann (1973), it will be advantageous to retain also the time derivative. The integration can then be carried out as an initial value problem with fading memory, rather than as a boundary-value problem that would require relaxation at every time step.

The necessity to designate ℓ poses the greatest conceptual difficulty for the Poor Man's Method. When the grid-spacing is smaller than the length scale of the energy containing turbulence, it is reasonable to identify ℓ as that length which separates the subgrid scales from the scales of motion that are predicted by the model. If, on the other hand, the peak of the subgrid scale turbulence spectrum falls at length scales smaller than the grid spacing, ℓ must be identified with the spectral peak, and is probably best defined by (13). This would make Rotta's relaxation time proportional to $q^2/\bar{\varepsilon}$ as assumed by Lumley. There appears to be no simple scheme for accomplishing a realistic specifiction for ℓ in the Poor Man's Method. It is suggested that reasonable predictions could be made by rewriting (14) in the following way:

$$\frac{1}{2}\frac{\partial q^2}{\partial t} + \frac{1}{2}[U\frac{\partial q^2}{\partial y} + V\frac{\partial q^2}{\partial y}] = c_1 \ \ell q \ [(\frac{\partial U}{\partial z})^2 + (\frac{\partial V}{\partial z})^2] - c_2 \ \ell q \ \frac{g}{\bar{\theta}}\frac{\partial \bar{\theta}}{\partial z} \tag{16}$$
$$+ \frac{\partial}{\partial z} c_3 \ \ell q \frac{\partial q^2}{\partial z} - \frac{c_E}{\Delta z} q^3$$

It is then suggested that if the Richardson number is less than zero, or some other more appropriate value, ℓ be made equal to the vertical grid spacing Δz and that otherwise it be made zero. Since negative solutions of q^2 could conceivably result from errors in the initial values or from parameterization errors, it will probably be necessary to change negative values to zero artifically. By this proposed scheme the largest precentage errors will be confined to conditions when the fluxes are small and therefore relatively unimportant.

7.3 Semicomprehensive Methods

a. Approximations

Between the poor-man's method and the truly comprehensive method of Lumley and Kahjeh-Nouri lie a number of possibilities for more or less simplified methods for modeling exchange. Whether such simplified methods are necessary or sufficient for the needs of the regional model is not readily apparent, and may not be definitely known until a truly comprehensive method has been perfected and applied in a way that can provide comparisons. It is possible, however, to subject semicomprehensive methods to rigorous tests in the atmospheric surface layer where the behavior of the various turbulent fluctuations statistics has been well observed.

Parameterizations similar to those to be described in this section have been used by Deardorff (1972) and by Wyngaard et al. (1973) to predict the distribution of fluctuation statistics in the planetary boundary layer. Wyngaard, and to a lesser extent, Deardorff, have used surface layer observations to provide values of the constants used in the integration. Neither author appears to have tested his method in detail within the surface layer itself, and throughout the planetary boundary layer, the needed quantities for verification of these methods are not generally known from observations.

The method to be discussed below is one of several that have been tried; it is also the most comprehensive one, and the one that was most successful in predicting the surface layer moments. It is incomplete in that all of the flux-divergence terms, some of which are known to be important, have been neglected. This shortcoming has been to a large extent removed in experiments now underway, but these have not yet been completed.

In addition to the neglect of the flux-divergence terms, it is assumed that the surface layer is horizontally homogeneous and, in a steady mean state. The equations (1), (2), and (3) yield the following set, after eliminating $\bar{\varepsilon}$ with the use of the energy equation.

$$\frac{1}{\rho_o}\left[\overline{w\frac{\partial p}{\partial x}} + \overline{u\frac{\partial p}{\partial z}}\right] = -\sigma_w^2\frac{\partial U}{\partial z} + \frac{g}{\bar{\theta}}\overline{u\theta'} \tag{17}$$

$$\frac{2}{\rho_o}\overline{w\frac{\partial p}{\partial z}} = \frac{2}{3}\overline{wu}\frac{\partial U}{\partial z} + \frac{4}{3}\frac{g}{\bar{\theta}}\overline{w\theta'} \tag{18}$$

$$\bar{\varepsilon} = -\overline{wu}\frac{\partial U}{\partial z} + \frac{g}{\bar{\theta}}\overline{w\theta'} \tag{19}$$

$$\frac{1}{\rho_o}\overline{\theta'\frac{\partial p}{\partial x}} = -\overline{w\theta'}\frac{\partial U}{\partial z} - \overline{uw}\frac{\partial\bar{\theta}}{\partial z} \tag{20}$$

$$\frac{1}{\rho_o}\overline{\theta'\frac{\partial p}{\partial z}} = -\sigma_w^2\frac{\partial\bar{\theta}}{\partial z} + \frac{g}{\bar{\theta}}\overline{\theta'^2} \tag{21}$$

$$\bar{\varepsilon}_\theta = -\overline{w\theta'}\frac{\partial\bar{\theta}}{\partial z} \tag{22}$$

b. Parameterizations

As in the poor-man's method we shall use a Rotta type parameterization of the pressure-correlation terms. However, in view of the presence of distinctly anisotropic modes of turbulence, it is possible that better expressions for the relaxation time can be found.

The regional-scale model being considered is characterized by a large horizontal grid length. The vertical grid-dimension is, by contrast, at least an order of magnitude smaller. Since the dimensions of the horizontal grid-scale eddies, if they exist, are so much larger than the vertical scale, it does not seem that this scale should be relevant in determining the relaxation time for the return to isotropy. At the same time the velocities of the horizontal modes are less likely to be relevant for the same reason. It seems, therefore, that a more reasonable measure of the relaxation time relevant to the vertical transfer should be ℓc_w^{-1} rather than ℓq^{-1}, with ℓ being identified with the vertical scale of the eddies, which would correspond to a small multiple of the vertical grid separation, at most.

Accordingly, we introduce the following expressions

$$\frac{1}{\rho_o}\left[\overline{u\frac{\partial p}{\partial z}} + \overline{w\frac{\partial p}{\partial z}}\right] = c_m \ell^{-1} \sigma_w \overline{wu} - \beta_m \sigma_w^2 \frac{\partial U}{\partial z} \qquad (23)$$

in which c_m is some constant to be determined empirically.

$\beta_m \sigma_w^2 \partial U/\partial z$ is an expression for the Lilly-Crow compensation term. Crow has pictured this term as an effect of the stretching of "vortex springs" by the deformation field of the mean flow. Each vortex filament, supposed to be randomly oriented in an isotropic turbulence field, is associated with a negative pressure disturbance. When the fluid is stretched in one direction, the vortices whose axes lie in this direction suffer a further depression of their pressures and thus give an elastic resistance to the deformation. The elastic response to this stretching of "vortex springs" is, at the same time, being destroyed by the scrambling effect of the turbulence over a time interval proportional to ℓq^{-1} or, in this case, perhaps better, $\ell^{-1} \sigma_w$. For isotropic turbulence β_m is 3/5, but is value for typical surface-layer anisotropies is not known at the present time.

In like manner, one obtains

$$2 \overline{w \frac{\partial p}{\partial z}} = c_m \ell^{-1} \sigma_w (\sigma_w^2 - \frac{1}{3} q^2) \tag{24}$$

The shear compensation term for this equation depends only on the tangential components of the anisotropic stress tensor, and is too small to be important. Lumley has recently suggested that this pressure-correlation term contains a part that modifies the buoyancy term very slightly.

In a similar manner, one obtains

$$\overline{\theta' \frac{\partial p}{\partial x}} = c_h \ell^{-1} \sigma_w \overline{u\theta'} \tag{25}$$

and

$$\overline{\theta' \frac{\partial p}{\partial z}} = c_h \ell^{-1} \sigma_w \overline{w\theta'} - \beta_h \frac{g}{\theta} \overline{\theta'^2} \tag{26}$$

The compensation term for the heat flux pressure-correlation may be pictured as arising in the following way. Consider, in Figure 1, a single Fourier mode of the vertical temperature distribution. At A and A' the buoyant forces are upward while at B, B', etc. they are downward. The result is to create positive pressure fluctuations at b, b', etc. and negative fluctuations at a, a', etc. Thus negative temperature fluctuations are associated with negative values of $\partial p/\partial z$ and vice versa. According to Deardorff (1973) this effect was first quantitatively evaluated for isotropic turbulence by Taulbee in a private communication. For isotropic turbulence, β_w is 1/3.

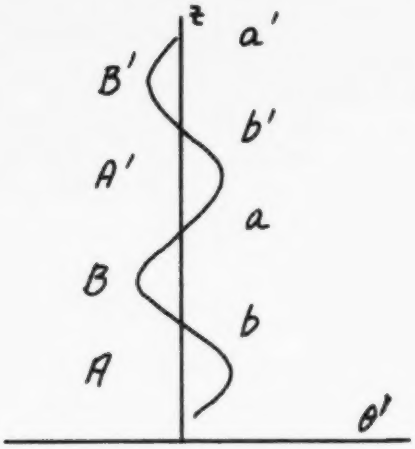

Fig. 1 BUOYANCY COMPENSATION.

The dissipation term in (22) may be written, at least for isotropic fields, as

$$\varepsilon_\theta = 6\gamma \frac{\overline{\theta'^2}}{\lambda_\theta^2} \qquad (27)$$

where λ_θ is the Taylor microscale for temperature fluctuations (see Tennekes and Lumley, 1973, p. 96). In the absence of a flux-divergence of θ'^2, this term must be of the same order of magnitude as the gradient-production term, which is of order $\sigma_w \overline{\theta'^2}/\ell$. We may thus arrive at the result

$$\varepsilon_\theta = \frac{c_\theta \sigma_w}{\ell} \overline{\theta'^2} \tag{28}$$

where c_θ is some constant to be determined empirically. Similar reasoning suggests the relation

$$\varepsilon = c_E \sigma_w q^2/\ell \tag{29}$$

where c_E is another constant to be derived from observations.

The parameterizations described here enable us to arrive at a closed set of six diagnostic equations for the turbulent moments, applicable to steady-state, horizontally homogeneous situations. These equations ar

$$c_m \ell^{-1} \sigma_w \overline{wu} = - \alpha_m \sigma_w^2 \frac{\partial U}{\partial z} + \frac{g}{\bar{\theta}} \overline{u\theta'} \tag{30}$$

$$c_m \ell^{-1} \sigma_w (\sigma_w^2 - \frac{1}{3} q^2) = \frac{2}{3} \overline{wu} \frac{\partial U}{\partial z} + \frac{4}{3} \frac{g}{\bar{\theta}} \overline{w'\theta'} \tag{31}$$

$$c_h \ell^{-1} \sigma_w \overline{u\theta'} = - \overline{wu} \frac{\partial \bar{\theta}}{\partial z} - \overline{w\theta'} \frac{\partial U}{\partial z} \tag{32}$$

$$c_h \ell^{-1} \sigma_w \overline{w\theta'} = - \sigma_w^2 \frac{\partial \bar{\theta}}{\partial z} + \alpha_h \frac{g}{\bar{\theta}} \overline{\theta'^2} \tag{33}$$

$$c_\theta \ell^{-1} \sigma_w \overline{\theta'^2} = -2\, \overline{w\theta'} \frac{\partial \bar{\theta}}{\partial z} \tag{34}$$

$$c_E \ell^{-1} \sigma_w q^2 = -\overline{wu} \frac{\partial U}{\partial z} + \frac{g}{\bar{\theta}} \overline{w\theta'} \tag{35}$$

c. Application to regional models

Although the parameterization described above has not yet been incorporated into the regional model, such incorporation appears to be quite simple to do. The set can be simplified considerably by algebraic substitution and reduced to a dependence on a single parameter that can be furnished at each time step by the model.

Elimination of $\overline{\theta'^2}$ between (33) and (34) gives

$$-\overline{w\theta'}/\frac{\partial \bar{\theta}}{\partial z} = K_h = \frac{\ell \sigma_w}{c_h} \left(1 + \frac{2\ell^2 \alpha_h}{c_\theta\, \sigma_w^2} \frac{g}{\bar{\theta}} \frac{\partial \bar{\theta}}{\partial z}\right)^{-1} \tag{36}$$

Thus a generalized exchange coefficient of the type suggested by simple mixing length theory results from these equations. Even though the relation between σ_w and $\partial\bar{\theta}/\partial z$ has not yet been determined, it is clear that with lapse conditions K_h is larger than with inversion conditions. The equation suggests the non-dimensional form

$$k_h = K_h/\ell\sigma_w = \frac{1}{c_h} \left(1 + \frac{2s\ \alpha_h}{c_h\ c_\theta}\right)^{-1} \tag{37}$$

where the parameter s defined by

$$s = \frac{\ell^2}{\sigma_w^{\ 2}} \frac{g}{\bar{\theta}} \frac{\partial\bar{\theta}}{\partial z} \tag{38}$$

is calculable at each grid point at the conclusion of any time step.

Using (30) and (32) we proceed similarly to eliminate $\overline{u\theta'}$ with the result

$$\frac{c_m \sigma_w}{\ell} \left(1 + \frac{s}{c_m c_h}\right) \overline{wu} = - \sigma_w^{\ 2} \left(1 - \frac{k_h s}{c_h}\right) \frac{\partial U}{\partial z} \tag{39}$$

Thus the Reynolds stress is proportional to the shear of the mean motion and we can define a momentum transfer coefficient

$$k_m = \frac{K_m}{\sigma_w \ell} = \frac{1}{c_m} \left(1 - \frac{k_h s}{c_h}\right) / \left(1 + \frac{s}{c_h c_m}\right) \tag{40}$$

In order to obtain σ_w, q must be eliminated between (31) and (35). The result is

$$\begin{aligned} 3c_E c_m \sigma_w^{\ 2} &= (c_m - 2c_E)\ k_m \ell^2 \left(\frac{\partial U}{\partial z}\right)^2 \\ &\quad - (c_m + 4c_E) \frac{g}{\bar{\theta}} k_h \ell^2 \frac{\partial\bar{\theta}}{\partial z} \end{aligned} \tag{41}$$

which suffices for obtaining σ_w since k_m and k_h are already known. The original set of six equations is thus reduced to a set of thee explicit algebraic equations that can be evaluated sequentially.

The most important difficulty in this procedure is that at the initial time s cannot be determined unless σ_w is given at each point. To overcome this difficulty it may be expedient to retain the time derivative and advective terms in (41) and to simply guess at the initial σ_w distribution. It is reasonable to expect that the state of turbulence will lose its dependence on the initial state over a period comparable to $\sigma_w{}^2/\bar{\varepsilon}$.

If other statistics are desired they can be calculated from the equations. For example, the Richardson number is obtainable from

$$Ri = (c_m - 2c_E)\ k_m s/[(4c_E + c_m)\ k_h s + 3c_E\ c_m] \tag{42}$$

We may note that as s → ∞, Ri approaches the limit

$$Ri_c = (c_m - 2c_E)\ (2\alpha_m\ \alpha_h\ c_h - c_\theta)/[(c_m + 4c_E)\ c_\theta + 6c_E\ c_m\ \alpha_h] \tag{43}$$

a quantity which observations indicate to be about 1/4.

d. Application to the surface layer

Although the application of the method to predictive models appears to be quite straightforward, it makes sense first to apply it in the surface layer for two reasons. First, the wealth of empirical knowledge of this layer provides an opportunity for a critical test of the parameterization, which has so far been only partially justified. Secondly, comparison of the derived equations with emprical data provides values of c_m, c_θ, c_h, and c_E that are needed for more general application.

The success of the empirically based similarity theory suggests that it would be useful to attempt to nondimensionalize the equations by scaling ℓ by the Monin length

$$L = - \frac{\bar{\theta} \; \overline{(-wu)}^{3/2}}{kg \; \overline{w\theta'}} \tag{44}$$

The definition (38) of s gives

$$s = \frac{1}{kk_h} x^3 \zeta \tag{45}$$

where

$$x = u_*/\sigma_w \tag{46}$$

$$u_*^2 = - \overline{wu} \tag{47}$$

and

$$\zeta = \ell/L \tag{48}$$

It is useful here to treat as the independent parameter a quantity defined as

$$p = x^3 \zeta \tag{49}$$

We then obtain, by transformation of (37), (40), and (41), the set

$$k_h = \frac{1}{c_h} \left(1 - \frac{2\alpha_h p}{k\ c_\theta}\right) \tag{50}$$

$$k_m = \frac{c_h k\ \alpha_m - p}{k c_h c_m + p/k_h} \tag{51}$$

and

$$x^4 = \left(\frac{u_*}{\sigma_w}\right)^4 = \frac{k_m}{k(c_m - 2c_E)} \left[3kc_E c_m + p\ (c_m + 4c_E)\right] \tag{52}$$

To complete the set it is necessary to adopt an appropriate assumption for ℓ. Experience in the surface layers has shown that the largest flux-supporting eddies are proportional in size to the height. With no loss of generality we can make the coefficient of proportionality equal to unity since the values of c_m, c_h, c_θ, and c_E have yet to be determined. Accordingly, we have from (49)

$$\frac{z}{L} = p/x^3 \tag{53}$$

The set of four equations (50) through (53) thus permit k_h, k_m, and σ_w/u_* to be calculated as functions of z/L.

The equation set (30) to (35) permits other functions to be calculated as well. After some reduction one can obtain

$$\frac{\sigma_\theta}{T_*} = \left(\frac{2}{c_\theta k_h}\right)^{1/2} \frac{u_*}{\sigma_w} \tag{54}$$

where

$$T_* = -\overline{w\theta'}/u_* \tag{55}$$

$$-\frac{\overline{u\theta'}}{\overline{w\theta'}} = \frac{1}{c_h} \left(\frac{1}{k_h} + \frac{1}{k_m}\right) \frac{u_*^2}{\sigma_w^2} \tag{56}$$

and

$$\frac{q^2}{u_*^2} = \frac{1}{c_E} \left[\frac{u_*^2}{k_m \sigma_w^2} - \frac{u_*\zeta}{k\sigma_w}\right] \tag{57}$$

Additional derived quantities may also be calculated, such as

$$\phi_m = \frac{kz}{u_*} \frac{\partial U}{\partial z} = \frac{k}{k_m} \frac{u_*}{\sigma_w} \tag{58}$$

$$\phi_h = \frac{kz}{T_*}\frac{\partial\bar{\theta}}{\partial z} = \frac{k}{k_h}\frac{u_*}{\sigma_w} \qquad (59)$$

$$Ri = \frac{k_m^2}{kk_h}\frac{\sigma w}{u_*}\zeta \qquad (60)$$

Although p is the independent parameter, there are constraints imposed on the range of its values by the equations. The upper limit comes when k_h approaches zero, which then implies that k_m, u_*, and σ_w also become zero. This is the critical state. The negative limit of p is found when x goes to zero implying u_* approaching zero and $\sigma_w \neq 0$. We associate this limit with free convection. From (50) and (52) we thus observe

$$-\frac{3k\ c_E\ c_m}{c_m + 4c_E} \leq p \leq \frac{kc_\theta}{2\alpha_h} \qquad (61)$$

It is easily observed that the critical state condition is identical to the earlier condition that $s \to \infty$. The Richardson number associated with this state is given by (43).

Let us denote by the subscript L the limiting value under free convection. Thus

$$-p_L = \frac{3k\ c_E\ c_m}{c_m + 4c_E} \qquad (62)$$

One easily finds that both k_h and k_m have limiting values for free convection. From (53) we have

$$(\frac{\sigma_w}{u_*}) = a_w\,(\frac{z}{-L})^{1/3}; \qquad a_w = (-p_L)^{-1/3} \tag{63}$$

for free convection, a result that is in agreement with similarity theory. It follows immediately from (54) that σ_θ/T_* must approach $a_\theta(z/-L)^{-1/3}$ where a_θ is a predictable coefficient, again in accordance with similarity theory. Another prediction is that the total turbulent energy should satisfy

$$\frac{q^2}{u_*^2} = \frac{1}{kc_E}\,(-p_L)^{1/3}\,(\frac{z}{-L})^{2/3} \text{ and } \frac{q^2}{\sigma_w^2} = -\frac{p_L}{kc_E} \tag{64}$$

It has been found from experience, however, that the turbulent energy does not behave in this manner (which is also predicted by similarity theory); the discrepancy is believed to be due to the vertical transport of larger scale fluctuations into the surface layer from the free-atmosphere above.

Under conditions of free-convection, the well-known KEYPS equation reduces to

$$\phi_m = (\frac{\gamma z}{-L})^{-1/3} \tag{65}$$

This result also follows from (58) provided γ satisfies

$$\gamma = \frac{1}{-p_L}\,(\frac{k_m L}{k})^3 \tag{66}$$

The KEYPS equation has been largely replaced by an equation $\phi_m = (1 - 15z/L)^{-1/4}$ suggested by Businger as being more convenient to use and shown to satisfy the data from the Kansas 1968 Field Program. This equation gives ϕ_m a different limiting behavior than predicted from the present theory. It must, however, be kept in mind that the range of observed values of z/L was quite limited, and that over the observed range the observations were also well fitted by the KEYPS equation with $\gamma = 9$.

Finally, we can verify Priestley's equation for the heat flux with free-convection

$$\overline{w\theta'} = h \left(\frac{g}{\bar{\theta}}\right)^{1/2} z^2 \left(- \frac{\partial\theta}{\partial z}\right)^{3/2} \tag{67}$$

and find

$$h = \left(\frac{k k_{hL}^{3}}{-P_L}\right)^{1/2} \tag{68}$$

For the determination of the constants c_m, c_h, c_θ, and c_E in our experiments, only the neutral state has been utilized. The selection of the neutral state was made for two reasons. First, under neutral conditions the neglect of the vertical flux-divergence of u_*, σ_w, heat, and energy can be justified, leading one to have some confidence that the calculated constants are universal. Secondly, the application of empirical relations is particularly simple in this case.

The following expressions were used. These follow from (50), (51), (52), and (54) using well known empirical relationships for neutral conditions.

$$c_m = \frac{\alpha_m}{k} \left(\frac{\sigma_w}{u_*}\right)_N \tag{69}$$

$$c_h = \left(\frac{K_m}{K_h}\right)_N \frac{c_m}{\alpha_m} \tag{70}$$

$$c_\theta = 2c_h / \left[\frac{\sigma_w}{u_*} \frac{\sigma_\theta}{T_*}\right]^2_N \tag{71}$$

$$c_E = c_m / \left[3\alpha_m \left(\frac{\sigma_w}{u_*}\right)^4_N + 2\right] \tag{72}$$

The four constants thus depend on three observed quantities, σ_w/u_*, k_m/k_h, and σ_θ/T_* for neutral conditions, plus α_m. The last has a value of 2/5 for isotropic conditions, but its value for the anisotropic conditions in the surface layer is not currently known.

For the experiment described here, the value 2/5 was used for α_m. An even better over-all fit was achieved using a value of .55. It may be noted however, that a value of 1.0, which would be equivalent to ignoring the vortex-spring stretching completely, led to a totally unacceptable prediction of the effects of instability on the turbulent statistics. The values of the four constants are invariant with respect to α_h.

The following values were adopted from an analysis of the AFCRL Kansas field experiment data published by Izumi (1971). It was assumed that k = .40; a different value would have led to somewhat different values of each of the constants, but would not have affected the predicted values of the statistics in any way.

$$\left(\frac{\sigma_w}{u_*}\right)_N = 1.30 \qquad \left(\frac{\sigma_\theta}{T_*}\right)_N = 2.60 \qquad \left(\frac{K_h}{K_m}\right)_N = 1.18 \qquad (73)$$

The constants were then found to be

$$c_m = 1.30 \qquad c_h = 2.76 \qquad c_\theta = .484 \qquad c_E = .240 \quad (74)$$

Deardorff (1972) and Wyngaard et al. (1973) have evaluated constants of a similar nature. However, it is not possible to compare these values with either of the others. The main reason is that σ_w rather than q was used in the Rotta parameterization.

The value of α_h for isotropic conditions should be 2/3; its value for anisotropic conditions in the surface boundary layer is not known. In general the value 2/3 did not work very well and a value of 1.0 was used instead. This question requires clarification, and it is noted that Lumley (personal communication) has recently developed functional expansions for the buoyancy compensation that are expected to be very helpful in fixing this quantity.

The use of these constants in the various equations leads to quantitative predictions about the limiting behavior of various fluctuation statistics for free-convection that can be compared with observations. This comparison is given in Table 1.

Figures 2 to 7 show predicted functions of z/L in comparison with observations reported by Izumi (1971) for the AFCRL Kansas Field Experiment. It is interesting that although ϕ_m deviates systematically from the observed values, the calculated values of ϕ_m are in general indistinguishable from those calculated from the KEYPS equation

$$\phi_m^{\,4} - \gamma \frac{z}{L} \phi_m^{\,3} = 1 \qquad (75)$$

with $\gamma = 10.36$ to three significant figures over the entire negative range of z/L.

The agreement of most predictions is acceptable for unstable conditions with the exception of $-\overline{u\theta'}/\overline{w\theta'}$. The predictions of $q^2/\sigma_w^{\,2}$ are also not very realistic - a fact already discussed. The predictions for the stable side are generally unacceptable. A part of the failure may be due to the obviously unacceptable association of ℓ with z under stable conditions. [The critical Richardson number prediction is independent of this assumption.] Other causes of the failure may be due to changes of α_m and α_h as the anistropy tends toward rather extreme states.

Table 1

Comparison of Predicted and Observed Constants

Column three values were reported by Businger et al. (1971) and Wyngaard et al. (1971) for the AFCRL Kansas Field Experiments. Column 4 indicates values reported by other sources.

Statistics	Predicted	Observed	
		Kansas	Other
$(\sigma_w/u_\star)_N$	1.30[1]	1.15 - 1.4[2]	0.7 - 1.4
$(\sigma_\theta/T_\star)_N$	2.60[1]	2.9	~2.5
$(K_m/K_h)_N$	.85[1]	.74	~1.
R_{ic}	.48	.21	~1/4
a_w	1.82	1.9	1.9 - 2.8
a_θ	1.13	.95	~1.
γ	10.4	9.	9 - 15
h	1.5		0.6 - ~2
$[-\frac{\overline{u'\theta'}}{\overline{w'\theta'}} / (\frac{u_\star}{\sigma_w})^2]_L$	1.12		1.0[3]
$(K_h/K_m)_L$	~2.		2.05

---

1. Assumed values

2. Higher value is that approached from stable side.

3. Value predicted from the automatic correlation hypothesis, eq. (9).

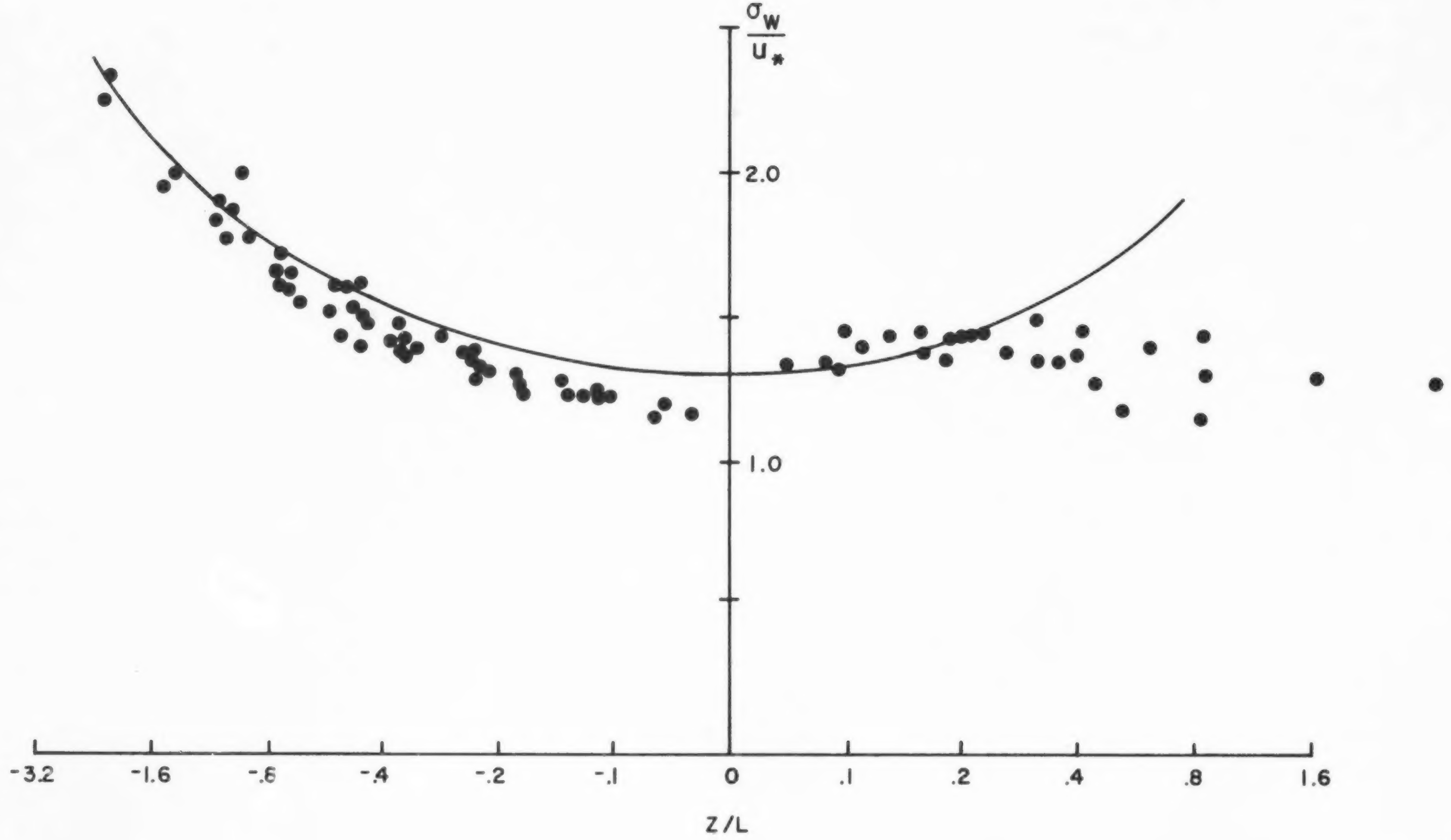

FIGURE 2: COMPARISON OF PREDICTED RELATION BETWEEN σ_w/u_* AND Z/L WITH OBSERVATIONS FROM THE AFCRL KANSAS 1966 FIELD PROGRAM.

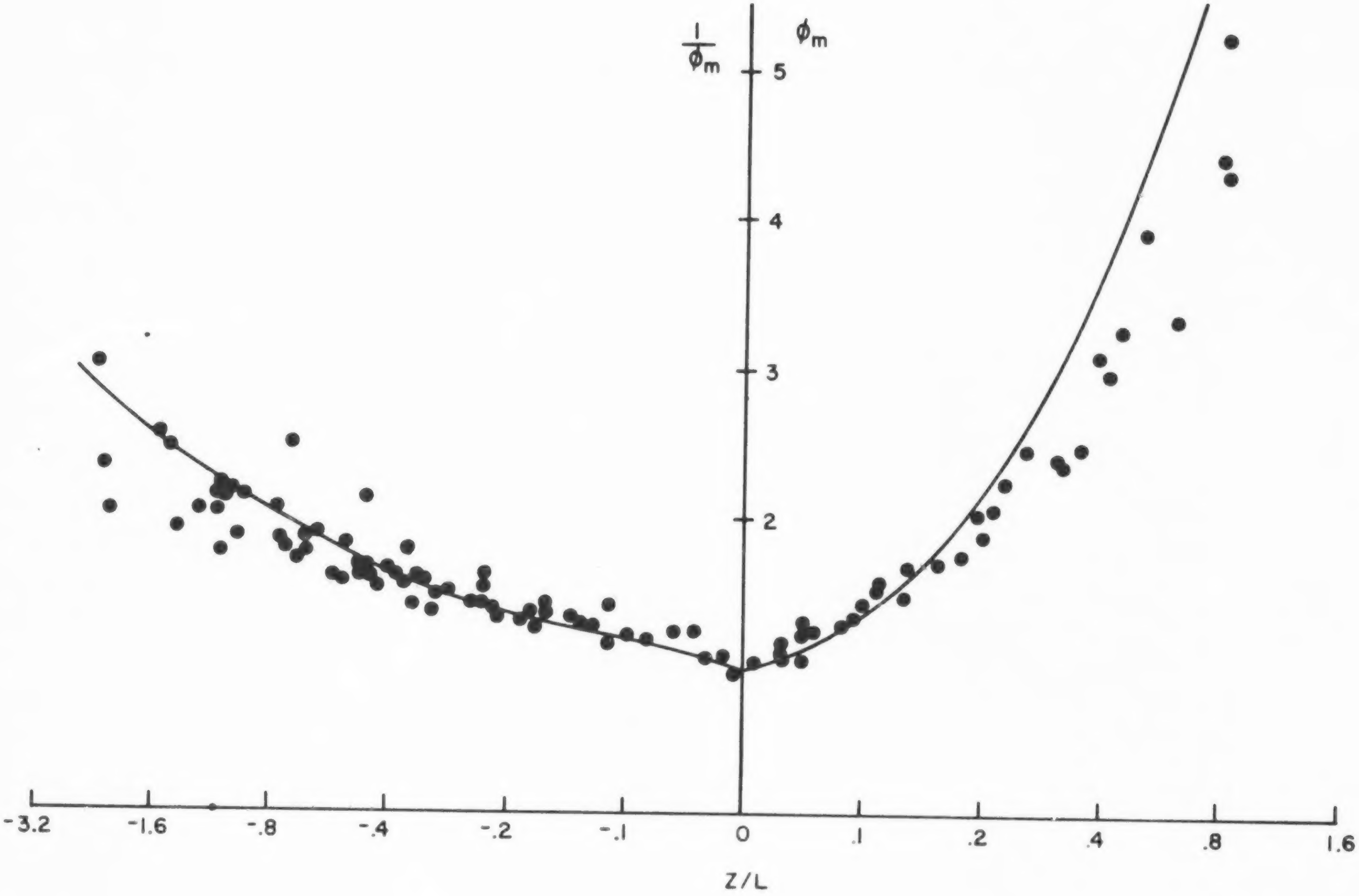

FIGURE 3 : COMPARISON OF PREDICTED RELATION BETWEEN $1/\phi_m$ (UNSTABLE SIDE) OR ϕ_m (STABLE SIDE) AND Z/L WITH OBSERVATIONS FROM THE AFCRL KANSAS 1968 FIELD PROGRAM.

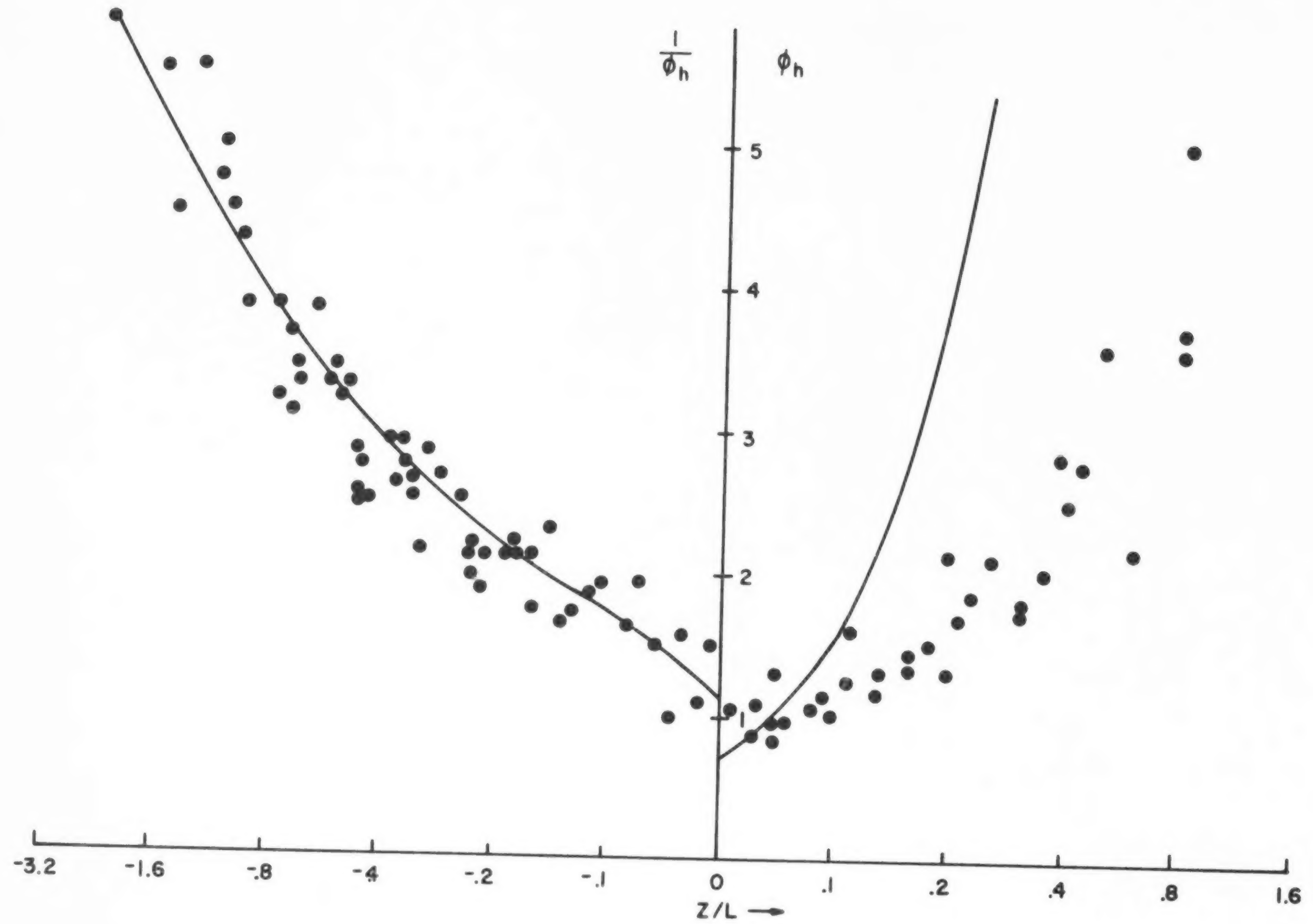

FIGURE 4 : COMPARISON OF PREDICTED RELATION BETWEEN $1/\phi_h$ (UNSTABLE SIDE) OR ϕ_h (STABLE SIDE) AND Z/L WITH OBSERVATIONS FROM THE AFCRL KANSAS 1968 FIELD PROGRAM.

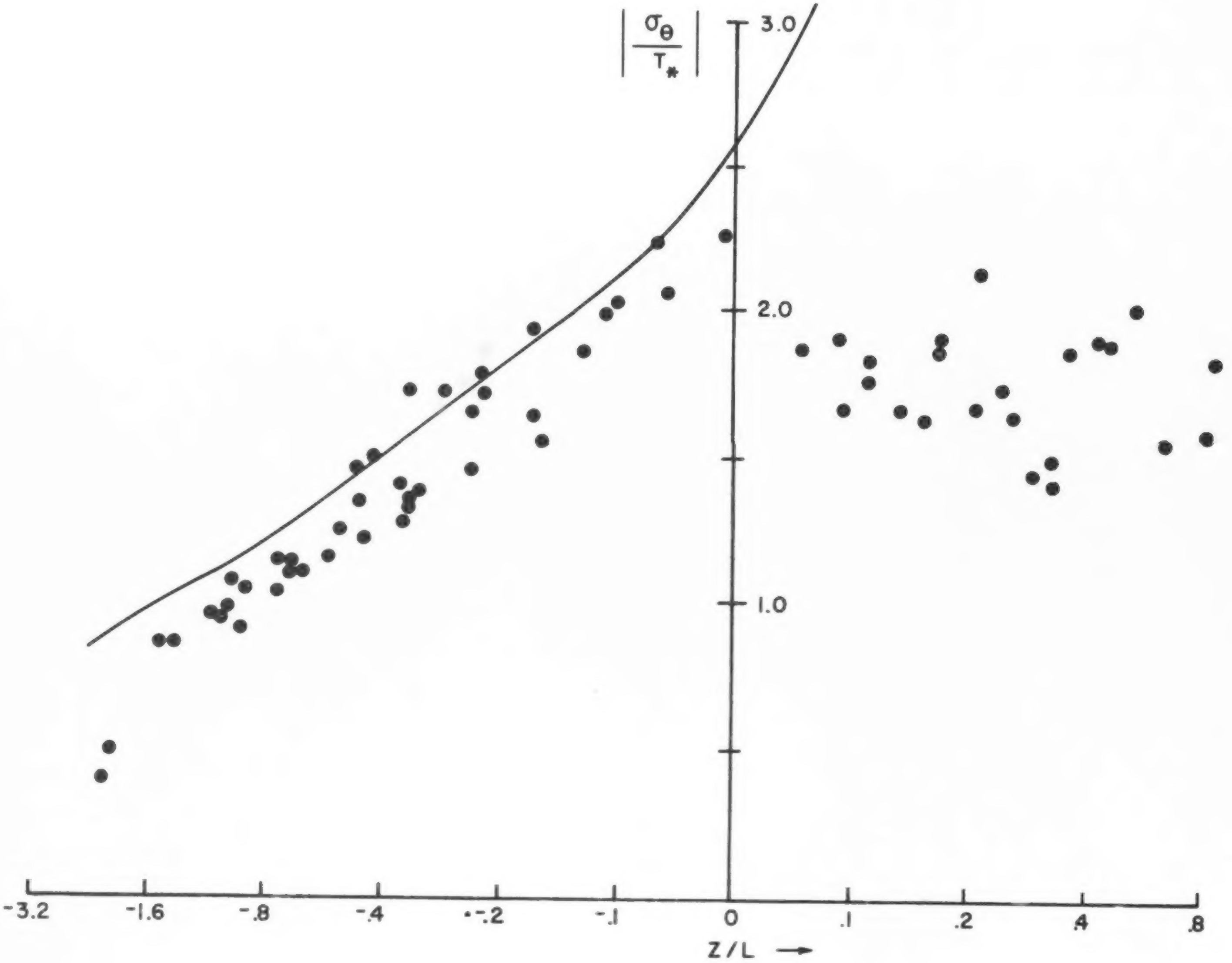

FIGURE 5: COMPARISON OF PREDICTED RELATION BETWEEN $|\sigma_\theta / T_*|$ AND Z/L WITH OBSERVATIONS FROM THE AFCRL KANSAS 1968 FIELD PROGRAM.

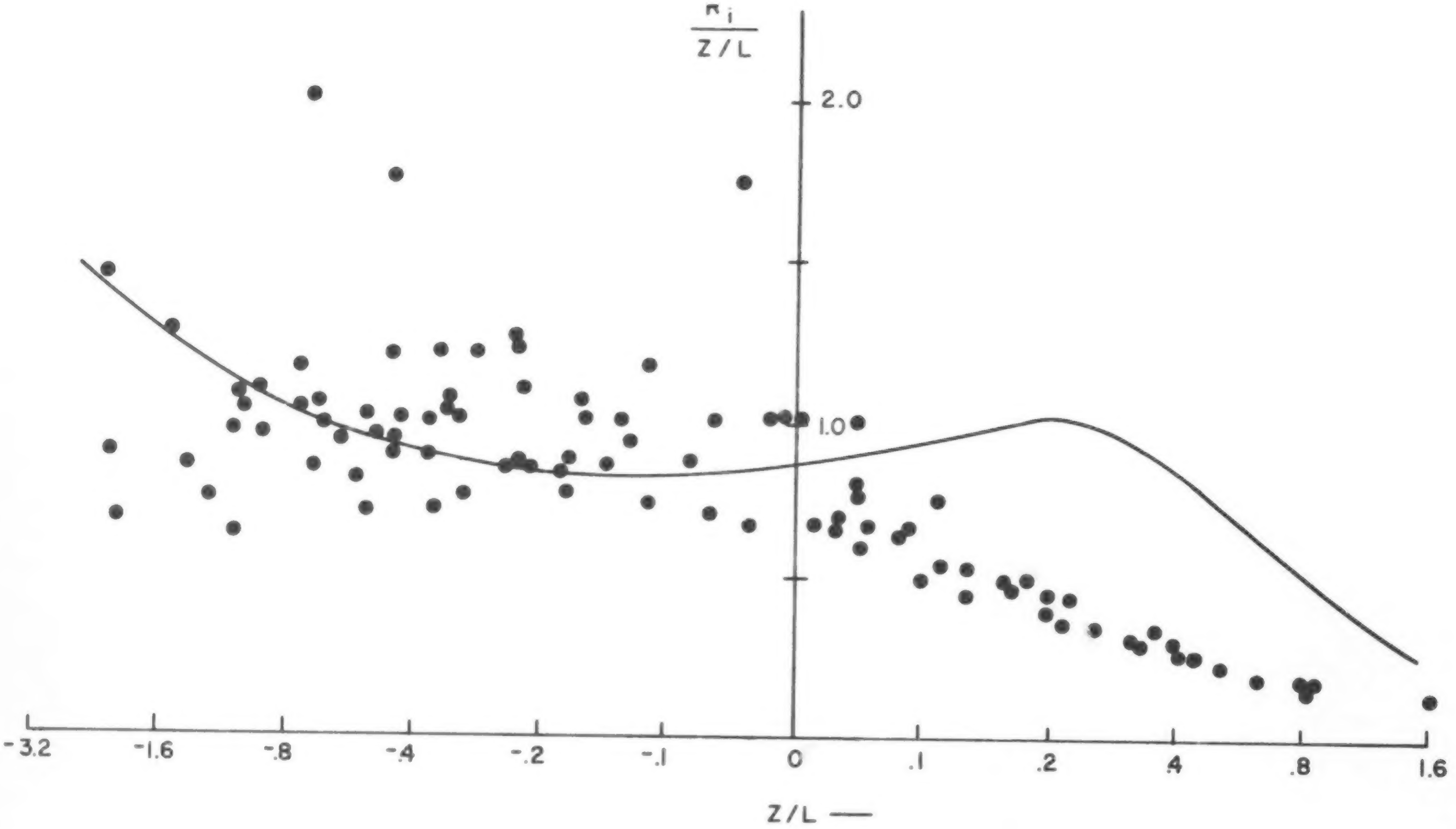

FIGURE 6 : COMPARISON OF PREDICTED RELATION BETWEEN R_i / (Z/L) AND Z/L WITH OBSERVATIONS FROM THE AFCRL KANSAS 1968 FIELD PROGRAM.

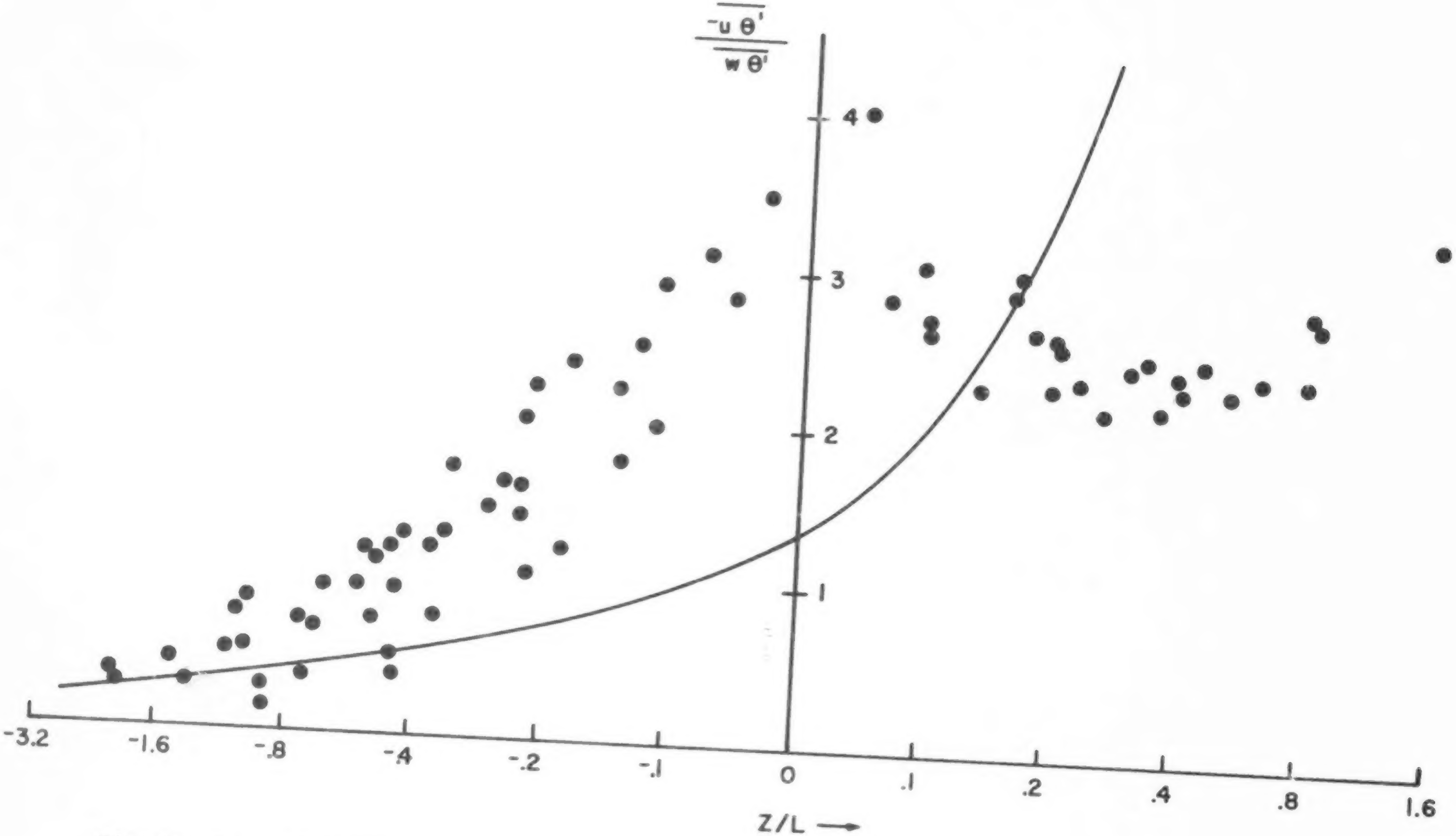

FIGURE 7: COMPARISON OF PREDICTED RELATION BETWEEN $-\overline{u\theta'}/\overline{w\theta'}$ AND Z/L WITH OBSERVATIONS FROM THE AFCRL KANSAS 1968 FIELD PROGRAM.

It is indeed surprising to find such good agreement between predicted and observed free-convection statistics when one reflects on the large effects that the neglected flux-divergence terms might be expected to have under these conditions. These terms have been reasonably well observed for the energy and vertical velocity variances. There are good reasons to think that the flux divergence is also important in the $\overline{u\theta'}$ equation. Work is currently in progress to include these terms in the surface layer verification. At the same time, it is hoped that more acceptable estimates of α_m and α_h can be obtained by application of Lumley's work.

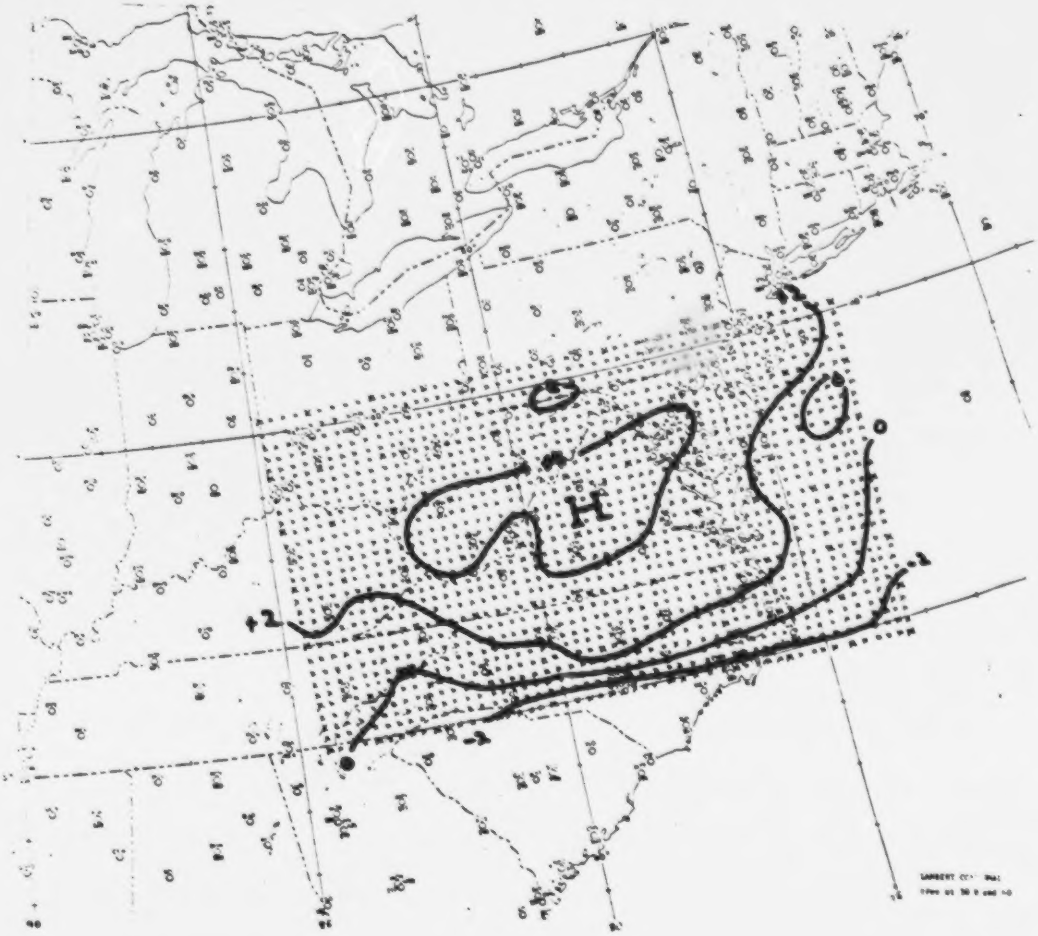

Figure 3.8 Forecast 12-hour surface pressure change (mb) for Exp. 1 ending 00Z Oct. 17, 1973

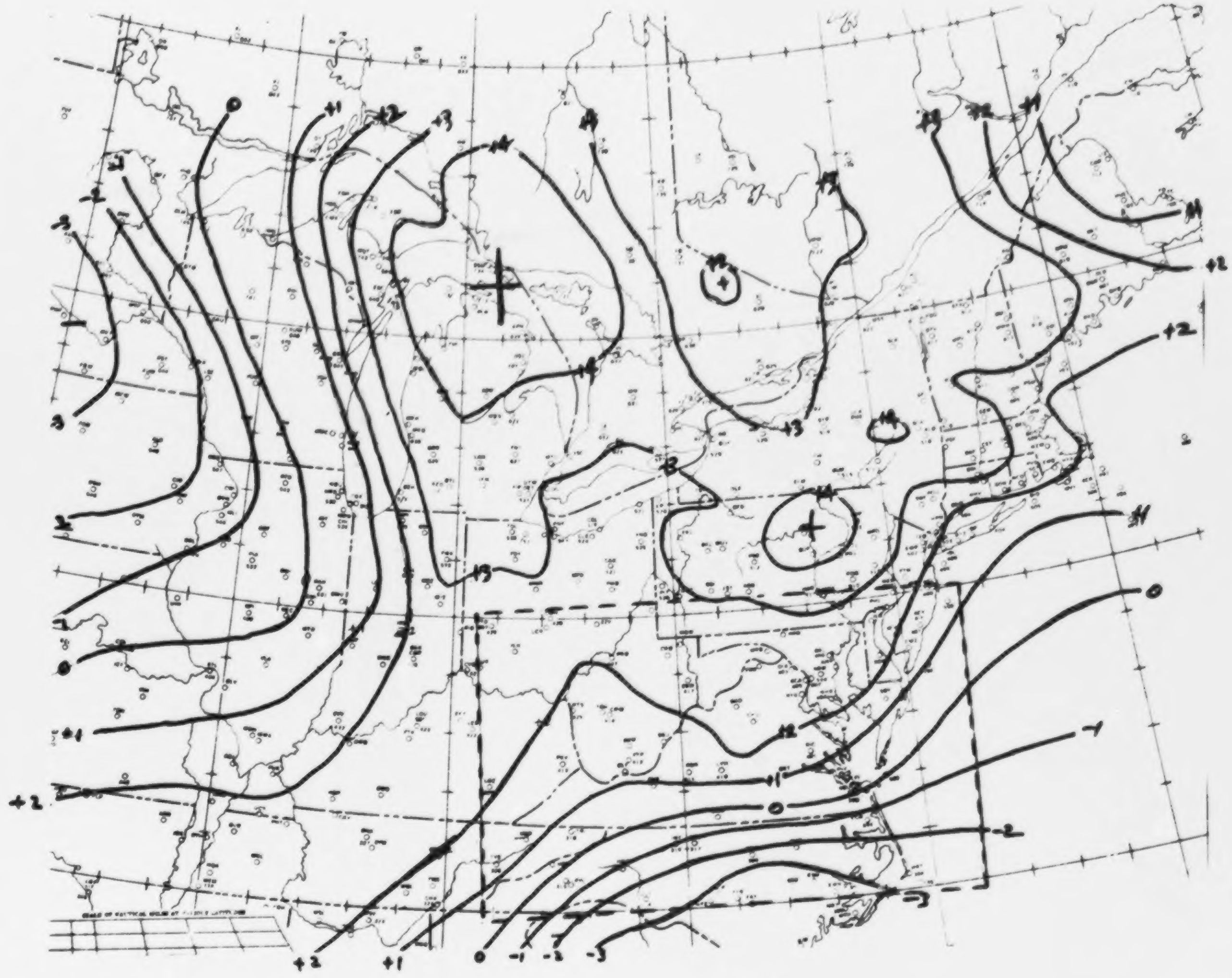
0
+1
+2
-1
-2
-3
+2
+1
0
-1
-2
-3

Figure 3.9 Observed 12-hour surface pressure change (mb) ending 00Z Oct. 17. 1973

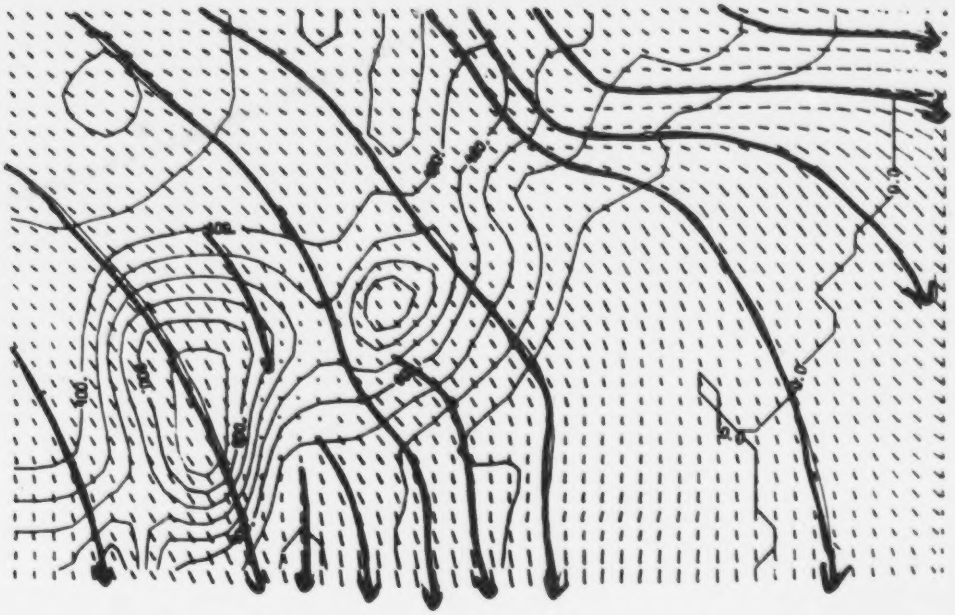

Figure 3.10 Twelve-hour forecast velocities at level 6 ($\sigma = 0.925$, $\bar{p} = 939$ mb) from Exp. 1. Contours of terrain are labeled in m.

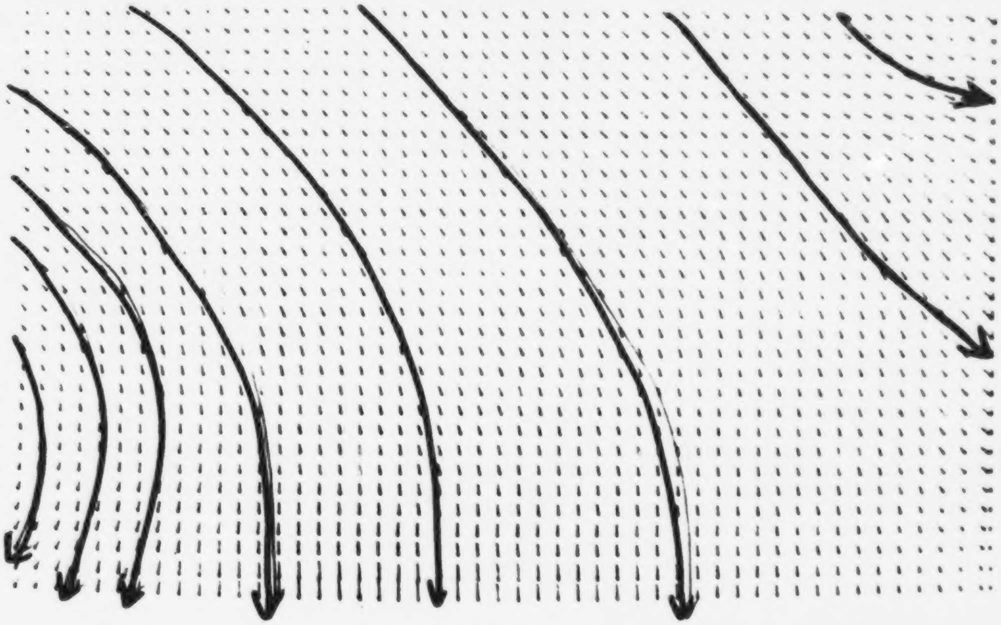

Figure 3.11 Twelve-hour forecast velocities at level 6 ($\sigma = 0.925$, $\bar{p} = 929$ mb) from Exp. 1A, no terrain

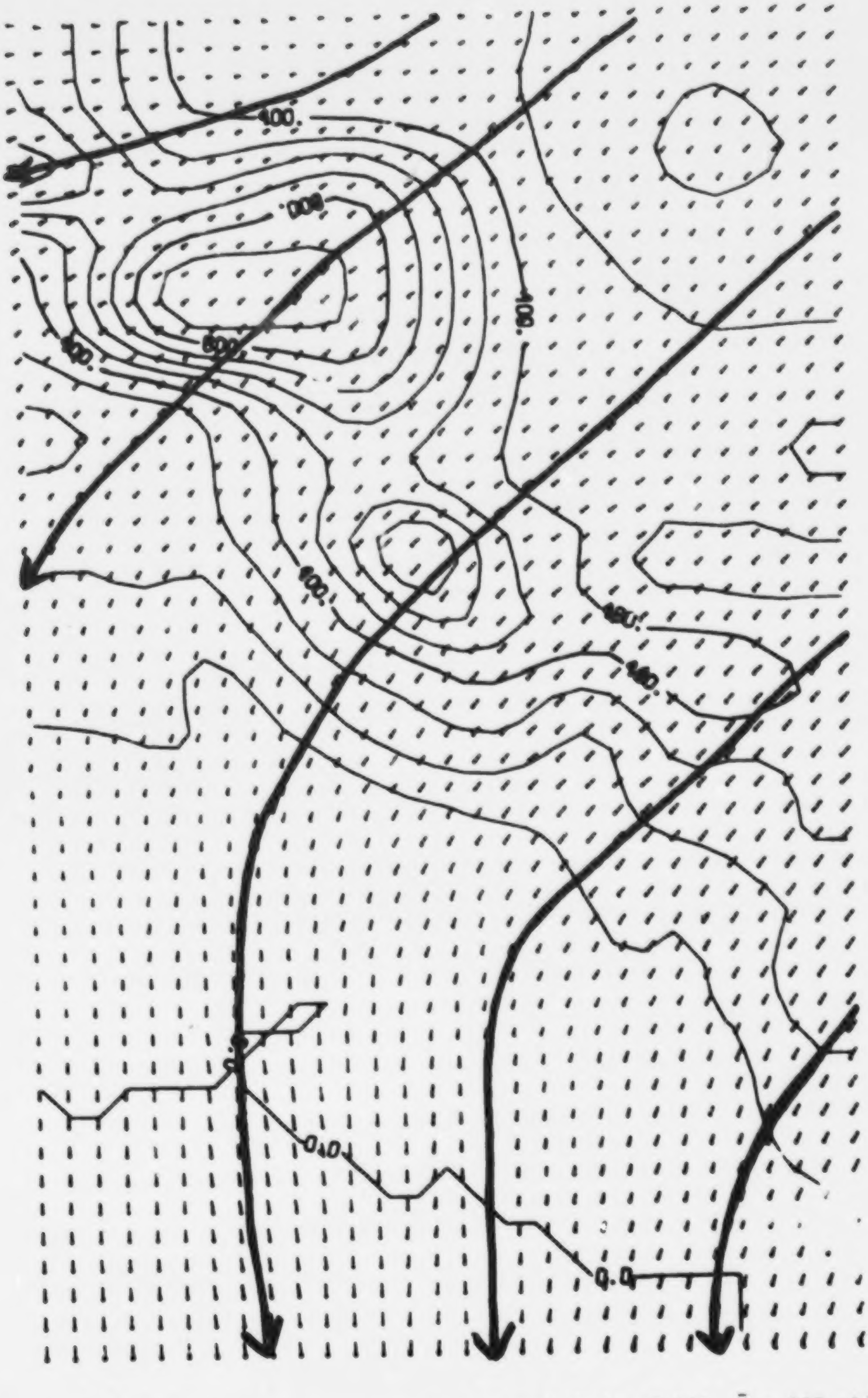

Figure 3.12 Verification velocities at level 6 (σ =0.925, $\bar{p}$ = 929 mb) from interpolation of synoptic analysis to mesoscale grid

more northerly in the low levels in agreement with the observed tendency for stronger northerly winds. However, both experiments overemphasize the magnitude of the northerly winds, especially near the southern boundary, where northerly components approach 15 ms^{-1}. These speeds are much stronger than the observed surface velocities. This error is related to the erroneous pressure change discussed earlier; the north-south pressure gradient is too strong. A second reason may be the weak effect of surface friction caused by the small value of the drag coefficient. Nevertheless, the low-level winds do illustrate the effect of terrain, with the terrain (Exp. 1) producing a lee-side trough, especially in the northern half of the domain.

3.4.2 Middle level results. Under the influence of the vertically propagating gravity waves, the effect of terrain is strongly evident at middle as well as low levels. Figures 3.13 and 3.14 show the 12-hour forecast flow at level 4 ($\bar{p}$ = 709 mb) in Exps. 1 and 1A. Without terrain the flow is smooth with a broad trough traversing the domain. With terrain, however, a sharp mesoscale trough appears in the lee of the Appalachians. This perturbation is so strong that the wind at several grid points is reduced nearly to zero.

Because of the low vertical resolution there are undoubtedly serious phase and amplitude errors in the vertically propagating waves. However, these experiments show that the mesoscale terrain variations are capable of producing mesoscale perturbations to the flow which can be resolved by the model in a stable 12-hour forecast. For improved accuracy, the model could, of course, be run with more layers.

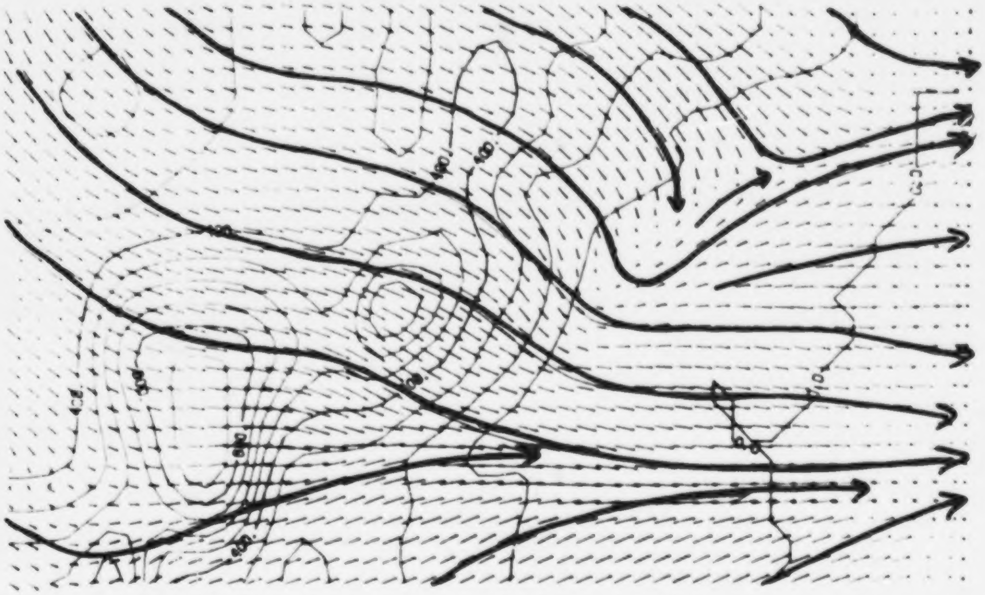

Figure 3.13 Twelve-hour forecast velocities at level 4 ($\sigma = 0.625$, $\bar{p} = 709$ mb) from Exp. 1

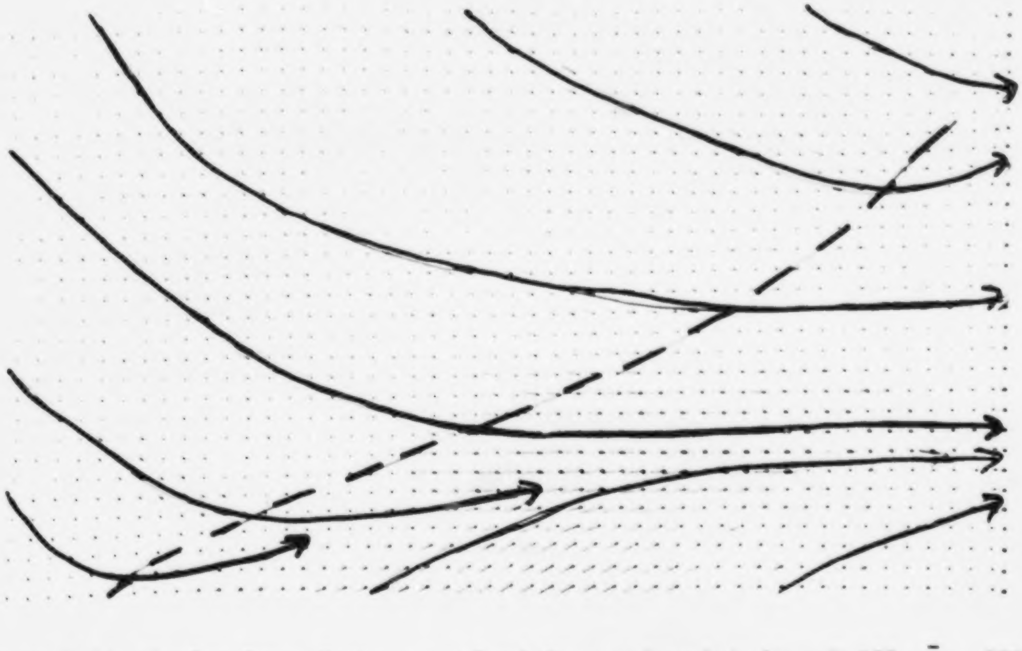

Figure 3.14 Twelve-hour forecast velocities at level 4 ($\sigma = 0.625$, $\bar{p} = 709$ mb) from Exp. 1A, no terrain

3.4.3 Upper level results. Finally, the upper level flow (level 2, $\bar{p} = 489$ mb) is shown in Figures 3.15 and 3.16. Even at this level, the terrain has produced a noticeable distortion in the large-scale flow. Also notable in Figures 3.15 and 3.16 is the smoothness of the flow in spite of the strong winds (60 m/s) blowing across the boundaries.

The temperature change field (Figure 3.17) in Exp. 1A at level 2 ($\bar{p} = 489$ mb) illustrates the southward propagation of the observed intense baroclinic zone and shows how the time-dependent boundary conditions affect the temperature. On the whole, the temperature forecast is reasonable, except near the eastern (outflow) boundary where $2\Delta x$ noise is apparent. This noise is caused by the overspecification of the temperatures on the outflow boundary and the subsequent upstream propagation of the short-wavelength advective temperature waves. This noise could, of course, be reduced by using a higher value for horizontal diffusion or by occasionally smoothing the temperature forecasts in space. However, this noise is preferable to the alternative of extrapolating the temperature outward to the boundary from the interior, in which case the errors in temperature along the boundary adversely affect the inner motion on the grid through the processes described in Section 2.6. The effect of terrain on the temperature forecast at all levels is to perturb the large-scale temperature field by several degrees Celsius. Figure 3.18 illustrates the temperature perturbations for level 2 in Exp. 1 with terrain for comparison with Figure 3.17.

3.5 Budget equations for the model domain and the implications of the lateral boundary conditions

In the previous section, a sample of the 12-hour forecast results in experiments with and without terrain were presented. The results,

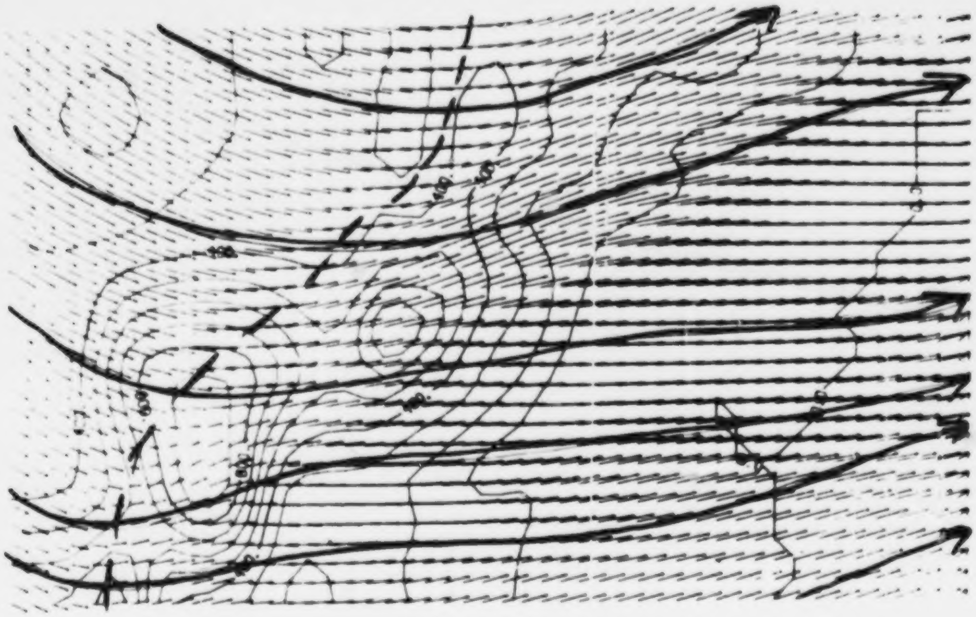

Figure 3.15 Twelve-hour forecast velocities at level 2 ($\sigma = 0.325$, $\bar{p} = 489$ mb) from Exp. 1

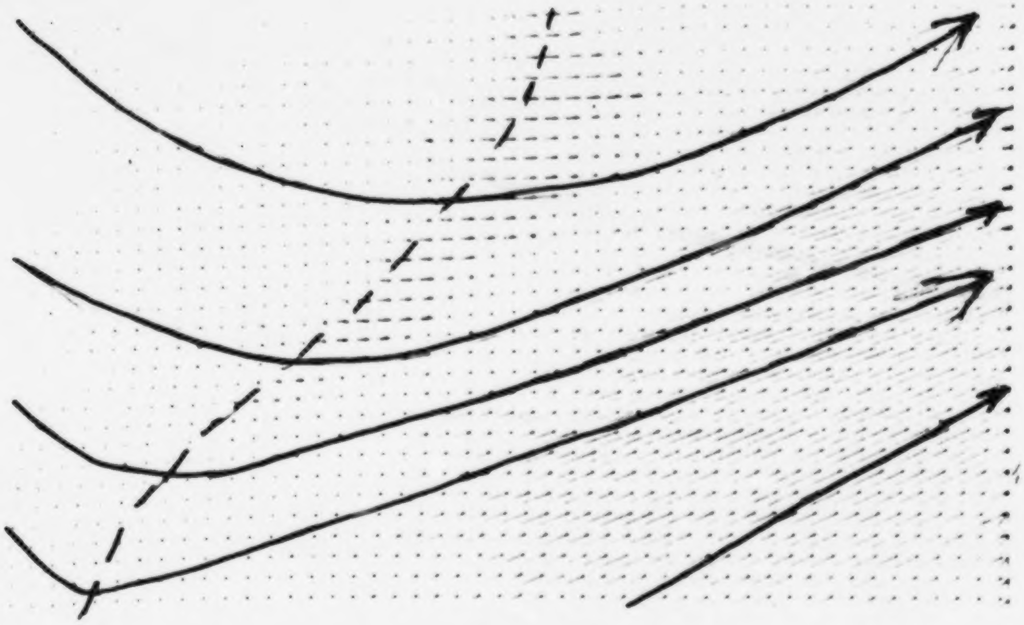

Figure 3.16 Twelve hour forecast velocities at level 2 ($\sigma = 0.325$, $\bar{p} = 489$ mb) from Exp. 1A, no terrain

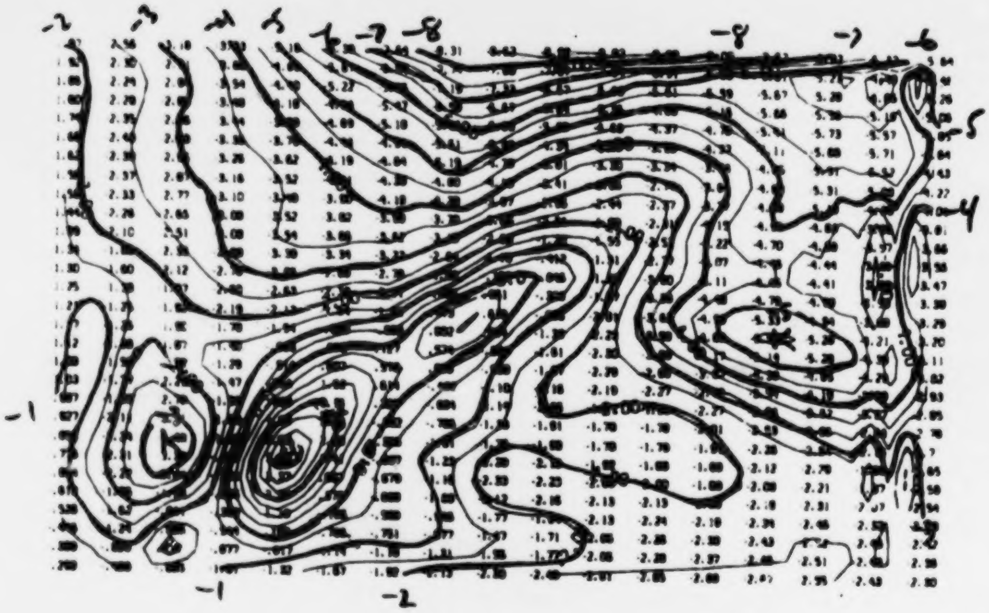
-2
-3
-4
-5
-6
-7
-8
-8
-7
-6
-5
-4
-1
-1
-2

Figure 3.17 Twelve-hour forecast temperature change at level 2 ($\bar{p}$ = 489 mb) from Exp. 1A, no terrain

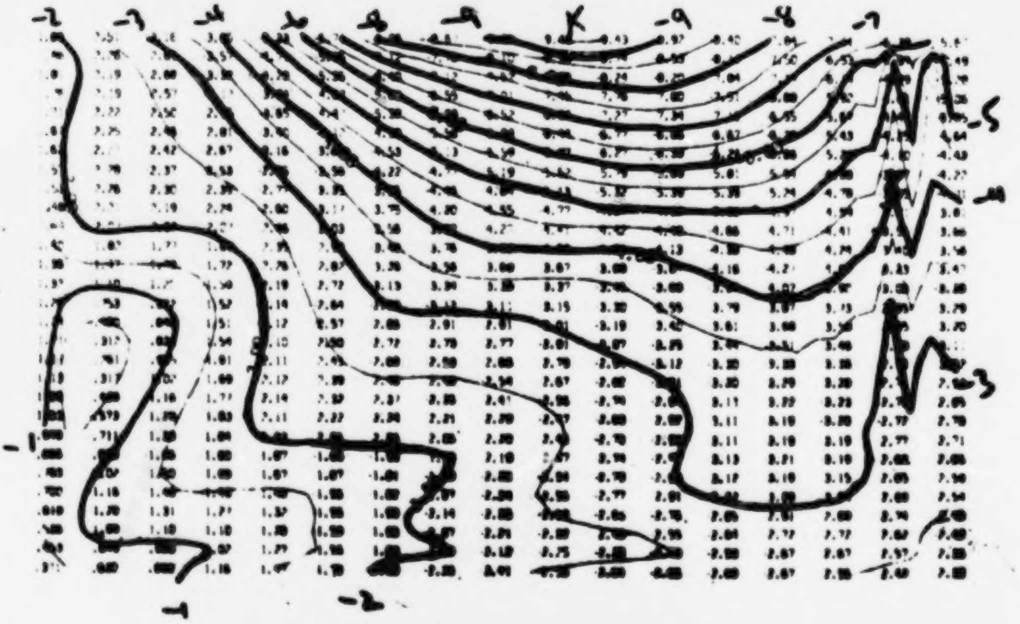
-2
-3
-4
-6
-8
-9
-10
-9
-8
-7
-5
-4
-3
-1
-1
-2

Figure 3.18 Twelve-hour forecast temperature change at level 2 ($\bar{p}$ = 489 mb) from Exp. 1, with terrain

while emphasizing the importance of terrain and the "smoothness" of the solutions, showed large accelerations in the mean motion at some of the levels, indicating that large-scale imbalances between the mass and momentum fields in the initial, and probably the boundary conditions, were producing a "sloshing" of the winds and temperatures over the domain. In this section we seek to explain these imbalances by an examination of the mean kinetic energy budget for the domain and the time-dependent behavior of the mean motion at various levels.

3.5.1 Mean kinetic energy budget for the 12-hour forecast period. The mean kinetic energy budget for the entire mesoscale domain provides an important check on the consistency of the model as well as gives some clues on the importance of the various processes in determining the mean motion.

The components of the kinetic energy budget (eq. (2.25)) for Exp. 1 and 1A are presented in Figure 3.19. The total kinetic energy tendency evaluated from the right side of (2.25) is shown for Exp. 1. As a check, a second budget is computed by mulitplying the left side of (2.15) and (2.16) (the actual tendencies used in the forecast) by u and v and integrating over the domain. The total budget from this method is labeled LS in Fig. 3.19. The difference between these two budgets is the uncertainty in evaluating the boundary flux of kinetic energy terms in (2.25). As shown by the close agreement of the two budgets, this uncertainty is small compared to the magnitude of the boundary flux terms.

Although the presence of terrain greatly affects the components of the generation of kinetic energy by cross-isobar flow, these two terms tend to cancel and the net effect is a similar total budget for

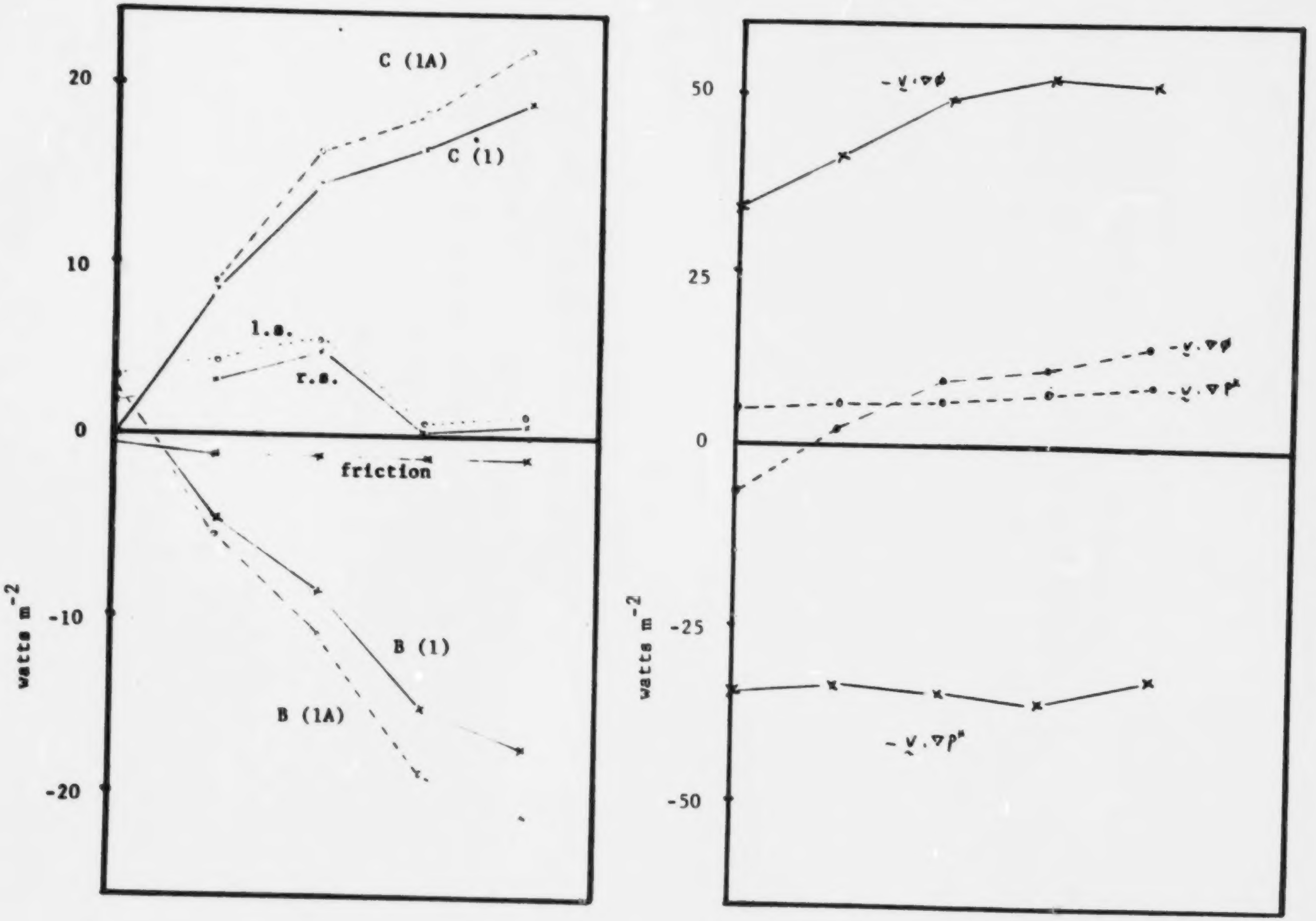

Figure 3.19 Components of kinetic energy budget from Exp. 1 and 1A

both experiments. (The net kinetic energy tendency for Exp. 1A would be nearly indistinguishable from the tendency plotted for Exp. 1 in Figure 3.19.) Thus the effect of terrain in this experiment is mainly to redistribute kinetic energy within the domain rather than to create or destroy large amounts of kinetic energy.

The striking feature in the kinetic energy budgets of both experiments is the near cancellation between the large, positive production of kinetic energy by cross-isobar flow and the large loss of kinetic energy through the non-linear, boundary flux terms. Frictional dissipation by horizontal diffusion and surface friction is very small compared to these two components. As discussed in Section 2.6, the acc^e^leration of the mean motion over the domain is strongly dependent on the lateral boundary conditions of mass and momentum. In the kinetic energy budget, we see this point again; the net loss of kinetic energy through the lateral flux of kinetic energy appears to be acting like friction, causing the winds to deflect toward low pressure and resulting in a large, positive generation of kinetic energy through cross isobaric flow. This point may be further illustrated by considering the behavior of the mean motion at various levels in the domain.

3.5.2 Time variation of the mean motion. Before presenting the results for the time variation of the mean motion at various levels over the domain, we present the solution for the mean equation of motion (2.28) and (2.29). With the definitions

$$B_u = - \frac{\overline{(u_E^2 - u_W^2)}^{L_y}}{L_x} - \frac{\overline{(uv)_N - (uv)_S}^{L_x}}{L_y}$$

$$B_v = - \frac{\overline{[(uv)_E - (uv)_W]}^{L_y}}{L_x} - \frac{\overline{(v_N^2 - v_S^2)}^{L_x}}{L_y}$$

$$\underset{\sim}{B} = B_u + i\, B_v \qquad (3.2)$$

$$\underset{\sim}{V} = \bar{u}^D + i\, \bar{v}^D$$

$$\underset{\sim}{V}_g = \overline{u_g}^D + i\, \overline{v_g}^D \quad ,$$

the equation of mean motion may be written

$$\frac{\partial \underset{\sim}{V}}{\partial t} = \underset{\sim}{B} - if\,(\underset{\sim}{V} - \underset{\sim}{V}_g) \quad . \qquad (3.3)$$

The complete solution to this equation with $\underset{\sim}{B}$ and $\underset{\sim}{V}_g$ equal to a constant is

$$\underset{\sim}{V}(t) = \underset{\sim}{V}_g - \frac{i\underset{\sim}{B}}{f} + [\underset{\sim}{V}^o - \underset{\sim}{V}_g + \frac{i\underset{\sim}{B}}{f}]\, e^{-ift}$$

This solution, which is pictured in Fig. 3.20, consists of an oscillation with the inertial period about the stationary solution, $\underset{\sim}{V}_g - i\underset{\sim}{B}/f$. If

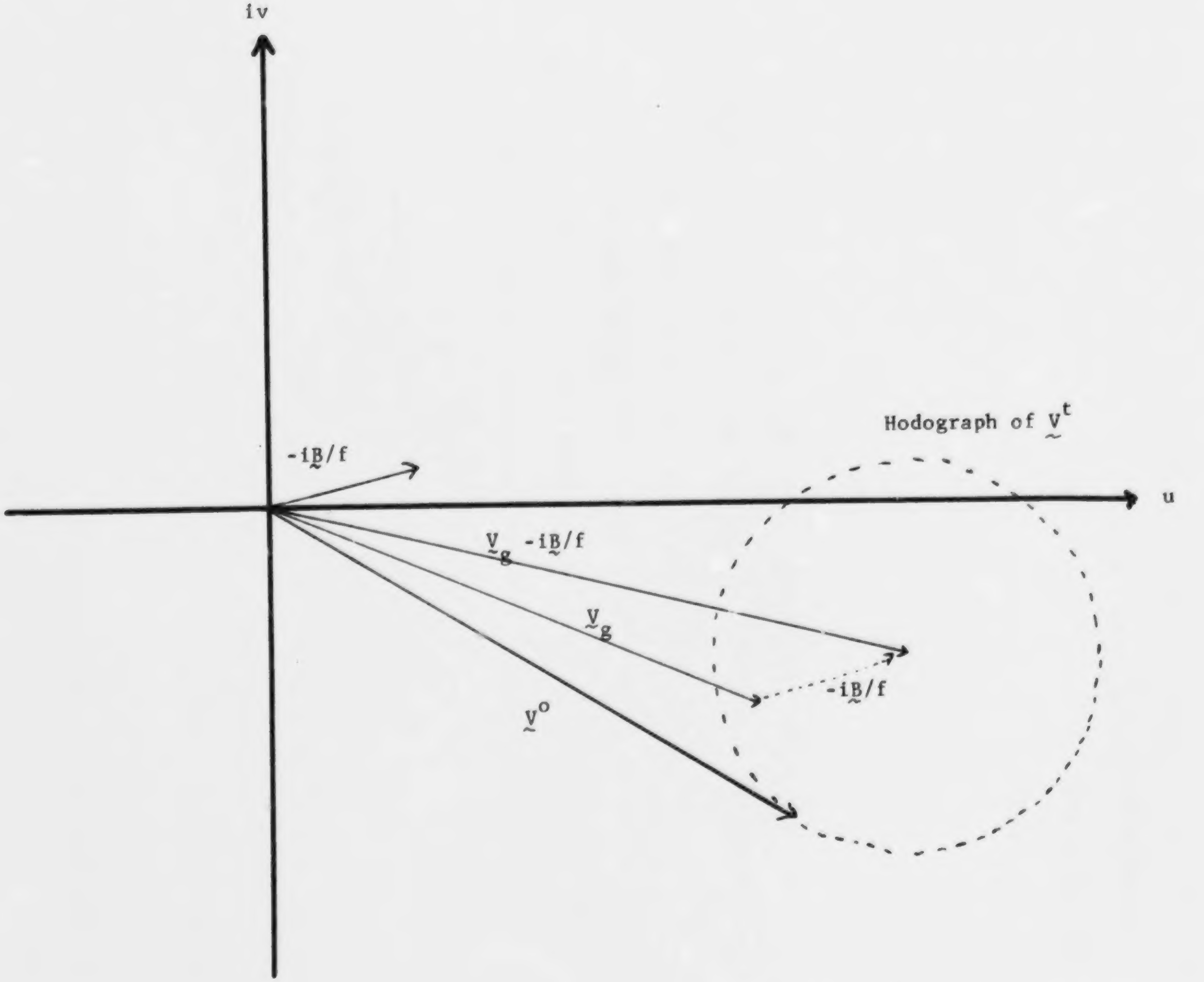
iv
u
$-i\underset{\sim}{B}/f$
Hodograph of $\underset{\sim}{V}^t$
$\underset{\sim}{V}_g - i\underset{\sim}{B}/f$
$\underset{\sim}{V}_g$
$-i\underset{\sim}{B}/f$
$\underset{\sim}{V}^o$

Figure 3.20 Solution of mean vector motion over domain for constant $\underset{\sim}{B}$ and $\underset{\sim}{V}_g$

the large scale motion is not in balance with the prescribed boundary conditions for mass ($\underset{\sim}{V}_g$) and momentum ($- i\underset{\sim}{B}/f$), the mean motion over the domain will undergo the oscillation indicated in Fig. 3.20. It is therefore desirable to minimize the departure from equilibrium, given by

$$[\underset{\sim}{V}^o - \underset{\sim}{V}_g + i\underset{\sim}{B}/f]$$

Fig. 3.21 shows the magnitude of the components B_u/f and B_v/f at the various levels as a function of time for Exp. 1A. In the upper levels this non-linear acceleration is very large, and verifies the crude analysis of Section 2.6. Only in the lowest two layers are the f-scaled, non-linear accelerations less than 3 ms^{-1}. In the upper layers, these scaled accelerations exceed 15 ms^{-1}, dominating the ageostrophic flow at these levels.

Although the boundary conditions for mass and momentum were not constant in time, so that $\underset{\sim}{V}_g$ and $\underset{\sim}{B}$ varied over the 12-hour period, the type of oscillation present in the simple solution with constant $\underset{\sim}{B}$ and $\underset{\sim}{V}_g$ is clearly present in the hodographs of the mean motion at the various levels. For example, Fig. 3.22 shows the values of $\underset{\sim}{V}_g$ and $-i\underset{\sim}{B}/f$, for the 12-hour period and the hodograph of the mean motion, $\underset{\sim}{V}^{(t)}$. During the 12-hour period the mean wind swings toward low pressure, producing the large generation of kinetic energy by the cross-isobar flow.

In the low-levels, the term $\underset{\sim}{B}/f$ is small, and the mean wind is observed to chase the time-dependent, mean geostrophic wind, as shown in Fig. 3.23. We see now why the low-level winds become too strong from

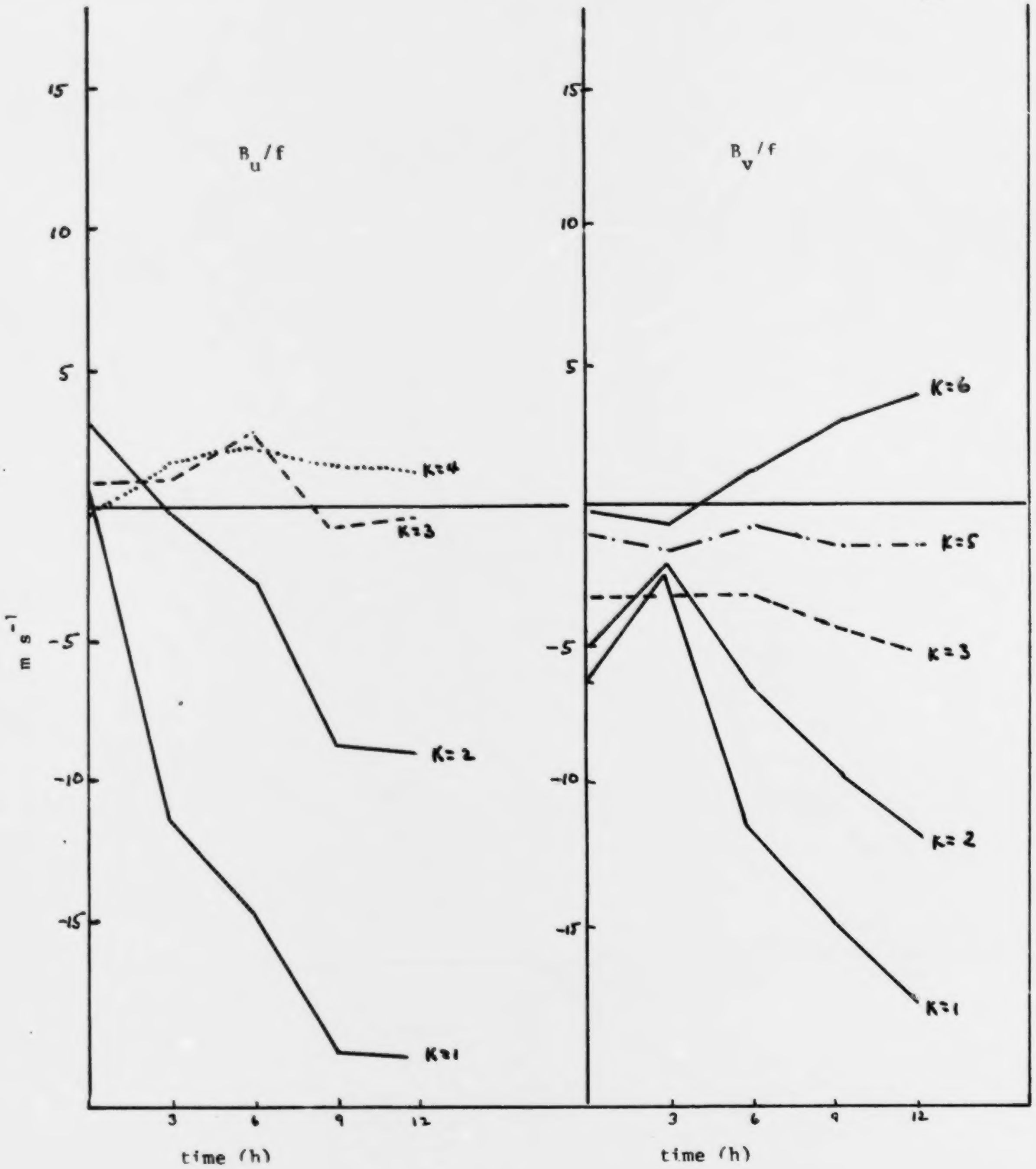

Figure 3.21 Components B_u/f and B_v/f (mean non-linear accelerations scaled by f) for Exp. 1A

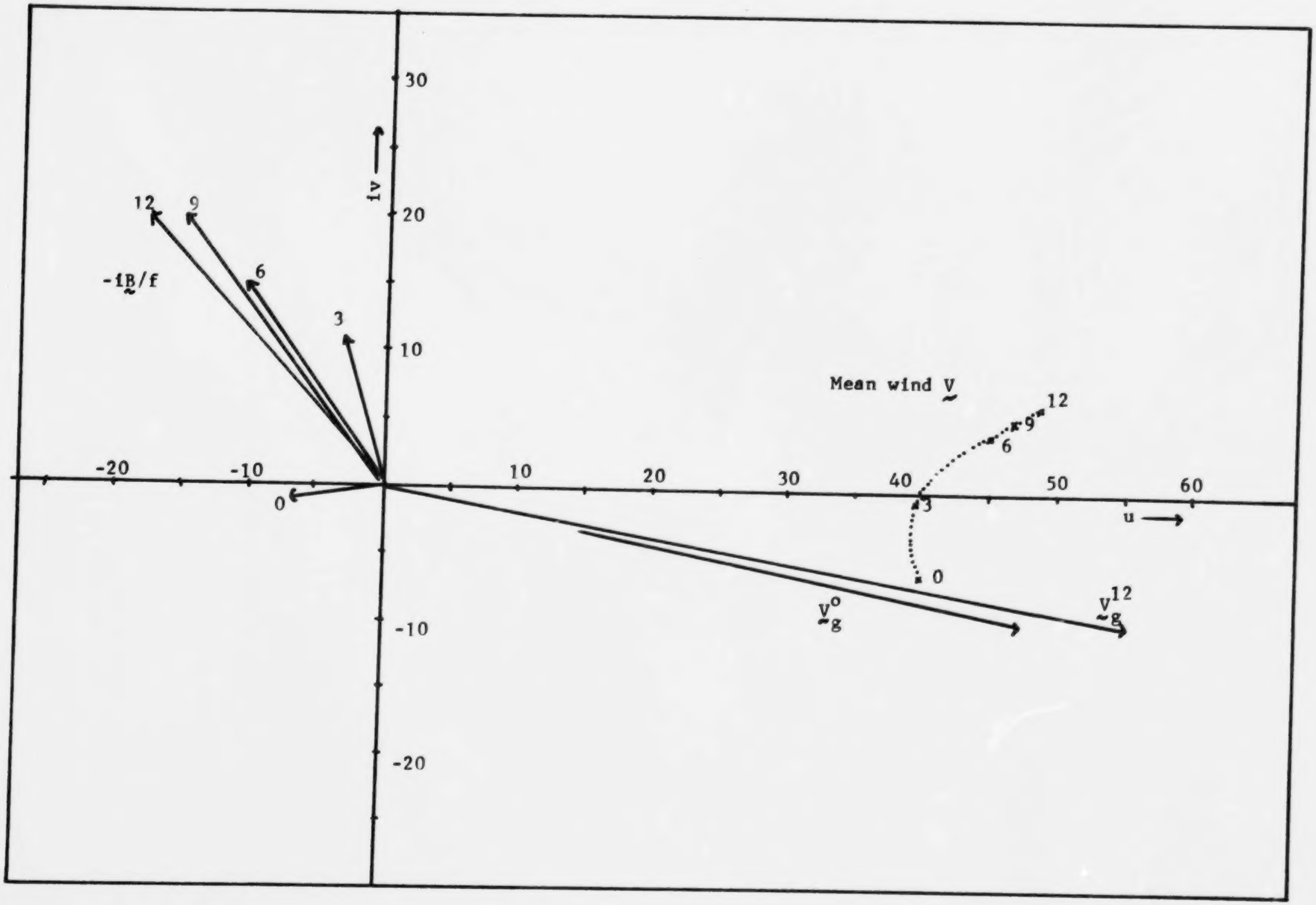

Figure 3.22 Hodographs of mean wind ($\underset{\sim}{V}$) , mean geostrophic wind ($\underset{\sim}{V}_g$) , and $-i\underset{\sim}{B}/f$ for various times in Exp. 1a at level 1 ($\bar{p}$=342 mb)

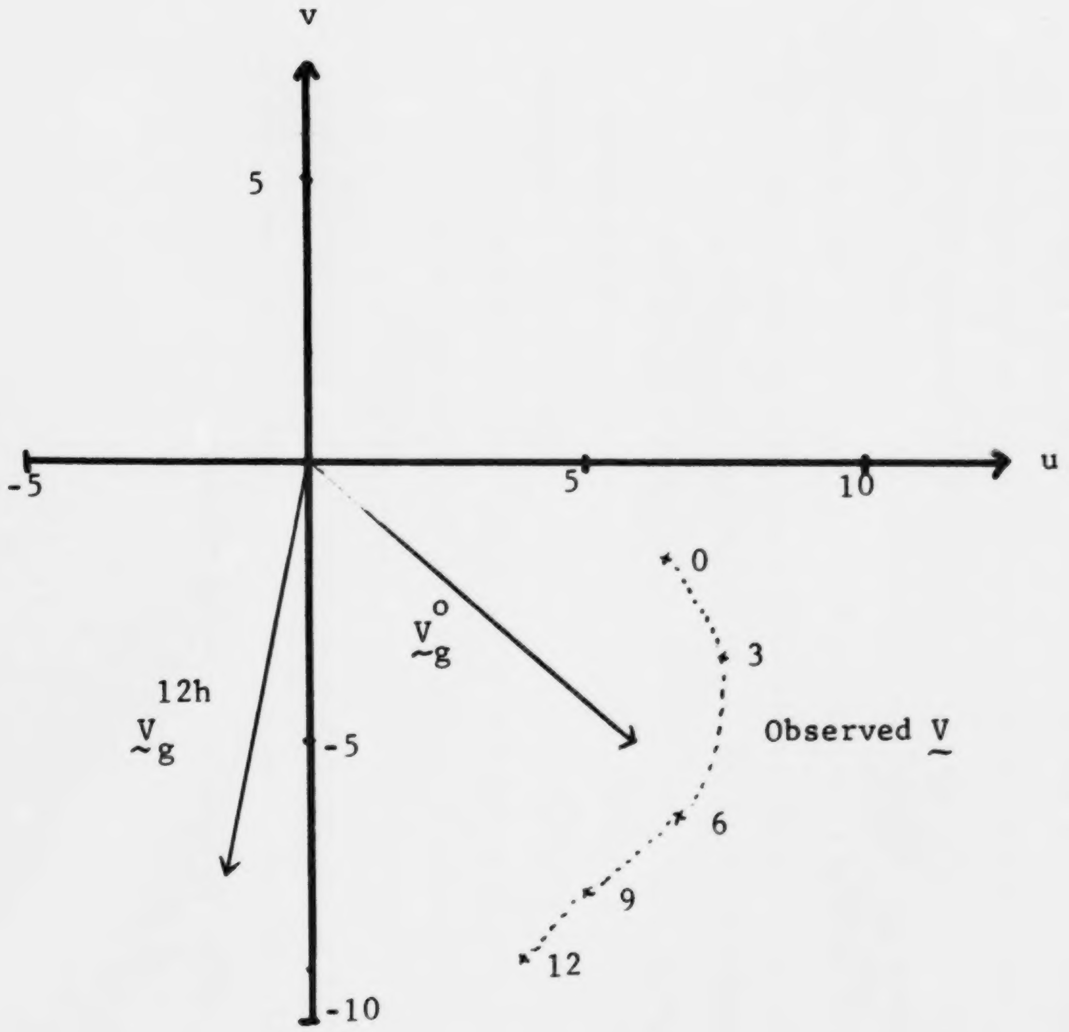

Figure 3.23 $\underset{\sim}{V}_g$ at t = 0 and t = 12 hours and hodograph of mean velocity, $\underset{\sim}{V}$ for 12-hour forecast, Exp. 1A

the north -- the mean geostrophic wind, specified through the boundary conditions on temperature and pressure, becomes strong northerly.

The conclusion from these results is that for mesoscale domains of order 1,000 km across, the boundary values of mass and momentum may produce very large accelerations in the mean flow over the domain. Unless proper care in the initialization and specification of the time-dependent boundary conditions is taken, the mean motion will undergo large oscillations which may completely ruin the mesoscale forecast. In contrast to large domains, therefore, boundary conditions which simply minimize the noise generated at the boundaries are not sufficient to guarantee realistic solutions on the interior of the domain. These results suggest that it is more important in the initialization and specification of lateral boundary conditions to make sure that the large-scale motions are balanced than to eliminate small-scale imbalances within the domain. Provided that the winds are initialized accurately, the small-scale mass imbalances will quickly adjust to the wind field. Large-scale imbalances, however, which are forced by the lateral boundary conditions, may adversely affect the solution for the entire forecast.

4.0 NUMERICAL EXPERIMENTS WITH A TWO-DIMENSIONAL NESTED GRID

The motivation for nesting a fine mesh within a larger mesh is obvious; the horizontal resolution in a numerical model may be concentrated where it is needed the most (e.g., over populated regions or over atmospheric phenomena which have sharp gradients and fine scales). Furthermore, by nesting a fine mesh model such as the regional model within a synoptic-scale model, some of the deleterious effects of the proximity of lateral boundaries to the center of interest may be avoided. On the other hand, additional computational difficulties may be expected where the grid meshes change size.

At least two approaches to the nested grid problem exist. In the first, and simplest, a large scale model is integrated independently of the fine mesh model, and the output from the coarse mesh model utilized to provide time-dependent boundary conditions for the fine mesh model. In the other approach, the model equations on the two (or more) meshes are integrated simultaneously so that two-way interactions are possible. Phillips and Shukla (1973) have argued from a theoretical point of view that the simultaneous, two-way interaction approach is preferable, and their arguments tend to be confirmed by the results of Harrison and Elsberry (1972).

However, the two-way interacting mode is considerably more difficult to treat within operational constraints, and it is apparent from some results (Hovermale, 1974) that a one-way interacting meshed model can produce very good results. Furthermore, in both cases the difference in computational phase speeds of waves on meshes of varying size produces problems along the interface. In the 2-way system, this noise can eventually contaminate both grids. In the 1-way system, of course, the noise cannot feed back to the coarse mesh. The problem of different phase speeds is aggravated as the ratio of course mesh grid (CMG) to fine mesh grid (FMG) increases. Indeed, it may turn out that for a ratio CMG/FMG of 2, the two-way interacting system is preferable, while for larger ratios (say 5 to 10), the one-way interaction is more desirable.

With the ultimate goal being the meshing of the regional model with 20 km resolution with a larger scale model (say with 100 km or greater resolution), we first investigate the numerical problems associated with the horizontal meshing of staggered grids in a simple numerical model - the barotropic shallow-fluid equations. In spite of the simplicity of this model, meteorologically relevant solutions corresponding to gravity waves, gravity inertia waves, Rossby and Haurwitz waves exist, and the behavior of these waves in the meshed model provides valuable insight into the meshing of multi-level, baroclinic atmospheric models.

4.1 The basic equations

The basic equations consist of the well-known shallow fluid equations of motion on an f-plane, written in flux form as

$$\frac{\partial uh}{\partial t} + \frac{\partial uuh}{\partial x} + \frac{\partial uvh}{\partial y} + gh\,\frac{\partial h}{\partial x} - fvh = 0 \qquad (4.1)$$

$$\frac{\partial vh}{\partial t} + \frac{\partial uvh}{\partial x} + \frac{\partial vvh}{\partial y} + gh\,\frac{\partial h}{\partial y} + fuh = 0 \qquad (4.2)$$

and the continuity equation

$$\frac{\partial h}{\partial t} + \frac{\partial uh}{\partial x} + \frac{\partial vh}{\partial y} = 0 \quad . \qquad (4.3)$$

Here, the symbols, u, v, h, f, and g have their usual meteorological meanings. In addition to the model described by these basic equations, some experiments consider the advection of a passive quantity, A, governed by the conservation equation

$$\frac{\partial hA}{\partial t} + \frac{\partial uhA}{\partial x} + \frac{\partial vhA}{\partial y} = 0 \quad . \qquad (4.4)$$

4.2 The meshed grid system

Because the prediction variables in the regional model are staggered in the horizontal (in order to economically reduce truncation errors), the CMG and the FMG are both staggered, with h (and A) defined at x-points and the velocity components defined at •-points (Figures 4.1 and 4.2). The grids are meshed so that the momentum (•) points coincide. In the two-way interacting experiment, tendencies at the CMG points that lie within the FMG are not calculated. The FMG consists of 21 x 21 •-points and 20 x 20 x-points. The ratio of coarse to fine mesh size is 4:1.

The finite difference equations for the two-way interacting model are written to conserve fluxes exactly across the interfaces of each "box", which are (in general) centered on a grid point. The boxes, representing incremental volumes of mass or A, are centered on the x-points as shown in Fig. 4.1. Because of the geometry of the meshed grids, each mass "box" is a

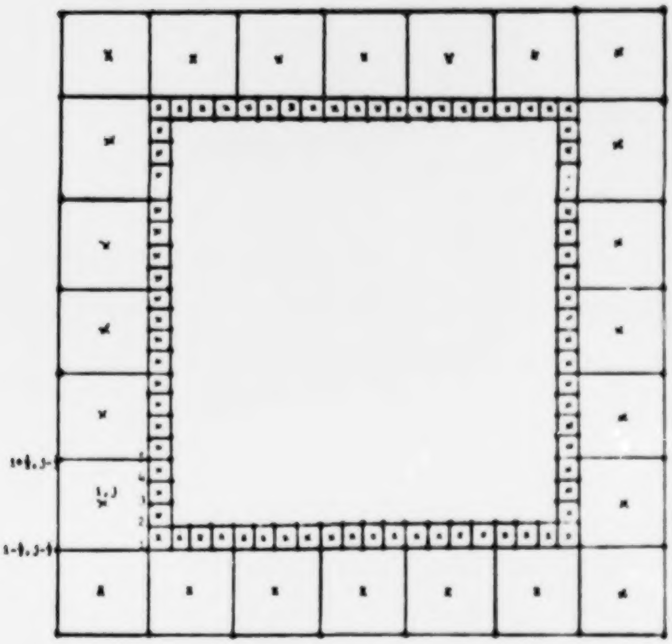

Figure 4.1 Boxes representing incremental volumes of mass in the 4:1 meshed grid system

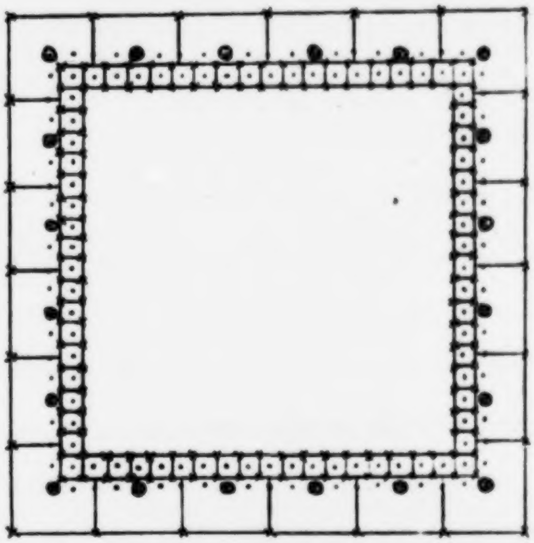

Figure 4.2 Boxes representing incremental volumes of momentum in the 4:1 meshed grid system

square. However, with a staggered grid, it is not possible to preserve square boxes for the momentum points (Fig. 4.2), and therefore, some of the •-points near the interface represent irregular shaped volumes.

The finite difference equations across the interface of the various boxes were written following Koss (1971). A difference between Koss's model and this one is that Koss used the same time step for all grids. In these experiments, Δt is varied with the grid size Δx to increase the computational efficiency. Because of this variation in time step, special care must be taken to insure that the fluxes of momentum and mass are conserved across the interface between the CMG and FMG. The procedure for the conservation of mass is illustrated for the grid volume labeled i,j in Fig. 4.1. The continuity equation for this volume is written

$$\left(\frac{\partial h}{\partial t}\right)^{\tau}_{ij} = \frac{uh^{\tau}_{i+1/2,\ j-1/2} + uh^{\tau}_{i-1/2,\ j-1/2}}{2} - \overline{uh}^{t,y} \qquad (4.5)$$

where

$$\overline{(uh)}^{t,y} = \frac{1}{16} \sum_{\tau'=1}^{4} \frac{(uh)^{\tau'}_{1}}{2} + (uh)^{\tau'}_{2} + (uh)^{\tau'}_{3} + (uh)^{\tau'}_{4} + \frac{(uh)^{\tau'}_{5}}{2} . \qquad (4.6)$$

Here τ denotes the time step of the CMG (Δt), and τ' denotes the time step of the FMG ($\Delta t/4$). Thus, given values of uh on both grids at time τ, the continuity equation is first integrated forward on the FMG to $\tau + \Delta t$ in a series of four short ($\Delta t/4$) time steps. The fluxes of mass across the FMG interface are accumulated and used to calculate the flux divergence of mass at the CMG point. In this manner, at time ($\tau + \Delta t$), the flux of mass (or A) into (out of) the CMG equals the flux out of (into) the four adjacent FMG volumes.

The conservation of the momentum fluxes is more complicated because of the irregularly shaped boxes at the interface, particularly at the corners. As discussed later, the boxes at the interface can be treated as CMG or FMG points. The best results (to be discussed later) were obtained when these boxes were treated as FMG points. If treated as CMG points, the variables at the momentum points within the FMG are integrated first using four time steps of $\Delta t/4$ to arrive at values of time $\tau + \Delta t$. The fluxes across the interface wall between the FMG and CMG are accumulated and used in the evaluation of the horizontal flux divergence of momentum at the circled CMG points only. (Values of mass weighted momentum are linearly interpolated between the circled •-points for the FMG forecasts.) If the boundaries are treated as FMG points, it is not necessary to accumulate fluxes, but it is necessary to assume that the fluxes through the CMG side of the interface momentum boxes are constant during the four FMG time steps. As in the CMG case, forecasts are made only at the circled points, with the remaining momentum values calculated by linear interpolation.

The finite difference equations corresponding to (4.1) - (4.4) at the grid points away from the interface are

$$\frac{\partial uh}{\partial t} = -\left(\overline{\overbrace{hu}^{y}\,\overline{u}^{x}}^{x}\right)_{x} - \left(\overline{\overbrace{hv}^{x}\,\overline{u}^{y}}^{y}\right)_{y} - \frac{1}{2g}\left(\overline{h^{2}}^{y}\right)_{x} + fvh \tag{4.7}$$

$$\frac{\partial vh}{\partial t} = -\left(\overline{\overbrace{hu}^{y}\,\overline{v}^{x}}^{x}\right)_{x} - \left(\overline{\overbrace{hv}^{x}\,\overline{v}^{y}}^{y}\right)_{y} - \frac{1}{2g}\left(\overline{h^{2}}^{x}\right)_{y} - fuh \tag{4.8}$$

$$\frac{\partial h}{\partial t} = -\overline{(hu)_x}^{y} - \overline{(hv)_y}^{x} \tag{4.9}$$

$$\frac{\partial hA}{\partial t} = - (\overline{hu}^{y}\ \overline{A}^{x})_x - (\overline{hv}^{x}\ \overline{A}^{y})_y \tag{4.10}$$

where the finite difference notation is defined by (2.12) and (2.13). The lateral boundary condition on the CMG consists of free-slip walls on the northern and southern boundaries (hv = 0, hu = specified according to mean geostrophic flow, constant in time). The CMG domain is assumed to be periodic in the east-west direction, eliminating these boundaries.

4.3 Experimental results

4.3.1. Background experiment with uniform mesh. The conservation of mass and total energy will be an important criterion in the assessment of the performance of the meshed grid system in the experiments to follow. Therefore, an experiment is first performed with a uniform mesh to provide a background against which the meshed grid results can be compared. In this experiment the initial wind is zero and the height field is initialized by adding random noise of amplitude 1 m on the mean height field (1000 m).

Because of the treatment of the continuity equation in both the uniform and meshed grid experiments, mass is conserved exactly except for round-off error. These experiments were run on an IBM 360-65 system which has a word size of 16 bits. In single precision, the round-off error produced a steady mass loss which reached $-10 \times 10^{(-3)}\%$ after

1300 time steps. With double precision, a similar steady mass loss occurred, but the total loss after 1300 steps was only $-20 \times 10^{-13}\%$, verifying that round-off errors were responsible for the slight loss.

The variation with time of the total energy on the uniform CMG is illustrated in Fig. 4.3. The total energy, defined as

$$E = \sum_{ij} [g(h-\bar{h})^2 + \frac{1}{2}\bar{h}(u^2 + v^2)] \tag{4.11}$$

shows an oscillation between about ± 5% of the initial energy. In contrast to the cause of the variation in mass, the oscillations in total energy are not caused by round-off errors, since an experiment run in double precision showed the same variations in total energy. Instead, these small oscillations are probably caused by the artificial numerical treatment of the northern and southern boundaries. Whatever the cause, the amplitude of the oscillation does not change with time. The relatively high percentage change (up to 5%) is a consequence of the small amount of perturbation energy present initially; in later experiments with stronger perturbations, the percent changes in total energy are much smaller.

4.3.2 The treatment of the interface momentum points in the meshed grid experiments. The experiments in this section are designed to determine the most stable way of treating the prediction points for momentum which lie on the interface between the two meshes (Fig. 4.2). The treatment of the prediction points for mass (Fig. 4.1) is much more obvious, since each x-point belongs entirely within either the CMG or the FMG.

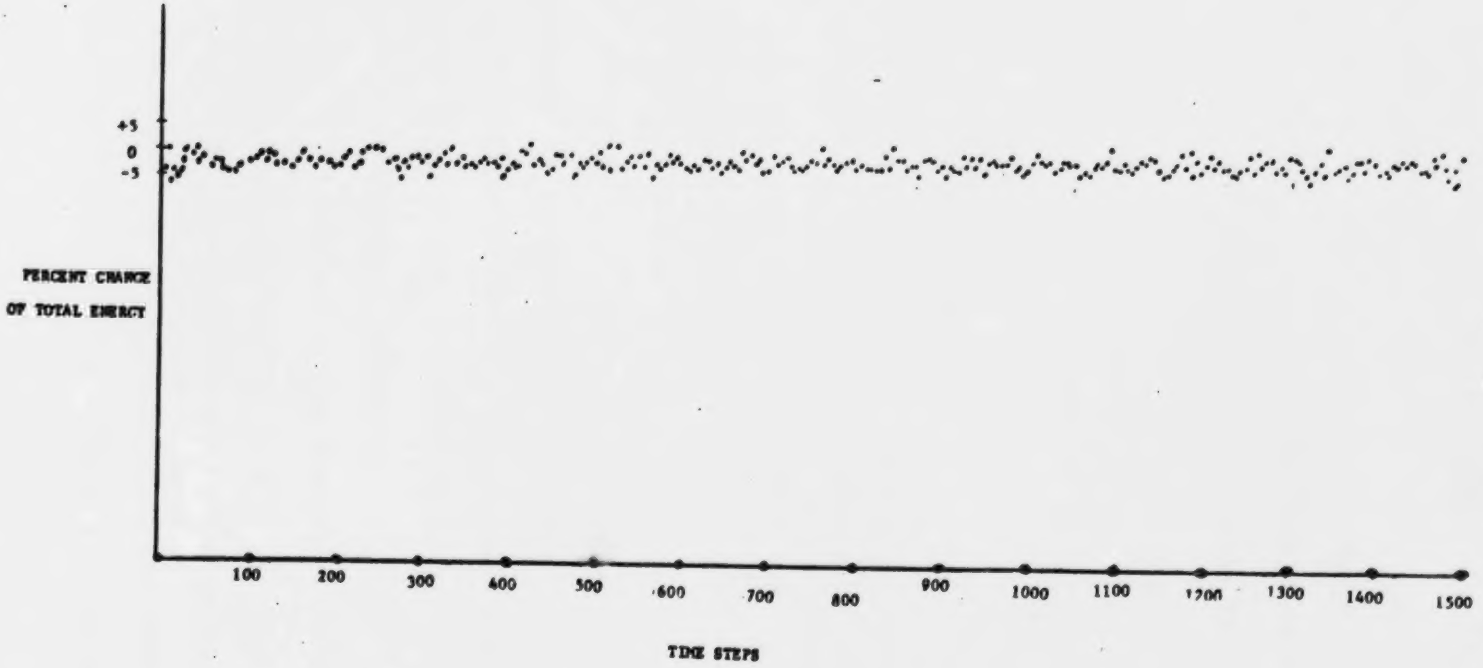

Figure 4.3 Time variation of total energy in uniform CMG experiment (Exp. 1)

The basic choice in the treatment of the interfacial momentum points is whether to treat them as FMG or CMG points. If treated as FMG points, forecasts are made with the smaller time step of $\frac{\Delta t}{4}$ at the same time that the other FMG forecasts are made. If treated as CMG points, the forecasts are made with the larger time step of Δt before the FMG forecasts are made.

A second important parameter in determining the relative stability of the meshed integration is the CMG time step, Δt. One might expect that the computations would be linearly stable if the CFL criterion for a staggered grid $(\frac{C\Delta t}{\Delta x} < \frac{\sqrt{2}}{2})$ were satisfied on both grids. The effect of the size of Δt on non-linear instability is less certain, however. Several experiments with varying Δt are run to determine its effect on the overall stability of the meshed system.

In the first set of experiments (Exp. 2 through 7) with the meshed grid, the initial conditions consist of zero mean wind superimposed with random perturbations of maximum amplitude 1 ms^{-1}. Experiments 2 through 7 are identical except for the treatment of the momentum points on the interface between the two meshes. Some of the important details of the experiments are summarized in Table 4.1. Note that none of these experiments utilizes any spatial or temporal damping devices.

The behavior of the six meshed grid experiments may be summarized by considering the time variation of total energy, which is shown in Fig. 4.4. In contrast to the uniform mesh experiment (Experiment 1), all of the meshed grid experiments show an increase of total energy. However, the rate of increase varies strongly depending on how the interface momentu

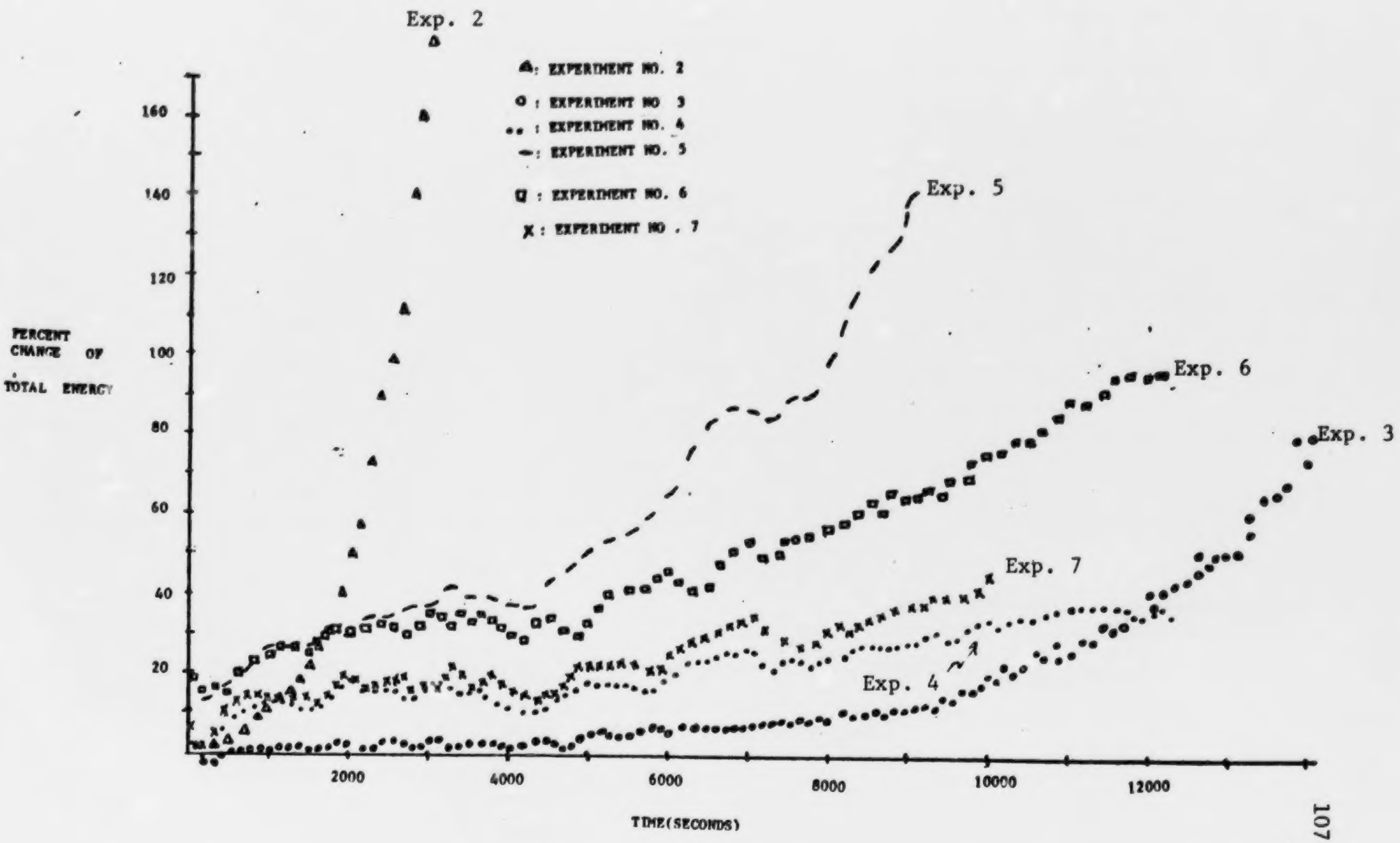

Figure 4.4 Time variation of total energy in Exp. 2-7

Table 4.1

Summary of Experiments

Exp.	ΔS_{CMG} (km)	Δt_{CMG} (s)	K_H	Treatment of Interfacial Momentum Points	Initial Conditions	Length of Integration (time steps) FMG	Remarks
1	20	80	0	-	u = 0 v = 0 ± random noise	1500	Uniform CMG to establish basis for comparison with meshed grid experiment
2	20	80	0	CMG	"	40	Linearly unstable. 100% change in E after 40 steps
3	20	40	0	CMG	"	1400	Slow, then more rapid growth of E (see Fig. 4.4)
4	20	40	0	FMG	"	1200	Slow growth of E (see Fig. 4.4)
5	20	80	0	FMG	"	450	Rapid growth of E (Fig. 4.4)
6	20	60	0	FMG	"	800	Less rapid growth of E than in Exp. 5
7	20	50	0	FMG	"	800	Less rapid growth of E than in Exp. 6
8	20	40	0	FMG	u = 10 ± random noise	1200	Some growth of noise after 1000 time steps.
9	20	40	0	FMG		1200	Euler backward time differencing, noise is suppressed.
10	20	40	2.5×10^3	FMG	"	1400	Some noise but growth is controlled.
11	20	40	0	FMG	u = 20 ± random noise	1200	FMG moves within CMG in order to follow a cloud of a passive contaminant.

points are treated and the size of the time step. In Experiment 2, in which the points are treated as CMG points and the CMG time step is 80, the model exhibits a very rapid increase in total energy. This increase resembles a linear instability, even though the linear CFL criterion is satisfied on both grids ($\frac{c\Delta t}{\Delta s} = \sqrt{gH}\,\frac{\Delta t}{\Delta s} = 0.4 < \sqrt{2}/2$). However, the grid size along the interface is less than the CMG Δs (See Fig. 4.2), and this smaller grid size is apparently one of the causes of instability. To test this hypothesis, the CMG time step is halved in Exp. 3, and as shown in Fig. 4.4 the model becomes linearly stable, even though the energy does begin to show a rapid increase after 10000 seconds.

In Exp. 4, the interfacial momentum points are integrated as FMG points, rather than CMG points. The total energy (Fig. 4.4) shows a gradual increase in total energy, but in contrast to Exp. 3, the total energy does not rapidly increase after 10000 seconds. We conclude from this result (and later experiments which are not discussed) that it is preferable to treat the interfacial momentum points as FMG rather than CMG points.

The remaining experiments (5-7) in this section test the effect of varying Δt when the interfacial momentum points are treated as FMG points. Even though the CFL criterion is satisfied for all the choices of Δt (80, 60 and 50 s), the growth of total energy is less for the smaller time steps. We conclude that it is advantageous to use a somewhat smaller time step than the CFL criterion would indicate, and future experiments are conducted with a Δt of 40 s.

4.3.3 Meshed grid experiments with a mean wind of 10 ms^{-1}. The experiments discussed in the previous sections investigated mainly the effect of gravity waves passing through the meshed system. Advective effects were negligible in the absence of a mean velocity. In this section, three experiments (Experiments 8, 9, and 10) are run with a mean west wind of 10 ms^{-1}. This mean wind is initially in geostrophic balance with a north-south pressure gradient. The Coriolis parameter is 10^{-4} s^{-1}. Two measures of the behavior of the meshed systems are shown, the percent variation of total energy and the time variation of the maximum north-south component. Ideally, the current should remain in approximate geostrophic balance, so that the growth of the maximum north-south velocity is a measure of the error in the forecast.

Experiment 8 is identical to Experiment 4, except for the initial conditions, and contains no spatial or temporal damping. Experiments 9 and 10 are identical to Experiment 8, except that an effort is made to reduce the growth of noise and energy through the damping of high spatial or temporal frequencies. In experiment 9, the Euler-backward scheme is used (rather than the leapfrog) to damp the high time frequencies. In Experiment 10, a constant horizontal eddy diffusivity coefficient of 2.5×10^3 m^2s^{-1} is used on both meshes.

The results from Exp. 8-10 are summarized in Fig. 4.5 Without any smoothing devices in space or time, the meshed system exhibits a slow, irregular increase in total energy, reaching a value of 0.01% after 1200 FMG time steps of 10 s (3.3h). During this time the maximum v-components

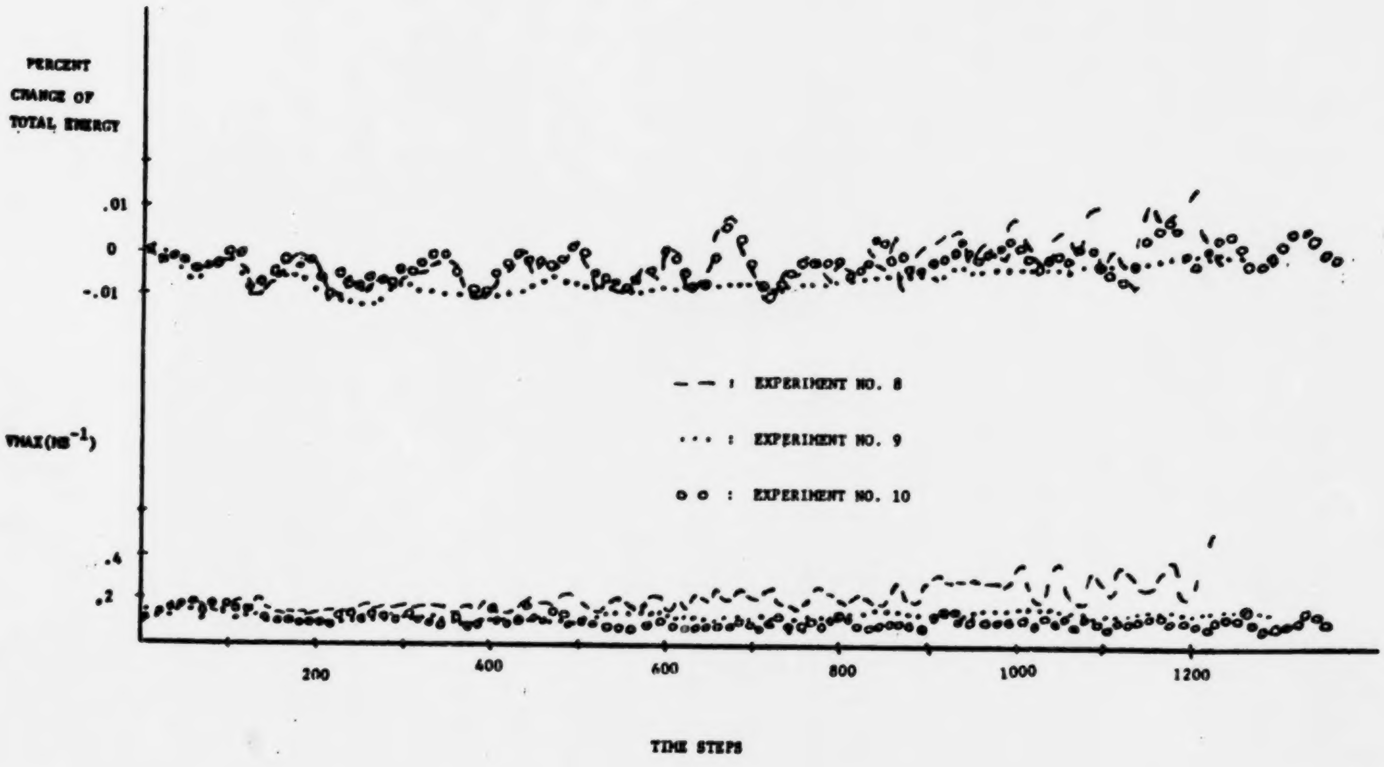

Figure 4.5 Time variation of total energy and maximum v-component in Exp. 8, 9, 10

show a high frequency oscillation superimposed upon a gradual increase. Values of 0.8 ms^{-1} are reached late in the forecast.

When the Euler-backward time integration scheme is used (Exp. 9), the high frequency time oscillation in both the total energy and the maximum v-component is nearly eliminated. Furthermore, the total increases in energy and the maximum v-component are greatly reduced, indicating that the high time frequencies are primarily responsible for the overall growth in Exp. 8. The disadvantage is that the Euler-backward scheme requires nearly twice as much time.

In Exp. 10, the effect of damping the high spatial frequencies through the addition of the terms $K_H \nabla^2 (hu)$ and $K_H \nabla^2 (hv)$ in equations (4.1) and (4.2) is investigated. This value of K_H is rather small for the present grid size; on the FMG, for example, $\frac{K_H \Delta t}{\Delta s^2} = .001$. As shown by Fig. 4.5, damping the short wavelengths improves the behavior of the model. The rate of growth of the total energy is slowed and the growth of the maximum v-component is nearly eliminated. These results suggest that the meshed grid system can be integrated for reasonably long periods of time, even in the presence of a substantial advecting velocity, provided some method is used to prevent the increase of energy in the short wavelengths or high frequencies.

4.3.4 Experiment with mutually interacting grids with the fine mesh moving through the coarse mesh. In the numerical modeling of certain atmospheric phenomena such as hurricanes, it may be desirable to follow a certain portion of the flow by allowing the fine mesh to move within the coarse mesh. In this section, the fine mesh is initialized with a "cloud" of a passive contaminant, A, in a mean flow of 20 ms^{-1}. As the cloud is advected downwind, the FMG is allowed to move within the CMG in order to remain centered over the cloud.

When the maximum concentration of A travels four FMG grid points downstream, the FMG moves one CMG grid length as illustrated in Fig. 4.6. New values for mass and momentum on the points on the leading edge of the FMG that now coincide with old CMG points are set equal to the old CMG values. All other new FMG points near the leading edge (Fig. 4.6) are obtained by a linear interpolation between the neighboring CMG and FMG values. The data on the trailing edge of the FMG are utilized to define the newly uncovered CMG points.

Fig. 4.7 shows the time variation of total energy and the maximum north-south velocity component in Exp. 11. The * indicates the times at which the FMG moves. As can be seen by a comparison of Fig. 4.7 with 4.5, the behavior of the integration on the moving grid is quite comparable to the behavior of the stationary grid experiments. In fact, the variations of total energy and maximum v are less when the FMG is moved. This somewhat surprising result is apparently caused by the initialization procedure on the new FMG points each time the grid is moved. The interpolation periodically replaces a developing noisy field on the first four columns of FMG points with a smoothly varying field. We conclude that completely interacting meshed systems in which the FMG moves within the CMG introduce no special stability problems compared to integrations on stationary grids.

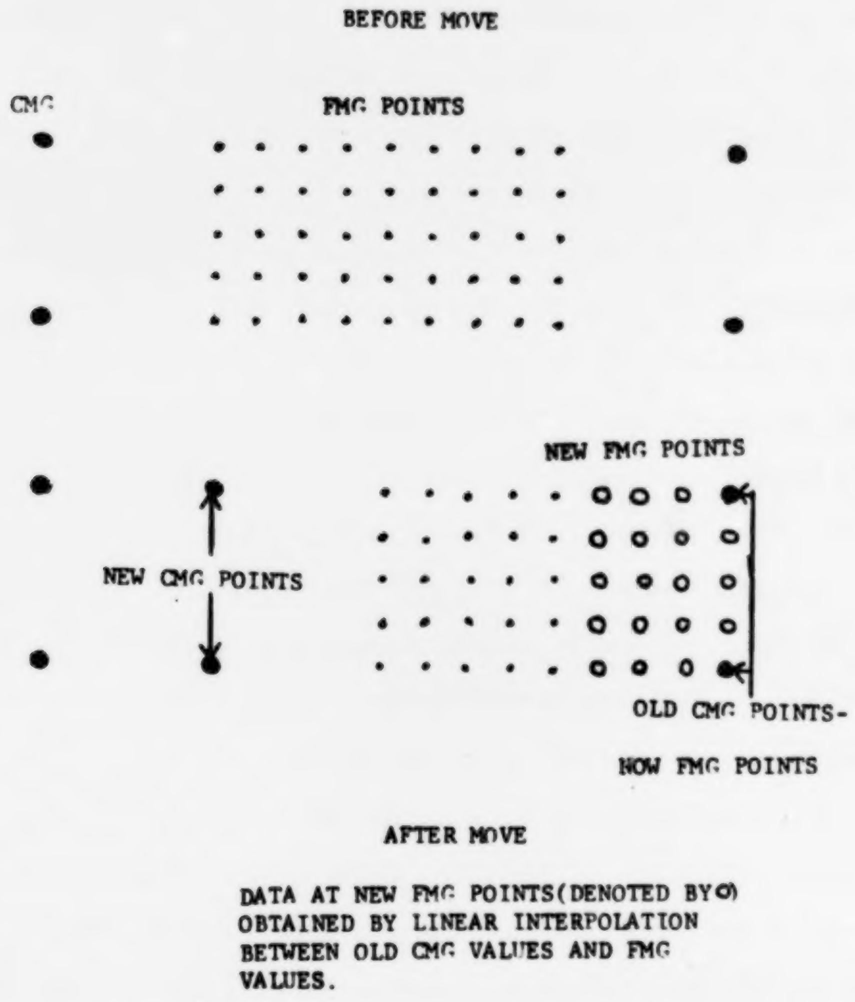
BEFORE MOVE
CMG
FMG POINTS
CMG
NEW FMG POINTS
NEW CMG POINTS
OLD CMG POINTS-
NOW FMG POINTS
AFTER MOVE
DATA AT NEW FMG POINTS(DENOTED BY o)
OBTAINED BY LINEAR INTERPOLATION
BETWEEN OLD CMG VALUES AND FMG
VALUES.

Figure 4.6 Illustration of movement of FMG within CMG

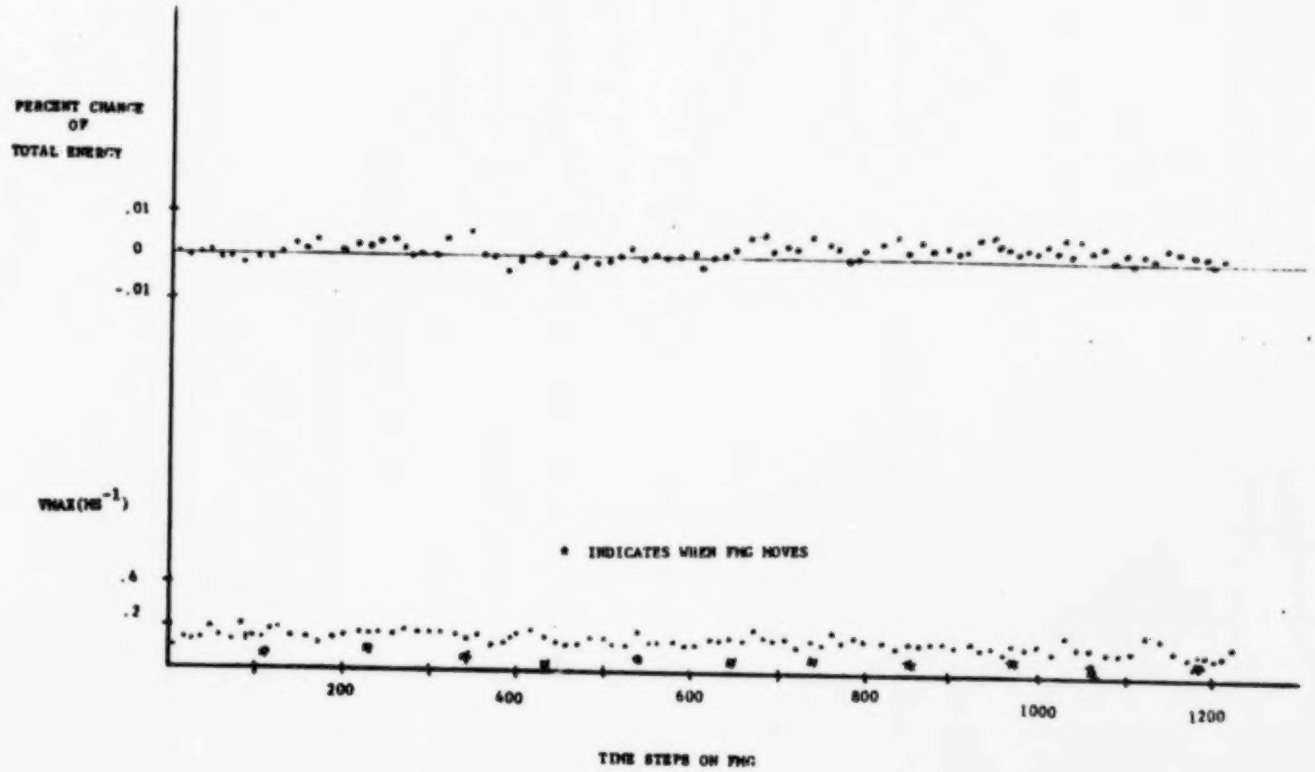

Figure 4.7 Time variation of total energy and maximum north-south velocity component in Exp. 11

4.4 Mesh grid experiments initialized with Haurwitz waves

In order to examine the effects of the moving and meshing techniques on a different physical system, a series of experiments was initialized with Haurwitz waves of various wavelengths. Haurwitz waves are well suited for such a test, not only because they are analogous to waves in the real atmosphere, but also because they have linear solutions which can be qualitatively and quantitatively compared to the numerical forecasts. Several of the critical questions these experiments are designed to explore are:

(1) How do the meshing and moving techniques affect the forecast of waves that can be adequately forecast on a uniform course mesh grid?

(2) How do differences in numerical phase speed on the grids of different size contaminate the forecasts?

(3) How does the nested grid structure handle the non-linear interaction of disturbances with different wavelengths?

(4) Which of the following meshing techniques is superior?

   a. The one-way interacting system in which the boundary values of ϕ, u and v on the FMG are interpolated in time and space from a previous independent forecast on the CMG. In this case the grids can interact in only one direction - from the CMG to the FMG.

   b. The two-way interacting system - the boundary values of ϕ, u and v on the FMG are computation points, and mutual interactions between the CMG and FMG are allowed.

Table 4.2 summarizes the Haurwitz wave experiments. The experiments can be broken into three groups with the primary difference being the east-west wavelength. Experiments 1 through 5 (Group A) were initialized with a 3200 km wave (wave number 1 on the CMG). Experiments 6 through 9 (Group B) are identical except the wavelength is only 800 km (wave number 4 on the CMG. Experiments 10 through 12 (Group C) include both wavelengths.

4.4.1. Initial conditions and the linear solutions. A Haurwitz wave is a Rossby-type wave restricted to a channel of finite width (D) and subject to the boundary conditions that v (the cross-channel component of velocity) be a maximum at the center and vanish at both edges of the channel. In order to derive the linear non-divergent solution we start with the linearized equations of motion for a rotating fluid restricted to horizontal non-divergent motion,

$$\frac{\partial u}{\partial t} + \overline{U}\frac{\partial u}{\partial x} - fv + \frac{\partial \phi}{\partial x} = 0 \tag{4.12}$$

$$\frac{\partial v}{\partial t} + \overline{U}\frac{\partial v}{\partial x} + fu + \frac{\partial \phi}{\partial y} = 0 \tag{4.13}$$

$$\frac{\partial u}{\partial x} + \frac{\partial v}{\partial y} = 0 \quad , \tag{4.14}$$

where ϕ is the geopotential.

Table 4.2

Summary of Meshed Experiments Initialized with Haurwitz Wave

Experiment		Wavelength of Initial Wave	Grid Structure	$K_h (m^2 s^{-1})$	Number of Time Steps and Length of Forecast
Group	Number				
A	1	3200 km	Uniform CMG	0	350/24 hrs
	2	"	1 way meshed	0	1400/24 hrs
	3	"	2 way meshed	0	1400/24 hrs
	4	"	1 way meshed	2×10^5	1400/24 hrs
	5	"	2 way meshed	2×10^5	1400/24 hrs
B	6	800 km	Uniform CMG	0	350/24 hrs
	7	"	1 way meshed	2×10^5	1400/24 hrs
	8	"	2 way meshed	2×10^5	1400/24 hrs
C	9	Combined 800 and 3200 km	Uniform FMG	2×10^5	800/13.3 hrs
	10		1 way meshed	2×10^5 on FMG 8×10^5 on CMG	800/13.3 hrs
	11		2 way meshed	2×10^5 on FMG 8×10^5 on CMG	800/13.3 hrs

We restrict propagation of the wave to the x direction and seek solutions of the form

$$\frac{u}{\hat{u}(y)} = \frac{v}{\hat{v}(y)} = \frac{\phi}{\hat{\phi}(y)} = Ae^{i(\omega t + Kx)} \tag{4.15}$$

where

A is amplitude

ω is frequency

t is time,

and K is the wave number in the x direction = $\frac{2\pi}{\lambda_x}$ where λ_x is the wavelength.

Substituting (4.15) into (4.12) - (4.14), we obtain

$$i(\omega + K\bar{U})\,\hat{u} - f\hat{v} + iK\hat{\phi} = 0 \tag{4.16}$$

$$i(\omega + K\bar{U})\,\hat{v} + f\hat{u} + \frac{\partial\hat{\phi}}{\partial y} = 0 \tag{4.17}$$

$$iK\hat{u} + \frac{\partial\hat{v}}{\partial y} = 0 \quad . \tag{4.18}$$

With the assumption that the phase speed $C = -\,\omega/K \neq \bar{U}$, we can eliminate $\hat{\phi}$ and $\hat{u}$ to get a second order differential equation for $\hat{v}$,

$$\frac{\partial^2 \hat{v}}{\partial y^2} + \left(\frac{\beta}{\overline{U} - C} - K^2\right) \hat{v} = 0 \quad , \qquad (4.19)$$

where $\beta = \frac{\partial f}{\partial y}$ is a constant.

With the simplification $S = \left(\frac{\beta}{\overline{U} - C} - K^2\right)^{1/2}$, the general solution becomes

$$\hat{v} = C_1 e^{iSy} + C_2 e^{-iSy} \quad . \qquad (4.20)$$

An expression for $\hat{u}$ may be found by substituting (4.20) into (4.18),

$$\hat{u} = -\frac{C_1 S}{K} e^{iSy} + \frac{C_2 S}{K} e^{-iSy} \quad . \qquad (4.21)$$

Next (4.21) and (4.20) are substituted into (4.16) to yield

$$\hat{\phi} = -i\frac{f}{K}\left(C_1 e^{iSy} + C_2 e^{-iSy}\right) - \frac{(\omega + K\overline{U})}{K^2} \cdot \left(C_2 S e^{-iSy} - C_1 S e^{-iSy}\right) \quad . \qquad (4.22)$$

To evaluate the constants C_1 and C_2, we apply the first boundary condition:

1) at $y = 0$,

$\hat{v}$ is a maximum, or $\frac{\partial \hat{v}}{\partial y} = 0$,

to (4.20) in order to obtain $C_1 = C_2$.

The second condition,

2) at $y = \pm D/2$, $\hat{v} = 0$,

applied to (4.20) yields

$$2C_1 \cos Sy = 0 \quad . \tag{4.23}$$

For the non-trivial case C_1 is non-zero but arbitrary and

$$\cos Sy = \cos[(\frac{\beta}{\bar{U} - C} - K^2)^{1/2} \quad (\pm D/2)] = 0 \quad , \tag{4.24}$$

which implies that the phase speed of the wave is given by

$$C = \bar{U} - \frac{\beta}{(\frac{\pi}{D})^2 + K^2} \quad . \tag{4.25}$$

Now let L be the wave number in the y direction. It can be shown that

$$S = \frac{\pi}{D} = L \tag{4.26}$$

if the wavelength in the y direction (λ_y) is 2D.

We can now rewrite (4.20), (4.21), and (4.22)

$$\hat{v} = 2C_1 \cos Ly \tag{4.27}$$

$$\hat{u} = - i \frac{2C_1L}{K} \sin Ly \qquad (4.28)$$

$$\hat{\phi} = - i \frac{2fC_1}{K} \cos Ly + i2 \frac{(\omega + K\bar{U})}{K^2} LC_1 \sin Ly \qquad (4.29)$$

Now to get the initial fields we use (4.15) with $t = 0$. Also, since C_1 is arbitrary, let $C_1 = i/2$ and solve for the real parts of u, v, and ϕ.

$$\mathrm{Re}(v) = - A \cos Ly \sin Kx \qquad (4.30)$$

$$\mathrm{Re}(u) = \frac{L}{K} A \sin Ly \cos Kx \qquad (4.31)$$

$$\mathrm{Re}(\phi) = \frac{f}{K} A \cos Ly \cos Kx - \frac{(\omega + K\bar{U})}{K^2} LA \sin Ly \cos Kx. \qquad (4.32)$$

Finally, upon substituting $\omega = - CK$ in (4.32) we get

$$\mathrm{Re}(\phi) = \frac{f}{K} A \cos Ly \cos Kx - \frac{\beta}{(L^2 + K^2)} \frac{L}{K} \cdot \qquad (4.33)$$
$$A \sin Ly \cos Kx$$

Equations (4.30), (4.31), and (4.33) are used to determine the initial conditions for the numerical experiments by specifying f, β, K, L, and A. Similarly, at any time t the complete analytic solution is

$$u = \frac{L}{K} A \sin Ly \cos (\omega t + Kx) \qquad (4.34)$$

$$v = - A \cos Ly \sin (\omega t + Kx) \qquad (4.35)$$

and

$$\phi = \left[\frac{f}{K} A \cos Ly \cos Kx - \frac{\beta}{(L^2 + K^2)} \frac{L}{K} A \sin Ly\right] \cdot \cos(\omega t + Kx) \tag{4.36}$$

This solution can be compared to the numerical forecasts to quantitatively and qualitatively evaluate the effects of the various grid structures, provided the non-linear terms in the numerical forecasts remain small.

4.4.2 Quantitative analysis of errors. One simple statistic for quantitatively comparing the forecast fields to the analytic solutions is the mean square error (MSE). Another measure of the skill of a forecast is the ratio of the variance of a particular field to its MSE. A large value of the ratio means the forecast has considerable skill. When the ratio decreases to 1, we can say the forecast has no skill. For example, consider the effect of phase errors on this quantitative measure of forecast skill.

If the analytic solution of v is given by

$$v = A \cos y \sin x \quad , \tag{4.37}$$

then the variance of v when we integrate over the entire forecast domain is

$$VAR_v = \frac{A^2}{4} \quad . \tag{4.38}$$

Furthermore we define

$$MSE_v = \frac{\sum_x \sum_y (v_f - v_a)^2}{N} \tag{4.39}$$

where v_f is the forecast value and v_a is the analytic value of the v-component and N is the total number of grid points.

In the limit as the grid size becomes small, the MSE_v becomes

$$\frac{\iint (v_f - v_a)^2 \, dx \, dy}{\iint dx \, dy} \quad . \tag{4.40}$$

If we consider only phase errors in the x-direction in the numerical solutions, we can express the forecast solution of v as

$$v_f = - A \cos y \sin (x-\gamma) \tag{4.41}$$

where γ is the phase error.

Then the mean square error is

$$MSE_V = \frac{\iint (-A \cos y \sin (x-\gamma) + A \cos y \sin x)^2 \, dx \, dy}{\iint dx \, dy} \quad . \tag{4.42}$$

When integrated over the entire domain, we get

$$MSE_V = \frac{A^2}{2} (1 - \cos \gamma) \quad . \tag{4.43}$$

The maximum MSE_V (A^2) occurs when the analytic and forecast waves are 180 degrees out of phase, in which case the measure of forecast skill is

$$R = \frac{VAR_v}{MSE_v} = 0.25 \quad .$$

A ratio of 1.0 occurs when the forecast and true waves are 60° out of phase. These examples will be useful in judging the effect of phase errors in the numerical solutions on the meshed grids.

4.4.3 Long-wave results: Exp. 1-5. This set of experiments was designed to test the effects of the meshing and moving techniques on a wave that can be adequately resolved on a uniform course mesh grid. Equations (4.30), (4.31), and (4.33) with the following parameters were used to initialize the model:

$A = 10$

$\bar{U} = 20$ mps

$\Delta x_{CMG} = \Delta y_{CMG} = 1.6 \times 10^5$m

$\Delta x_{FMG} = \Delta y_{FMG} = 4 \times 10^4$m

$\Delta T_{CMG} = 240$ seconds

$\Delta T_{FMG} = 60$ seconds

f at south end of channel $= 7.0 \times 10^{-5}\ s^{-1}$

f at north end of channel $= 1.0 \times 10^{-4}\ s^{-1}$

$\beta = 1.6 \times 10^{-11}\ m^{-1}\ s^{-1}$

$\lambda_x = 20\ \Delta x_{CMG} = 3200$ km

$\lambda_y = 26\ \Delta y_{CMG} = 4160$ km

In the nested grid experiments (2-5) the FMG is initially positioned along the trough axis in the center of the channel. When the trough moves four FMG increments downstream, the FMG is moved in order to remain nearly centered along the axis. The movement is described in Section 4.3.4.

The numerical wave speed, C_N, can be computed from

$$C_N = \frac{1}{K\Delta T} \text{ARCSIN} \left(\frac{C\ \Delta T}{\Delta x} \text{SIN } K\Delta X\right) \quad , \qquad (4.44)$$

where C is the analytic phase speed (Thompson, 1961). Both equation (4.25) for the analytic phase speed and (4.44) give 17.39 mps indicating that the uniform CMG should forecast the phase speed of this wave very accurately.

Figures 4.8 and 4.9 show the initial height, velocity and vorticity fields on the CMG for the experiments of Group A and also indicate where the FMG is located when a meshed grid structure is appropriate. Figures 4.10 and 4.11 show the same initial fields on the FMG for experiments 2-5. Figures 4.12 - 4.13 show the results of experiment 1 (uniform CMG) after 24 hours. All the fields are quite smooth with only a slight loss of amplitude of the initial disturbance. The trough axis has moved nearly 9 grid points which yields a phase speed of about 16.5 ms^{-1}. This value is about 5 percent less than the analytic linear phase speed, but still quite satisfactory considering the effects of the numerical lateral boundary conditions and the non-linear terms in the forecast equations.

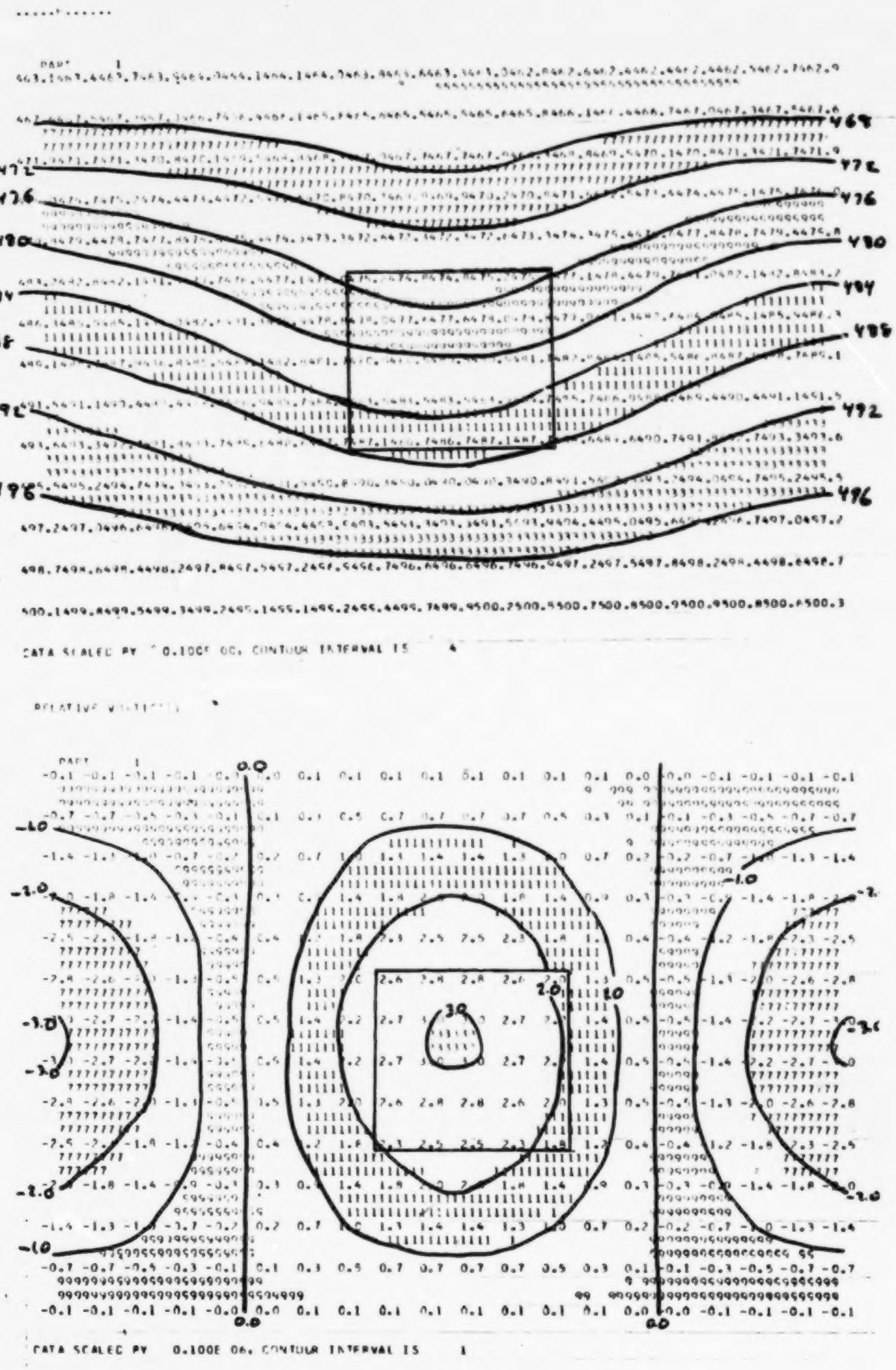

Figure 4.8 Initial height and vorticity field on CMG for Exp. 1-5

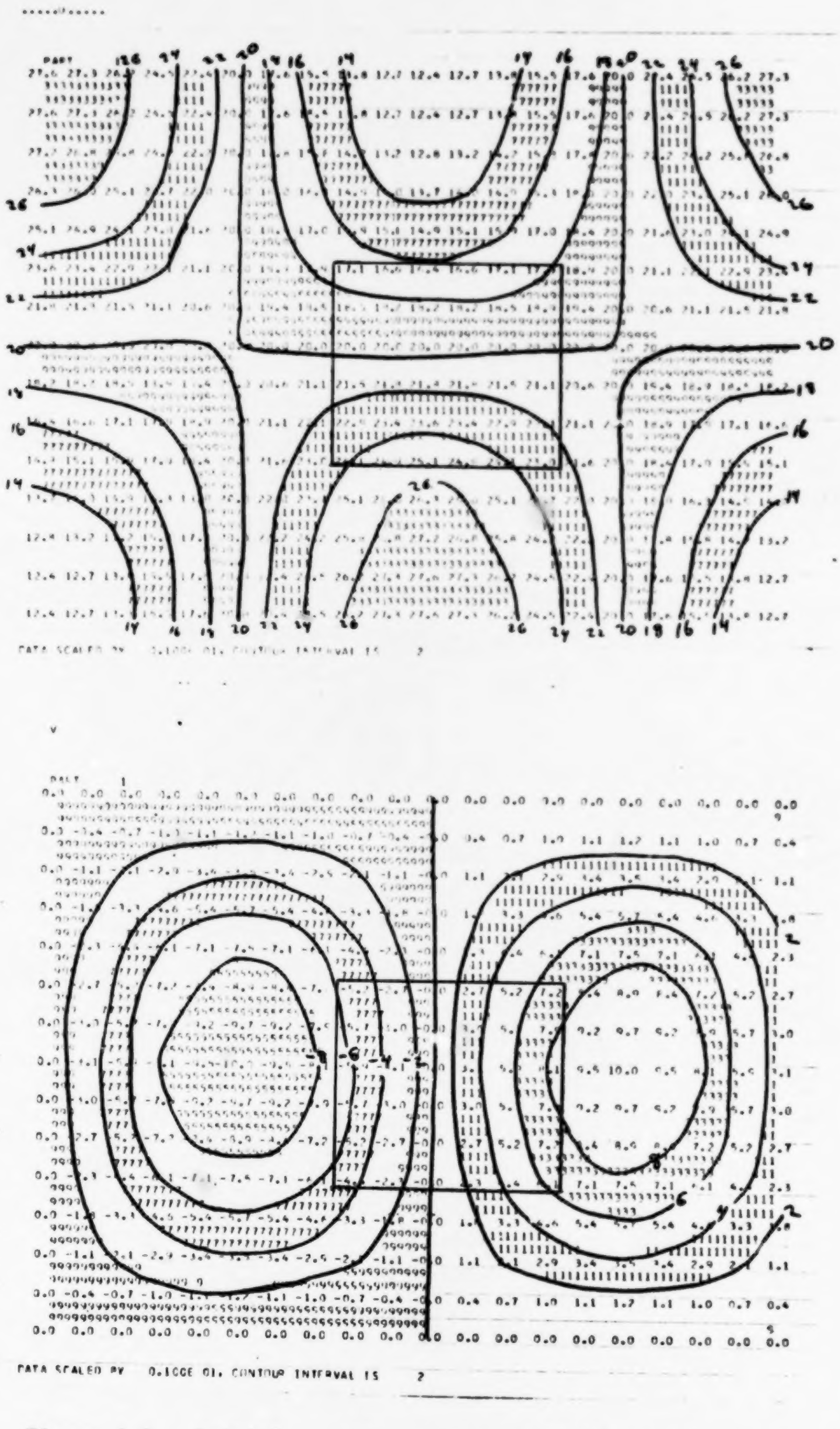

Figure 4.9 Initial u- and v-component fields on CMG for Exp. 1-5

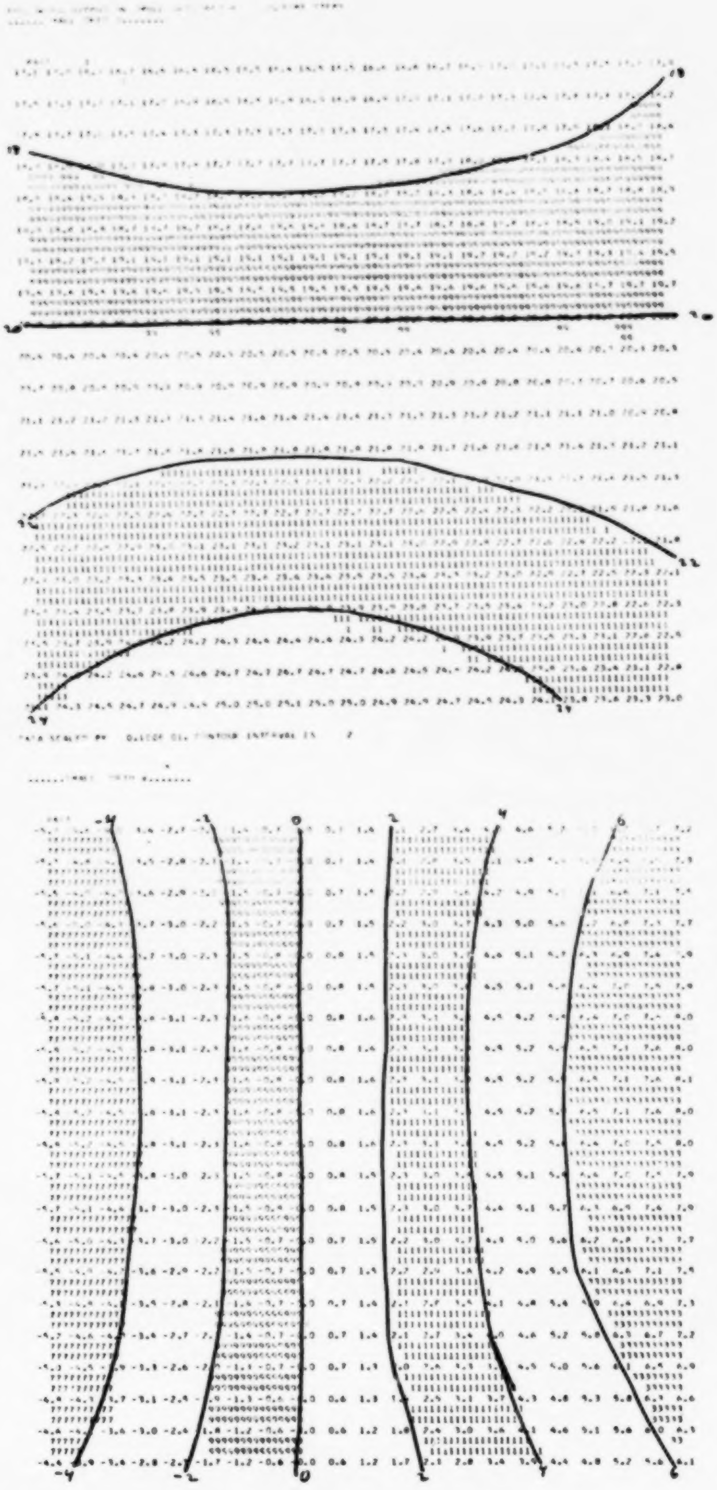

Figure 4.10 Initial height and vorticity field on FMG for Exp. 1-5

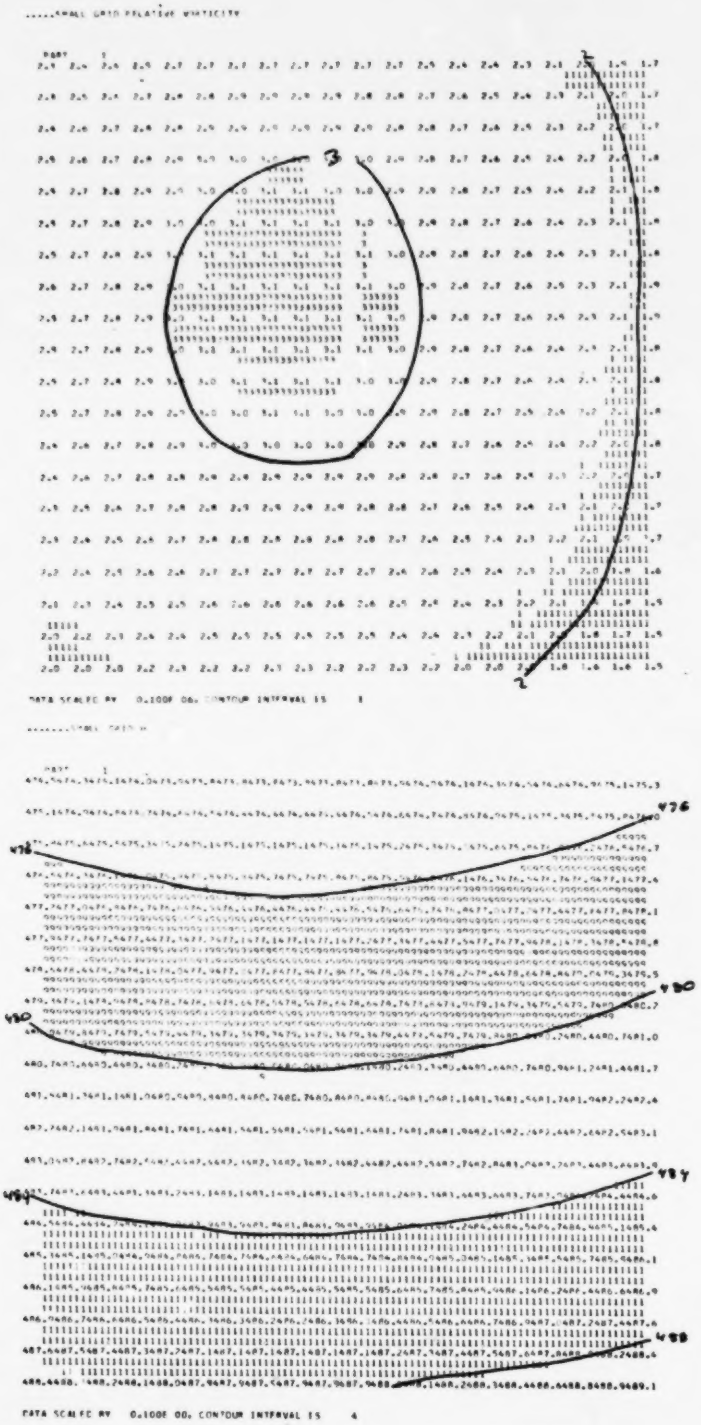

Figure 4.11 Initial u- and v-component fields on CMG for Exp. 1-5

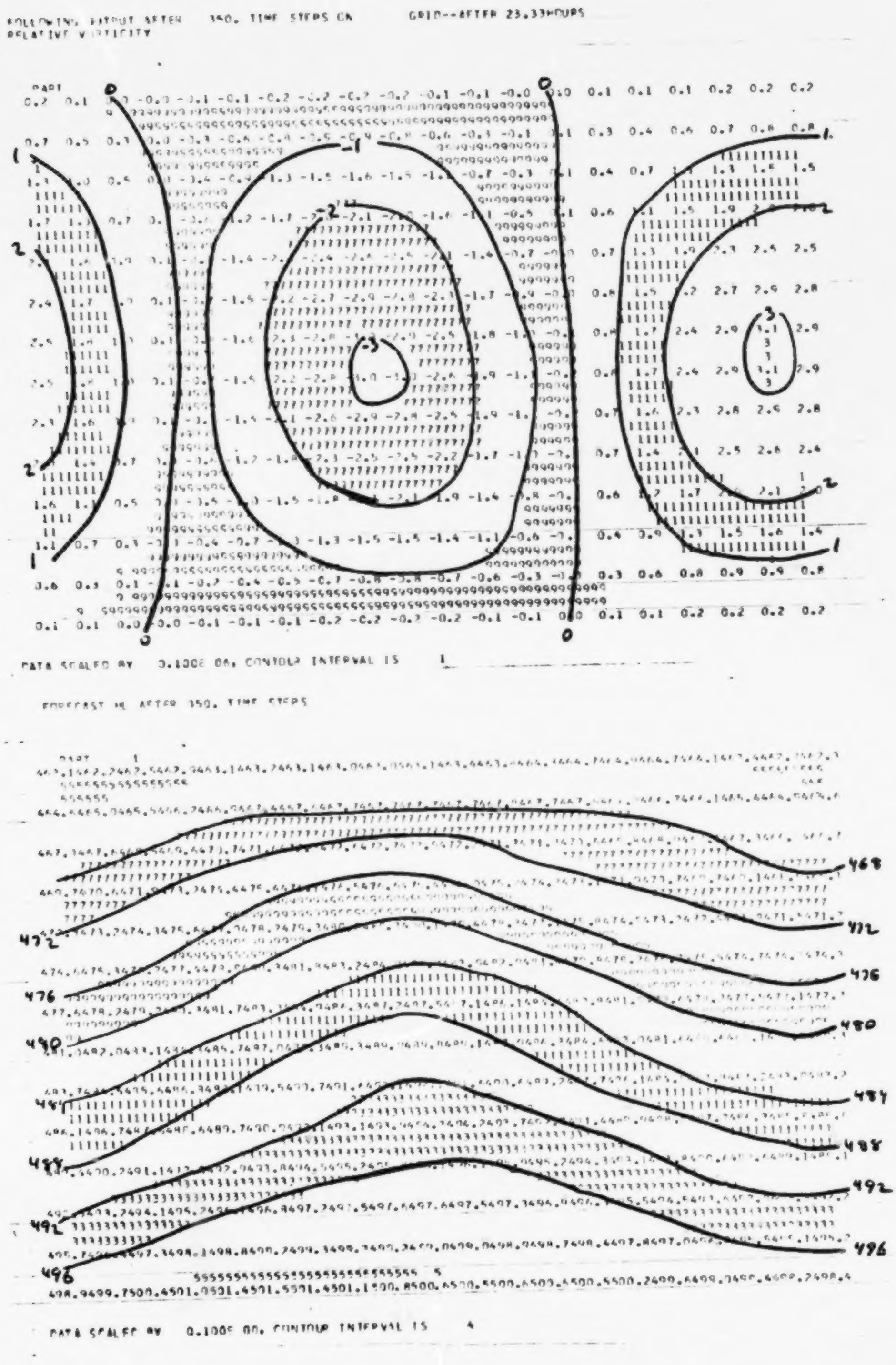

```
FOLLOWING OUTPUT AFTER   350. TIME STEPS ON       GRID--AFTER 23.33HOURS
RELATIVE VORTICITY
```

```
DATA SCALED BY   0.100E 06. CONTOUR INTERVAL IS    1
```

```
FORECAST H  AFTER 350. TIME STEPS
```

```
DATA SCALED BY   0.100E 00. CONTOUR INTERVAL IS    4
```

Figure 4.12 Forecast height and vorticity fields on CMG for Exp. 1

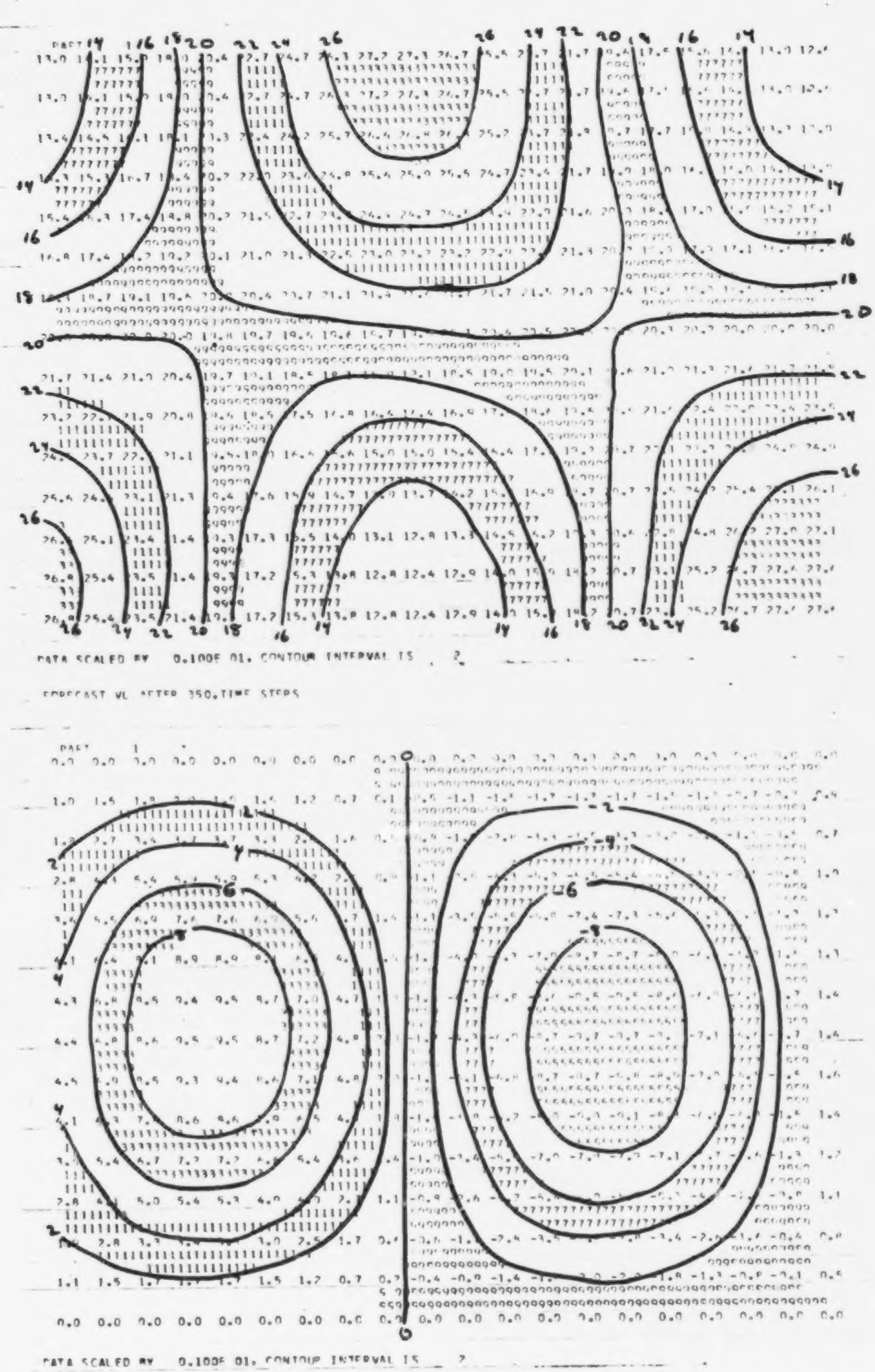

Figure 4.13 Forecast u- and v-component fields on CMG for Exp. 1

Experiment 1 is now used as a standard for comparing the performances of the different meshing techniques. Because the wave is well-forecast on the CMG, the addition of the FMG cannot greatly improve the forecast. In fact, there is no small-scale information in the initial fields. However, because of the discontinuity in grid spacing and the moving of the FMG, small-scale noise will be continuously generated at the interface and may grow and contaminate the forecasts on both grids. Since we cannot improve on the large-scale forecast, we would hope that the addition of the movable FMG does not lead to a deterioration of the entire forecast.

Figures 4.14 and 4.15 show the results after 1400 ΔT_{FMG} for Exp. 2 and 3 when no numerical smoothing devices were used. The FMG has moved 8 times. The results from both meshing techniques look similar. There is some small-scale noise in all fields although it is most noticeable in the vorticity patterns. In both experiments, the phase velocity has increased slightly to about 17 mps approaching the linear phase speed.

Figures 4.16 and 4.17 show the results after 1400 ΔT_{FMG} from Exp. 4 and 5 where a horizontal diffusion term with $K = 2 \times 10^5 \ m^2 s^{-1}$ was added to the momentum tendencies. All the fields are noticeably smoother, especially the vorticity. The phase speed does not change. From inspection of the velocity and height forecasts, there is little reason to choose one meshing technique over the other. However, the vorticity fields associated with the one-way interacting system appear to be somewhat better.

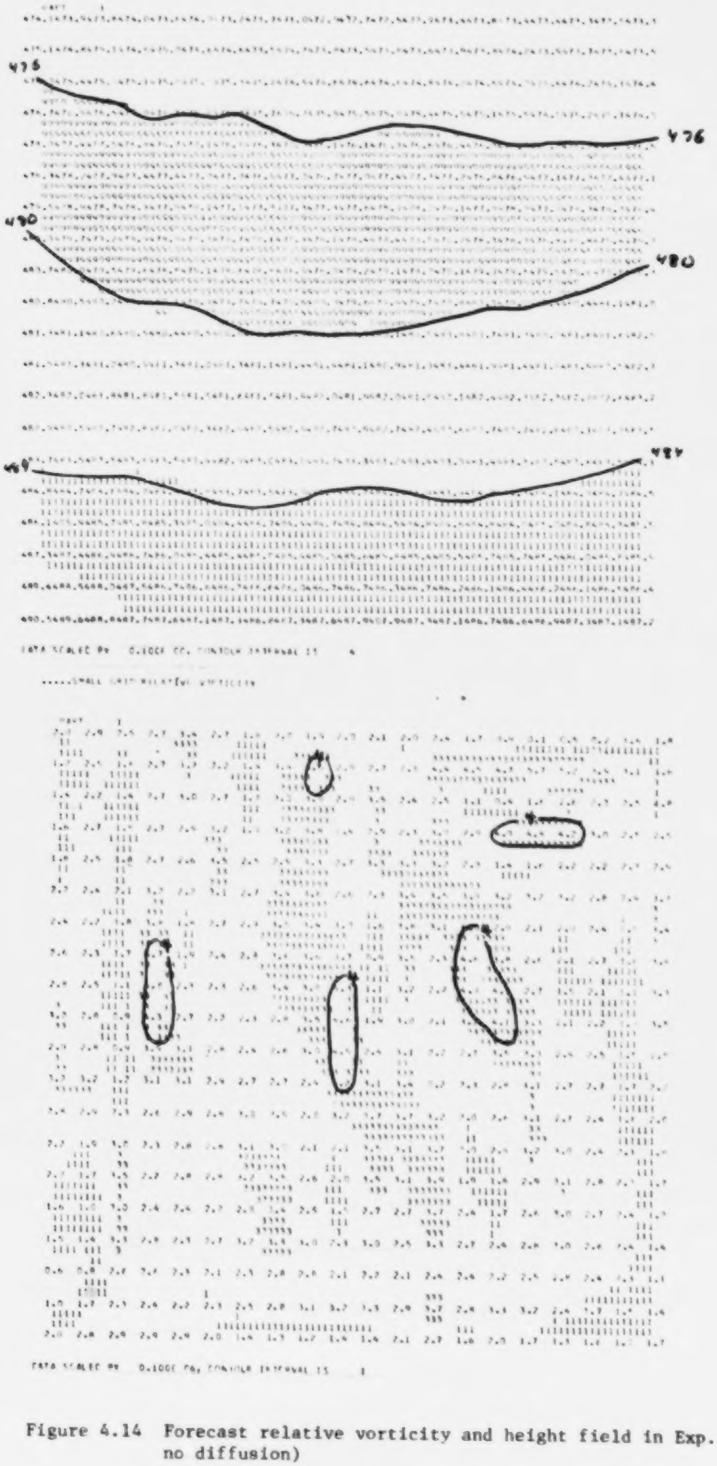

```
DATA SCALED BY   0.100E 00, CONTOUR INTERVAL IS    4

.....SMALL GRID RELATIVE VORTICITY

DATA SCALED BY   0.100E 00, CONTOUR INTERVAL IS    1
```

Figure 4.14 Forecast relative vorticity and height field in Exp. 2 (1-way, no diffusion)

.......SMALL GRID H

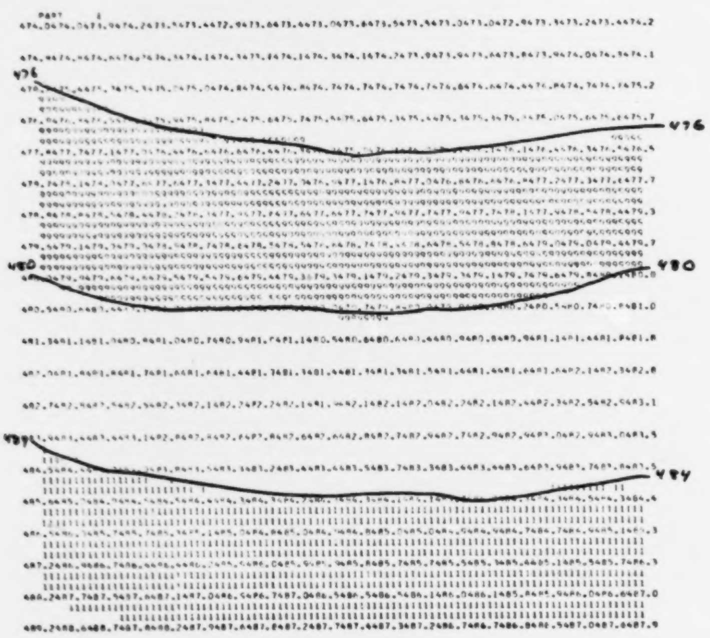

DATA SCALED BY 0.100E 00, CONTOUR INTERVAL IS 4

.....SMALL GRID RELATIVE VORTICITY

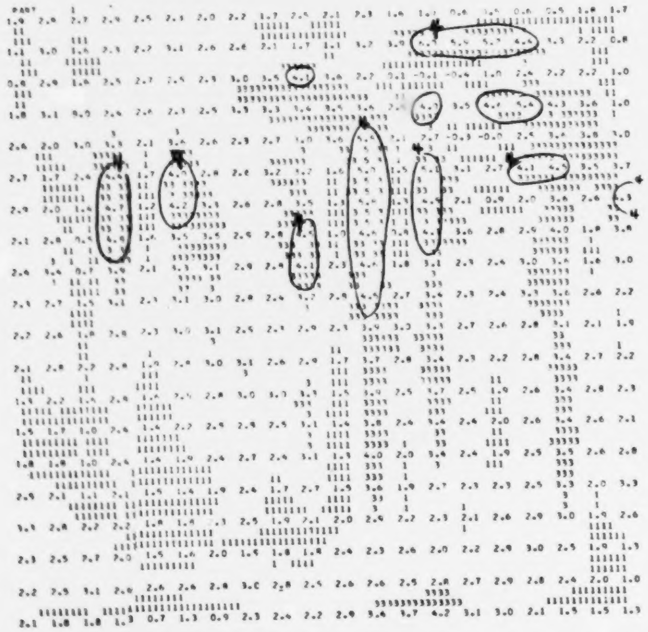

DATA SCALED BY 0.100E 06, CONTOUR INTERVAL IS 1

Figure 4.15 Forecast relative vorticity and height field in Exp. 3 (2-way, no diffusion)

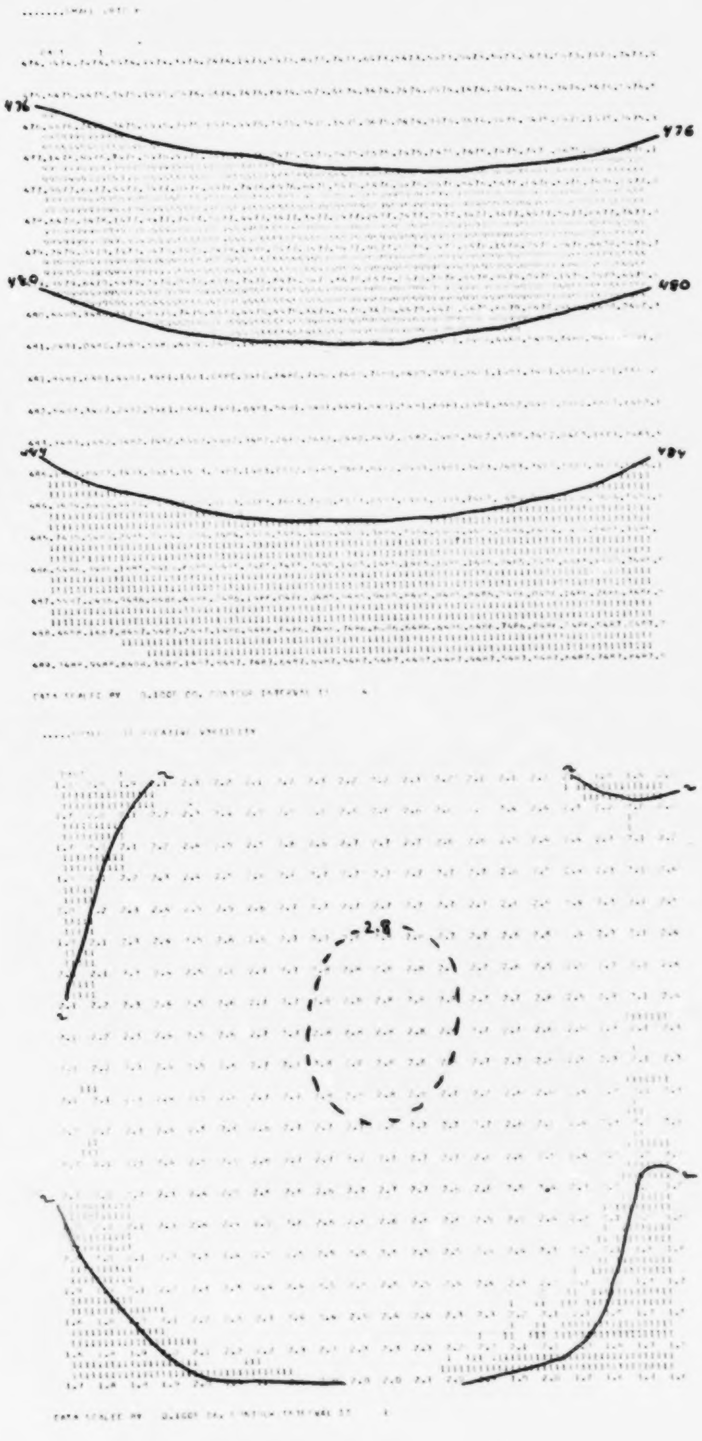

Figure 4.16 Forecast relative vorticity and height field in Exp. 4 (1-way with diffusion)

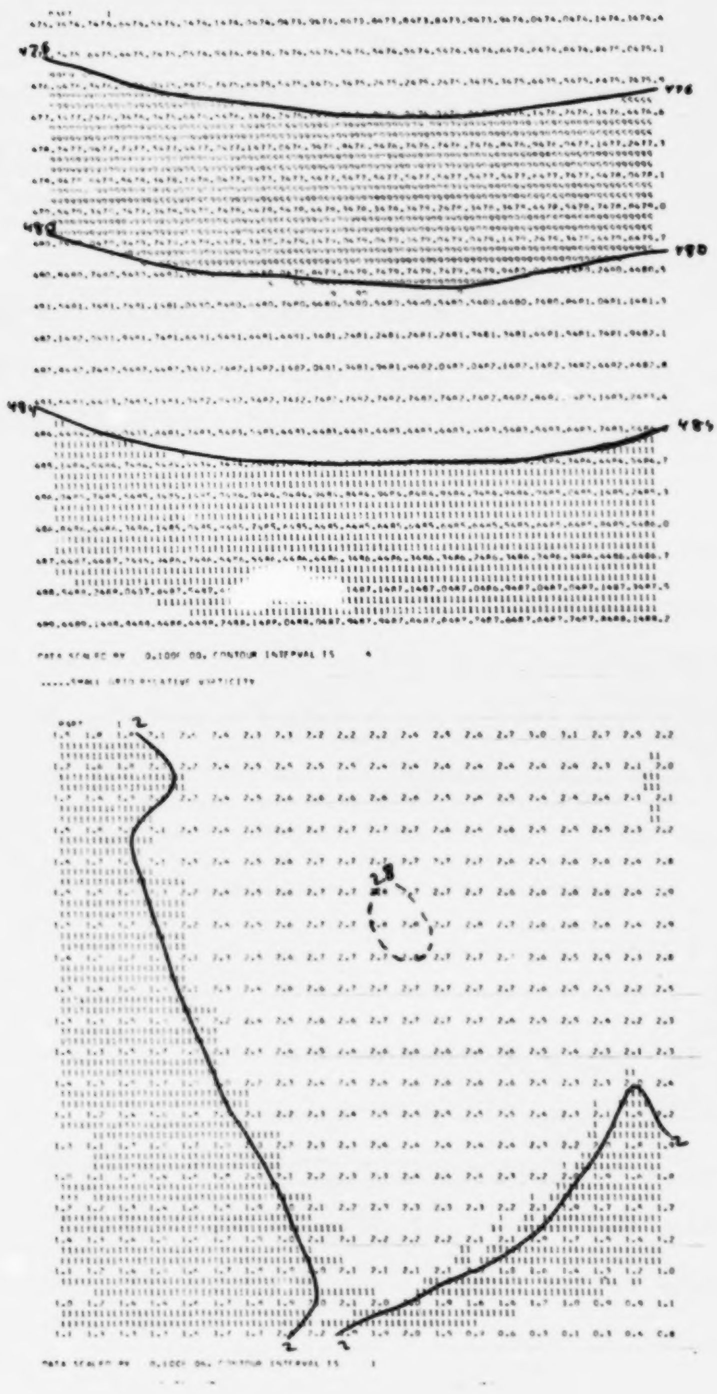

Figure 4.17 Forecast relative vorticity and height field in Exp. 5 (2-way with diffusion)

The statistics for Exp. 1 in Table 4.3 do show a high level of skill - the MSE are low and R is high. As mentioned previously, the phase speed in Exp. 1 is about 0.9 mps slower than the analytic value. If this were the only error in the forecast, after 24 hours, the phase lag would be between 9 and 10 degrees. Letting $\gamma = 9.5°$ in (4.43) we get R = 35. Because of the lateral boundary conditions, the non-linear term, and round-off errors, R in Exp. 1 is not equal to 35. However, it is close enough to suggest that much of the forecast errors is caused by the phase lag.

Both meshing techniques show a decrease of skill compared to the uniform CMG. As a result of the differences in the numerical phase speeds on the CMG and FMG, the solutions will tend to separate at the interface and shortwave noise will develop and gradually contaminate the solutions - most noticeably on the FMG. However, the statistics still indicate a high level of skill, with the one-way technique appearing to be slightly superior. This is especially true on the CMG because the noise generated at the interface cannot feed back to the large scale forecast in the one-way system.

Although the addition of diffusion (Exp. 4 and 5) does produce noticeably smoother fields (Fig. 9 and 10), the MSE actually increase slightly in some cases as the amplitude of the wave is reduced. This is another indication that most of the errors in the forecast are due to phase errors which are not reduced by any numerical smoothing devices such as diffusion.

Table 4.3

Measures of Error for Meshed Grid Experiments

Experiment Number	MSE_v	VAR_v	R_v	MSE_u	VAR_u	R_u
			CMG POINTS			
1	0.91	22.2	24.3	0.52	15.7	30.5
2	0.91	22.2	24.3	0.52	15.7	30.5
3	0.94	22.1	23.5	0.56	15.8	28.4
4	0.95	18.2	19.2	0.67	13.1	19.6
5	1.07	17.0	16.0	0.62	12.1	19.6
			FMG POINTS			
2	1.57	17.3	11.0	0.226	5.7	25.4
3	1.52	10.6	10.6	0.292	5.7	19.5
4	1.59	14.1	8.9	0.291	4.6	15.8
5	1.58	10.8	6.8	0.248	4.2	17.1

In summary, for a long wave that can be well resolved on a grid with uniform size, the addition of a nested fine mesh grid will not necessarily produce a better forecast. For example, the National Weather Service's addition of a Limited Fine Mesh (LFM) model - no matter how the boundaries are treated - will not improve the forecasts of the planetary scale waves which are well-forecast by the larger scale model. It is encouraging however, that the meshed forecast is still of high quality despite the continuous generation of noise at the interface.

4.4.4 Short wave results: Exp. 6-8.

Experiments 6, 7, and 8 are essentially identical to Exp. 1, 4, and 5 except that the wavelength is reduced by a factor of four. The initial height and v fields (Fig. 4.18 and 4.19) show four 800-km waves on the CMG. The FMG contains one complete wave. The purpose of these experiments is to test the meshing techniques under very severe conditions - when the numerical phase speed of the wave becomes quite different on the two grids. The analytic phase speed of an 800 km wave is 19.9 ms^{-1}, nearly equal to the mean wind speed. The numerical phase speed computed from (4.44) is 19.8 ms^{-1} on the FMG but only 14.9 ms^{-1} on the CMG. Thus, there is nearly a 5 ms^{-1} difference in numerical phase speeds between the grids. After six hours, this difference will result in a 45° phase difference, and after 24 hours the waves will be approximately 180° out of phase. These errors, of course, will introduce very large errors at the interface and greatly contaminate the forecasts on both grids. We should therefore expect the forecasts to rapidly deteriorate in skill with time.

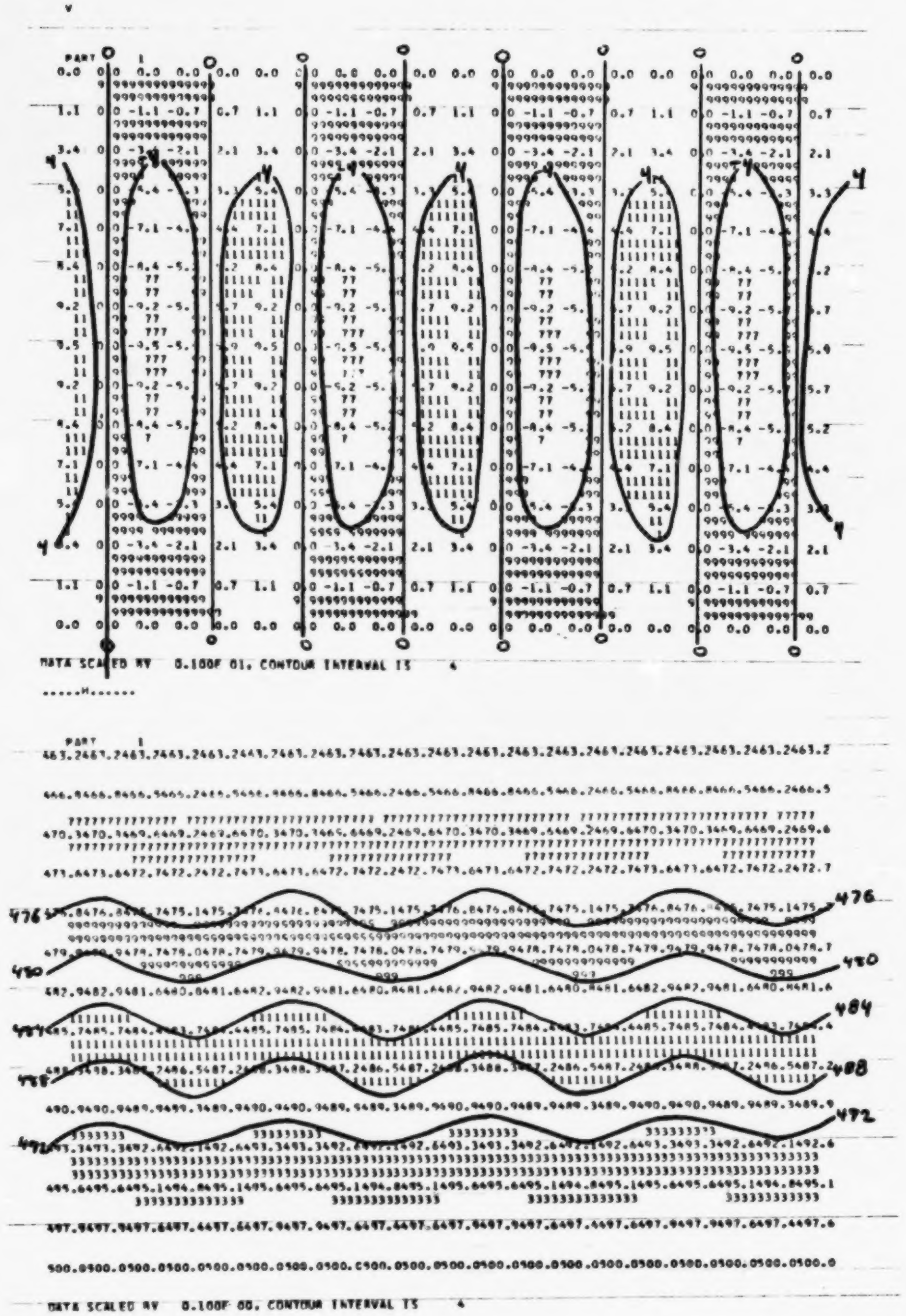

Figure 4.18 Initial height and v-component field on CMG for Exp. 6-8

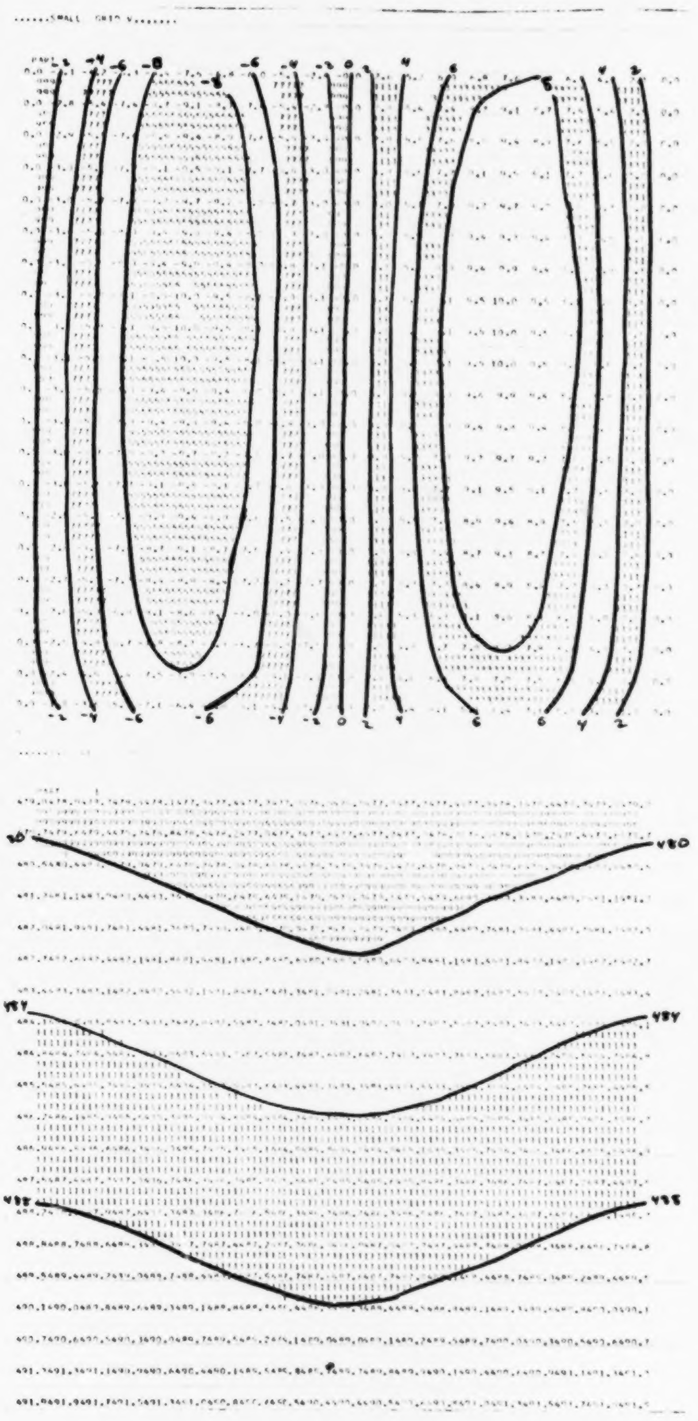

Figure 4.19 Initial height and v-component field on FMG for Exp. 6-8

Figures 4.20 and 4.23 show the height and v-component fields after six and twelve hours from Exp. 7 and 8. The difference in phase speeds is obvious in the v fields, where the wave moves faster in the middle of the FMG compared to points close to the north or south boundaries which are affected by the slower moving wave on the CMG. The height fields have become noisy by 12 hours and all fields continue to deteriorate out to 24 hours. Qualitatively, there again is little difference between the two meshing techniques.

The ratio of MSE to variance, R, for Exp. 6-8 are shown in Fig. 4.24. There is considerable skill in all experiments on both the FMG and CMG at 6 hours, although not nearly as much as for the experiments in Group A. By 18 hours, the difference of phase speeds and the resultant noise generated at the interface has virtually destroyed all skill in the forecasts, and R_v is close to 1.

The statistics in Fig. 4.24 indicate that at least out to 12 hours, the two-way meshing technique is somewhat better than the one-way technique. However, this apparent superiority is not consistently shown by the statistics for the other variables. These experiments indicate that neither meshing technique will be satisfactory when there is a large phase speed difference in waves which move along the interface. This difference occurs when the wave is too short to be adequately resolved on the CMG.

One encouraging result of these experiments is that the meshing of a grid with finer resolution in a larger domain does produce a better solution on the FMG than on the CMG. Fig. 4.24 shows that R for Exp. 7 and 8 is consistently higher on the FMG out to 12 hours. The improvement is observed for all variables. However, it must be noted that eventually

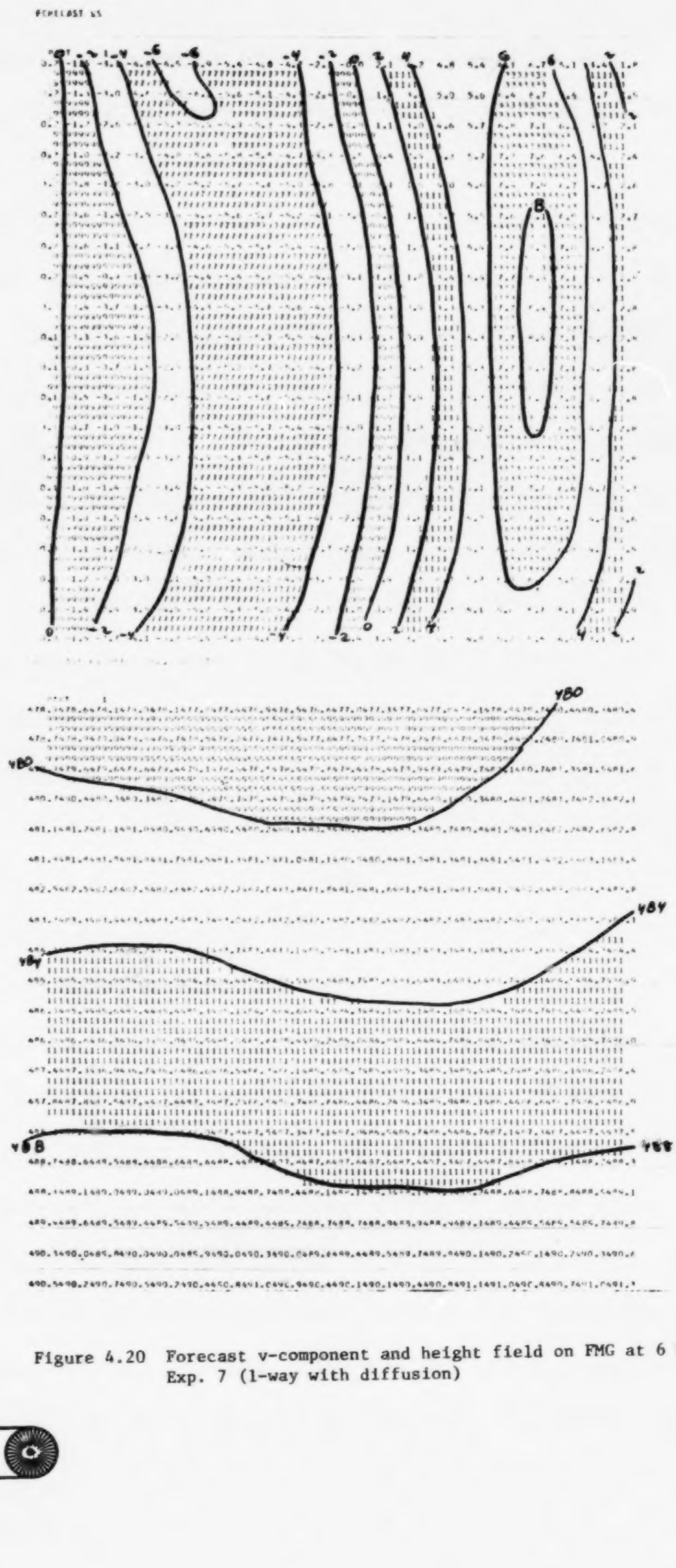

Figure 4.20 Forecast v-component and height field on FMG at 6 hours for Exp. 7 (1-way with diffusion)

Reproduced from best available copy.

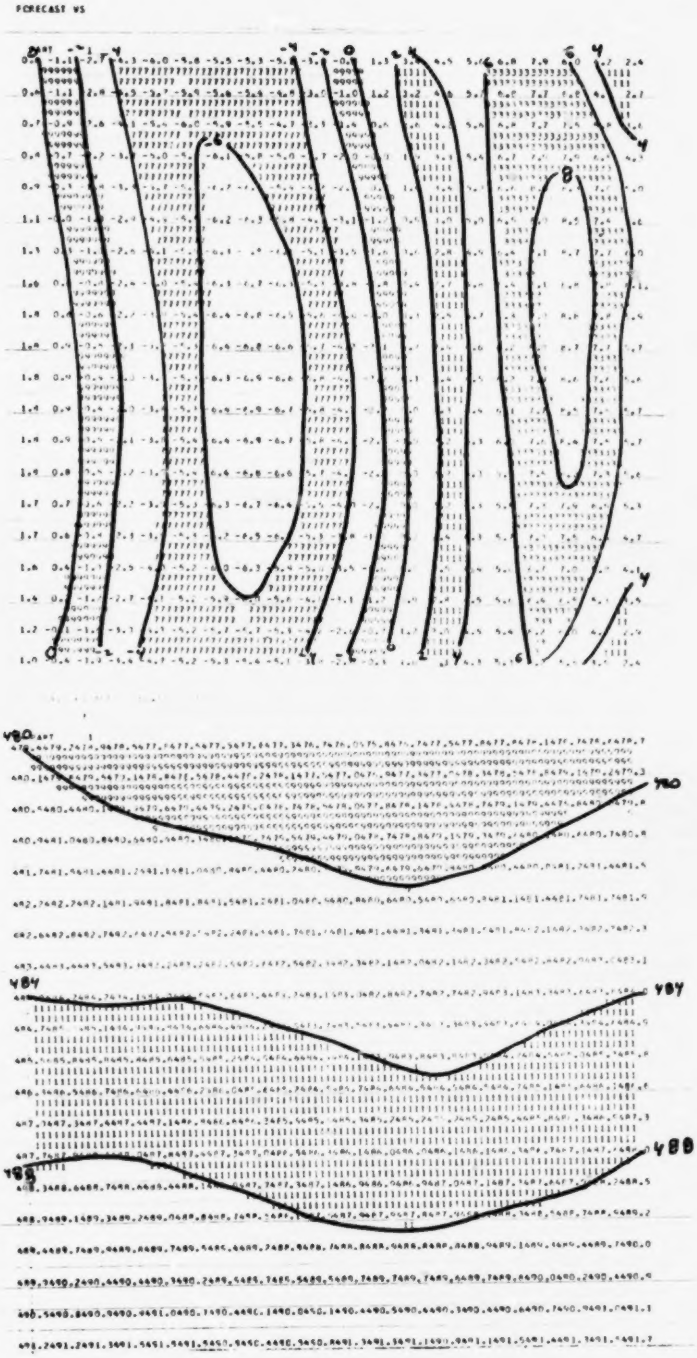

Figure 4.21 Forecast v-component and height field on FMG at 6 hours for Exp. 8 (2-way with diffusion)

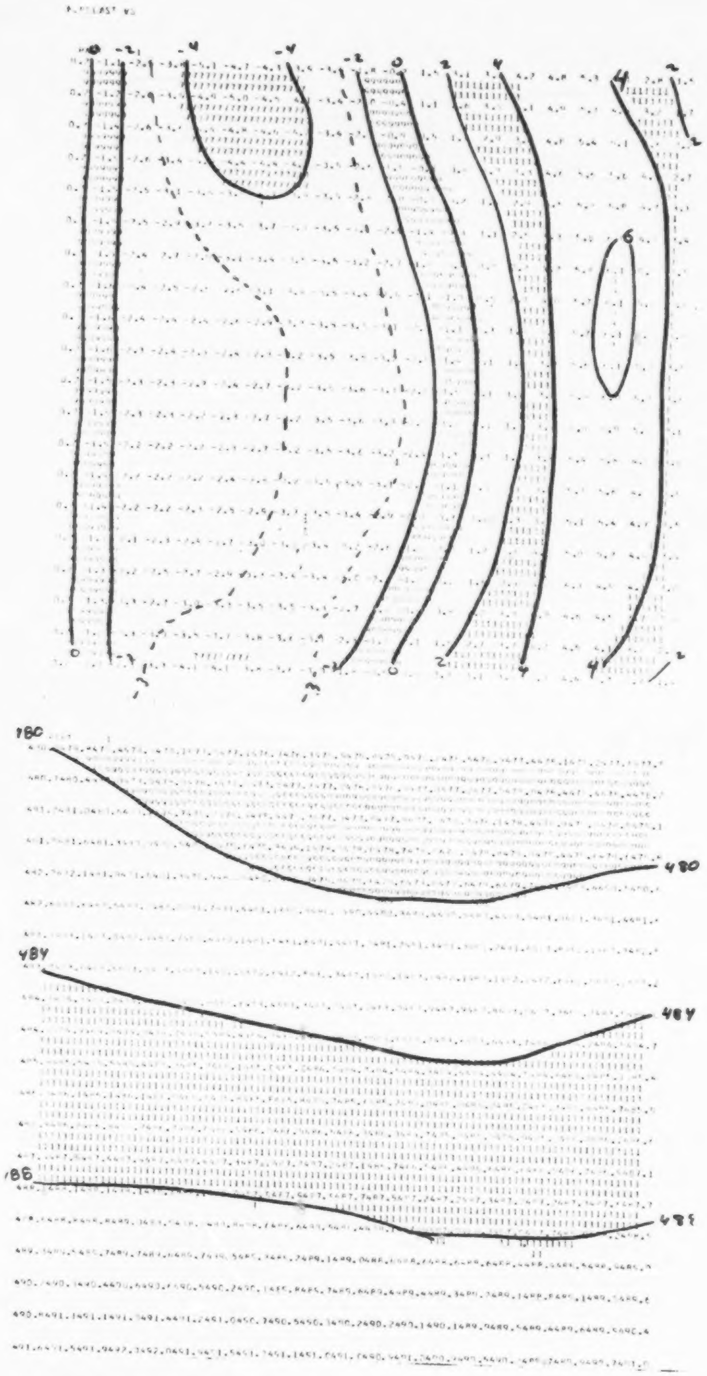

Figure 4.22 Forecast v-component and height field on FMG at 12 hours for Exp. 7 (1-way with diffusion)

Reproduced from best available copy.

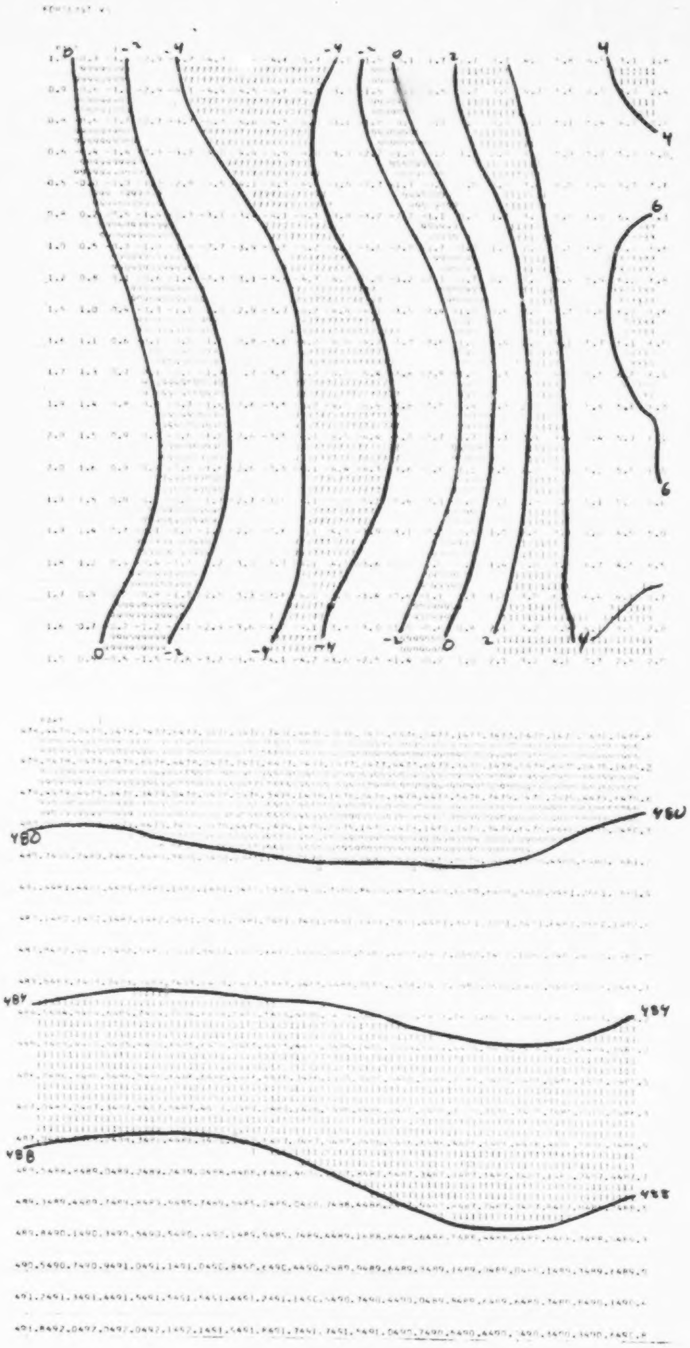

Figure 4.23 Forecast v-component and height field on FMG at 12 hours for Exp. 8 (2-way with diffusion)

Reproduced from best available copy.

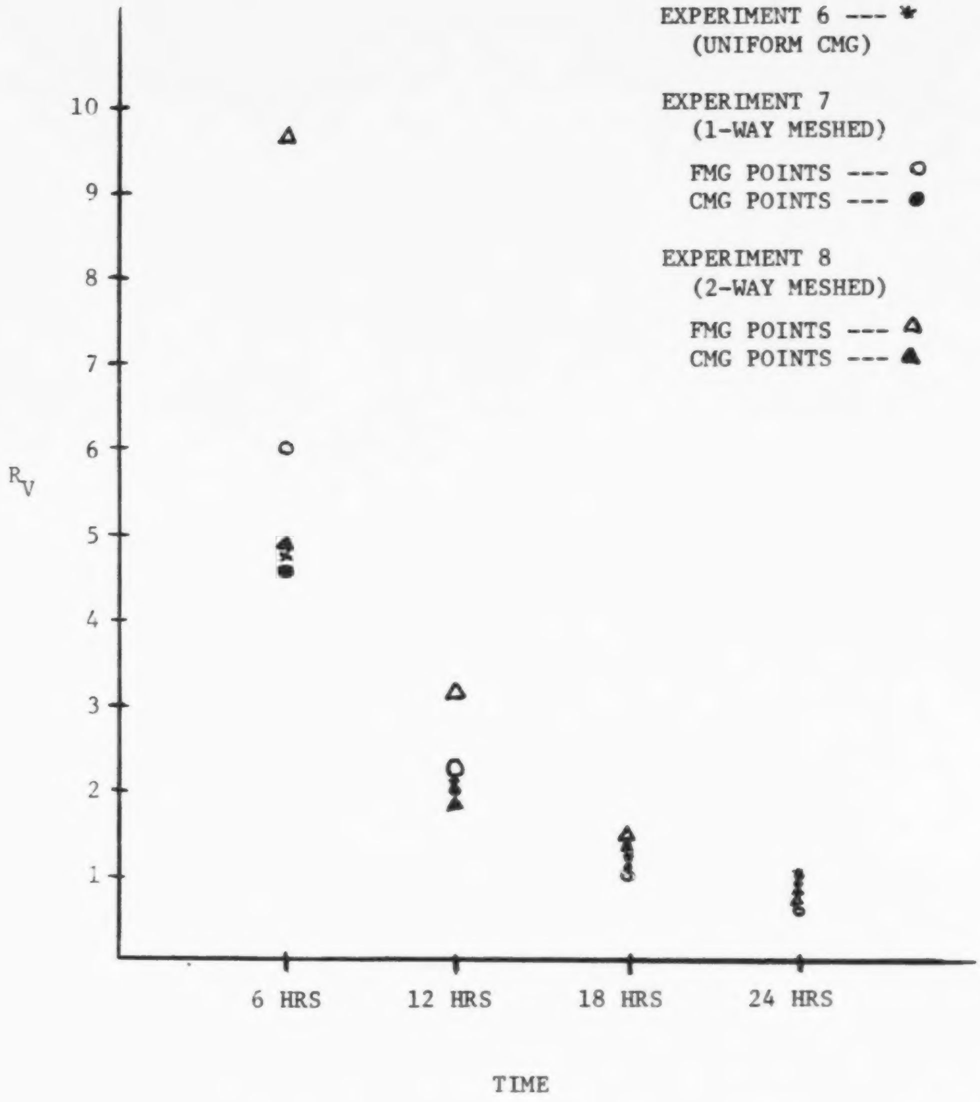

Figure 4.24 Ratio of variance to MSE for Exp. 6-8

the noise generated at the interface will contaminate the forecast on the FMG to the point where the advantage of the finer resolution is lost. This critical point in time is undoubtedly a function of the ratio of the grid sizes, but in this particular case, it occurs at about the period of the short wave on the CMG (13 hours). We might speculate that in a meshed, mesoscale model, for a traveling disturbance of the small cyclone scale that may not be well resolved on the CMG, this critical time would be on the order of 2 or 3 days. It is encouraging that this is probably longer than we would want to run a mesoscale forecast model.

4.4.5 Mixed long and short wave results. The use of nested grids is warranted when the fine mesh contains energy in shorter wavelengths than does the coarse mesh. To test the meshing technique under these conditions, a final set of experiments was run combining the 3200 km wave of Group A and the 800 km wave of Group B. The long wave covers the entire forecast domain. The short wave has an 800 km wavelength in the x direction, a 1600 km wavelength in the y direction, and is totally contained on the FMG. The short wave trough axis is initially located 5 FMG points upstream of the long wave trough axis (Fig. 4.25). Since analytically and computationally the short wave moves faster than the long wave, the waves will tend to phase during the first 12 hours as the short wave moves into the long wave trough position.

Because of the non-linear interaction between the two waves, it is not valid to linearly add the analytic solutions at any given time to produce a control forecast. Instead, a uniform FMG forecast (Exp. 9) over the entire domain was made and used as the control to compare with the results of the nested grid experiments.

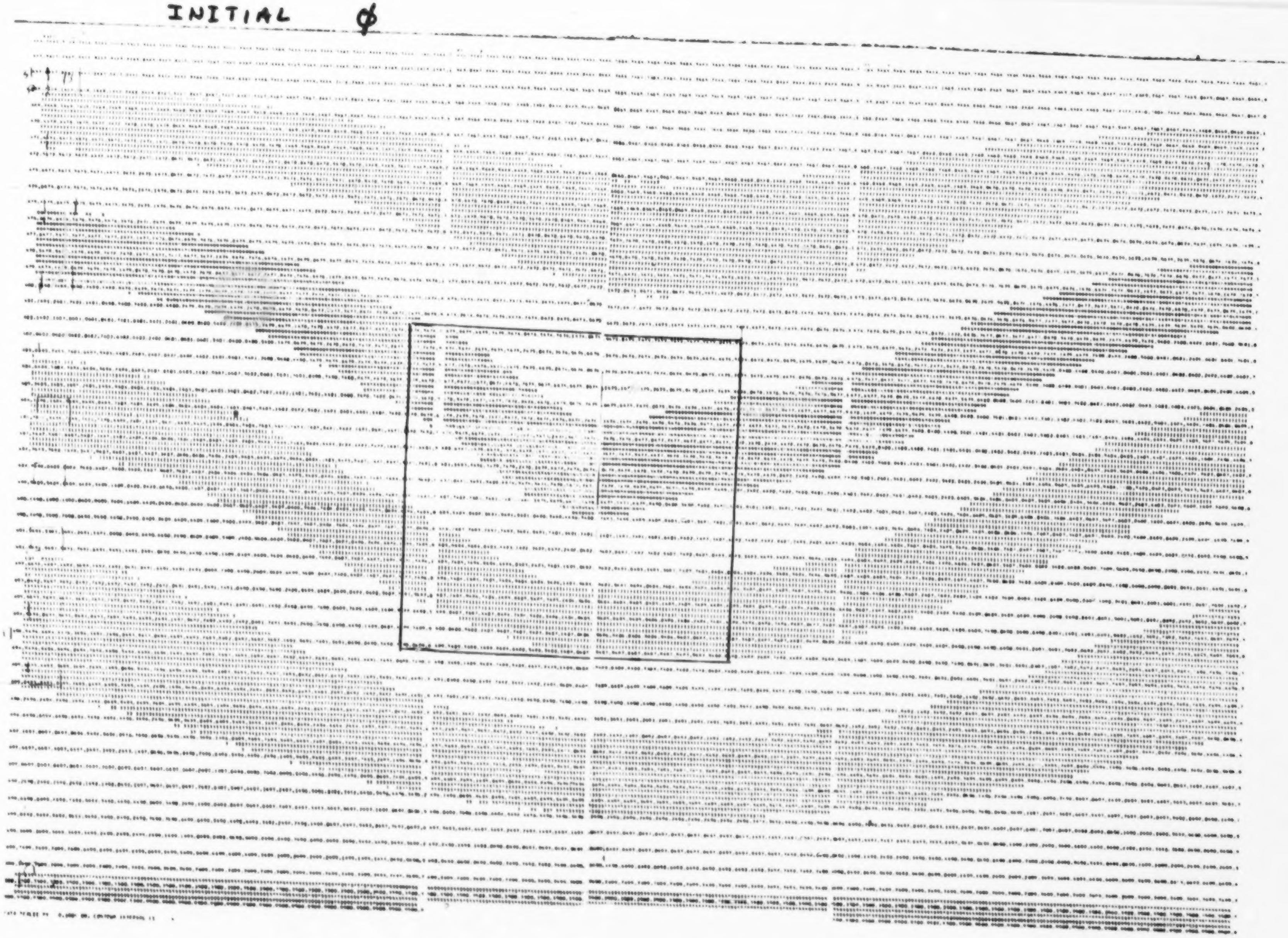

Figure 4.25 Initial ϕ for Experiments 9-11 (mixed long and short wave)

Reproduced from best available copy.

The initial geopotential and v-component fields for the control Exp. 9 are shown in Fig. 4.25 and 4.26. The square outline indicates the initial location of the FMG for Exp. 10 and 11. In the one-way case (Exp. 10), the CMG is initialized only with the long wave. Because the CMG is integrated independently of the FMG in Exp. 11, it never senses the existence of the short wave. As the results of Group A show, the CMG adequately forecasts the long wave. However, the boundary points of the FMG, specified continuously by the CMG and therefore containing no short wave information, introduce noise on the FMG.

Unlike earlier experiments, a larger diffusion coefficient on the CMG was found to be necessary in order to control the spread of noise from the interface of the meshed grids. $K = 2 \times 10^5$ was still used on the FMG, but $K = 8 \times 10^5$ was used on the CMG.

Fig. 4.27 shows the v-field from Exp. 9 after 800 ΔT_{FMG} or 13.3 h. Fig. 4.28 and 4.29 show the v-fields on the FMG from Exp. 10 and 11 at the same time. The velocity fields show quite clearly that the short wave has moved into the long wave trough position. The 0 ms^{-1} isotach marks the trough axis. Initially the short wave trough was 5 ΔX_{FMG} upstream of the long wave trough. After 800 time steps, the 0 isotach runs nearly north-south indicating the waves have phased.

Both the two-way and one-way interacting systems produce solutions with skill, however, the two-way experiment appears qualitatively more like the control uniform FMG experiment. In fact the v-field from Exp. 11 (two-way system) looks very similar to that of the control experiment.

INITIAL V-COMPONENT

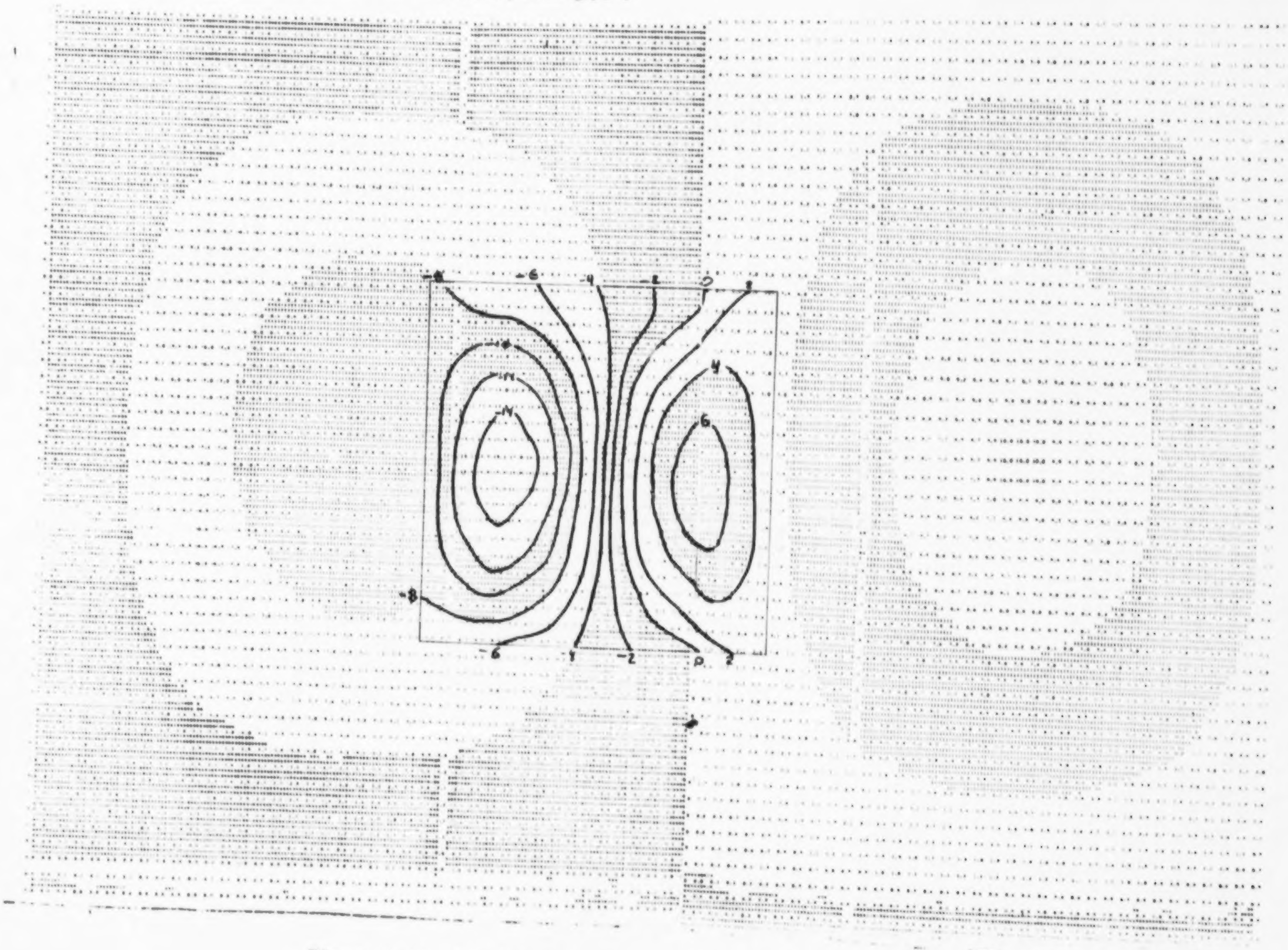

Figure 4.26 Initial v-component for Exp. 9-11 (mixed long and short waves)

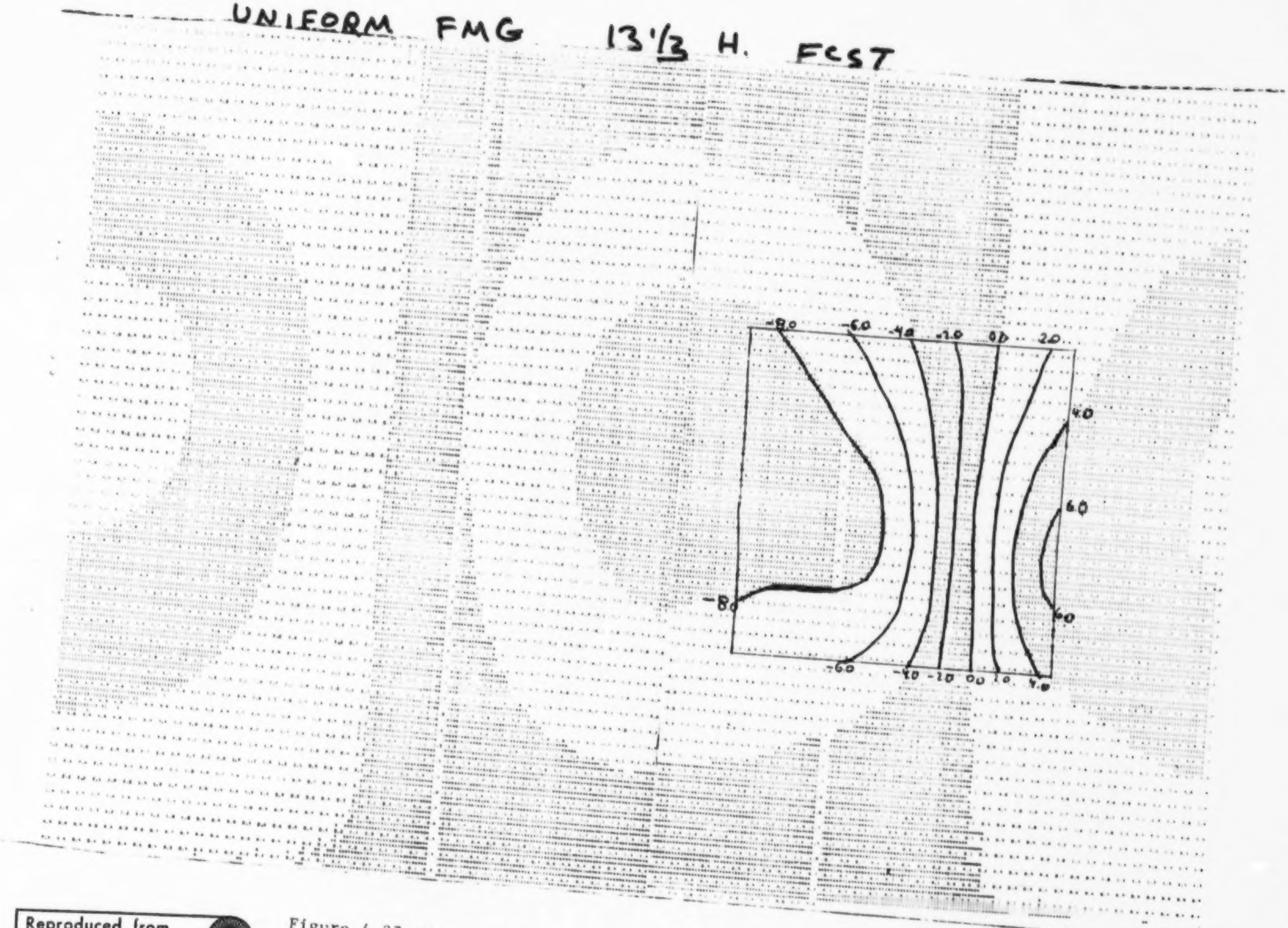

Reproduced from best available copy.

Figure 4.27 Forecast v-component at 13.3 h from Exp. 9 (uniform FMG)

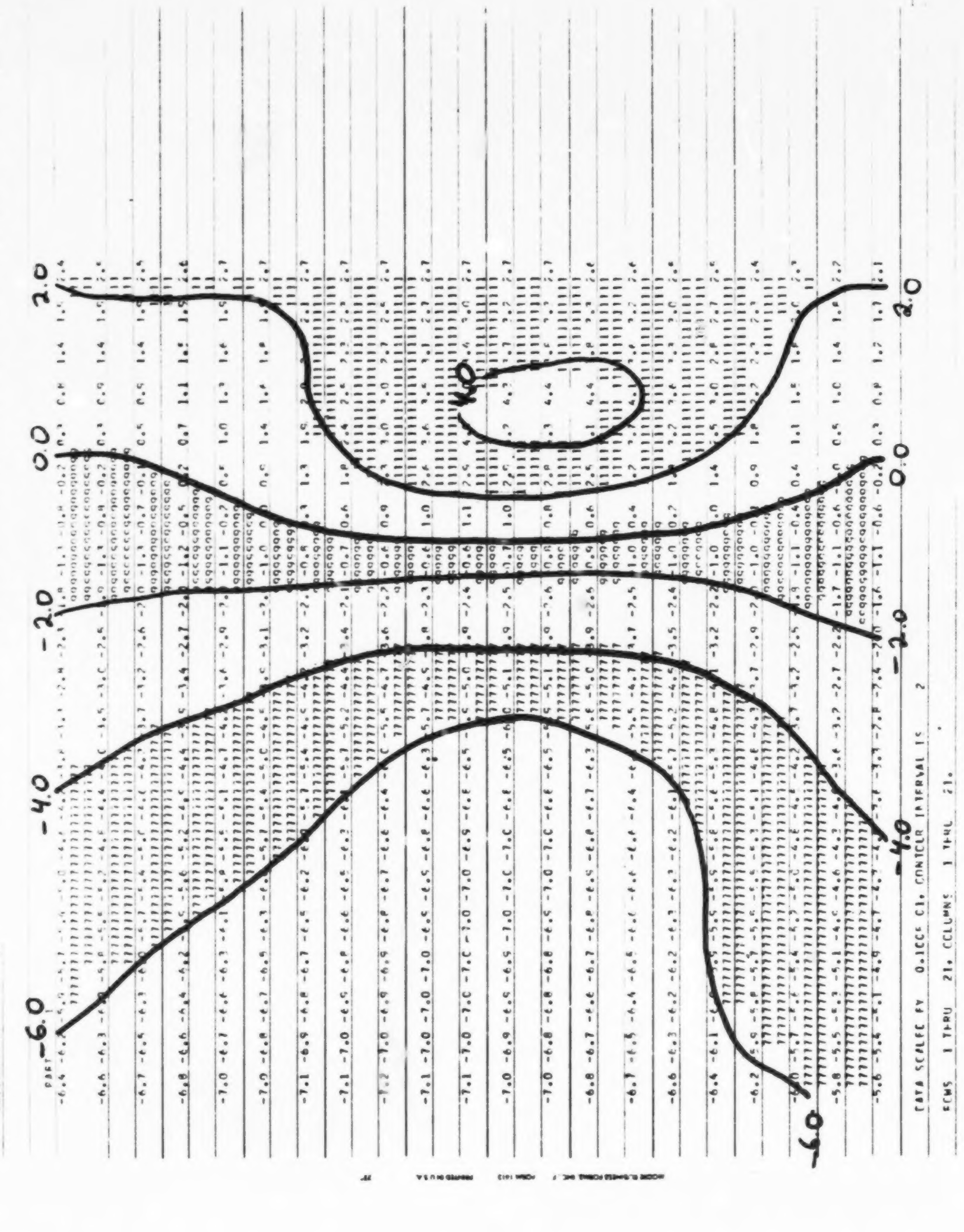

Figure 4.28 Forecast v-component at 13.3 h from Exp. 10 (1-way meshed system)

Figure 4.29 Forecast v-component at 13.3 h from Exp. 11 (2-way meshed system)

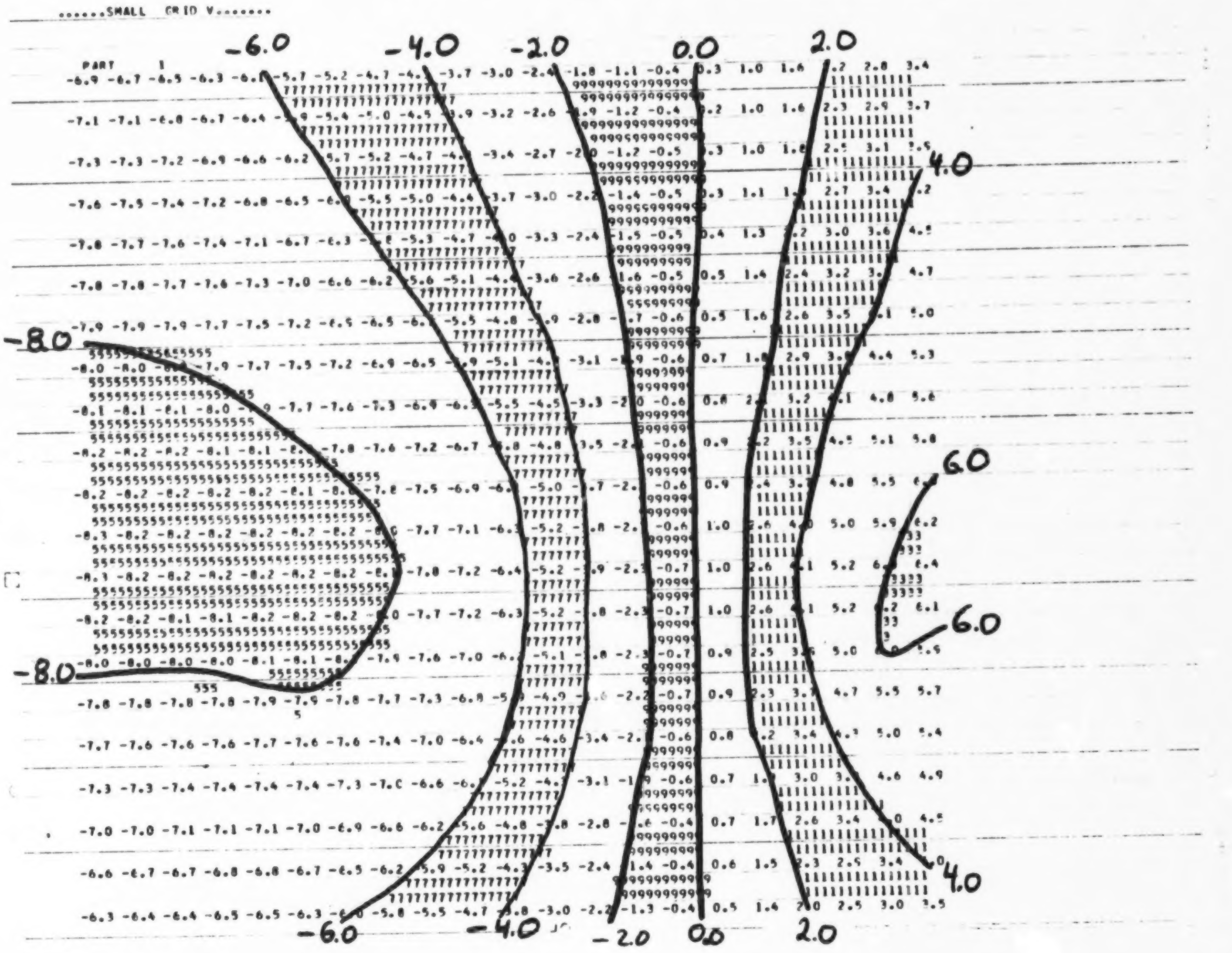

Table 4.4 shows quantitatively the same result. There is considerable skill in both methods at 13.3 hours, certainly more than the experiments of Group B where the short wave is very poorly forecast on the CMG. Unlike the previous experiments, there is a clear choice as to the preferred methods. In all cases, the two-way MSE's and R's are better than the comparable one-way results.

Other investigators (Harrison and Elsberry, 1972 - Phillips and Shukla, 1973) have indicated that the two-way system is the superior technique to use in a meshed numerical model. The last group of experiments in which there was a clear, distinct separation of the scales of motion on the two grids tends to confirm this result. However, the results from the experiments in which only a single scale of disturbance was present, indicate there was little difference in the two techniques. It is also possible that as the ratio of the grid lengths on the CMG to the FMG increases, the one-way system will prove more viable than the two-way system, because disturbances which are adequately resolved on the FMG will be badly aliased as they move onto the CMG. In such a two-way system, the disturbances entering the CMG would have to be diffused in space to prevent large numerical errors.

Table 4.4

Integrated Measures of Errors for Mixed Haurwitz Waves - 13-1/3 hours

		VAR_u	MSE_u	$\frac{VAR}{MSE_u}$	VAR_v	MSE_v	$\frac{VAR}{MSE_v}$
ALL CMG	1 way	10.95	.89	12.30	14.32	1.06	13.51
	2 way	11.93	.66	18.08	16.44	.75	21.92
COINCIDENT CMG	1 way	5.99	1.71	3.50	13.99	2.02	6.93
	2 way	12.32	.60	20.53	22.65	.95	24.62
ALL FMG	1 way	6.41	1.63	3.93	13.20	1.98	6.67
	2 way	11.94	.61	19.57	20.53	.93	22.08

5.0 INVESTIGATION OF SEMI-IMPLICIT MODELS

5.1 Advantages of semi-implicit models over explicit models

Because of the small grid sizes demanded by regional-scale models, the time step must be quite small in order to maintain the CFL criterion ($\frac{c\Delta t}{\Delta x} < 1$) which is necessary for the stability of explicit models. For an external gravity wave speed of 300 m/s and a grid length of 20 km, the maximum possible time step is 66.7 s for an unstaggered grid. For the staggered grid used in the 3-D mesoscale model, the criterion is $\frac{c\Delta t}{\Delta x} < \frac{\sqrt{2}}{2}$, which yields a maximum time step of 47 s for the 20 km grid.

In many meteorological modelling applications, as the horizontal grid scale decreases, so does the time-scale of the dominant scale of motion. Thus a thunderstorm model may require a 200 m grid and a time step of 0.67 s, but the time scale of the thunderstorm is one hour, requiring roughly 5400 time steps of calculation for the complete forecast. However, the mesoscale includes phenomena with not only short time scales (as mountain waves or squall lines), but also longer scales associated with diurnal variation in heating or inertial effects. Thus, it may be necessary for mesoscale models to predict on a relatively fine mesh for 24 hours in order to model diurnal heating effects and inertial oscillations. For these longer integrations, it would be more desirable than ever to utilize computational methods that can tolerate larger time steps. For example, the maximum time step of 47 s discussed above for the 20 km regional model is much smaller than is necessary to adequately resolve the diurnal heating cycle. If a method could be found which would be stable for a time step of 5 minutes, for example, the part of the solution determined by the diurnal heating variation would likely be very nearly the same.

Recently, Kwizak and Robert (1971), and Gerrity et al, (1973) have utilized so called "semi-implicit" models to allow the use of greater time steps in atmospheric models. By writing the finite difference analogs to the relevant dynamic equations in a form which treats the terms in the equations that are primarily responsible for the propagation of gravity waves implicitly rather than explicitly, larger time steps than those specified by the CFL restriction can be used. The "rule of thumb" appears to be that the time required to make a forecast can be reduced by a factor of four to six through the use of "semi-implicit" techniques. One of the costs of such a gain is an increase in the complexity of the model; another may be a loss of accuracy or a significant change in the adjustment times of models. The latter possibility needs further investigation with atmospheric models, especially on the mesoscale where external and internal gravity waves play a very important role in the adjustment of the mass and momentum fields.

In spite of the potential drawbacks, however, the probable gain in speed by a factor of four is attractive and we are investigating the possibility of utilizing semi-implicit modeling techniques for the mesoscale model. In order to develop familiarity with the technique and to isolate such problems as lateral boundary conditions and staggered horizontal grids, a number of one- and two-dimensional experiments have been conducted with the "shallow fluid" equations with both explicit and implicit models. The results from these experiments (presented in the following sections) have been sufficiently encouraging to warrant the coding of a 3-D semi-implicit atmospheric model to be analogous as far as possible to the explicit regional model already under development.

5.2 Comparison of one-dimensional explicit and semi-implicit shallow fluid model

The initial comparisons of the explicit and semi-implicit (S.I.) techniques are made with one-dimensional shallow fluid models, which are governed by the equation of motion and continuity equation,

$$\frac{\partial hu}{\partial t} = - \frac{\partial huu}{\partial x} - gh \frac{\partial h}{\partial x} \tag{5.1}$$

$$\frac{\partial h}{\partial t} = - \frac{\partial hu}{\partial x} \tag{5.2}$$

In analogy with the 3-D atmospheric regional model, a staggered grid is used with the velocity components and height defined at alternate grid points. The staggered grid provides for a better resolution of the pressure gradient force ($\frac{\partial h}{\partial x}$) and the horizontal mass divergence ($\frac{\partial hu}{\partial x}$) than a grid in which all variables are defined at all grid points.

5.2.1 Development of explicit model. With the notation:

$$\alpha_x = \frac{\alpha_{j + 1/2} - \alpha_{j - 1/2}}{\Delta x} \tag{5.3}$$

$$\overline{\alpha}^x = \frac{\alpha_{j + 1/2} + \alpha_{j - 1/2}}{2} \quad , \tag{5.4}$$

the finite difference equations for the explicit model may be written:

$$\overline{(hu)}^t_t = - (\overline{hu}^x \, \overline{u}^x)_x - g\overline{h}^x \, h_x \tag{5.5}$$

$$\overline{h}^t_t = - (hu)_x \quad , \tag{5.6}$$

where (hu) is defined at $x_j = (j - 1)\ \Delta x$, $j = 1, 2 \ldots J_{max}$; and h is defined at $x_j = (j - 1/2)\ \Delta x$ for $j = 1, 2 \ldots, J_{max}-1$. The decoupled velocity, u_j, is obtained from (hu); according to

$$u = \frac{2(hu)_j}{(h_{j+1/2} + h_{j-1/2})} \quad . \tag{5.7}$$

The finite difference equations (5.5) and (5.6) provide a complete set of finite difference equations which may be integrated as an initial value problem. The first time step consists of a forward rather than centered time difference.

5.2.2 Development of semi-implicit model. The semi-implicit model is also based upon equations (5.1) and (5.2) in accordance with the semi-implicit form of primitive equations as used by Kwizak and Robert (1971) and by Gerrity, McPherson, and Scolnik (1973)[1]. The pressure gradient and divergence terms are treated implicitly; other terms (except temporal derivatives, of course) explicitly. However, in the flux form of the equations, the term $(hu)_x$ is a combination of the advection and divergence terms of the continuity equation. It was considered to be the divergence of the mass-weighted momentum, hu, and as such was treated implicitly.

---

[1] The semi-implicit scheme was also reported by Kurihara (1965) as "partly-implicit" and by McPherson (1973) as "implicit-backward".

After linearization of the pressure gradient term by the perturbation method, the semi-implicit finite difference forms of equations (5.1) and (5.2) become, with

$$h = H + h' \tag{5.8}$$

and τ denoting the time step ($t = \tau\Delta t$),

$$\begin{aligned} \overline{hu}^{2t} + \Delta t \; gH \; \overline{h}^{2t} &= hu^{\tau-1} - \Delta t \; \overline{gh'^{\tau}}^{x} \; h_x^{\tau} \\ &\quad - \Delta t \; (\overline{u^{\tau}}^{x} \; \overline{hu^{\tau}}^{x})_x \equiv F_1 \end{aligned} \tag{5.9}$$

$$\overline{h}^{2t} + \Delta t \; \overline{hu}_x^{2t} = h^{\tau-1} \equiv F_2 \quad . \tag{5.10}$$

In equations (5.9) and (5.10)

$$\overline{L}^{2t} = \frac{1}{2} (L^{\tau+1} + L^{\tau-1}) \quad , \tag{5.11}$$

where L is any variable.

Equations (5.8) - (5.10) now constitute a system of semi-implicit finite difference equations. They cannot be solved directly, as can the explicit equations, because the left sides of (5.9) and (5.10) each contain two terms which are unknown at time $t = \tau$.

Differentiation of (5.9) by x yields

$$\overline{hu}^{2t}_{x} = -\Delta t\, gH\, \overline{h}^{2t}_{xx} + F_{1_x} \quad , \qquad (5.12)$$

and the substitution of (5.12) into (5.10) gives

$$\overline{h}^{2t} - \Delta t^2\, gH\, \overline{h}^{2t}_{xx} = \Delta t\, F_{1_x} + F_2 \equiv G \quad . \qquad (5.13)$$

Equation (5.13) is a Helmholtz type equation and can be solved for $\overline{h}^{2t}$ by the relaxation method. If we define $\overline{h}^{2t} \equiv T$ and:

$$\boldsymbol{\nabla}^2 T \equiv (\Delta x)^2 \nabla^2 T \quad , \qquad (5.14)$$

then equation (5.13) becomes

$$\boldsymbol{\nabla}^2 T - \lambda^2 T = E \qquad (5.15)$$

where

$$T \equiv \overline{h}^{2t} \qquad (5.16)$$

$$\lambda^2 \equiv \frac{(\Delta x)^2}{\Delta t^2 \, gH} \tag{5.17}$$

$$E = -\lambda^2 G \quad . \tag{5.18}$$

The unknown T may be found by relaxation. The quantity E is known at $t = \tau\Delta t$ for each grid point. An initial guess, T^o, must be made for T at each time step. After experimentation, the best first guess was found to be linear extrapolation of the height tendency,

$$T^o = h^\tau + \frac{1}{2}\,(h^{\tau-1} + T^{\tau-1}) \quad . \tag{5.19}$$

The quantity T is solved by Leibmann (simultaneous) relaxation. A residual is calculated and used to correct the current guess at a particular grid point, followed by an alteration of the value of T based on the residual. The m^{th} iteration is calculated by

$$R_j^{\,m} = T^{m+1}_{j-1} + T^m_{j+1} - (2 + \lambda^2)\, T^m_j - E_j \tag{5.20}$$

$$T^{m+1}_j = T^m_j + \frac{\alpha R^m_j}{2 + \lambda^2} \quad , \tag{5.21}$$

where α is the relaxation coefficient and varies between 0.5 and 2.0 in these experiments. This iterative procedure is continued until the maximum residual across the grid is less than some arbitrary value, ε. The choice of ε influences the number of iterations (and thus the speed of computation), and the accuracy of the resulting forecast.

Once a value of $T = \overline{h}^{2t}$ is found, $\overline{hu}^{2t}$ is obtained by substitution of $\overline{h}^{2t}$ into equation (5.9). Then the forecast values are easily recovered according to

$$h^{\tau+1} = 2\overline{h}^{2t} - h^{\tau-1} \tag{5.22}$$

$$(hu)^{\tau+1} = 2\,\overline{hu}^{2t} - hu^{\tau-1} \quad , \tag{5.23}$$

5.2.3. Initialization of models. Both one-dimensional models are initialized in the same manner. The number of grid points is 96, the grid size Δx is 50 km, and cyclic boundary conditions are used. The mean fluid depth is 1000 m and since the model is meant to be isentropic, a reduced value of gravity $g^* = 1/4\ g$, is used (Seaman, 1973). A perturbation of amplitude $\hat{h} = 25$ m and wave number one is superimposed on the fluid. The initial velocity field is placed in linear balance with the height field by the relation

$$\hat{u} = \frac{g^*}{(g^* H)^{1/2}}\ \hat{h} \quad . \tag{5.24}$$

With all energy initially in wave number one, numerical and physical dispersion should be minimized during the forecast process. Both models use explicit, forward-in-time, centered-in-space finite differences for the initial time step.

5.2.4. Results. The explicit model was run with $\Delta t = 300$ sec. For the above values of g^* and mean depth, the linear phase speed of the gravity wave is 49.44 m/sec. (same for the S.I. model case).

For these choices of parameters, $\frac{c\Delta t}{\Delta x} = 0.3$ which satisfies the linear computational stability requirement for the centered-in-time, staggered-in-space finite difference scheme in the explicit model, which is $\frac{c\Delta t}{\Delta x} < 1/2$.

Several 24-hour forecasts were performed with the S.I. model to "tune" the model parameters, α, ε, and Δt. The basis for comparison in these experiments was the 24-hour explicit forecast, in which the wave moved at a speed of 49.35 ms^{-1}, which is 99.82% of the linear phase speed. The forecast height profiles from two of the S.I. model forecasts (with Δt = 1800 and 3600 s) are compared to the height profile from the explicit model in Fig. 5.1. In the S.I. experiment in which Δt = 1800 s (six times greater than the explicit model time step), the forecast profiles from the S.I. and explicit models agree very closely. For a S.I. time step of 3600 s (12 times the explicit model's Δt), the S.I. wave lags noticeably the explicit wave.

Sensitivity experiments with the S.I. model revealed the dependency of the forecast accuracy upon the choice of ε. It was necessary to decrease ε as the length of the time step increased, in order to prevent the growth of short wavelength errors in the forecast (2 Δx noise). By reducing ε from 6.27 to 0.0627, the time step could be increased from 300 sec to 1800 sec. This resulted in a 24-hour forecast essentially free of short wavelength noise, as shown in Fig. 5.1.

Although short wavelength noise could be successfully controlled by reducing ε as Δt increased, other distortions from the explicit results increased as the time step was lengthened. With a Δt = 1800 sec, the

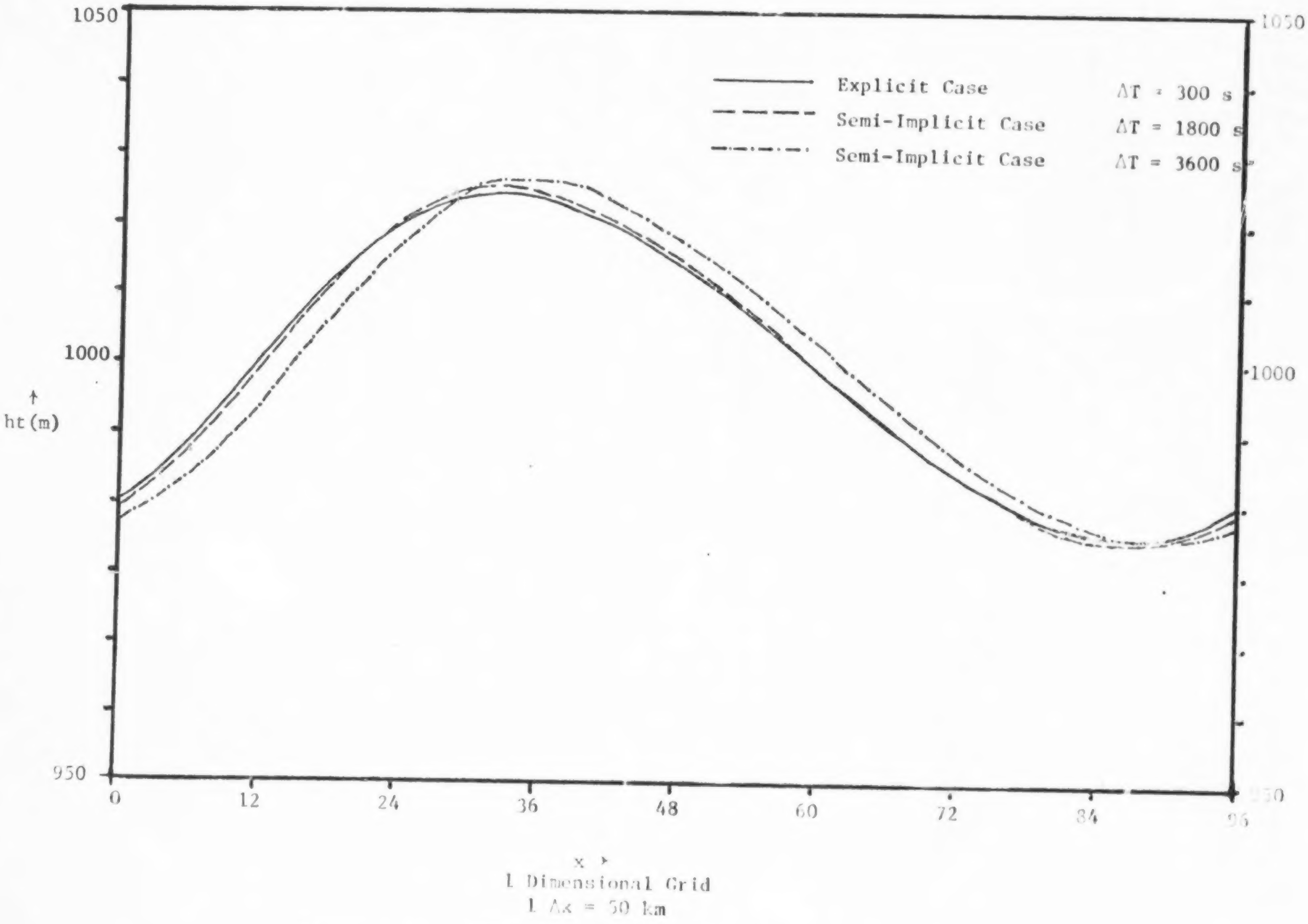

Figure 5.1 Comparison of one dimensional explicit and S.I. forecasts at 24 hours

observed phase speed decreased to 49.02 m/sec or 99.16% of the analytic phase speed. Also, the amplitude of the wave oscillated by ± 1.1 m.

In spite of the above problems, the S.I. forecast using a time step of 1800 s was still quite acceptable at 24 h. Mass remains constant within 0.007%, and the total energy change is only 0.012%. Furthermore, the wave remains smooth and moves at nearly the linear phase speed.

Several S.I. experiments were conducted with even longer time steps, up to 3600 s. A smooth solution was obtained by decreasing ε, but other errors increased significantly. With Δt equal to 3600 s, the computational phase speed was only 47.74 m/sec, or 96.6% of the linear phase speed. Also, the oscillation of the height of the wave crest increased to ± 1.8 meters. For these reasons, a $\Delta t = 1800$ s was chosen as the maximum time step capable of giving an acceptable forecast.

In addition to accuracy, the second important aspect of the S.I. model results is the efficiency of the computations. The efficiency or speed depends not only on the length of the time step, but also on the number of relaxation iterations required for a 24-hour forecast. The objective is to use the fewest possible iterations per 24 hour forecast period that are consistent with accurate results. The number of iterations per time step is dependent on Δt, α and ε. If ε is too large, the resulting "noisy" solutions required more iterations to satisfy even this coarse tolerance. On the other hand, if ε was too small, the noise was suppressed, but extra iterations were required to achieve the fine tolerance. Efficiency was obtained by a compromise between the two extremes.

A third factor affecting the rate of convergence is the overrelaxation coefficient, α. The number of iterations required per time step was found to be highly dependent upon α, with $\alpha = 1.4$ being the best choice for the 1-D model. Fig. 5.2 shows the dependency of the number of iterations required for a 24-hour forecast (and the average number of iterations per time step) as a function of α for four different first guesses.

The sensitivity tests showed that by judicious choice of ε, α and the first guess, the number of iterations per 24 hours could be reduced to 255, or between 5 and 6 iterations per time step with $\Delta t = 1800$ sec. When $\Delta t = 3600$ sec, the iterations per time step rose rapidly to between 17 and 18, or 421 per 24 hour forecast. Thus, the 1 hour time step is not only of poor quality, but is less efficient as well. An efficiency ratio may be defined as

$$E = T_{EX}/T_{S.I.} \tag{5.25}$$

where T_{EX} and $T_{S.I.}$ are the times required to compute a 24 hour forecast with the explicit and S.I. models respectively. The maximum efficiency obtained with acceptable accuracy with $\Delta t = 1800$ s was found to be 2.35.

Much of the literature, for example Kwizak and Robert (1971), indicates that implicit models should be able to produce efficiency ratios of roughly 4.0. The efficiency ratio of the S.I. model results discussed above might therefore appear disappointing. However, it must be remembered that models

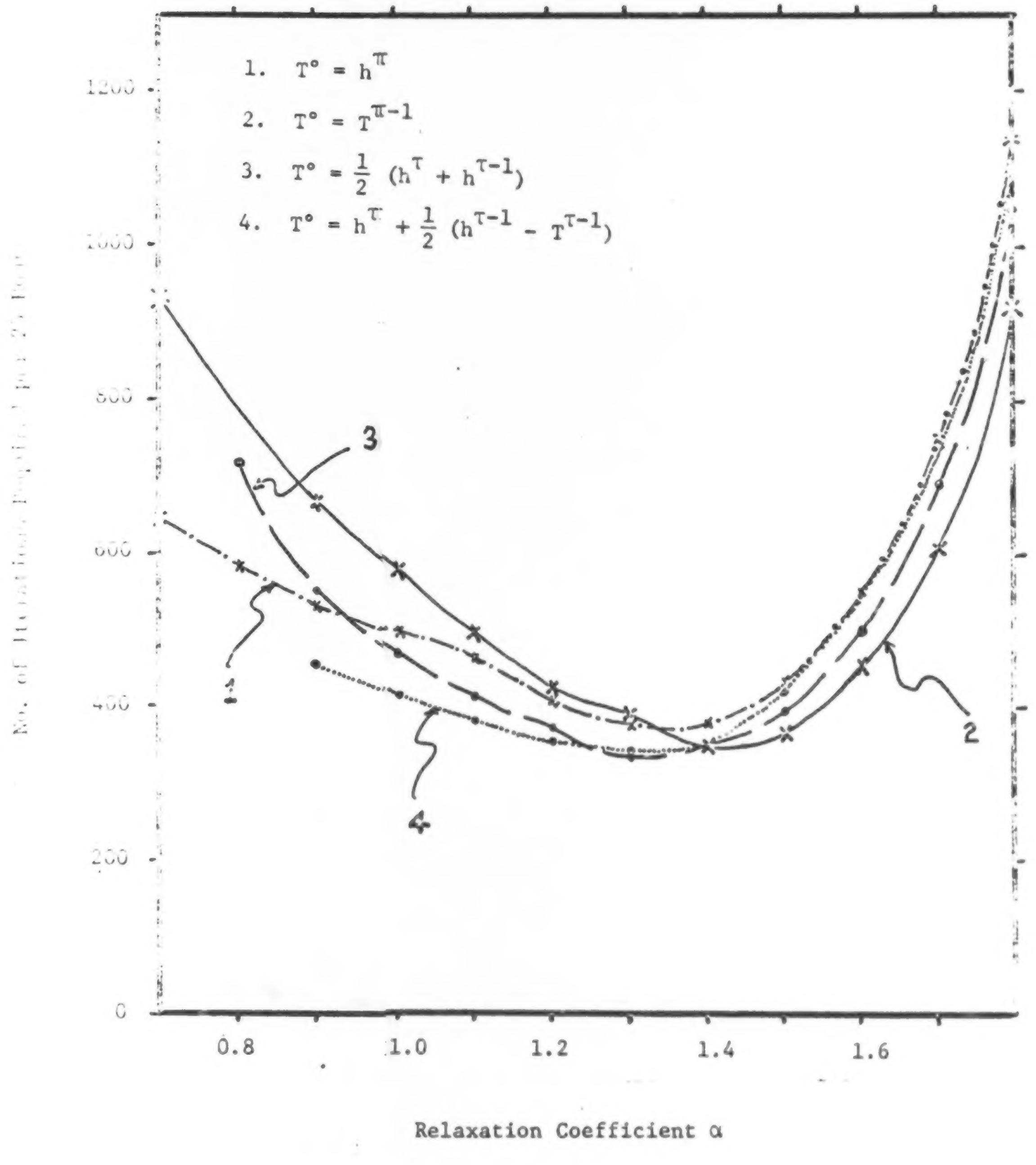

Figure 5.2 Number of iterations required per time step as a function of α for four different first guesses

Reproduced from best available copy.

discussed in the literature are 2- and 3-dimensional. Here, the extreme simplicity of the one-dimensional explicit model means that relatively few computational operations are required to make a 24 hour forecast when compared to the more complex equations and the relaxation process in the S.I. model. While both implicit and explicit models of two-dimensional flow are more complex and require more computations to produce a 24 hour forecast, the relative increase is greater in the explicit case. Thus the S.I. model should become more efficient compared to the explicit model as the number of dimensions increases.

5.3 Comparison of two-dimensional explicit and semi-implicit models

In this section, two-dimensional explicit and S.I. solutions of Haurwitz waves are compared. The basic equations of the explicit model are given in Section 4; the staggered grid for these experiments is shown in Fig. 5.3.

5.3.1 Development of the two-dimensional S.I. model. Equations (4.1) - (4.3) were the basis of the S.I. model. The pressure gradient terms, divergence terms, and tendency terms are treated implicitly, while all other terms were treated explicitly.

After linearization of the pressure gradient term, (4.1) - (4.3) are written:

$$\overline{h}^{2t} + \Delta t \; \overline{[\overline{(hu)}^{y}_{x} + \overline{(hv)}^{x}_{y}]}^{2t} = h^{\tau-1} \equiv F_4 \qquad (5.26)$$

$$\begin{aligned} \overline{hu}^{2t} + \Delta t\ g\ H\ \overline{\overline{h}^{y}_{x}}^{2t} &= (hu)^{\tau-1} - \Delta t g\ (\overline{h'}^{xy}\ \overline{h}^{y}_{x})^{\tau} \\ &\quad - \Delta t\ \left(\overline{\overline{u}^{x}\ \widehat{\overline{hu}}^{y}}^{x}\right)^{\tau}_{x} - \Delta t\ \left(\overline{\overline{u}^{y}\ \widehat{\overline{hv}}^{x}}^{y}\right)^{\tau}_{y} + \Delta t\ f(hv)^{\tau} \equiv F_{5} \end{aligned} \tag{5.27}$$

$$\begin{aligned} \overline{hv}^{2t} + \Delta t\ g\ H\ \overline{\overline{h}^{x}_{y}}^{2t} &= (hv)^{\tau-1} - \Delta t\ g(\overline{h'}^{xy}\ \overline{h}^{x}_{y})^{\tau} \\ &\quad - \Delta t\ \left(\overline{\overline{v}^{x}\ \widehat{\overline{hu}}^{y}}^{x}\right)^{\tau}_{x} - \Delta t\ \left(\overline{\overline{v}^{y}\ \widehat{\overline{hv}}^{x}}^{y}\right)^{\tau}_{y} - \Delta t\ f(hu)^{\tau} \equiv F_{6} \end{aligned} \tag{5.28}$$

Equations (5.26) - (5.28) now constitute a system of semi-implicit finite difference equations. As in the one-dimensional case, these equations cannot be solved directly; they must be altered and then solved by relaxation. First, equation (5.27) is differentiated by x and equation (5.28) by y in order that the divergence term may be eliminated in equation (5.26).

$$\overline{\overline{hu}^{y}_{x}}^{2t} + \Delta t\ g\ H\ \overline{\overline{h}^{yy}_{xx}}^{2t} = \overline{F_{5}}^{y}_{x} \tag{5.29}$$

$$\overline{\overline{hv}^{x}_{y}}^{2t} + \Delta t\ gH\ \overline{\overline{h}^{xx}_{yy}}^{2t} = \overline{F_{6}}^{x}_{y} \tag{5.30}$$

A substitution of equations (5.29) and (5.30) into (5.26) yields

$$\begin{aligned} \overline{h}^{2t} + \Delta t\ [-\Delta t\ g\ H\ \overline{\overline{h}^{yy}_{xx}}^{2t} -\Delta t\ g\ H\ \overline{\overline{h}^{xx}_{yy}}^{2t} + \overline{F_{5}}^{y}_{x} \\ + \overline{F_{6}}^{x}_{y}] = F_{4} \end{aligned} \tag{5.31}$$

$$\overline{h}^{2t} - \Delta t^2 \; g \; H \; [\overline{\overline{h}^{yy}_{xx} + \overline{h}^{xx}_{yy}}^{2t} \;] = F_4 - \Delta t \; (\overline{F}^{y}_{5} + \overline{F}^{x}_{6_y}) = G \quad (5.32)$$

Equation (5.32) is a Helmholtz equation and may be solved by the relaxation method for $\overline{h}^{2t}$, hereafter referred to as T. Then since $\Delta x - \Delta y$ on the two-dimensional grid, equations (5.14) and (5.15) are valid for the 2-D model as well as the 1-D model.

In order to solve for T, values of E_{ij} must be known at all interior x grid points (see Fig. 5.3). Then, a Liebmann (simultaneous) relaxation is carried out given a first guess of T, according to the relations

$$\begin{aligned} R^m_{i,j} = {} & T^m_{i+1,j} + T^{m+1}_{i-1,j} + T^m_{i,j+1} + T^{m+1}_{i,j-1} \\ & - (4 + \lambda^2) \, T^m_{i,j} - E_{i,j} \end{aligned} \quad (5.33)$$

$$T^{m+1}_{i,j} = T^m_{i,j} + \frac{\alpha R^m_{i,j}}{4 + \lambda^2} \quad , \quad (5.34)$$

where $\lambda^2 = \Delta x^2/(\Delta t^2 gH)$ and the relaxation coefficient, α, satisfies $0.5 < \alpha < 2.0$. The relaxation process is considered completed when the maximum residual across the grid has become less than some arbitrary ε. The choice of ε influences the number of iterations, and thus the speed of the computation, and the accuracy of the resulting forecast. For

ACKNOWLEDGEMENT

During the past year, the author was on sabbatical leave in Mainz, Germany, and in Risø, Denmark. A substantial portion of the author's support during this period was provided by the Alexander von Humboldt Foundation and the Danish Atomic Energy Commission; the remainder was provided out of general funds by The Pennsylvania State University. The author wishes to thank Professors K. Hinkelmann, F. Wippermann, and F. Fiedler for many stimulating dialogues about poor-man's methods of modeling boundary layer processes. These prepared the way for the fruitful experiments on semiquantitative methods that were conducted over a three-month period in Risø amid the encouragement of and helpful discussions with Dr. Niels Busch and his associates.

REFERENCES

Businger, J., J. C. Wyngaard, Y. Izumi, and E. F. Bradley, 1971: Flux-profile relationships in the atmospheric surface layer. J. Atm. Sci., V. 28, 181-189.

Crow, S. C., 1968: Viscoelastic properties of fine-grained incompressible turbulence. J. Fl. Mech., V. 33, 1-20.

Deardorff, J. W., 1972: Numerical invesitgation of neutral and unstable planetary boundary layers. J. Atm. Sci., V. 29, 91-115.

Hinkelmann, J., 1973: Personal communication.

Izumi, Y., 1971: Kansas 1968 Field Program Data. AFCRL Environmental Research Papers, No. 379. Air Force Cambridge Research Laboratories, L. G. Hanscom Field, Bedford, Mass.

Lilly, D. K., 1967: The representation of small-scale turbulence in numerical simulation experiments. Proc. IBM Sci. Comput. Symp. Environmental Sci., IBM Form No. 320-1951, 195-210.

Lumley, J. L., 1973: Modeling homogeneous deformation of turbulence. Symposium on Turbulence in the Planetary Boundary Layer, Moscow, August 28-31, 1973.

Lumley, J. L., and B. Khajeh-Nouri, 1973: Computational modeling of turbulent transport. pp. 84-133 in Select Research Group in Air Pollution Meteorology, First Annual Report. Department of Meteorology and Center for Air Environment Studies, The Pennsylvania State University, 210 pp.

Mahrt, L. J., 1973: A relationship of the Reynolds stress to local shear and heat fluxes in the planetary boundary layer. J. Atm. Sci., V. 30, 1577-1583.

Müller, E., 1973: Ph.D. Dissertation, Universität Mainz.

Rotta, J., 1951a: Statistische Theorie nichthomogener Turbulenz, 1 Mitteilung. Zeitschrift für Physik, V. 129, 547-572.

Rotta, J., 1951b: Statische Theorie nichthomogener Turbulenz, 2 Mitteilung. Zeitschrift für Physik, V. 131, 51-77.

Tennekes, H., and J. L. Lumley, 1973: A first course in turbulence, MIT Press, 300 pp.

Wyngaard, J. C., S. P. Arya, and O. R. Coté, 1974: Some aspects of convective planetary layers. J. Atm. Sci., V. 31, 747-754.

Wyngaard, J. C., O. R. Coté, and K. S. Rao, 1973: Modeling the Atmospheric Boundary Layer. 2nd IUTAM-IUGG Symposium on Turbulent Diffusion in Environmental Pollution, April 8-14, 1973, Charlottesville, Va.